Electronic structure of transition metal silicides and related compounds and interfaces

Witchlow, G. P.

Award date:
1988

Awarding institution:
University of Bath

ELECTRONIC STRUCTURE

OF

TRANSITION METAL SILICIDES

AND

RELATED COMPOUNDS AND INTERFACES

submitted by
G.P. Witchlow B.Sc.
for the degree of
Doctor of Philosophy
of the University of Bath
1988

G. P. Witchlow

ProQuest LLC
789 East Eisenhower Parkway
P.O. Box 1346
Ann Arbor, MI 48106-1346

ABSTRACT

An ab initio linear-combination-of-atomic-orbitals method is used to calculate the electronic structure of a number of systems, some with large unit cells. Considered are a number of near noble metal silicides (Ni_3Si, Ni_2Si, NiSi, $NiSi_2$, Pd_2Si, PdSi, Pt_2Si and PtSi) and a number of refractory metal disilicides ($CoSi_2$, $CrSi_2$, VSi_2, $NbSi_2$, $TaSi_2$, $MoSi_2$, WSi_2 and $ReSi_2$). There are features found to be common to the electronic structures of all of these silicides: a nonbonding metal d peak which is the dominant feature of the valence states, the presence of metal d-Si p hybridization giving rise to bonding states below and antibonding states above the nonbonding metal d peak, negligible contribution to the valence electronic structure from the metal s and p orbitals, little involvement of the Si s orbitals in bonding and little ionic contribution to the bonding. Also considered are three $NiSi_2$-Si(111) superlattices ($(NiSi_2)_1(Si)_5$, $(NiSi_2)_3(Si)_7$ and $(NiSi_2)_5(Si)_6$). For each of these there are found to be interface states with energies lying in the Si band gap. Another two systems studied are AuGeAs, which is formed at Ohmic Au-Ge-In contacts to GaAs Gunn diodes, and the isostructural and isoelectronic compound NiP_2. NiP_2 is found to be a semiconductor with an energy gap of 0.16 eV and AuGeAs is found to be a metal. Calculations are also

carried out for three other materials, the recently synthesized novel family of silver-cluster compounds $Ag_6Ge_{10}P_{12}$, $Ag_6Ge_6Sn_4P_{12}$ and $Ag_6Si_6Sn_4P_{12}$, and these are found to all be semiconducting and have energy gaps of 1.0, 0.7 and 0.8 eV respectively. An explanation of the origin of the semiconducting gap is proposed using formal electron counting.

ACKNOWLEDGEMENTS

I wish to thank Dr D.W. Bullett for his supervision of me in the work carried out for this thesis.

Also I thank Dr M.J. Kelly for the hospitality he showed me during my visits to the Hirst Research Centre.

Finally I thank Dr E.P. O'Reilly for the help and encouragement he gave me in the finishing of this thesis.

I would like to acknowledge the financial support of the Science and Engineering Research Council and the GEC Hirst Research Centre.

"who knows, perhaps He is a little malicious."

A. Einstein

CONTENTS

CHAPTER 1

INTRODUCTION

This thesis is concerned with the calculation of the electronic structure of a number of different systems. By the electronic structure of a solid what is meant is the quantum mechanical energy eigenvalue and eigenvector spectrum of its valence electrons. The reason that the electronic structure of a solid is of interest is because it determines virtually all of the properties of the solid: the optical properties, the transport properties, the magnetic properties, the elastic properties and lattice dynamics, the cohesion, and the crystal structure of a solid are all dependent on its electronic structure.

The valence electrons of a solid not only feel the potential due to the ions in the solid (which are usually considered as being immobile) but also interact with each other so that they form a many-body system. It is thus not strictly correct to talk of the energy of an individual electron. None the less, the electronic structure of a solid is invariably found by solving a one-electron-like equation of the form

$$\left\{-\frac{\hbar^2}{2m}\nabla^2 + V_{ion}(\underline{r}) + V(\underline{r}) + \Sigma\right\}\phi_j(\underline{r}) = E_j\,\phi_j(\underline{r}) \qquad (1.1)$$

where the E_j's are the energy eigenvalues sought. In equation (1.1) the terms in the braces refer to the different contributions to the energy of the electron (or quasi-electron) described by this equation. Going from left to right the first term is the kinetic energy, the second is the potential energy due to the ions, and the third and forth, $V(\underline{r})$ and Σ, together give the energy of the electron due to its interaction with all the other valence

electrons. $V(\underline{r})$ is called the Hartree potential and Σ is known as the exchange-correlation potential.

There are several ways of arriving at a one-particle equation such as (1.1) and the form of Σ and the interpretation of the eigenfunctions ϕ_j will depend upon the way it is done. It could be derived, for example, using Green's function theory (Hedin and Lundqvist, 1969), when Σ is also known as the electron self-energy and the E_j's are complex, or it could be derived using density functional theory (Hohenberg and Kohn, 1964; Kohn and Sham, 1965; Callaway and March, 1984), or then again it could be arrived at from the Hartree-Fock approximation (Ashcroft and Mermin, 1976).

Σ and $V(\underline{r})$ are themselves dependent upon the eigenfunctions ϕ_j so that (1.1) must be solved self-consistently. Furthermore, Σ almost always contains a complicated nonlocal (i.e. integral) operator. This can make solving (1.1) very difficult and it is therefore usual to approximate the nonlocal operator by a local one. Such an approximation is called a local density approximation (LDA) and there are many of them, but all are based on the behaviour of a homogenous electron gas. (Some LDA's have recently been briefly discussed by Callaway and March, 1984).

In density functional calculations of the electronic structure of metals the LDA has proved very successful. However, the electronic structure calculations for semiconductors which have used the LDA have been found to give band gaps that are 20-50% too small (Pickett and Wang,

1984). It is usually said that the LDA is only valid for systems where the valence charge density varies slowly in space and that this is why it fails for semiconductors, in which charge is found in bonds and is thus far from being uniformly distributed.

Once a suitable one-electron equation has been settled upon there are a large number of different methods available by which it can be solved. (This situation is nicely suggested by the Kipling quotation used in Ziman (1972) at the beginning of the chapter on electron states: "There are nine and sixty ways of constructing tribal lays, and-every-single-one-of-them-is-right."). One of the important differences between different methods is the choice that is made for the set of basis functions used to expand the eigenfunctions of (1.1). In general only the less energetic solutions of (1.1) are of interest: the valence states and the lower lying conduction states. The basis functions chosen to expand this finite set of eigenfunctions are usually a subset of a complete set of functions. When this is the case the more basis functions that are used the more accurate are the calculated eigenvalues and eigenfunctions. Using more basis functions, however, also, of course, means that a greater amount of computation is required to obtain these results. If, for example, plane waves were used as basis functions several hundred would be required to yield accurate answers, and this would represent an unacceptably long calculation. By careful choice of the form of the basis functions used,

however, accurate answers can be obtained using a reasonably small number of them.

A general survey of the methods used to solve the one-electron problem for a solid has been given by Ziman (1971), and the methods described therein have been used to find the electronic structure of simple periodic solids with great success. However, for a crystal with a large unit cell these methods can still require prohibitive amounts of computation. Consider also, for example, the problem of calculating the electronic structure of a solid with a free surface. This is usually tackled by considering a slab of solid infinite in extent in two dimensions and thick enough in the third so that each of the two surfaces of the slab are "unaware" of the presence of the other. The unit cell of this system will span the thickness of the slab and will thus contain many atoms. Hence the solid itself may be simple but the unit cell of the system will be very large, probably too large to be easily dealt with using one of the sophisticated methods of electronic structure calculation.

For systems with a large unit cell the method which comes into its own is the linear-combination-of-atomic-orbitals (LCAO) method. In this the eigenfunctions of the system are expanded in the valence atomic orbitals of the atoms in the solid. Although the LCAO method dates back to the beginnings of solid state physics (Bloch, 1928), until quite recently it has only been regarded as a qualitative method. This is because it was by no means clear that the valence atomic orbitals span the space of the crystal valance eigenfunctions. If they did not it was then

doubtful whether including higher energy atomic orbitals in the expansion would help as this might then introduce linear dependence into the basis functions (i.e. give an overcomplete set of basis functions).

In the last few years, there has been a renaissance of the LCAO method with a substantial amount of quantitative calculation being done with it (Bullett, 1980a). Furthermore, the relatively recent theory of chemical pseudopotentials (for a gentle introduction see Anderson, 1984) has shown that a set of localized basis functions may be defined in which the expansion of the crystal valence eigenfucntions is exact and that these basis functions are atomic-orbital-like and has thus given a quantum mechanical justification of the LCAO method.

Bullett, the main exponent of the chemical pseudopotential LCAO method, has demonstrated the value of that LCAO method in particular by using it to do electronic structure calculations for many crystals with large unit cells, for which more elaborate calculations would be very difficult. He has, for example, used it with much success for transition metal layered dichalcogenides (Bullett, 1978), transition metal trichalcogenides (Bullett, 1979), niobium chalcogenides (Bullett, 1980b, 1982a), transition metal disulphides (Bullett, 1982b), several different phases of elemental boron (Bullett, 1982c), iron borides (Joyner et al., 1981), and Cu-III-IV_2 chalcopyrites (Neumann et al., 1984). It is this LCAO method which is used to investigate the electronic structure of the systems considered in this thesis.

In Chapter 2 the meaning of the electronic structure of a solid is considered further, and a suitable one-electron equation is derived. The LCAO method used to solve this equation is then outlined, and after that so is the theory of chemical pseudopotentials. Considered last is the computational procedure actually followed when calculating the electronic structure of a solid.

There is at present a great deal of interest in the electronic structure of transition metal silicides and silicon-silicide interfaces. This is testified to by, for example, the recent review article on the subject by Calandra et al. (1985) and the references cited therein. Much of this interest arises from the possible use of silicides in integrated circuits as Schottky barriers, Ohmic contacts, and low resistance gates and interconnections (Murarka, 1980).

Silicides take up a large number of different atomic structures, some of which are quite complicated. Consequently the more elaborate self-consistent calculations of the electronic structure of silicides (e.g. the augmented-spherical wave calculations of Weaver et al., 1984) have been based on different, simpler crystal structures while calculations which have treated silicides in their correct structures have been of the LCAO type (e.g. the extended Hückel calculations of Bisi and Calandra, 1981). Here also, in order to calculate the electronic structure of a number of silicides in their actual crystal structures an LCAO method was used. Chapter 3 presents the results of chemical pseudopotential LCAO calculations for

the electronic structure of the near noble metal silicides Ni_3Si, Ni_2Si, NiSi, $NiSi_2$, Pd_2Si, PdSi, Pt_2Si, and PtSi and of the refractory metal disilicides $CoSi_2$, $CrSi_2$, VSi_2, $NbSi_2$, $TaSi_2$, $MoSi_2$, WSi_2, and $ReSi_2$.

It has been found that some metal silicides grow epitaxially on a silicon substrate, and there is at present much interest in these systems also (Tung, et al., 1982a, 1986a). In particular it has been found that two silicides $CoSi_2$ (Tung et al., 1982b) and $NiSi_2$ (Tung et al., 1983a) can be grown as epitaxial monocrystals on Si(111). The resulting Si-silicide interfaces have been found to be abrupt and have a regular lattice structure on the atomic scale. They represent the closest systems in existence to a structurally perfect and abrupt metal-semiconductor junction. This perfection makes them very attractive systems to study when considering the physics of metal-semiconductor interfaces, both theoretically (Bisi et al., 1984) and experimentally (Tung, 1984a). Also, it has further been found possible to grow epitaxial Si-silicide-Si systems with both $CoSi_2$ and $NiSi_2$ (Bean and Poate, 1980; Tung et al., 1986b). Such buried metal layers open up the possibility of new types of device (Shiraki, 1985) and even three-dimensional integration.

In Chapter 4 the results are presented of a theoretical study of the electronic structure of a number of systems containing $NiSi_2$-Si(111) interfaces. To calculate the electronic structure of these complicated systems the chemical pseudopotential LCAO method was once again employed.

Chapter 5 presents chemical pseudopotential LCAO electronic structure calculations for the equiatomic ternary compound AuGeAs, which is formed at Ohmic Au-Ge-In contacts to GaAs Gunn diodes, for the isostructural compound NiP_2, and for the recently synthesized novel family of silver-cluster compounds $Ag_6Ge_{10}P_{12}$, $Ag_6Ge_6Sn_4P_{12}$, and $Ag_6Si_6Sn_4P_{12}$.

CHAPTER 2

THEORY AND METHOD OF CALCULATION

2.1 Introduction

A solid is a system of some 10^{23} particles, electrons and atomic nuclei, each interacting with every other via the long range Coulomb force. Many properties of a solid may be considered in a classical framework, but a much deeper insight is gained, and in many cases insight is only gained by treating it as a quantum mechanical system. As with any other quantum mechanical system, it will possess a spectrum of allowed energy states E_n given by the solutions of the Schrödinger equation

$$H\Psi_n = E_n\Psi_n \,, \tag{2.1}$$

where H is the Hamiltonian for the solid and Ψ_n is the wave function describing the solid in the energy eigenstate n. Knowledge of Ψ_n would allow the expectation value of any observable of the solid in state n to be calculated so that if, for example, Ψ_o was known all the ground state properties of the solid could be calculated. Further, if all the energy eigenvalues and corresponding wave functions were known then the expectation value of any observable A of the solid in thermal equilibrium could be found using

$$\langle A \rangle = tr\{\rho A\} \,, \tag{2.2}$$

where ρ is the density operator and is given by

$$\rho = e^{-\beta H}/Z \,. \tag{2.3}$$

Here Z is the canonical partition function and is

given by

$$Z = tr\{e^{-\beta H}\} \tag{2.4}$$

and

$$\beta = 1/kT \tag{2.5}$$

as usual. However, as the Hamiltonian and the wave function are both functions of the order of 10^{23} parameters, solving (2.1) exactly is, of course, impossible.

Finding the solution in (2.1) constitutes what is commonly called a many-body problem. It should be noted that the necessary ingredients of a many-body problem are many bodies together with an interbody interaction: without the interbody interaction it would simply become many one-body problems. For example, if there was no Coulomb interaction in (2.1) it would decompose into a single-particle Schrödinger equation for each electron and nucleus. An energy eigenstate of the solid could then be described by which single-particle state each of the constituent particles occupied and the eigenenergy of the solid would be the sum of the single particle eigenenergies, as is the case for an ideal quantum gas. In the case of an actual solid it is not possible to identify an eigenstate with the states of the constituent particles in this way.

It is not possible to find an approximate solution to (2.1) using conventional perturbation theory, treating the solid as a collection of free particles perturbed by a Coulomb interaction, because here the perturbation term will

not be small compared to the unperturbed energy eigenvalues (the kinetic energy of the particles). There do exist, however, other systematic perturbation techniques that can be used to help solve many-body problems such as (2.1) and these are generally referred to as many-body, quantum-field-theoretical or Green's functions methods.

Green's functions methods can be used to calculate the properties of solids in their ground state, slightly excited states and in thermal equilibrium at non-zero temperatures. They are, however, complicated and of considerable mathematical sophistication and will not be used anywhere in this work. They do, however, provide the theoretical underpinning for what has become a unifying concept of solid state physics, the idea of elementary excitations.

It is often found that the state of a strongly interacting many-body system can be regarded as a state of weakly interacting, or in some cases, non-interacting elementary excitations. For example, the states of a harmonic lattice where each particle interacts strongly with its neighbour via a quadratic potential can be regarded as the states of a system of non-interacting phonons. Here the phonons cannot be associated obviously with any one of the "real" particles of the system, and such elementary excitations are often called collective modes.

Another example occurs in the Jellium model of a solid. This is a system consisting of electrons moving in a

constant potential due to a uniform distribution of positive background charge. The positive charge is exactly equal in magnitude to the charge of the electrons so that the system, like a real solid, is overall neutral. The low-lying excited states of the interacting electron gas can be represented by a ground state together with a small number of weakly interacting quasi-electrons. This kind of elementary excitation can be associated with a real particle and is often generically referred to as a quasi-particle. The quasi-electron can be pictured as a real electron together with a hole in the distribution of the other electrons centred on it. (Electrons will avoid each other because of their electrostatic repulsion, an effect known as correlation, and, if they are of like spin, because of the Pauli exclusion principle, an effect known as exchange). This hole, which is often referred to as an exchange and correlation hole, screens the electron by allowing the background positive charge to "show through" around it and this is why the quasi-electrons are only weakly interacting.

If only the ground state properties of the solid are to be considered then (2.1) need only be solved for its lowest eigenvalue, but even then a series of approximations is still necessary to be able to solve it. In particular, although it has been stressed above that (2.1) does not decompose into separate one-particle Schrödinger equations, the approximation that assumes it does will simplify the problem greatly and is almost always used in non-quantum-field-theoretical methods of solving (2.1).

The form that the one-electron Schödinger equation should take is what is considered in section 2.2. The energy spectrum of the one-electron Schödinger equation for a particular material is often referred to as the electronic structure of that material, and it is calculating the electronic structure for a variety of different materials with which this thesis is concerned. Given a one-electron Schrödinger equation, however, there are still many different ways of solving it. The method used herein (an ab initio LCAO method) is described in section 2.3 and section 2.4 outlines the justification for its use. The calculational procedure that was followed in order to carry out this method is described in section 2.5.

2.2 The one-electron equation

Firstly the explicit form of the Hamiltonian appearing in (2.1) needs to be considered. It is made up of the kinetic energy of all the electrons and nuclei in the solid and their interaction energies. As mentioned above a series of approximations has to be introduced if (2.1) is to be solved and the first that will be used here is to assume that a non-relativistic Hamiltonian can be used. For solids made up of light atoms this is quite reasonable, but the approximation becomes worse as the atomic number of the constituent atoms increases. Also the spin dependence of the electron energies will be neglected and in all the equations that follow (except where exchange is introduced) the dependence of the one-electron orbitals on spin will not be indicated. Next there are considered to be two

different types of electron in the solid; valence electrons, which contribute to the physical properties of the solid, and core electrons, which remain tightly bound to the nuclei of the solid and do not. Each nucleus together with its attendant core electrons is then regarded as a single entity, a lattice ion, and the solid is now considered as consisting of lattice ions and valence electrons (which henceforth will simply be referred to as electrons). With this approximation made the Hamiltonian for the solid can be written as

$$H = H^{el} + H^{ion} + H^{ion-el} . \qquad (2.6)$$

Writing out the electron part explicitly gives

$$H^{el} = \frac{-\hbar^2}{2m} \sum_i \nabla_i^2 + \frac{1}{2} \sum_{ii'}{}' \frac{e^2}{4\pi\epsilon_0 |\underline{r}_i - \underline{r}_{i'}|} , \qquad (2.7)$$

where the sums over i and i' are over all the electrons in the solid, ∇_i operates on the coordinates $\underline{r}_i$ of the i^{th} electron and m and e are the electron mass and charge respectively. The primed sum indicates that it does not include the terms for i = i'. Similarly the term for the ions is given by

$$H^{ion} = \sum_j \frac{-\hbar^2}{2M_j} \nabla_j^2 + \frac{1}{2} \sum_{jj'}{}' V^{ion}(\underline{R}_j - \underline{R}_{j'}) . \qquad (2.8)$$

Here M_j is the mass of the j^{th} ion. The explicit form of the ion-ion interaction has been left open except for assuming that it can be described as a sum over pair-wise potentials, that is to say terms which depend only on the

relative positions of two ions at a time with the positions of the rest of the ions being unimportant. In the same way the ion-electron term can be expressed as

$$H^{ion-el} = \sum_{Kl} V^{ion-el}(\underline{r}_K - \underline{R}_l) . \qquad (2.9)$$

The pair-wise assumption, that the potential due to an ion is independent of the configuration of the rest of the ions and electrons, is sometimes called the frozen core approximation.

Next it is useful to introduce the Born-Oppenheimer or adiabatic approximation (Born and Oppenheimer, 1927), that is to assume that the ions are infinitely massive so that they move infinitely slowly, or adiabatically. Although this is, of course, not the case, as the mass of the ions will be thousands of times greater than that of the electrons they will more very slowly (in response to changes in the electron configuration) compared to the electrons which can respond to changes in the ion configuration almost instantly. In the adiabatic approximation the wave function for the solid can be written as the product

$$\Psi(\underline{r}, \underline{R}) = \psi(\underline{r}, \underline{R})\,\phi(\underline{R}) , \qquad (2.10)$$

where $\psi(\underline{r},\underline{R})$ describes the state of the electrons for the instantaneous ion configuration $\underline{R}$ and satisfies

$$\{H^{el} + H^{ion-el}\}\psi(\underline{r}, \underline{R}) = E^{el}(\underline{R})\psi(\underline{r}, \underline{R}) , \qquad (2.11)$$

and $\phi(\underline{R})$ describes the state of the ions and satisfies

$$\{H^{ion} + E^{el}(\underline{R})\}\,\phi(\underline{R}) = E\,\phi(\underline{R}) . \qquad (2.12)$$

(Here $\underline{R}$ and $\underline{r}$ have been used to stand for the sets of values $\{\underline{R}_j\}$ and $\{\underline{r}_i\}$.) For a more detailed consideration of this approximation, including the condition for its applicability, see, for example, Davydov (1965).

As it is the ground state that is of interest the ground state ion configuration $\underline{R}^o$ should be used in (2.11) when solving it for the electronic ground state. To actually calculate $\underline{R}^o$ would require not only finding the ground state solution of (2.12) but also simultaneously that of (2.11) as (2.12) is coupled to it by virtue of the term $E^{el}(\underline{R})$. Consequently, as appealing as it would be to find $\underline{R}^o$ from first principles it is usual to solve (2.11) using experimentally found ion positions (e.g. by X-ray crystallography). The ions are not, of course, at rest in their ground state and it is the mean ion positions that are observed experimentally and used in solving (2.11).

The central equation for consideration is now (2.11). In future indication of its dependence on $\underline{R}$, which is taken from now on to be held at $\underline{R}^o$, will be dropped and its eigenvalues will be denoted simply by E. This equation is simpler than (2.1) but it is still a many-body equation. As mentioned above this will be tackled by making a one-electron approximation, but before doing so for the general problem of the solid the solution for the Jellium model will be considered as a short introductory aside.

An obvious form to try for the Jellium one-electron equation is

$$\frac{-\hbar^2}{2m}\nabla^2\phi_j(\underline{r}) - eV\phi_j(\underline{r}) - \frac{e}{4\pi\epsilon_o}\int\frac{\rho'(\underline{r}')}{|\underline{r}-\underline{r}'|}\,d^3\underline{r}'\,\phi_j(\underline{r}) = E_j\phi_j(\underline{r}). \qquad (2.13)$$

The first term is for the electron's kinetic energy, the second for its potential due to the uniform background positive charge, and the third term is for its potential due to its interaction with all the other electrons. In the third term $\rho'(r')$ is the charge density due to all the other electrons and is given by

$$\rho'(\underline{r}') = -e \sum_{\substack{i=1 \\ i\neq j}}^{N} |\phi_i(\underline{r}')|^2 \qquad (2.14)$$

where N is the total number of electrons in the solid. This expression assumes that all the electrons move independently of each other, that is to say it assumes that their motions are uncorrelated. It also depends on $\{\phi_i(\underline{r})\}$, but this is just what (2.13) is being solved for. Thus, in order to solve (2.13) a guess for the form of $\{\phi_i(\underline{r})\}$ must be made first, this guess used to calculate $\rho'(\underline{r}')$, and then this form for $\rho'(\underline{r}')$ used to calculate a new set of functions $\{\phi_i(\underline{r})\}$. The above process must then be repeated, each time using the new set $\{\phi_i(\underline{r})\}$ found from the previous calculation as the starting guess until the new calculated set is the same as the starting guess, that is to say until self-consistency is achieved. This is a common aspect of one-electron equations and such approximations are often referred to as self-consistent field (SCF) approximations. If a set of plane waves were used as the trial wave functions in (2.13) this would lead to $\rho'(\underline{r}')$ being uniform over the solid. This negative charge would almost entirely cancel the background positive charge leaving (2.13) the equation for an electron moving in a very shallow potential

well (+e spread evenly over the entire solid). The solutions to this equation are plane waves and thus it can be seen that the self-consistent solutions of (2.13) are plane waves.

It is interesting to write $\rho'(\underline{r}')$ in a different way. Defining the total electronic charge density $\rho(\underline{r})$ by

$$\rho(\underline{r}) = -e \sum_{i=1}^{N} |\phi_i(\underline{r})|^2 \qquad (2.15)$$

and the function $\rho^c(\underline{r})$ by

$$\rho^c(\underline{r}) = -e\,|\phi_j(\underline{r})|^2 \qquad (2.16)$$

allows $\rho'(\underline{r}')$ now to be written as

$$\rho'(\underline{r}') = \rho(\underline{r}') - \rho^c(\underline{r}') . \qquad (2.17)$$

It has been mentioned above that an electron will be accompanied by a hole in the distribution of the other electrons and in this case this hole is represented by $\rho^c(\underline{r}')$. Here, however, ρ^c is independent of $\underline{r}$, the position of the test electron (the j^{th} electron in equation (2.13)), so that this hole doesn't follow the motion of the test electron, and this corresponds to the statement made after the definition of ρ' (2.14) that this definition for ρ' ignores electron correlation.

In the same way that the eigenstates of a single-particle operator form a complete set in which any general single-particle state may be expanded, (NxN) Slater determinants made up from one-particle eigenfunctions form a complete set in which any general N-fermion wave function

may be expanded. For example, the N-fermion wave function $\psi(\underline{r}_1 \ldots \underline{r}_N)$ which satisfies (2.11) could be expanded thus

$$\psi(\underline{r}_1 \ldots \underline{r}_N) = \sum_{ij\ldots k} a_{ij\ldots k} \frac{1}{\sqrt{N!}} \begin{vmatrix} \phi_i(\underline{r}_1) \ldots \phi_i(\underline{r}_N) \\ \vdots \quad\quad \vdots \\ \phi_k(\underline{r}_1) \ldots \phi_k(\underline{r}_N) \end{vmatrix} \tag{2.18}$$

where $\{\phi_i(\underline{r})\}$ satisfy

$$h\phi_i(\underline{r}) = \varepsilon_i \phi_i(\underline{r}), \tag{2.19}$$

with h being any one-electron operator.

If ψ could be written as a single Slater determinant

$$\psi(\underline{r}_1 \ldots \underline{r}_N) = \frac{1}{\sqrt{N!}} \begin{vmatrix} \phi_i(\underline{r}_1) \ldots \phi_i(\underline{r}_N) \\ \vdots \quad\quad \vdots \\ \phi_k(\underline{r}_1) \ldots \phi_k(\underline{r}_N) \end{vmatrix} \tag{2.20}$$

it would correspond to a state in which there was a particle definitely in state i, other definitely in state j, and so on. With interacting particles this cannot be so, but (2.20) does represent an obvious approximation to (2.18). In this approximation (2.19) becomes the sought after one-electron equation. To find the form of it, because it is the ground state wave function that is of interest, the variational principle can be used.

The basis of the variational principle is that the wave function ψ which minimizes the expectation energy of the system

$$\langle E \rangle = \langle \psi | H | \psi \rangle \tag{2.21}$$

is the exact ground state wave function for the system. (ψ is assumed normalized in (2.21)). ψ must be allowed to take on any form when minimizing (2.21) if the exact ground state wave function is to be found, but minimizing (2.21) using a wave function of form (2.20) will give the best ground state

electron wave function within the limits of the ansatz (2.20). Doing this requires that

$$\frac{\delta}{\delta \phi_i^*} \langle E \rangle = 0 \qquad (2.22)$$

for each ϕ_i ($\frac{\delta}{\delta \phi_i^*}$ is the functional derivative with respect to the function ϕ_i^*) and using the Hamiltonian of (2.11) in (2.21) this leads to the Hartree-Fock (HF) equations (Madelung, 1978)

$$\left\{ \frac{-\hbar^2}{2m} \nabla^2 + U^{ion}(\underline{r}) + \frac{e^2}{4\pi\epsilon_0} \sum_{i \neq j} \int \frac{|\phi_i(\underline{r}')|^2}{|\underline{r} - \underline{r}'|} d^3\underline{r}' \right\} \phi_j(\underline{r})$$

$$\frac{-e^2}{4\pi\epsilon_0} \sum_{\substack{i \neq j \\ \text{spin parallel to } j}} \int \frac{\phi_i^*(\underline{r}') \phi_i(\underline{r}) \phi_j(\underline{r}')}{|\underline{r} - \underline{r}'|} d^3\underline{r}' = E_j \phi_j(\underline{r}). \qquad (2.23)$$

Here

$$U^{ion}(\underline{r}) = \sum_l V^{ion-el}(\underline{r} - \underline{R}_l). \qquad (2.24)$$

The E_j's are introduced initially as Lagrange multipliers, needed in the variational calculation to take into account the auxiliary condition

$$\langle \psi | \psi \rangle = 1, \qquad (2.25)$$

but consideration of the resulting equations leads to the conclusion that they represent the binding energies of the electrons in the solid. This result is known as Koopman's theorem. These equations, one for each electron, are the sought after one-electron equations. They are very similar to (2.13), but now there is an extra term which depends on the other electrons which have spin parallel to that of the test electron. This is the exchange term. To see what it

represents it is instructive to rewrite the last two terms of (2.23) using $\rho(\underline{r})$ defined in (2.15) and ρ^{ex} defined by

$$\rho^{ex}(\underline{r},\underline{r}') = -e \sum_{\substack{i \\ \text{spin parallel to } j}} \frac{\phi_i^*(\underline{r}')\,\phi_i(\underline{r})\,\phi_j^*(\underline{r})\,\phi_j(\underline{r}')}{\phi_j^*(\underline{r})\,\phi_j(\underline{r})} . \quad (2.26)$$

Using these the HF equations can be rewritten as

$$\left\{ \frac{-\hbar^2}{2m}\nabla^2 + U^{ion}(\underline{r}) - \frac{e}{4\pi\epsilon_0}\int \frac{\rho(\underline{r}') - \rho^{ex}(\underline{r},\underline{r}')}{|\underline{r}-\underline{r}'|}\, d^3\underline{r}' \right\} \phi_j(\underline{r})$$

$$= E_j\,\phi_j(\underline{r}) . \quad (2.27)$$

The exchange charge density $\rho^{ex}(\underline{r},\underline{r}')$, like $\rho^c(r')$ discussed above, intergrates over all space to -e, but unlike $\rho^c(r')$ it is localized around electron j at position $\underline{r}$ and represents the denudation around that electron of electrons of parallel spin expected from Pauli's principle.

As with equation (2.13) (2.27) has to be solved self-consistently. It is much more difficult to solve, however, because of the exchange term, which is non-local, and to do so for all but the simplest systems an approximation for the exchange term is generally made. The most commonly used is a local density approximation (LDA) called the Xα approximation. This is an extension of the Slater (Slater, 1951) and Dirac (Dirac, 1930) exchange approximations, the forms of which are given by averages of the Jellium exchange potential and depend only on the local

density of parallel-spin electrons in the system. In the Xα approximation the exchange term is replaced by

$$U^{ex}(\underline{r})\,\phi_j(\underline{r}) \qquad (2.28)$$

where

$$U^{ex}(\underline{r}) = -\alpha\, 3\, e^2 \left\{\frac{\rho(\underline{r})}{8\pi}\right\}^{1/3}. \qquad (2.29)$$

In this expression it has been assumed that there are an equal number of spin-up and spin-down electrons in the system, so that

$$\rho_{\uparrow}(\underline{r}) = \tfrac{1}{2}\,\rho(\underline{r}). \qquad (2.30)$$

With the parameter α set to 1 (2.29) becomes the Slater exchange approximation, while setting it to $^{2}/_{3}$ makes (2.29) the Dirac exchange approximation. In calculations α is chosen to have a value, somewhere between these two extremes, that is optimal for the particular system being considered (Slater, 1965). Using the Xα approximation in the HF equations (2.27) yields the Hartree-Fock-Slater (HFS) equations

$$\left\{\frac{-\hbar^2}{2m}\nabla^2 + U^{ion}(\underline{r}) + U^{el}(\underline{r}) + U^{ex}(\underline{r})\right\}\phi_j(\underline{r}) = E_j\,\phi_j(\underline{r}) \qquad (2.31)$$

where

$$U^{el}(\underline{r}) = \frac{-e}{4\pi\epsilon_o}\int \frac{\rho(\underline{r}')}{|\underline{r}-\underline{r}'|}\, d^3\underline{r}'. \qquad (2.32)$$

Although the correlation of the motion of the electrons of like spin has been taken into account to a certain degree, by the inclusion of an exchange potential, no account has

yet been taken of the correlation of the motion of the electrons simply due to their electrostatic repulsion. One way of treating this in a solid is to use an extention of the Wigner-Seitz approximation (Wigner and Seitz, 1933; Seitz, 1940) sometimes called the Wigner trick (Anderson, 1968a; Bullett, 1975; Heine, 1980). In this the solid is divided into spherical cells with one centred on each atom. Each of these cells is regarded as being electrically neutral and as having no higher electric moments so that the electrons and nucleus in a cell contributing nothing to the crystal potential outside their own cell. An electron inside a cell is thus then regarded as feeling only an appropriate atomic potential.

The fact that electrical neutrality is maintained in each of the cells indicates the way in which this approximation for the form of the crystal potential takes into account electron correlation. For each cell to remain neutral whenever an electron moves from one cell to another that electron must displace another electron from the new cell. The displaced electron must then displace another, and so on, ending with the originally vacated cell being refilled. This corresponds to an electron having a correlation hole that is the size of a cell. This hole, however, instead of being centred on the test electron and following its every move, only moves if the test electron moves into a new cell, when it jumps instantaneously and completely across to fill that new cell. Using the Wigner

trick crystal potential the one-electron equation can now be written as

$$H\psi(\underline{r}) \equiv \left\{T + \sum_l V_l^{cl}(\underline{r}-\underline{R}_l)\right\}\psi(\underline{r}) = E\psi(\underline{r}) \qquad (2.33)$$

where T is the kinetic energy operator, given by

$$T = \frac{-\hbar^2}{2m}\nabla^2 , \qquad (2.34)$$

$\underline{R}_1$ is the position of atom 1 in the solid and $V_1(\underline{r})$ is the free atom potential for that kind of atom. The superscript cl indicates that this potential extends only to the edge of the cell centred on site 1. This equation, unlike the HFS equation, is not self-consistent. The potential it uses does not depend upon the solutions $\psi(\underline{r})$. This makes it much easier to solve, but represents, of course, a further approximation.

An atom by itself represents a many-body system and in order to find the energy eigenstates of its electrons it is usual to solve an atomic HFS equation like

$$H_l^{at}\phi_\alpha(\underline{r}-\underline{R}_l) \equiv \left\{T + V_l(\underline{r}-\underline{R}_l)\right\}\phi_\alpha(\underline{r}-\underline{R}_l) = \varepsilon_{l\alpha}\phi_\alpha(\underline{r}-\underline{R}_l). \qquad (2.35)$$

In this the atom potential $V_1(\underline{r}-\underline{R}_1)$ is given by

$$V_l(\underline{r}-\underline{R}_l) = \frac{-Ze^2}{4\pi\epsilon_o|\underline{r}-\underline{R}_l|} + V^{el}(\underline{r}) + V^{ex}(\underline{r}) \qquad (2.36)$$

where the first term is the electron's potential due to the atomic nucleus, the second is its potential due to the other electrons and is given by equations like (2.32) and (2.15), and the last term is an $X\alpha$ exchange potential given by (2.29). It is self-consistent potentials of this kind,

found from solving (2.35), that can be used in setting up the Wigner trick crystal potential used in (2.33).

The one-electron equation (2.33) which uses a Wigner trick crystal potential constructed from SCF HFS atomic potentials was the equation that was solved in this work to find the electronic structure of the systems studied. The way in which it was solved is considered in the next section.

2.3 Solving the one-electron equation

To solve the one-electron Schrödinger equation

$$H\psi_i = E\psi_i \tag{2.37}$$

it is usual to start by expanding the eigenfunctions ψ_i in a complete set of basis functions $\{\phi_\alpha\}$ thus

$$\psi_i(\underline{r}) = \sum_\alpha c_{i\alpha}\phi_\alpha(\underline{r}). \tag{2.38}$$

Solving the Schrödinger equation then becomes equivalent to solving the secular equation

$$\det|H - SE| = 0 \tag{2.39}$$

or, equivalently,

$$\det|D - E| = 0 \tag{2.40}$$

where

$$D = S^{-1}H. \tag{2.41}$$

Here S and H are the overlap and Hamiltonian matrices in the particular representation chosen. In many calculations

plane-wave-like sets of basis functions are used. The expansion (2.38) can then be made as accurate as desired, but a very large number of terms may have to be included and this means that very large matrices then have to be processed in order to solve (2.39). The computational time required to do this can become prohibitive when dealing with complicated systems. Also, as the basis functions are extended, this approach can only be used for systems with tranlational symmetry.

In the linear-combination-of-atomic-orbitals (LCAO) method the basis functions chosen are the valence atomic orbitals of each of the atoms in the crystal. Unlike the basis sets of extended functions which are chosen in the knowledge that they form a complete set it is not obvious that this set spans the eigenfunctions of H and LCAO calculations were long regarded as a consequence as only being able to give qualitative results. However, the work of Adams (1961, 1962, 1971a, 1971b, 1971c, 1974), Gilbert (1964) and Anderson (1968b, 1969) has shown that a set of localized orbitals can be defined that exactly span the eigenfunctions of a solid and furthermore that these localized functions are very close to the actual atomic orbitals of the atoms in the solid. This work, which will be discussed briefly in section 2.4, thus provides a theoretical justification for the LCAO method.

When the solid possesses translational symmetry the problem can be greatly simplified by using Bloch functions constructed from the atomic orbitals as basis functions.

For each orbital type in a unit cell used a Bloch function can be constructed thus

$$\psi_{\alpha \underline{k}}(\underline{r}) = \frac{1}{\sqrt{N}} \sum_{i=1}^{N} e^{i\underline{k}.\underline{R}_i} \phi_\alpha(\underline{r} - \underline{R}_i). \qquad (2.42)$$

Here a finite amount of solid is considered containing N unit cells. So that the system still possesses translational symmetry periodic boundary conditions are taken to prevail. $\underline{R}_i$ is the position vector of the i^{th} site on which an orbital of type α is centred. (There are N of these sites, one per unit cell, and each is separated from any of the others by a crystal lattice vector). Expression (2.42) actually defines N new basis functions for each α, one for each of the allowed values of $\underline{k}$, so that, as must be the case, there are as many of the new basis functions as there were of the old.

The advantage of using Bloch functions as basis functions instead of the atomic orbitals themselves is that because of the translational symmetry of H the matrix elements of H between two Bloch functions with different values of $\underline{k}$ will be zero. This means that using Bloch functions for a system with p orbitals per unit cell will make the matrix H block diagonal with N blocks, one for each value of $\underline{k}$, each of dimension p. Thus the (Np x Np) secular equation (2.39) is decomposed into N(p x p) secular equations, which form a much more tractable problem. As N is usually taken to be very large the (p x p) matrices H and S and the scaler E are then regarded as $H(\underline{k})$, $S(\underline{k})$ and $E(\underline{k})$, functions of a continuous variable $\underline{k}$.

It was atomic orbitals, and Bloch functions constructed from them where translational symmetry existed, that were used as the basis functions in the calculations performed in this work. The form of the matrices H and S in this representation and how they were set up is now considered.

The overlap matrix is given by

$$S_{\alpha\beta}(\underline{k}) = \sum_j e^{i\underline{k}.(\underline{R}_i - \underline{R}_j)} \int \phi_\alpha^*(\underline{r}-\underline{R}_j)\,\phi_\beta(\underline{r}-\underline{R}_i)\, d^3\underline{r} \qquad (2.43)$$

and the Hamiltonian matrix is given by

$$H_{\alpha\beta}(\underline{k}) = \sum_j e^{i\underline{k}.(\underline{R}_i - \underline{R}_j)} \int \phi_\alpha^*(\underline{r}-\underline{R}_j)\, H\, \phi_\beta(\underline{r}-\underline{R}_i)\, d^3\underline{r}\ . \qquad (2.44)$$

The site $\underline{R}_i$ is fixed and the intergrations are over all space. Before substituting the actual form of H, from (2.33), into (2.44) it is desirable to write it in a different way. Firstly the free atom potential $V_i(\underline{r}-\underline{R}_i)$ (not confined to a cell) is written as

$$V_i(\underline{r}-\underline{R}_i) = \sum_l V_i^{cl}(\underline{r}-\underline{R}_i). \qquad (2.45)$$

In this the sum over l is over all atom positions in the solid and the term $V_i^{cl}(\underline{r}-\underline{R}_i)$ is the potential that would be felt in the cell centred on atom l due to a free atom at site i. Using this the crystal Hamiltonian can be written

$$H = \sum_l \left\{ V_l^{cl}(\underline{r}-\underline{R}_l) - V_i^{cl}(\underline{r}-\underline{R}_i) \right\} + T + V_i(\underline{r}-\underline{R}_i) \qquad (2.46)$$

and, using (2.35), this can be rewritten

$$H = \sum_{l \neq i} V_l + H_i^{at} \qquad (2.47)$$

where

$$V_\ell = V_\ell^{c\ell}(\underline{r}-\underline{R}_\ell) - V_i^{c\ell}(\underline{r}-\underline{R}_i). \qquad (2.48)$$

Now substituting (2.47) into (2.44) gives

$$H_{\alpha\beta}(\underline{k}) = \sum_j e^{i\underline{k}.(\underline{R}_i-\underline{R}_j)}\Big\{\sum_{\ell\neq i}\int\phi_\alpha^*(\underline{r}-\underline{R}_j)V_\ell\,\phi_\beta(\underline{r}-\underline{R}_i)\,d^3\underline{r} + \int\phi_\alpha^*(\underline{r}-\underline{R}_j)\,\phi_\beta(\underline{r}-\underline{R}_i)\,d^3\underline{r}\,\varepsilon_{i\beta}\Big\}. \qquad (2.49)$$

The three-centre integrals that appear in (2.49) are likely to be much smaller than the two-centre ones and in what is called the two-centre approximation the three-centre integrals are neglected altogether. Using the two-centre approximation here $H_{\alpha\beta}(\underline{k})$ is then given by

$$H_{\alpha\beta}(\underline{k}) = \sum_{\ell\neq i}\int\phi_\alpha^*(\underline{r}-\underline{R}_i)V_\ell\,\phi_\beta(\underline{r}-\underline{R}_i)\,d^3\underline{r} + \delta_{\alpha\beta}\,\varepsilon_{i\beta} + \sum_{j\neq i} e^{i\underline{k}.(\underline{R}_i-\underline{R}_j)}\Big\{\int\phi_\alpha^*(\underline{r}-\underline{R}_j)V_j\,\phi_\beta(\underline{r}-\underline{R}_i)\,d^3\underline{r} + \int\phi_\alpha^*(\underline{r}-\underline{R}_j)\phi_\beta(\underline{r}-\underline{R}_i)\,d^3\underline{r}\,\varepsilon_{i\beta}\Big\}. \qquad (2.50)$$

Notice that now in the integrals which have an integrand consisting of three terms two are on the same site. The first kind of integrals in (2.50), which have both orbitals on the same site and the potential on a second site, are often referred to as crystal field terms, and the second kind, which have one orbital and a potential on the same site with the other orbital on another, are known as hopping integrals. The third kind of integrals in (2.50) are simply overlap integrals.

There is no reason why the two-centre integrals should not be evaluated in the form that they appear in equations (2.43) and (2.50). It is found to be computationally more efficient, however, to deal with them in the way described below. These two-centre integrals depend not only on the separation of the centres, $|\underline{R}_i-\underline{R}_j|$, but also, because of the angular dependence of the atomic orbitals, upon the orientation of the orbitals to each other and hence on the direction of the vector $(\underline{R}_i-\underline{R}_j)$ joining them. It is most common to label atomic orbitals by the quantum numbers n, l and m. Often, however, instead of using orbitals that are eigenfunctions of the azimuthal angular momentum operator, orbitals which have a definite value of m and the angular dependence of a spherical harmonic function, linear combinations of these (with the same values of n and l) are taken to form another set of function that are also orthogonal and that are now real as well. (In other words a unitary transformation is carried out on the spherical harmonics.) Table 2.1 shows the form of the angular dependence that these orbitals have together with the label that is usually used to denote them, and Figure 2.1 shows the shapes of these orbitals. It was this set of orbitals that was used in calculating the two-centre integrals.

Firstly the case where the two-centre axis lies along the z-axis will be considered. In such cases the overlap integrals and the crystal field and hopping integrals when the potential involved is spherically symmetric, will be founded to be zero for certain combinations of orbitals.

$$|s\rangle = \frac{1}{\sqrt{4\pi}}$$

$$|p_x\rangle = \sqrt{\frac{3}{4\pi}}\,\frac{x}{r}$$

$$|p_y\rangle = \sqrt{\frac{3}{4\pi}}\,\frac{y}{r}$$

$$|p_z\rangle = \sqrt{\frac{3}{4\pi}}\,\frac{z}{r}$$

$$|d_{xy}\rangle = \sqrt{\frac{15}{4\pi}}\,\frac{xy}{r^2}$$

$$|d_{yz}\rangle = \sqrt{\frac{15}{4\pi}}\,\frac{yz}{r^2}$$

$$|d_{zx}\rangle = \sqrt{\frac{15}{4\pi}}\,\frac{zx}{r^2}$$

$$|d_{x^2-y^2}\rangle = \sqrt{\frac{15}{4\pi}}\,\frac{(x^2-y^2)}{2r^2}$$

$$|d_{z^2}\rangle = \sqrt{\frac{15}{4\pi}}\,\frac{(3z^2-r^2)}{2\sqrt{3}\,r^2}$$

Table 2.1 The angular dependence of atomic orbitals expressed in terms of Cartesian coordinates.

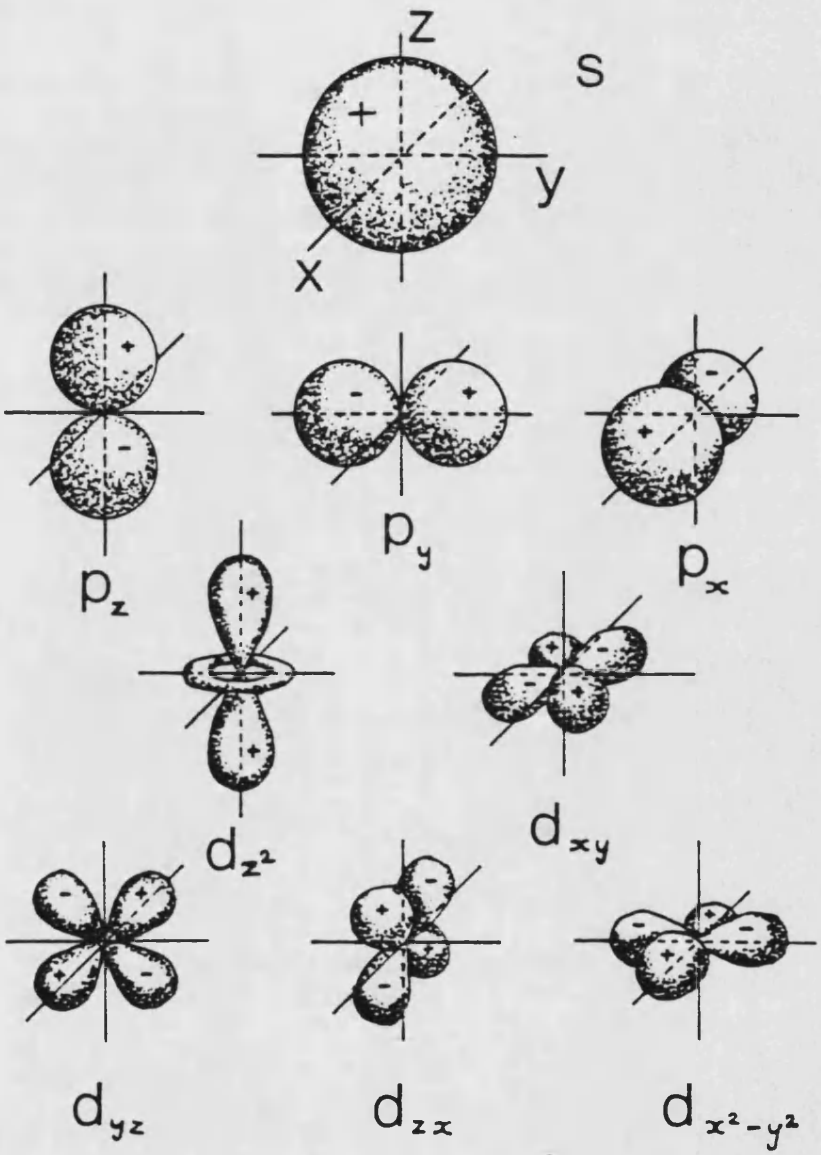

Figure 2.1 The angular dependence of atomic orbitals.

Table 2.2 lists some of the non-zero combinations and gives them the labels that such Slater-Koster integrals (Slater and Koster, 1954) are usually denoted by. Some of these combinations are illustrated in Figure 2.2.

Figure 2.3a shows two orbitals, joined by an axis AB pointing in a general direction, over which an integration is to be performed. The direction cosines of the axis l, m and n are also shown and specify its direction. The orbitals are both p_x types and this kind of integral will be denoted by $E_{x,x}(lmn)$. $E_{x,x}$ could represent an overlap integral or, if there was a potential at A, a hopping integral. In fact what is said about $E_{x,x}$ below also applies to the crystal field type of integral, but for this kind Figure 2.3 should be redrawn with a potential at A and both orbitals on B.

It can be shown that (see Appendix A and references therein) an integral such as $E_{x,x}$ can be decomposed into a linear combination of Slater-Koster integrals, and this is indicated schematically in Figure 2.3b. The angular dependence of the integral $E_{x,x}(lmn)$ is now contained entirely in the coefficients of the expansion as the Slater-Koster integrals themselves depend only on the distance AB. The coefficients for the expansion of the $E_{\alpha,\beta}$ integrals for α and β going over, s, p and d orbitals (the α state on site A and the β state on site B) are given in Table 2.3. This table is taken from Slater and Koster (1954).

Knowing the atomic structure of a solid and having a suitable set of atomic orbitals and potentials allows

$V_{ss\sigma}$	=	$\langle s \mid V \mid s \rangle$
$V_{sp\sigma}$	=	$\langle s \mid V \mid p_z \rangle$
$V_{pp\sigma}$	=	$\langle p_z \mid V \mid p_z \rangle$
$V_{pp\pi}$	=	$\langle p_x \mid V \mid p_x \rangle$
$V_{sd\sigma}$	=	$\langle s \mid V \mid d_{z^2} \rangle$
$V_{pd\sigma}$	=	$\langle p_z \mid V \mid d_{z^2} \rangle$
$V_{pd\pi}$	=	$\langle p_x \mid V \mid d_{zx} \rangle$
$V_{dd\sigma}$	=	$\langle d_{z^2} \mid V \mid d_{z^2} \rangle$
$V_{dd\pi}$	=	$\langle d_{zx} \mid V \mid d_{zx} \rangle$
$V_{dd\delta}$	=	$\langle d_{x^2-y^2} \mid V \mid d_{x^2-y^2} \rangle$

Table 2.2 The matrix elements of a potential V which are hopping Slater-Koster integrals. One orbital is centred on the potential V and the other is separated from it in, and only in, the z direction.

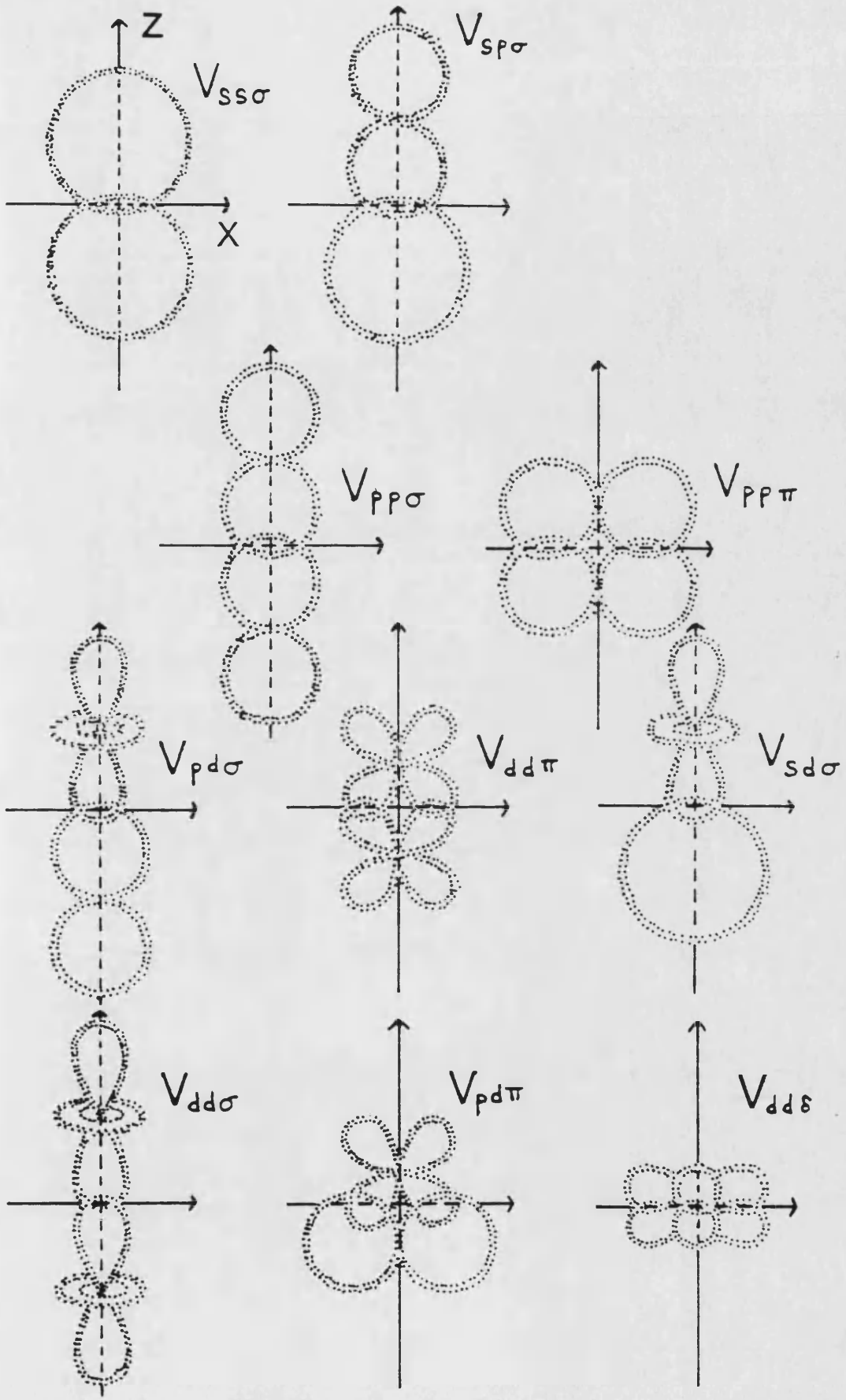

Figure 2.2 A pictorial representation of Slater-Koster integrals.

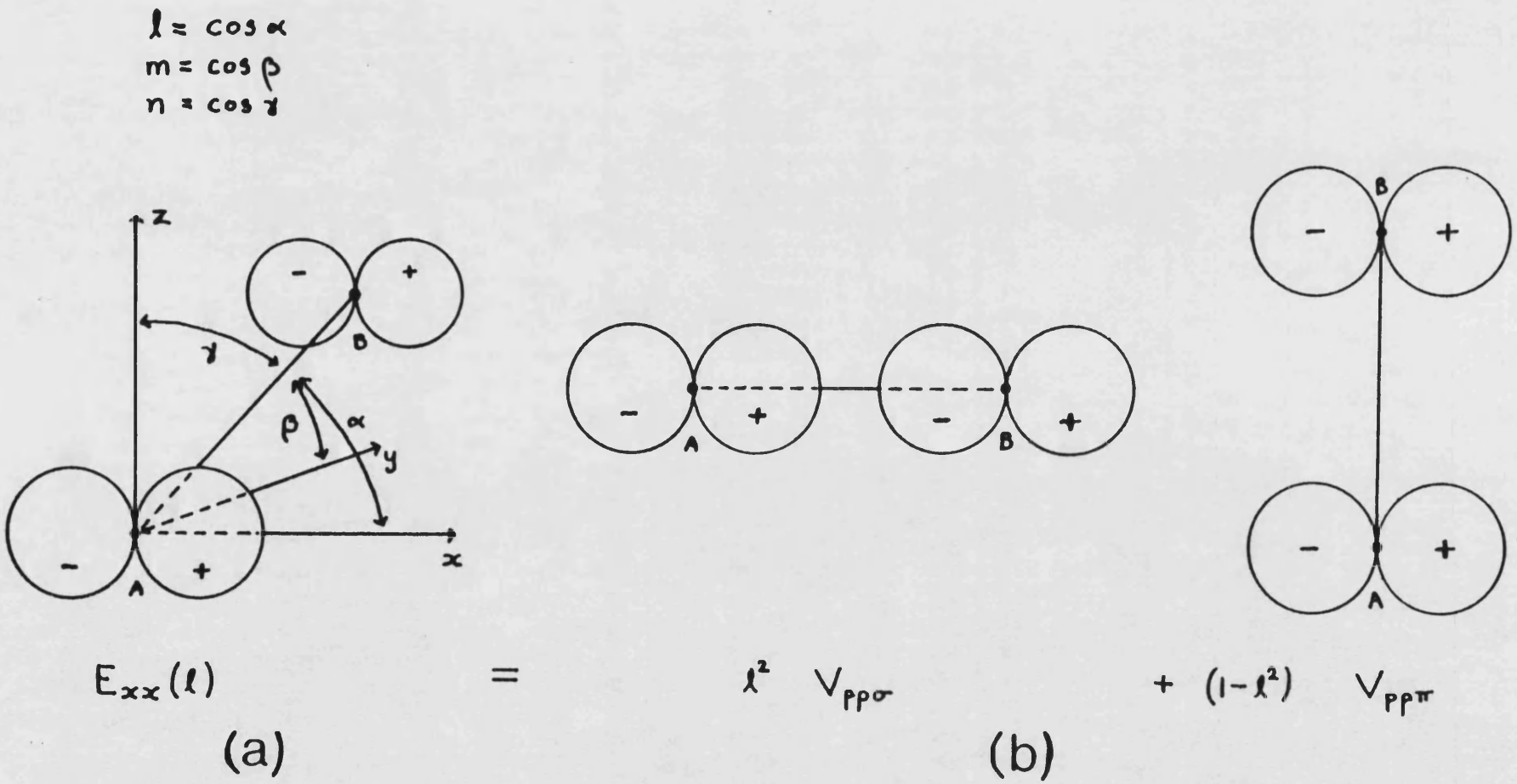

Figure 2.3 A schematic representation of the decomposition of a general two-centre integral (a) into a linear combination of Slater-Koster integrals (b).

$E_{s,s} =$	V_{sso}
$E_{s,x} =$	$lV_{sp\sigma}$
$E_{x,x} =$	$l^2V_{pp\sigma} + (1 - l^2)V_{pp\pi}$
$E_{x,y} =$	$lmV_{pp\sigma} - lmV_{pp\pi}$
$E_{x,z} =$	$lnV_{pp\sigma} - lnV_{pp\pi}$
$E_{s,xy} =$	$3^{1/2}lmV_{sd\sigma}$
$E_{s,x^2-y^2} =$	$\frac{1}{2}3^{1/2}(l^2 - m^2)V_{sd\sigma}$
$E_{s,3z^2-r^2} =$	$[n^2 - \frac{1}{2}(l^2 + m^2)]V_{sd\sigma}$
$E_{x,xy} =$	$3^{1/2}l^2mV_{pd\sigma} + m(1 - 2l^2)V_{pd\pi}$
$E_{x,yz} =$	$3^{1/2}lmnV_{pd\sigma} - 2lmnV_{pd\pi}$
$E_{x,zx} =$	$3^{1/2}l^2nV_{pd\sigma} + n(1 - 2l^2)V_{pd\pi}$
$E_{x,x^2-y^2} =$	$\frac{1}{2}3^{1/2}l(l^2 - m^2)V_{pd\sigma} + l(1 - l^2 + m^2)V_{pd\pi}$
$E_{y,x^2-y^2} =$	$\frac{1}{2}3^{1/2}m(l^2 - m^2)V_{pd\sigma} - m(1 + l^2 - m^2)V_{pd\pi}$
$E_{z,x^2-y^2} =$	$\frac{1}{2}3^{1/2}n(l^2 - m^2)V_{pd\sigma} - n(l^2 - m^2)V_{pd\pi}$
$E_{x,3z^2-r^2} =$	$l[n^2 - \frac{1}{2}(l^2 + m^2)]V_{pd\sigma} - 3^{1/2}ln^2V_{pd\pi}$
$E_{y,3z^2-r^2} =$	$m[n^2 - \frac{1}{2}(l^2 + m^2)]V_{pd\sigma} - 3^{1/2}mn^2V_{pd\pi}$
$E_{z,3z^2-r^2} =$	$n[n^2 - \frac{1}{2}(l^2 + m^2)]V_{pd\sigma} + 3^{1/2}n(l^2 + m^2)V_{pd\pi}$
$E_{xy,xy} =$	$3l^2m^2V_{dd\sigma} + (l^2 + m^2 - 4l^2m^2)V_{dd\pi} + (n^2 + l^2m^2)V_{dd\delta}$
$E_{xy,yz} =$	$3lm^2nV_{dd\sigma} + ln(1 - 4m^2)V_{dd\pi} + ln(m^2 - 1)V_{dd\delta}$
$E_{xy,zx} =$	$3l^2mnV_{dd\sigma} + mn(1 - 4l^2)V_{dd\pi} + mn(l^2 - 1)V_{dd\delta}$
$E_{xy,x^2-y^2} =$	$\frac{3}{2}lm(l^2 - m^2)V_{dd\sigma} + 2lm(m^2 - l^2)V_{dd\pi} + \frac{1}{2}lm(l^2 - m^2)V_{dd\delta}$
$E_{yz,x^2-y^2} =$	$\frac{3}{2}mn(l^2 - m^2)V_{dd\sigma} - mn[1 + 2(l^2 - m^2)]V_{dd\pi} + mn[1 + \frac{1}{2}(l^2 - m^2)]V_{dd\delta}$
$E_{zx,x^2-y^2} =$	$\frac{3}{2}nl(l^2 - m^2)V_{dd\sigma} + nl[1 - 2(l^2 - m^2)]V_{dd\pi} - nl[1 - \frac{1}{2}(l^2 - m^2)]V_{dd\delta}$
$E_{xy,3z^2-r^2} =$	$3^{1/2}lm[n^2 - \frac{1}{2}(l^2 + m^2)]V_{dd\sigma} - 3^{1/2}2lmn^2V_{dd\pi} + \frac{1}{2}3^{1/2}lm(1 + n^2)V_{dd\delta}$
$E_{yz,3z^2-r^2} =$	$3^{1/2}mn[n^2 - \frac{1}{2}(l^2 + m^2)]V_{dd\sigma} + 3^{1/2}mn(l^2 + m^2 - n^2)V_{dd\pi} - \frac{1}{2}3^{1/2}mn(l^2 + m^2)V_{dd\delta}$
$E_{zx,3z^2-r^2} =$	$3^{1/2}ln[n^2 - \frac{1}{2}(l^2 + m^2)]V_{dd\sigma} + 3^{1/2}ln(l^2 + m^2 - n^2)V_{dd\pi} - \frac{1}{2}3^{1/2}ln(l^2 + m^2)V_{dd\delta}$
$E_{x^2-y^2,x^2-y^2} =$	$\frac{3}{4}(l^2 - m^2)^2V_{dd\sigma} + [l^2 + m^2 - (l^2 - m^2)^2]V_{dd\pi} + [n^2 + \frac{1}{4}(l^2 - m^2)^2]V_{dd\delta}$
$E_{x^2-y^2,3z^2-r^2} =$	$\frac{1}{2}3^{1/2}(l^2 - m^2)[n^2 - \frac{1}{2}(l^2 + m^2)]V_{dd\sigma} + 3^{1/2}n^2(m^2 - l^2)V_{dd\pi} + \frac{1}{4}3^{1/2}(1 + n^2)(l^2 - m^2)V_{dd\delta}$
$E_{3z^2-r^2,3z^2-r^2} =$	$[n^2 - \frac{1}{2}(l^2 + m^2)]^2V_{dd\sigma} + 3n^2(l^2 + m^2)V_{dd\pi} + \frac{3}{4}(l^2 + m^2)^2V_{dd\delta}$

Table 2.3 Two-centre integrals, $E_{\alpha,\beta}$, expressed as linear combinations of Slater-Koster integrals. The expressions are functions of l,m, and n, the direction cosines of the vector from state α to state β ($\overrightarrow{AB}$ in Figure 2.3).

the overlap matrix (2.43) and Hamiltonian Matrix (2.50) to be set up. It is found in general to be faster to first calculate all the appropriate Slater-Koster integrals for a range of two-centre separations and then use these (using Table 2.3) to calculate the actual integrals required in (2.43) and (2.50) when doing this.

When H and S have been found the secular equation (2.40) can be set up and solved for the one-electron eigenenergies and eigenfunctions. The matrix D in (2.40) is non-Hermitian and will have different right and left eigenvectors for the same eigenvalue, that is

$$D_{\alpha\beta}\, a_{i\beta} = E_i\, a_{i\alpha} \tag{2.51}$$

and

$$b_{i\alpha}\, D_{\alpha\beta} = E_i\, b_{i\beta} \tag{2.52}$$

with

$$\underline{a}_i \neq \underline{b}_i \ . \tag{2.53}$$

Both vectors represent the same eigenfunctions ψ_i of H, but the right vector $\underline{a}_i$ is made of the coefficients for the expansion of this eigenfunction in the AOs (or Bloch functions made from them) $\{\phi_\alpha\}$, thus

$$\psi_i(\underline{r}) = \sum_\alpha a_{i\alpha}\, \phi_\alpha(\underline{r}) \ , \tag{2.54}$$

whereas the left vector $\underline{b}_i$ is made of the coefficients for the expansion of ψ_i in a different set of (unknown)

functions, the "reciprocal" functions $\{\phi^\alpha\}$ (see Appendix B), thus

$$\psi_i(\underline{r}) = \sum_\alpha b_{i\alpha}\,\phi^\alpha(\underline{r}). \qquad (2.55)$$

The two different types of expansion coefficient are related by (see Appendix B)

$$b_{i\alpha} = \sum_\beta S^{(i)}_{\alpha\beta}\, a_{i\beta} \qquad (2.56)$$

where

$$S^{(i)}_{\alpha\beta} = \langle \phi_\alpha | \phi_\beta \rangle. \qquad (2.57)$$

The normalization condition on the crystal eigenfunctions now becomes

$$\langle \psi_i | \psi_i \rangle = \sum_{\alpha\beta} a^*_{i\alpha}\, S^{(i)}_{\alpha\beta}\, a_{i\beta} = 1. \qquad (2.58)$$

Equation (2.58) can be interpreted in the following way: each of the terms in the sum with $\alpha=\beta$ (which contribute $|a_{i\alpha}|^2$ to the total) give the probability that an electron in state ψ_i will be found completely in state ϕ_α while the terms

$$a^*_{i\alpha}\, S^{(i)}_{\alpha\beta}\, a_{i\beta} + a^*_{i\beta}\, S^{(i)}_{\beta\alpha}\, a_{i\alpha} = 2\,(a^*_{i\alpha}\, S^{(i)}_{\alpha\beta}\, a_{i\beta}) \qquad (2.59)$$

give the probability that an electron will be found partly in state ϕ_α and partly in ϕ_β, that is to say in an overlap population or a bonding charge. It is convenient to assume that an electron will always be found completely in one of the basis states. One way of doing this is to divide the overlap populations like (2.59) equally between both basis

states so that then the probability of an electron in state ψ_i being found in state ϕ_α is given by

$$P_{i\alpha} = \sum_{\beta} a^*_{i\alpha} S^{(i)}_{\alpha\beta} a_{i\beta} , \qquad (2.60)$$

or using (2.56), by

$$P_{i\alpha} = a^*_{i\alpha} b_{i\alpha} . \qquad (2.61)$$

Mulliken (1955) refers to this particular population breakdown as the gross atomic population.

Solving the one-electron Schröding equation gives the energy levels E_i. If the system under investigation has translational symmetry these energies will form energy bands $E(\underline{k})$ which can be plotted out. Another way of presenting the electronic structure of a solid (which doesn't depend on it being translationally invariant) is as a density of (electronic) states (DOS), which is defined by

$$n(E) = \sum_i \delta(E-E_i) . \qquad (2.62)$$

Also of interest is the density of states associated with a particular basis function. This is called the projected or local density of states (LDOS) and for basis orbital ϕ_α it is given by

$$n_\alpha(E) = \sum_i P_{i\alpha} \delta(E-E_i) , \qquad (2.63)$$

or, using (2.61), by

$$n_\alpha(E) = \sum_i a^*_{i\alpha} b_{i\alpha} \delta(E-E_i) . \qquad (2.64)$$

Knowing the DOS for a system, if N, the total number of electrons in that system, is known also, the Fermi level E_F of the system can be found using

$$N = \int_{-\infty}^{E_F} n(E)\, dE. \qquad (2.65)$$

Knowing the LDOS and Fermi level of a system allows the charge in each of the basis states N_α to be calculated by

$$N_\alpha = \int_{-\infty}^{E_F} n_\alpha(E)\, dE. \qquad (2.66)$$

2.4 The theory of chemical pseudopotentials

The theory of chemical pseudopotentials was developed by Anderson (1968b, 1969) following the earlier work of Adams (1961, 1962) and Gilbert (1964) and was later taken up by Bullett (1980a). It shows how to write an equation defining a set of localized atomic-like orbitals which will exactly span the energy band of a solid. Furthermore it is evident from this equation that these orbitals are very close to the actual atomic orbitals of the solid. This theory thus justifies to a great extent the use of the atomic orbitals of a solid as a set of basis functions made in the LCAO method. In this section a brief outline of the theory of chemical pseudopotentials will be given which follows the presentation of it given by Weeks et al. (1973).

Consider N unit cells of a solid. Impose periodic boundary conditions so that the system is translationally invariant and for simplicity let there be one atom per unit cell. In the one-election approximation an energy band of the solid, E(k), is given by the solutions of

$$H|\psi_k\rangle = E(k)|\psi_k\rangle . \qquad (2.67)$$

H is the self-consistent Hamiltonian of the solid and $|\psi_k\rangle$ are the N orthogonal (extended) energy eigenkets. (In this section Dirac notation will be used). These eigenkets form a subspace of the total Hilbert space of (2.67). An operator P which projects onto this band subspace B can be written as

$$P = \sum_{k=1}^{N} |\psi_k\rangle\langle\psi_k| . \qquad (2.68)$$

P is an Hermitian operator which commutes with H,

$$[H, P] = 0 , \qquad (2.69)$$

and has the usual projection operator property of being idempotent (Messiah, 1961),

$$P^2 = P . \qquad (2.70)$$

In the LCAO method an eigenket $|\psi_k\rangle$ is expanded in atomic orbitals (AOs) (see equation (2.54)). It is not obvious, however, how accurate such an expansion is. Here a set of localized orbitals (LOs) is sought which exactly span the subspace B and in which any one of the eigenkets

$|\psi_k\rangle$ may be expanded exactly. If $\{|\phi_\alpha\rangle\}$ is such a set of orbitals they must satisfy

$$P|\phi_\alpha\rangle = |\phi_\alpha\rangle . \tag{2.71}$$

Furthermore the operator P can now be written as

$$P = \sum_{\alpha=1}^{N} |\phi_\alpha\rangle\langle\phi_\alpha| . \tag{2.72}$$

Here, however, the LOs have been assumed to be orthogonal. This is not necessary, and indeed it will be seen below that it is infact desirable to relax this restriction, when the expression for P becomes (see Appendix B)

$$P = \sum_{\alpha\beta} |\phi_\alpha\rangle (S^{-1})_{\alpha\beta} \langle\phi_\beta| \tag{2.73}$$

where S is the overlap between the LOs and is given by

$$S_{\alpha\beta} = \langle\phi_\alpha|\phi_\beta\rangle . \tag{2.74}$$

If the Hamiltonian for a free atom of the system located at site i is H_i^{at} then the AOs of the system $|\phi^\circ_{i\alpha}\rangle$ (centred on site i) would be given by

$$H_i^{at}|\phi^\circ_{i\alpha}\rangle = \varepsilon^\circ_{i\alpha}|\phi^\circ_{i\alpha}\rangle . \tag{2.75}$$

So that the LOs are similar to the AOs they can be required to satisfy

$$P H_i^{at} P |\phi_{i\alpha}\rangle = \varepsilon_{i\alpha}|\phi_{i\alpha}\rangle \tag{2.76}$$

with $\varepsilon_{i\alpha}$ as close as possible to $\varepsilon^{\circ}_{i\alpha}$. This is the Adams equation for the LOs (Adams, 1961, 1962, 1971a) and it defines the LOs uniquely if P is already known. It has N eigenket solutions which together will span B, but only the lowest energy one $|\phi_{io}\rangle$ will be localized. However, the set of N orbitals $\{|\phi_{io}\rangle\}$ consisting of the lowest energy eigenket of (2.76) located on each of the N atoms of the solid also provide a unique set of linearly independent kets which will span B (Weeks et al., 1973) and this is the set that will be considered further. (From now on the subscript o will be dropped). Notice that unlike the kets $|\phi_{\alpha}\rangle$ which are eigenkets of an Hermitian operator, the kets $|\phi_i\rangle$ do not have to be orthogonal to each other.

The operator $PH^{at}P$ is that part of H^{at} which operates in B. Likewise with PHP, so that when H operates on a state entirely in B it has the same effect as PHP acting on that state. Hence

$$H|\phi_i\rangle - PHP|\phi_i\rangle = 0. \qquad (2.77)$$

As P is not already known equation (2.76) cannot be used to find the LOs, but adding it to the above equation yields the Anderson LO equation

$$\{H_i^{at} + \bar{U}_i - P\bar{U}_i P\}|\phi_i\rangle = \varepsilon_i|\phi_i\rangle \qquad (2.78)$$

which can be. The quantity $\bar{U}_i$ is defined as

$$\bar{U}_i \equiv H - H_i^{at} \qquad (2.79)$$

so that it is the total crystal potential minus the potential of a free atom at site i. Using the Wigner trick potential (see section 2.2) this could be written as

$$\bar{U}_i = \sum_{\ell \neq i} V_\ell \,. \tag{2.80}$$

To solve the Anderson equation first expression (2.73) has to be substituted into it for P. The resulting equation for the LOs then depends on the LOs through P so that it has to be solved self-consistently. This can be done by an iterative procedure as for the SCF one-electron equations discussed in section 2.2.

Equation (2.78) for the LOs shows that they are dependent on the atomic potential around which they are centred, through H_i^{at}, and also on the rest of the crystal, through $\bar{U}_i - P\bar{U}_i P$. If the free atom orbitals $|\phi_i^\circ\rangle$ are used as a starting set in an iterative procedure to solve (2.78) they should fairly well span the function $\bar{U}_i$ as $\bar{U}_i$ is made from potentials localized around each atom so that

$$P\bar{U}_i P \simeq \bar{U}_i \tag{2.81}$$

and

$$\bar{U}_i - P\bar{U}_i P \ll H_i^{at}. \tag{2.82}$$

The influence of the rest of the crystal on orbital i almost cancels itself out so that the solutions to (2.78) in this cycle should be only slightly perturbed from the $\{|\phi_i^\circ\rangle\}$.

The extent of this cancellation in diamond and silicon has been demonstrated by Bullett (1975). As the solutions are close to the starting ansatz it is clear that the AOs are a good approximation of the completely self-consistent solutions of (2.78) and hence that they are a reasonable set of LOs in which to expand the crystal eigenfunctions. This serves as a justification of the LCAO method.

It is because a LO satisfying (2.78) is influenced by its environment only through the weak term $\bar{U}_i - P\bar{U}_i P$ (in the LCAO approximation, a sort of zeroth order approximation, this term is taken to be zero so that the orbital only depends on H_i^{at}) that there exist local properties of solids (bond lengths, for example) that are similar in different systems. Indeed, it was the desire to develop a quantum mechanical formalism which realized this intuitive "building block" picture of matter that largely motivated the development of the chemical pseudopotential theory.

There exists a better known set of localized orbitals which exactly span the energy band of a solid and they are the Wannier orbitals (Wannier, 1937). Wannier orbitals possess an extra property compared to the Adams LOs in that orbitals on different sites are orthogonal. In fact, if expression (2.72) was used instead of (2.73) for P in (2.78) the resulting equation would define Wannier orbitals, or, to put it another way, orthogonalizing the Adams LOs would turn them into Wannier orbitals. The orthogonality of Wannier orbitals makes them less localized because they need long "wiggley" tails where adjacent orbitals overlap. In terms of the above analysis the Wannier orbitals are less

localized because they satisfy (2.76), the Adams "least distortion criterion" (Adams, 1971a), less well.

It has been pointed out by Weeks et al. (1973) that orbitals that satisfy (2.78) must also satisfy the non-Hermitian equation

$$\{H_i^{o\dagger} + \bar{U}_i - P\bar{U}_i\}|\phi_i\rangle = \mathcal{E}_i|\phi_i\rangle \qquad (2.83)$$

and that this equation is formally analogous to the pseudopotential equation of Austin et al. (1962)

$$\{T + U - P_c U\}|\phi_K\rangle = \mathcal{E}_K|\phi_K\rangle . \qquad (2.84)$$

Here T is the kinetic energy operator and U is a total crystal potential. The operator P_c is the projection operator which projects onto the space of the lowest eigenstates of the crystal, those states which are formed from the atomic core orbitals of the solid. It can be shown (Austin et al., 1962) that the eigenenergies $\mathcal{E}_k$ of (2.84) are the same as the valence eigenenergies of the crystal Schrödinger equation

$$\{T + U\}|\psi_K\rangle = \mathcal{E}_K|\psi_K\rangle. \qquad (2.85)$$

The term in (2.84) $U-P_cU$ is known as the pseudopotential and is expected to be weak. This is because the strong parts of the crystal potential U, the deep Coulomb wells around each atom, are taken out by the term $-P_cU$, or, as it is sometimes expressed, because the core potentials have been projected out. Because the pseudopotential is weak the eigenfunctions of (2.84) $|\phi_k\rangle$, which are known as pseudo-wave-functions, will be only slightly perturbed from the eigenfunctions of

the operator T, that is to say they will be plane-wave-like. Furthermore, its eigenvalues, which are also the valence energy eigenvalues of (2.85), will be close to those of a free electron and this is often used as an explanation of the success of the free electron model of metals.

In (2.83) it is the potential due to the neighbours of site i that is being projected out. There is a new feature to the pseudopotential in (2.83) however in that it is self-consistent as P depends on the LOs $|\phi_i\rangle$ which are the solutions of the pseudopotential equation. It is this similarity to conventional pseudopotential theory that has lead to the theory of localized orbitals described in this section being called by Anderson a theory of self-consistent pseudopotentials and chemical pseudopotential theory in particular.

2.5 Calculational procedure

In this section the procedure that was followed in order to calculate the electronic structure of a solid is detailed. In the electronic structure calculations carried out in this work the one-electron approximation was used. The one-electron Hamiltonian used consisted of the kinetic energy operator and a Wigner trick potential. The eigenfunctions and energy eigenvalues of this Hamiltonian were found using an ab initio LCAO method which used the actual atomic orbitals of the solid as basis functions and in which the two-centre approximation was made. The details of all this has been described above.

The atomic eigenenergies, wave functions and potentials needed to calculate (2.43) and (2.50) were obtained using a computer program which solves the SCF HFS equations for an atom. The details of this program are given by Herman and Skillman (1963). The potentials from this include an $X\alpha$ exchange potential but no correlation term so that the correlation in the solid is taken into account solely by the use of the Wigner trick potential. The only input data required for this program were the occupations of the atom's energy levels and the value of α to be used in the exchange approximation. In all the calculations carried out α was set to 0.7. It was considered unlikely, however, that the details of the final calculated electronic structure of a solid would be very sensitive to the value of α chosen and hence this particular choice for the value of α was not regarded as being critical.

The core states of an atom in a solid will be completely filled as they are in the free atom, but the electron configuration in its valence states, which are the states used in the LCAO calculations, may be quite different from that found in the free atom. It might not be obvious, therefore, how to choose the occupations of the valence states when calculating the orbitals and potential of a particular atom. However, changing the occupation of the orbital of an atom does not much alter its shape, or, consequently, the potential of that atom. Hence the values of the overlap, hopping and crystal field integrals will not depend greatly on the atomic valence electronic configurations chosen.

What can be of significance is the variation of the energy of the valance states with different occupations. Figure 2.4 shows how the eigenenergies of the 4s, 4p and 3d states of a nickel atom vary as the number of electrons in each is changed. In each configuration the total number of electrons is the same, 10, the number of valence electrons of a free nickel atom, so that all the energy levels are for a neutral atom. Going from left to right in Figure 2.4 the occupations of the s and p levels each decrease by the same amount while the d level occupation increases by twice this amount. It can be seen that while the energy of the s and p levels are reasonably independent of their occupation the d level is not. This is because an extra electron placed in the d orbital will be on average closer to other electrons than it would be in either the s or p orbitals, the d orbital being smaller and containing more electrons than both of these, and thus will have a greater energy due to its larger electron-electron interaction energy. Accordingly in the calculations special care was taken only in choosing the d level energies and how this was done is described below.

Using the atomic orbitals and potentials obtained the Slater-Koster integrals were then calculated by numerical integration. They were calculated for two-centre separations of from 2 to 10 atomic units in steps of one atomic unit. Using s, p and d orbitals, with N different species of atom in the solid $14N^2$ Slater-Koster integrals of each kind had to be calculated for each separation.

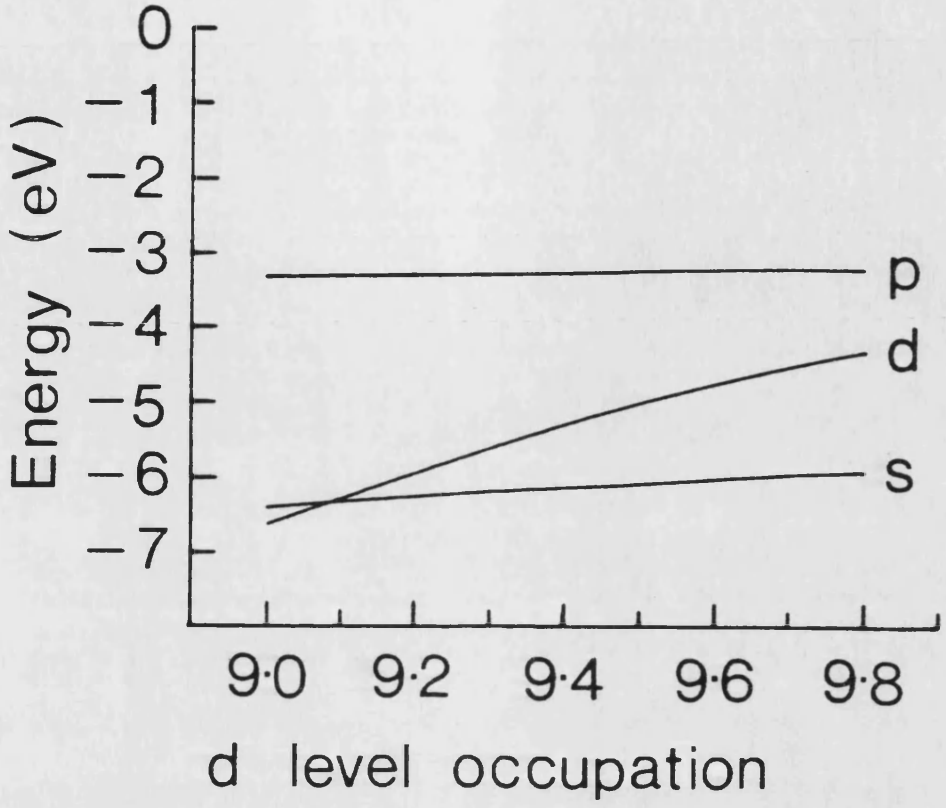

Figure 2.4 The variation of the valence orbital energies of a neutral Ni atom with changing d orbital occupation.

In calculating these integrals, because the Wigner trick crystal potential was being used, the atomic potentials had to be set to zero beyond a sphere of a certain radius centred on the atom. The size of this sphere for each atom was chosen so that the combined volumes of the spheres of all the atoms in a single unit cell was equal to the volume of that unit cell and so that the ratio of the sphere sizes for each of the atoms to each other was equal to the ratio of the sizes of the corresponding atoms to each other.

A computer program was then used which, given the atomic crystal structure of the system being considered, calculated the values of the Slater-Koster integrals for the actual two-centre separations occurring in the crystal by interpolating between the values already calculated and then combined these using the rules in Table 2.3 to give the required two-centre integrals of the sort appearing in (2.43) and (2.50). This program then constructed the matrix D from these and, using a NAG library subprogram, found its eigenvalues and (right) eigenvectors. It also found the left eigenvectors of D by finding the right eigenvectors of $D^{\dagger}$, the Hermitian conjugate of D. The matrix D, being a function of $\underline{k}$, was constructed and its eigenvalues and eigenvectors found by the program for each required value of $\underline{k}$.

When calculating the DOS (or LDOS) for a solid it was, of course, impracticable to find the eigenvalues of D for all possible values of $\underline{k}$ and so a sample of these was used instead. Usually the values of $\underline{k}$ chosen were at the points

of intersection of an even mesh over the irreducible part of the first Brillouin zone of the solid. The DOS and LDOS (using $\underline{a}_i$ and $\underline{b}_i$, the right and left eigenvectors of D) were calculated using (2.62) and (2.64) respectively. As, however, a finite number of eigenenergies was being used the δ-Dirac function was replaced by another function of unit area but finite width. In all the calculations presented in this work, in fact, a Gaussian of standard deviation 0.1 eV was used. Using (2.65) the Fermi level of the system was then calculated and having found this (2.66) was used to find the occupation of each orbital.

In this way the occupation of the d orbitals in particular could be found. It has been mentioned above that the input d level energies that were used in an electronic structure calculation were dependent upon the occupations of the atomic d levels that were assumed. Once a calculation had been performed, however, the d level energies corresponding to the calculated d occupations, found using a graph like the one shown in figure 2.4, could then be used as the input data for a second electronic structure calculation. This process was then repeated until self-consistency was achieved with the input d level energies used corresponding to the d level occupations calculated (to within about 0.1 eV).

CHAPTER 3

THE ELECTRONIC STRUCTURE OF TRANSITION METAL SILICIDES

3.1 Introduction

There are a number of reasons for the present interest in the compounds of metal and silicon, the so called silicides. The most important of these is that silicides are almost always formed at metal-silicon interfaces. (Metal-silicon interfaces are strongly reactive and indeed nickel and palladium can react spontaneously at room temperature to form silicide compounds upon deposition onto a clean silicon surface, Freeouf et al., 1979; Ho et al., 1979; Cohen, 1980). When silicides do form they of course contribute to the interface properties, and the behaviour of metal-silicon interfaces are of great technological importance.

In the past models of metal-semiconductor interfaces have assumed the existance of an abrupt metal-semiconductor boundary, as for example in the traditional explanations of Schottky barrier formation (Schottky, 1939; Bardeen, 1947). The complicated nature of real metal-semiconductor interfaces, where atomic intermixing and chemical reaction have taken place, has become apparent during the 1980's as they have been investigated using ultrahigh vacuum (UHV) surface science techniques. (A schematic diagram of a traditional and of a real metal-semiconductor interface are shown in Figure 3.1). Reviews of this work and of the advances made in the understanding of the properties of metal-semiconductor interfaces based on

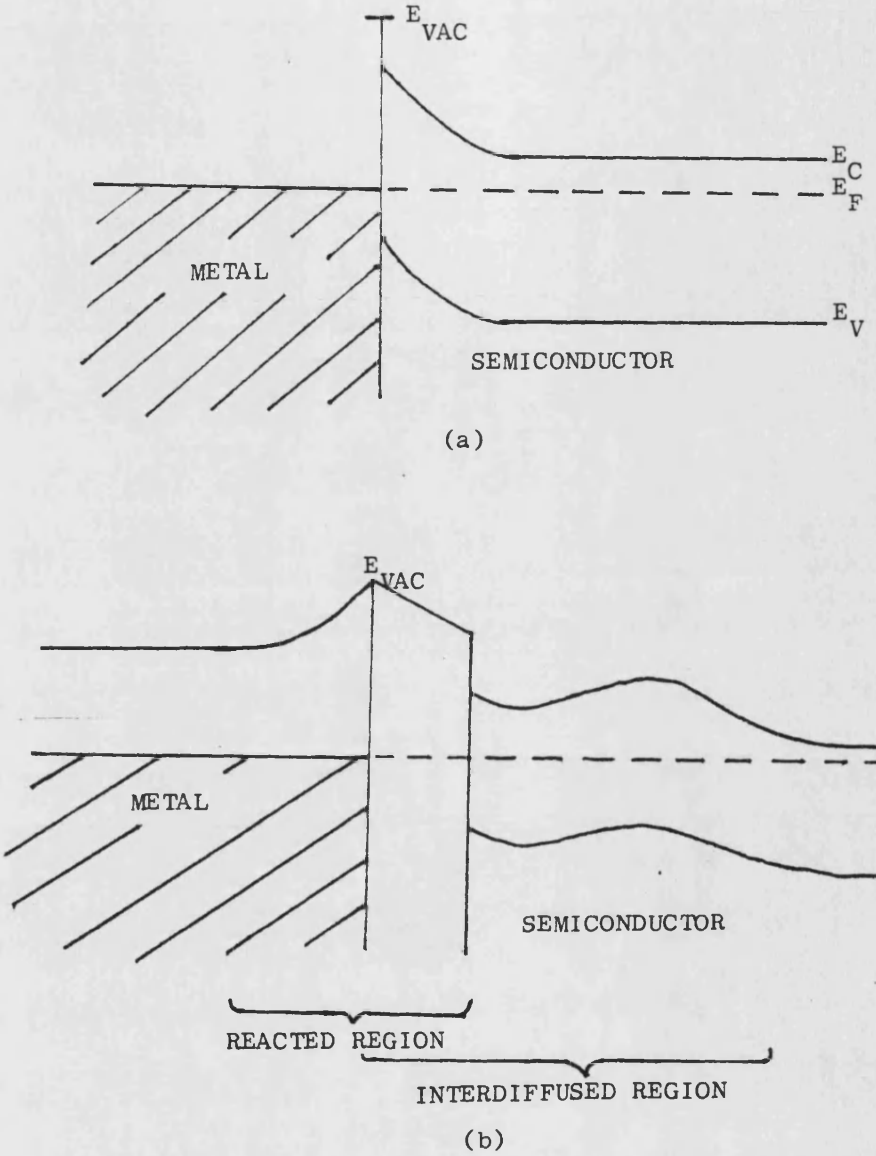

Figure 3.1 (a) Traditional schematic diagram of a metal-semiconductor interface. (b) Schematic diagram of a real metal-semiconductor interface showing reacted and interdiffused regions and nonparabolic band bending. After Brillson (1982).

it have been given by Brillson (1982, 1983), Williams (1981, 1982a, 1982b, 1983), Rubloff (1983a, 1983b), Ho (1983), Ho and Rubloff (1982), Schluter (1982), and Murarka (1980).

The electronic structure of transition metal-silicon interfaces in particular have been studied using ultraviolet photoemission spectroscopy (UPS), X-ray photoemission spectroscopy (XPS), synchrotron radiation photoemission spectroscopy (or soft X-ray photoemission spectroscopy (SXPS)) and Auger electron spectroscopy (AES). A review of these studies carried out before 1982 is given by Rubloff and Ho (1982). A more recent review of the experimental and theoretical work that has been carried out on the electronic properties of bulk transition metal silicides and on silicide-silicon interfaces is given by Calandra et al. (1985). The chemical reaction and diffusion at transition metal-silicon interfaces have been investigated using Rutherford backscattering spectroscopy (RBS) and AES coupled with sputter etching. Reviews of silicide formation based on RBS and AES studies have been given by Tu and Mayer (1978), Ottaviani (1979, 1981) and Ottaviani and Costato (1978).

To illustrate the development of a metal-silicon interface the sequence of phases formed at a platinum-silicon interface is shown in Figure 3.2.

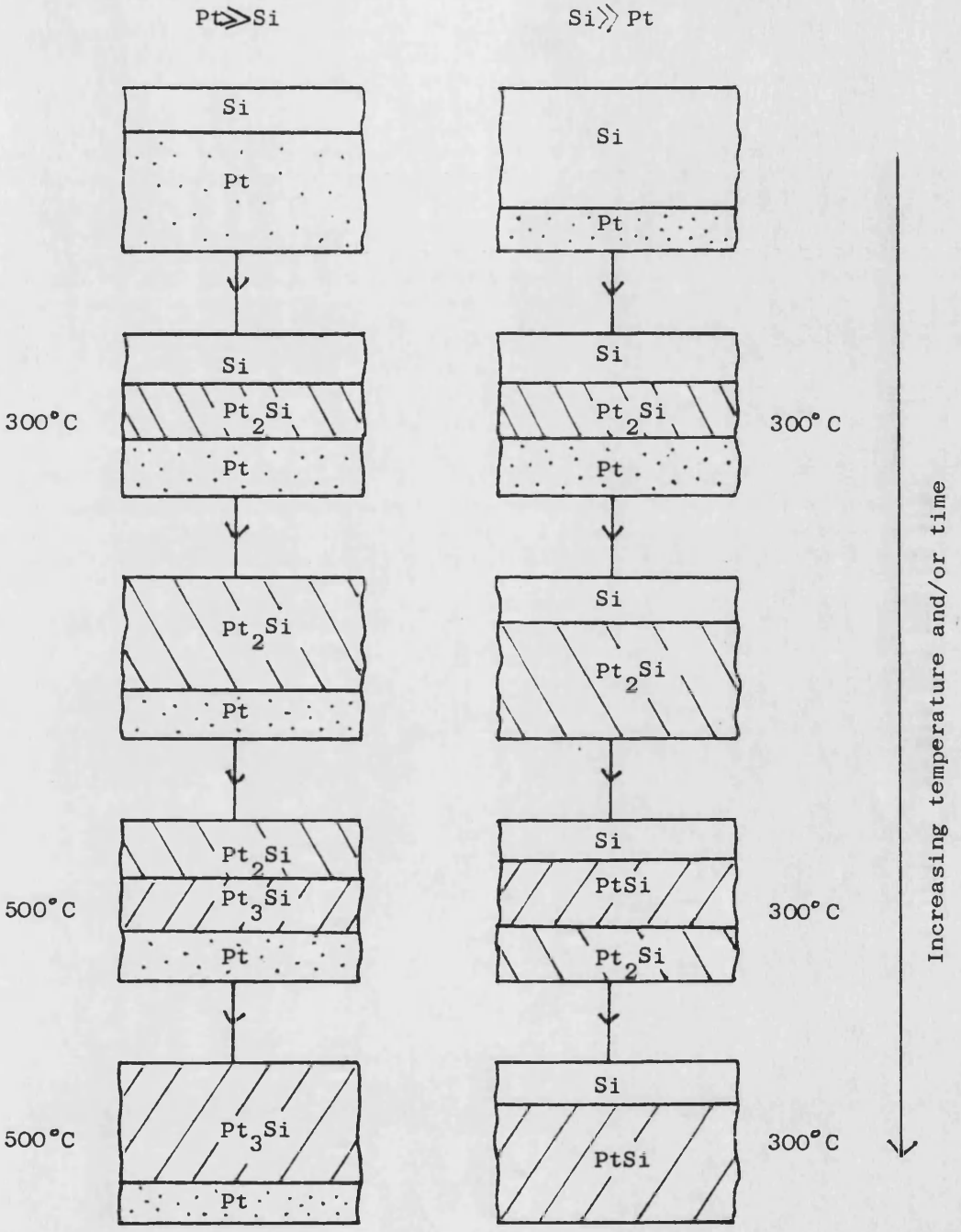

Figure 3.2 The sequence of phases formed at a Pt-Si interface with excess Pt and with excess Si. After Brillson (1982).

First Pt_2Si forms at 300°C (Canali et al., 1979). Depending on the ratio of platinum to silicon silicide formation continues until there is nothing left but a silicon rich silicide (PtSi) and excess silicon or a platinum rich silicide (Pt_3Si) and excess platinum.

Figure 3.3 shows the metals which form silicide compounds by thermal reaction at the metal-silicon interface and the silicide phases observed. There are now generally considered to be three different types of silicide; near noble metal silicides (the silicides of nickel, palladium and platinum), refractory metal silicides (silicides of the other non-noble transition metals) and rare earth metal silicides. The general characteristics of these three classes are summarized in Table 3.1. The near noble metals tend to form metal rich silicides (mainly M_2Si) and monosilicides (MSi) while the refractory metals favour the formation of monosilicides and disilicides (MSi_2) and the rare earth metals disilicides. The formation temperature is higher for refractory metal silicides (typically 500-700°C) than for the near noble metal silicides (typically 100-500°C). These temperatures are well below the lowest liquid phase eutectic temperature and, in most cases, are about one-third to one-half the melting point (in K) (Sundström et al., 1973; Mayer and Tu, 1971).

H																	He
Li	Be											B	C	N	O	F	Ne
Na	Mg											Al	Si	P	S	Cl	Ar
K	Ca	Sc	Ti	V	Cr	Mn	Fe	Co	Ni	Cu	Zn	Ga	Ge	As	Se	Br	Kr
Rb	Sr	Y	Zr	Nb	Mo	Tc	Ru	Rh	Pd	Ag	Cd	In	Sn	Sb	Te	I	Xe
Cs	Ba	Lu	Hf	Ta	W	Re	Os	Ir	Pt	Au	Hg	Tl	Pb	Bi	Po	At	Rn
Fr	Ra	Lr															

	La	Ce	Pr	Nd	Pm	Sm	Eu	Gd	Tb	Dy	Ho	Er	Tm	Yb
	Ac	Th	Pa	U	Np	Pu	Am	Cm	Bk	Cf	Es	Fm	Md	No

MSi_2:	Ti,Zr,Hf,V,Nb,Ta,Cr,Mo,W,Mn,Fe,Co,Ni,Gd,Dy,Ho,Er
MSi:	Ti,Hf,Mn,Fe,Co,Rh,Ir,Ni,Pt
M_2Si:	Mg,Co,Ni,Pd,Pt

Figure 3.3 The metals which form silicide compounds by thermal reaction at the metal-silicon interface and the phases observed. After Rubloff (1983a).

Property	Rare earth metal	Refractory metal	Near noble metal
Phases	Disilicides (MSi_2)	Silicon-rich (MSi_2, MSi)	Metal-rich (MSi, M_2Si)
Formation temperature (°C)	≈350	≈600	≈200
Barrier height to n-Si (eV)	≈0.40	0.52-0.68	0.66-0.93
Resistivity (μΩcm)	100-300	13-1000	20-100

Table 3.1 Comparison of the three silicide classes. After Thompson and Tu (1982).

Silicide	PtSi	Pd_2Si	$CoSi_2$	$NiSi_2$
Structure	Orthorhombic MnP	Hexagonal Fe_2P	Cubic CaF_2	Cubic CaF_2
Lattice Mismatch(%)	9.5	2.2	1.2	0.4
Formation temperature (°C)	300	100-700	550-1000	750-800
Substrate	(111)	(111)	(111) (100)	(111) (100)

Table 3.2 Details of the silicides observed to grow epitaxially on silicon. After Tung et al. (1982).

Silicides are also of interest as they have found many potential applications as Ohmic or rectifying contacts and low resistance interconnects in very-large-scale integrated circuits (Murarka, 1980; Crowder and Zirinsky, 1979). Further interest has been generated in them by the discovery that some phases can be grown epitaxially on silicon substrates. So far at least four silicides have been observed to do this: PtSi (Kawamura et al., 1967; Sinha et al., 1972; Ishiwara et al., 1979a), Pd_2Si (Buckley and Moss, 1972; Bower et al., 1973; Hutchins and Shepela, 1973; Ishiwara et al., 1979b; Saitoh et al., 1981), $NiSi_2$ (Ishiwara et al., 1979b; Saitoh et al., 1981; Chiu et al., 1980a; Tu et al., 1974) and $CoSi_2$ (Bean and Poate, 1980; Saitoh et al., 1980, 1981). Some general properties of these silicides and the silicide-silicon interfaces they form are given in Table 3.2. These interfaces can be formed by metal deposition and annealing and by molecular beam epitaxy (MBE) codeposition. The formation and structures of epitaxial silicides has been reviewed by Tung et al. (1982a). The atomic structures of some of these silicide-silicon interfaces have been studied using high resolution transmission electron microscopy (TEM) (Krakow, 1982; Cherns et al., 1982a, 1982b, 1984; Chen et al., 1982) The $NiSi_2$-Si(111) system in particular has been revealed (Cherns et al., 1982b) to be atomically abrupt at the interface and to have a regular lattice structure there.

This simplicity makes it an ideal system for the theoretical study of the electronic structure of a metal-semiconductor interface. Also silicon can be grown epitaxially on a layer of silicide grown epitaxially on a silicon substrate (Bean and Poate, 1980; Saitoh et al., 1980; Tung et al., 1986b) which raises the possibility of novel classes of devices employing buried metal layers and of manufacturing silicon-silicide-silicon superlattices.

In this chapter the results of calculations of the electronic structure of some bulk transition metal silicides are presented. In section 3.2 are presented the results of calculations for some near noble metal silicides and in section 3.3 are presented the results for some refractory metal disilicides.

3.2 Near Noble metal silicides

3.2.1 Introduction

In order to give an indication of the accuracy of the method used throughout this work the electronic structure of silicon and nickel calculated by this method are presented here. The energy bands and total density of states of silicon are shown in Figures 3.4 and 3.5 respectively, and the energy bands and the total density of states of nickel are shown in Figures 3.6 and 3.7 respectively. (See the Note on the presentation of densities of states at the end of this thesis.) The points and lines of high symmetry corresponding to the labels in Figures 3.4 and 3.6 are shown in Figure 3.8.

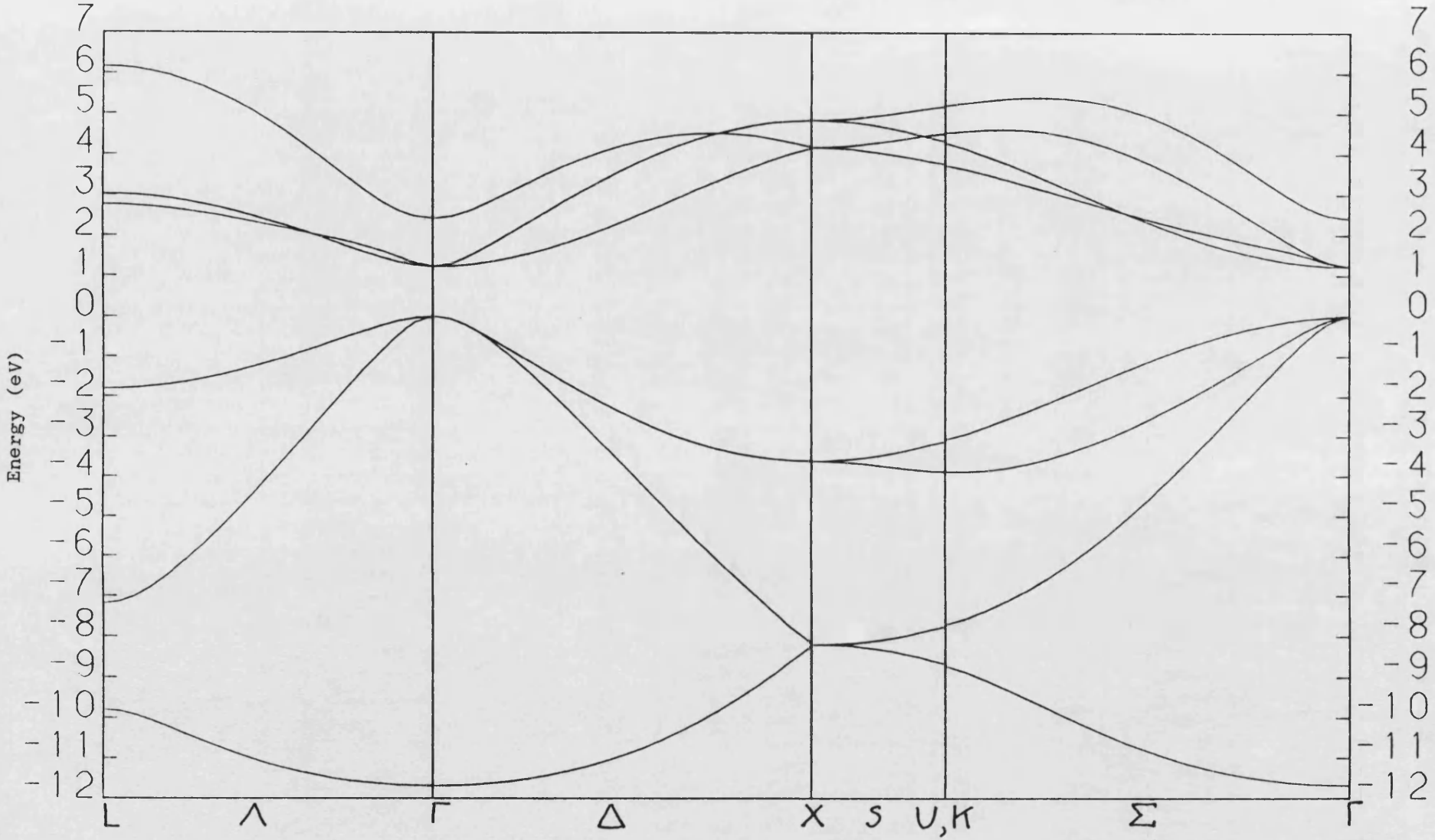

Figure 3.4 The energy bands of Si.

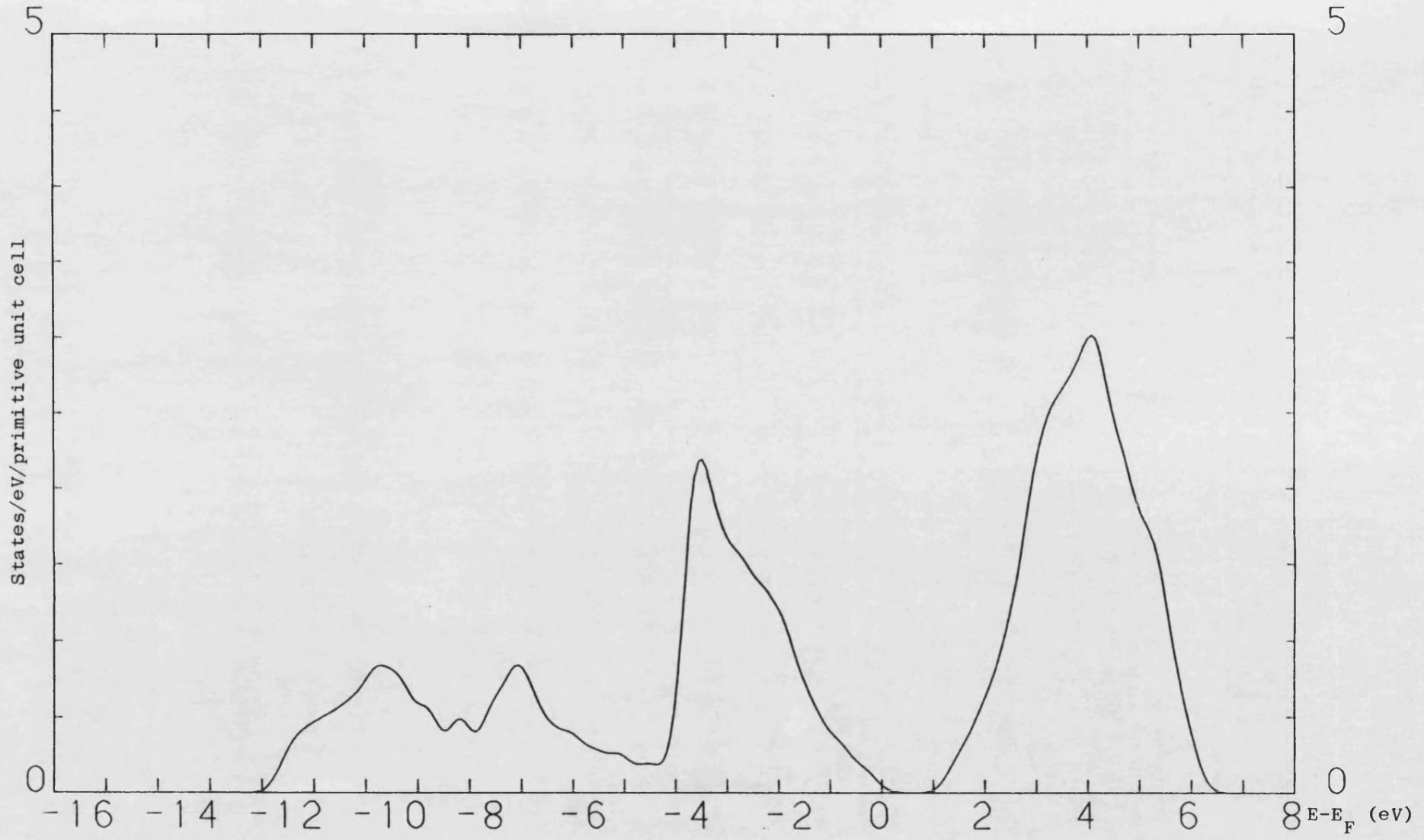

Figure 3.5 The calculated total DOS for Si.

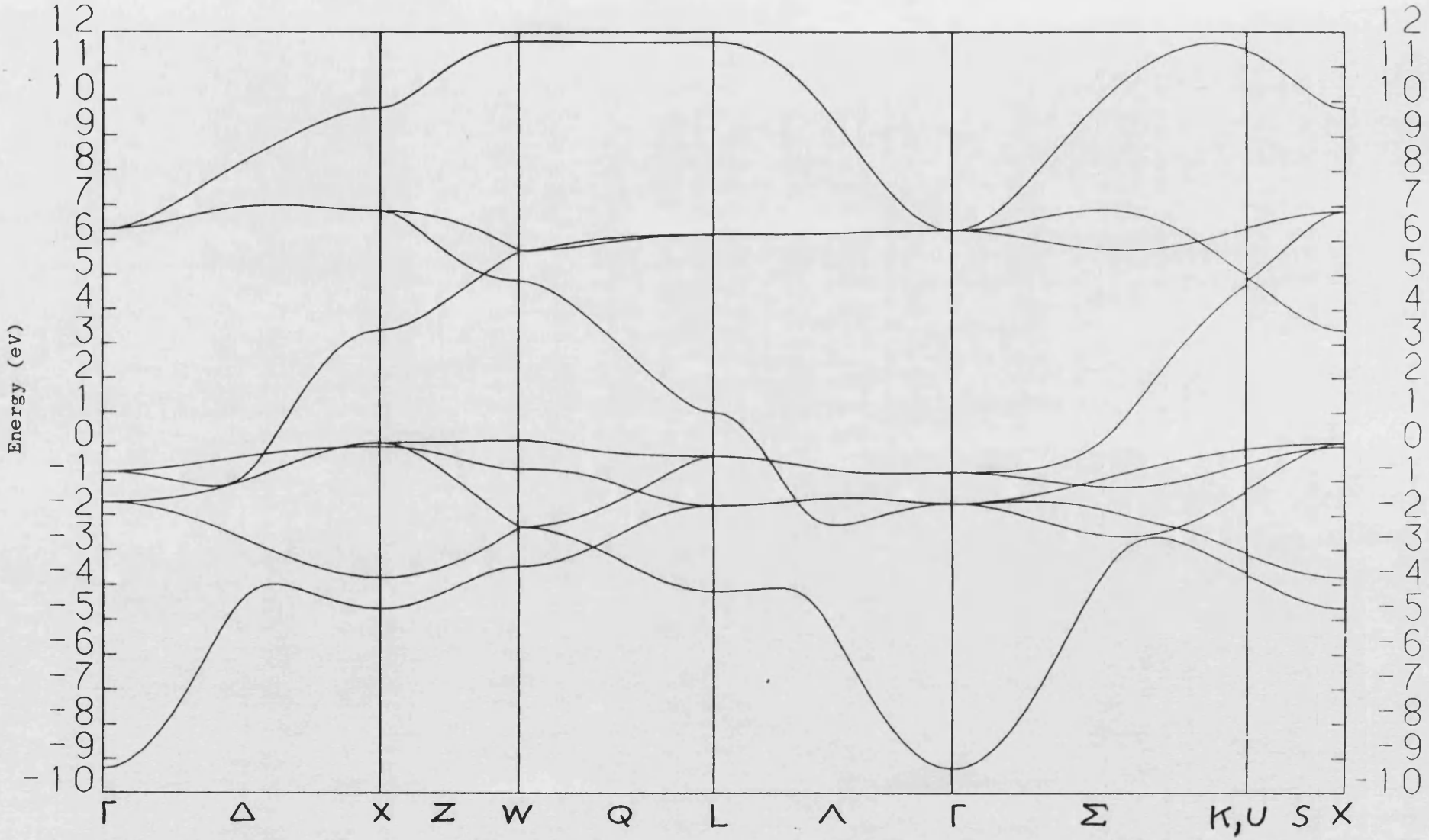

Figure 3.6 The energy bands of Ni.

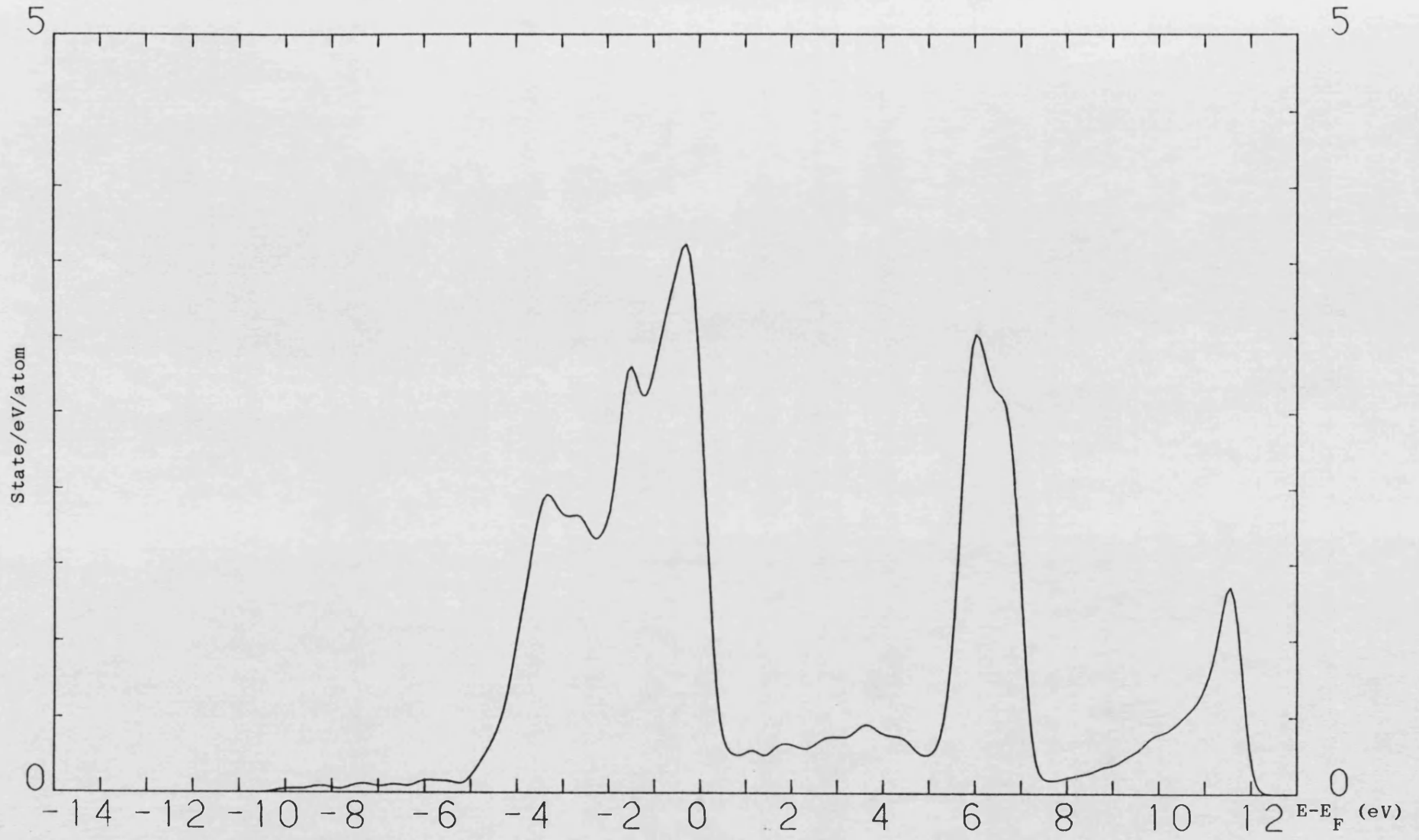

Figure 3.7 The calculated total DOS for Ni.

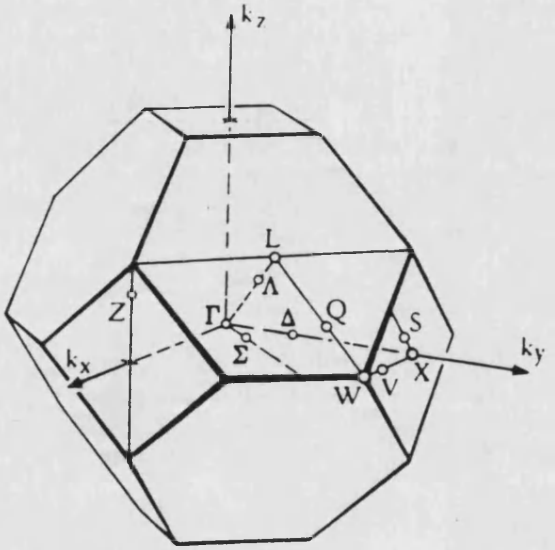

(a)

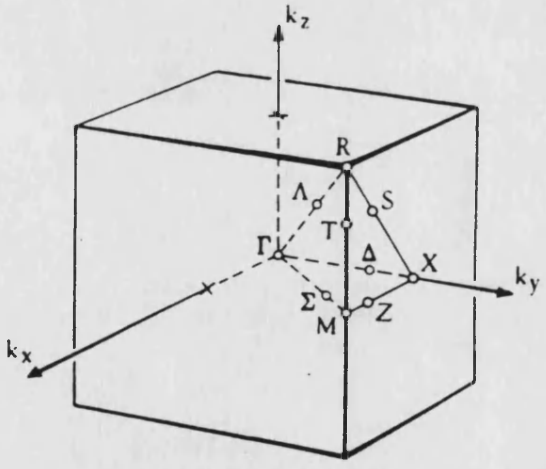

(b)

Figure 3.8 The points and lines of high symmetry in (a) the Brillouin zone of the face-centred cubic lattice, and (b) the Brillouin zone of the simple cubic lattice (Lax,1974).

The silicon valence band in Figure 3.5 shows the usual three peaks and has a width of 11.7 eV. The gap in the silicon density of states is 1.2 eV (it appears smaller in Figure 3.5 because of the smoothing that has been applied to the data appearing in this figure) which is the same as the experimental value (Kittel, 1976), but Figure 3.4 shows it to be direct gap when it is known to be an indirect gap with the conduction minimum along Δ.

The nickel density of states has a large d derived feature between about 0.5 and -5.0 eV so that the Fermi level lies just in the top of the d band as would be expected in a near noble metal. There is an sp derived tail stretching down to -9.3 eV which corresponds to the parabolic-like band starting at Γ seen in Figure 3.6. Here, as with all the other calculations in this work, results above the Fermi level cannot be trusted because of the small number of basis orbitals used. The energies of the silicon and nickel valence orbitals that were used and the Fermi energies calculated for bulk nickel and silicon are given in Table 3.12. The occupation of the nickel d orbital was found to be 9.3 electrons and the energy of the d orbital that was used which corresponds to this configuration was -5.6 eV.

3.2.2 Nickel silicides

The electronic structures of four nickel silicide phases were calculated, namely Ni_3Si, Ni_2Si, NiSi and $NiSi_2$. The crystallogrpahic details of these silicides are given in Table 3.3. The phase Ni_3Si will be considered first.

Phase	System	Structure Type	In Å a	b	c	Z	Space group	Atoms	Point Set	x	y	z
Ni_3Si	Cubic	$AuCu_3$	3.51	3.51	3.51	1	Pm3m	1Si	1a			
								3Ni	3c			
Ni_2Si	Orthorhombic	$PbCi_2$	5.00	3.73	7.04	4	Pnma	4Ni	4c	825		063
								4Ni	4c	958		703
								4Si	4c	236		114
NiSi	Orthorhombic	MnP	5.18	3.34	5.62	4	Pnma	4Ni	4c	006		184
								4Si	4c	170		580
$NiSi_2$	Cubic	CaF_2	5.41	5.41	5.41	4	Fm3m	4Ni	4a			
								8Si	8c			

Table 3.3 The crystallographic details of nickel silicides.

Ni_3Si crystallizes into the simple cubic Cu_3Au structure. In this structure, with the Si atoms on the cubic Bravais lattice sites, the Ni atoms are on the face centred sites (see Figure 3.9 and Table 3.4). In the calculations for Ni_3Si interactions between atoms separated by up to 3.55 Å were included and the interatomic distances in Ni_3Si less than 3.55 Å are given in Table 3.5.

The calculated band structure for Ni_3Si along lines of high symmetry in the simple cubic Brillouin zone (see Figure 3.8) is shown in Figure 3.10. The bands around the Fermi level are shown expanded in Figure 3.11. For comparison the energy bands calculated by Bylander et al. (1982a) using a self-consistent linear-combination-of-Gaussian-orbitals method are shown in Figure 3.12. It can be seen that the band structures obtained from these two calculations are very similar.

The calculated total and projected densities of states for Ni_3Si are shown in Figure 3.13. (See the Note at the end of this thesis.) The density of states projected onto the Si atoms is very small in Figure 3.13 because it is shown on the same scale as the total and Ni projected density of states and there are, of course, three times as many Ni atoms as Si atoms in Ni_3Si. The calculated occupied band width is 13.5 eV. At the bottom of the valence band, below -8 eV, there is a group of states which have split away from the rest. These are bonding states involving Si s and Ni s, p and d orbitals. Between -8 and 4 eV there is a large and broad d feature which has a narrow peak at -1 eV.

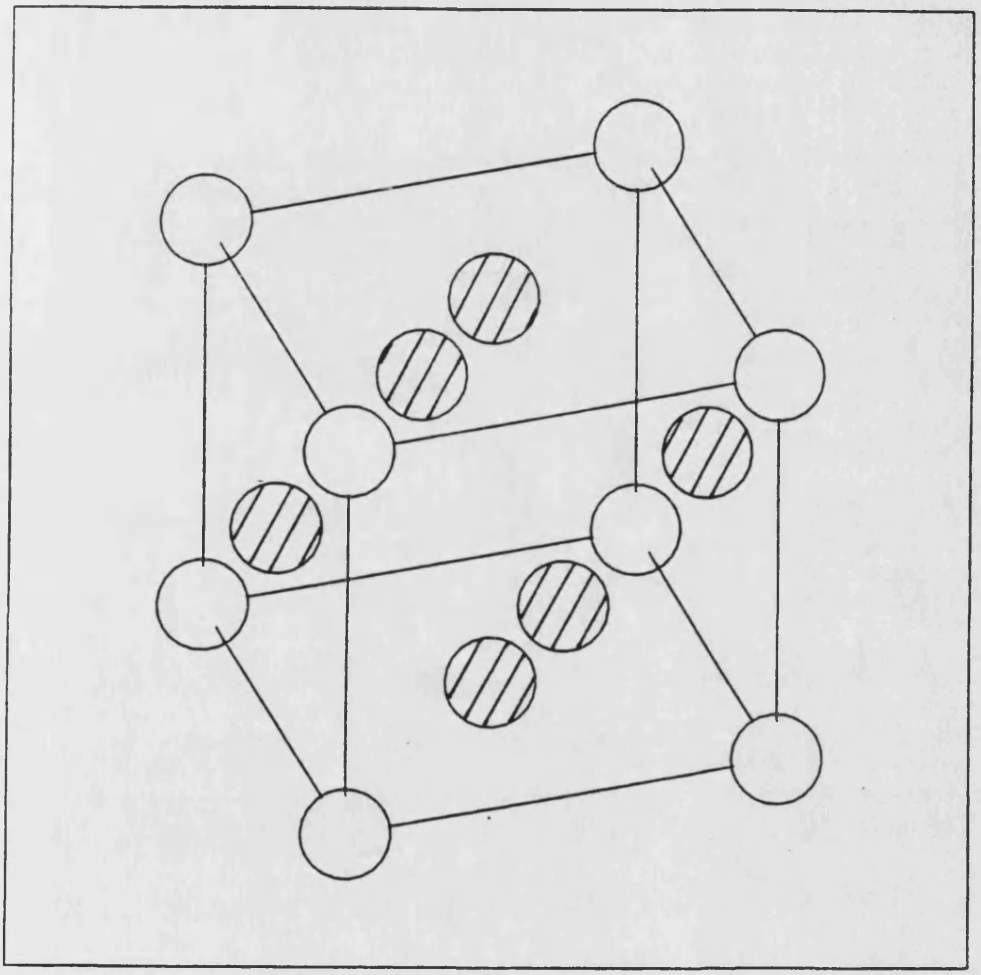

Figure 3.9 The Ni_3Si unit cell. The Si atoms are represented by open circles and the Ni atoms by shaded circles.

Number of positions (Wyckoff notation)	Position coordinates
1(a)	(0,0,0)
3(c)	$(\frac{1}{2},\frac{1}{2},0)$, $(\frac{1}{2},0,\frac{1}{2})$, $(0,\frac{1}{2},\frac{1}{2})$

Table 3.4 The equivalent positions of the space group Pm3m occupied in Ni_3Si.

Ni:	has 8 Ni neighbours at 2.48 Å	
	has 4 Si neighbours at 2.48 Å	
	has 6 Ni neighbours at 3.51 Å	
Si:	has 12 Ni neighbours at 2.48 Å	
	has 6 Si neighbours at 3.51 Å	

Table 3.5 Interatomic distances in Ni_3Si.

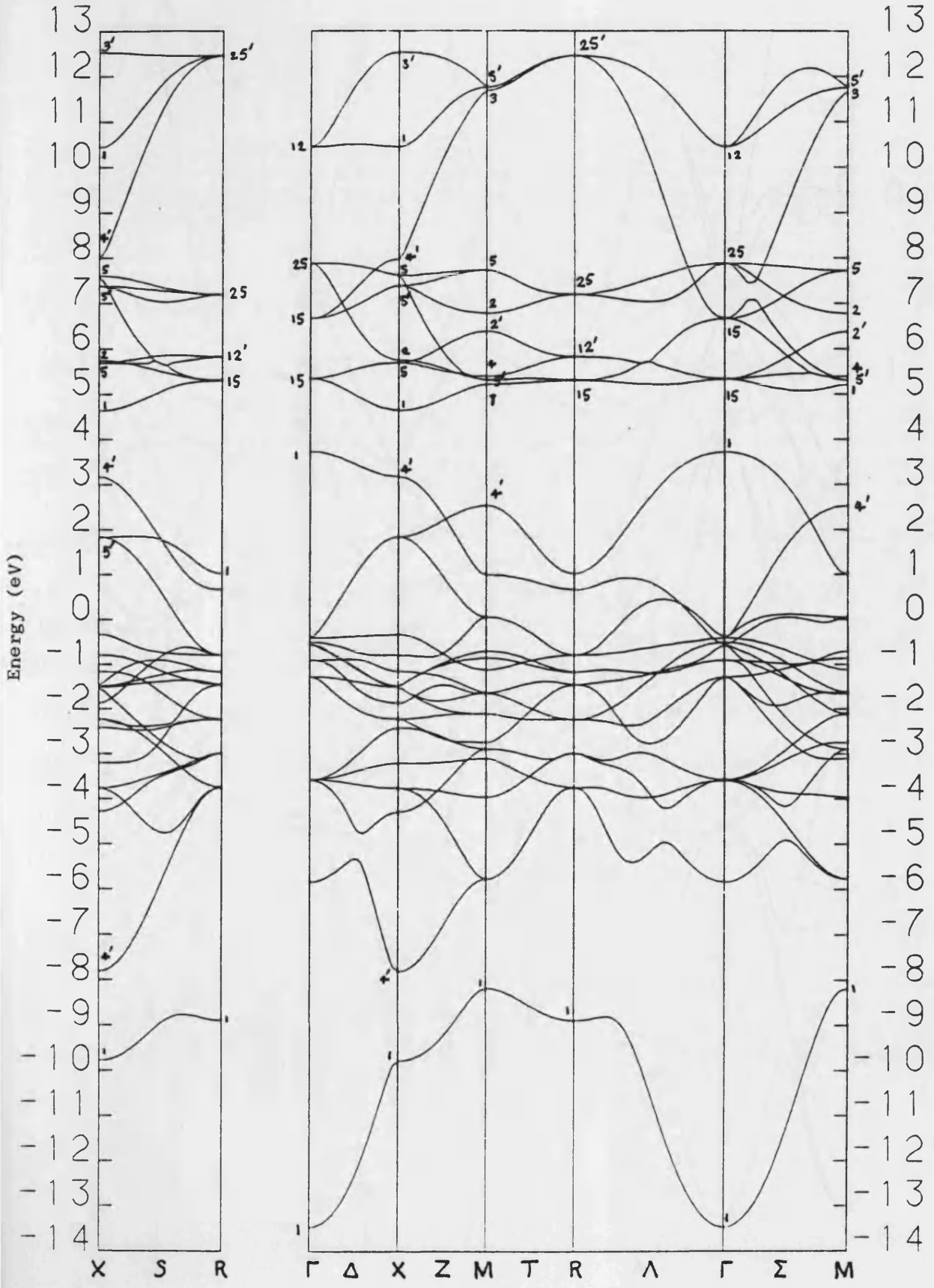

Figure 3.10 The energy bands of Ni_3Si.

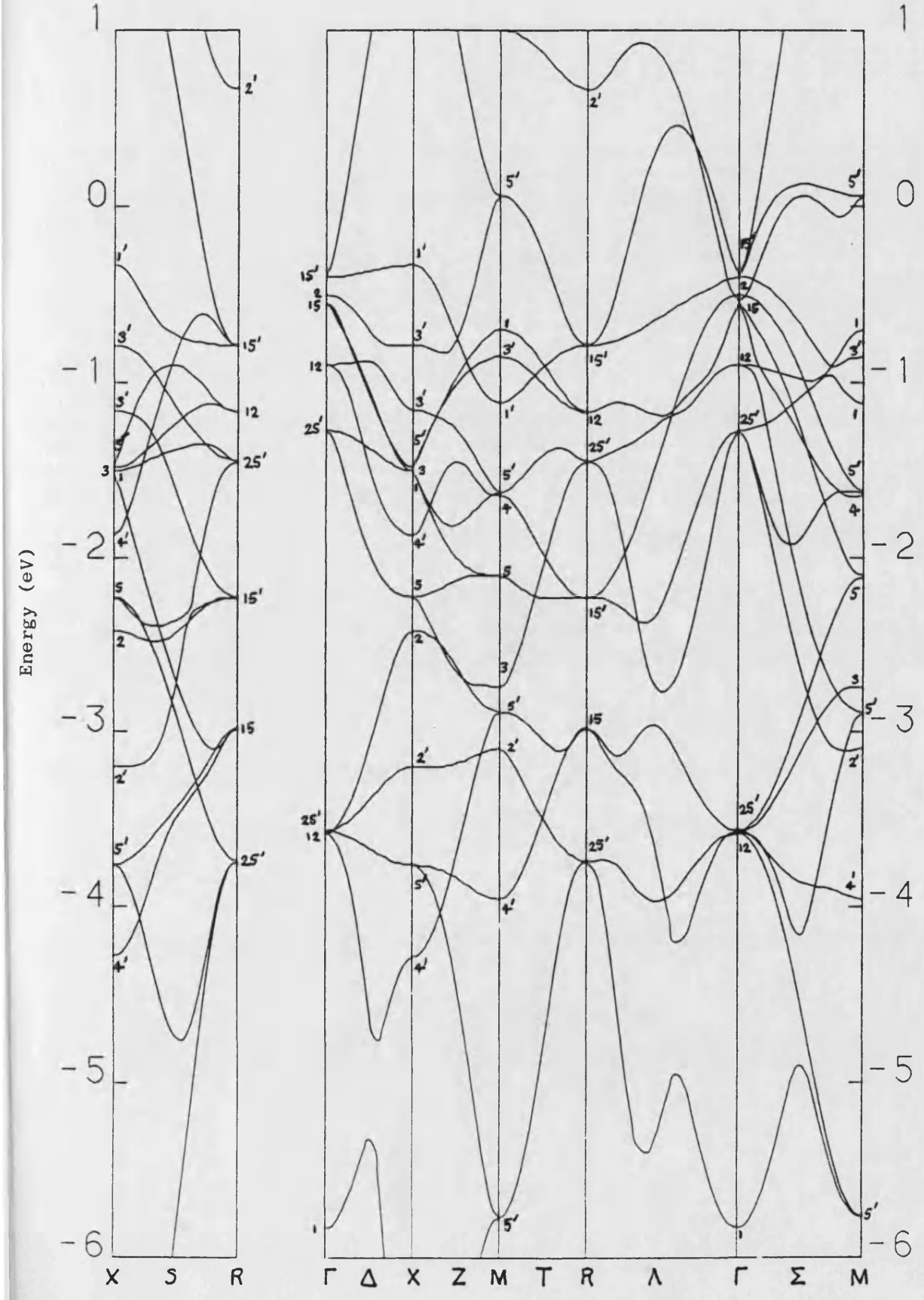

Figure 3.11 The energy bands of Ni_3Si near the Fermi level.

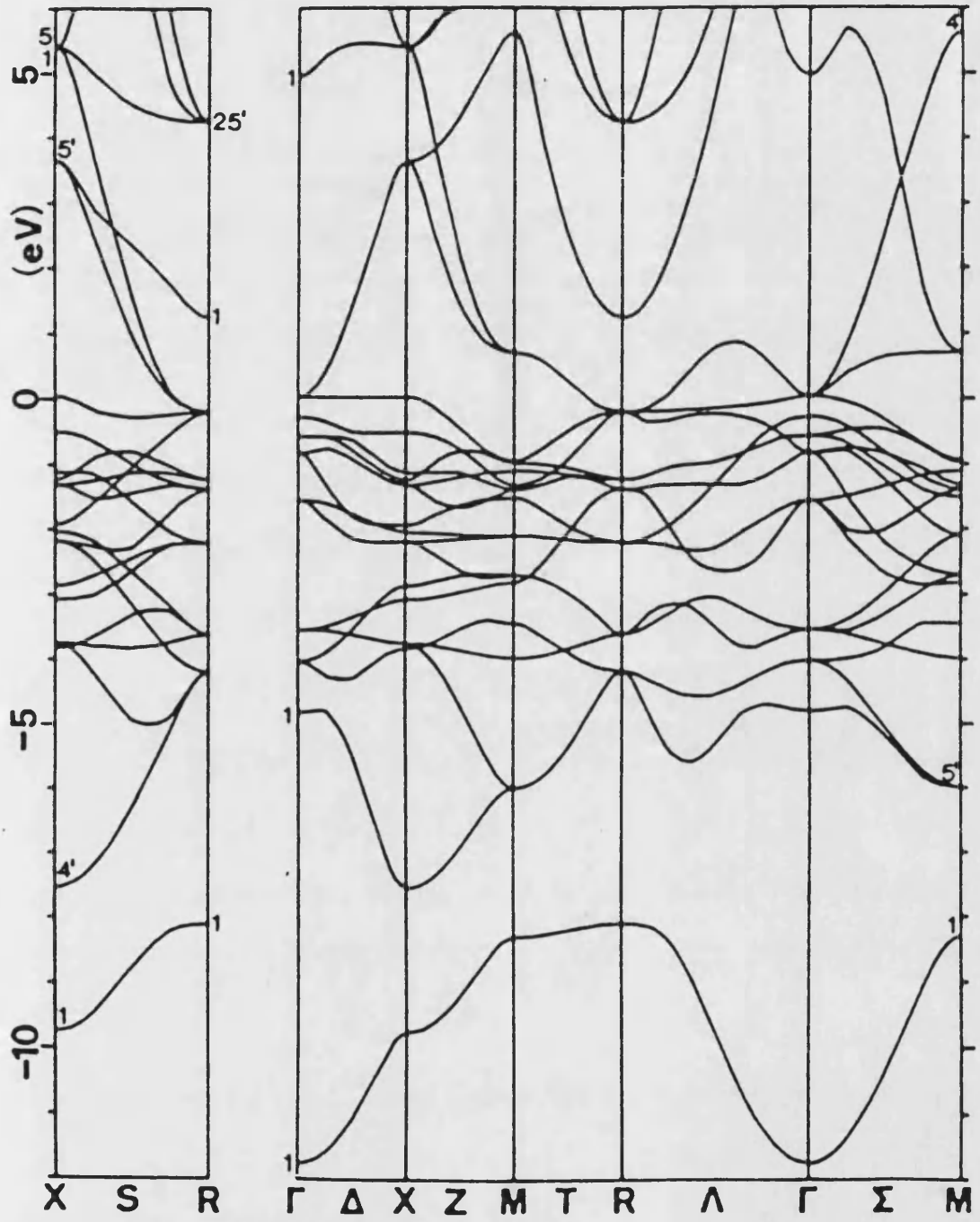

Figure 3.12 The energy bands of Ni_3Si as calculated by Bylander et al. (1982).

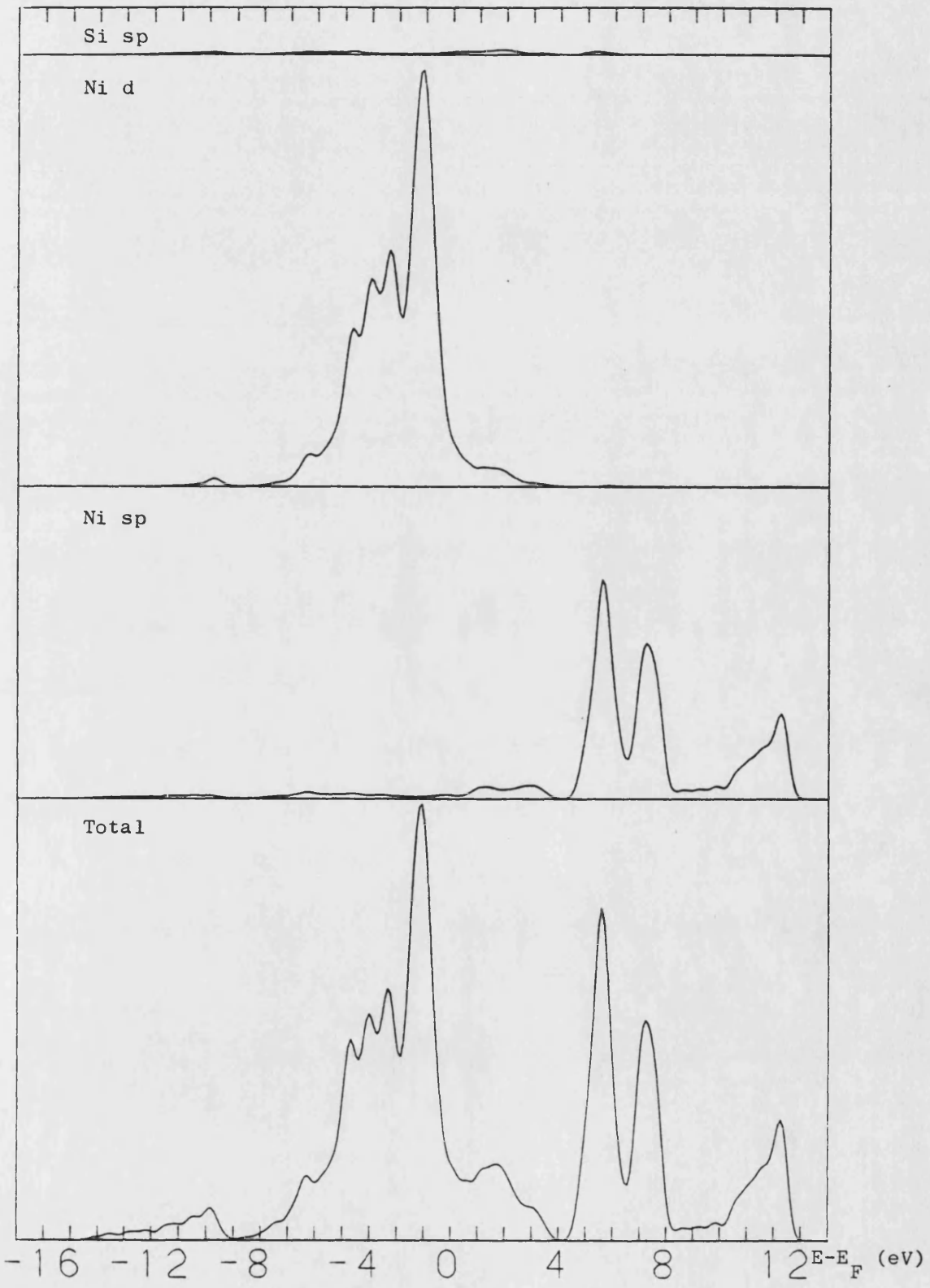

Figure 3.13 The calculated total and projected DOS for Ni_3Si.

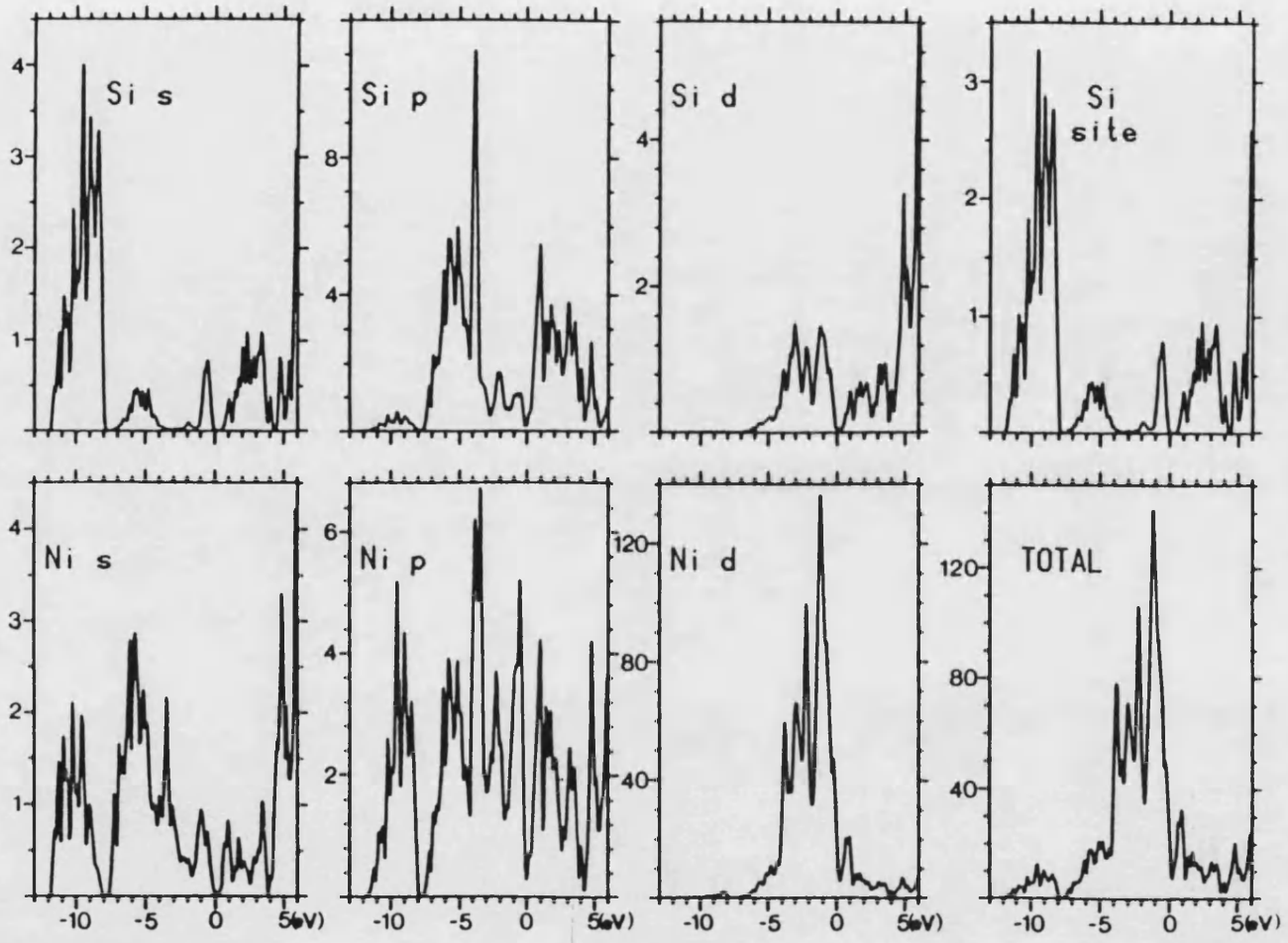

Figure 3.14 The total and projected DOS for Ni_3Si in units of tenths of an electron per unit cell per eV as calculated by Bylander et al. (1982).

The states between -8 and -2 eV are mainly Ni d in character but there are some Si p and some Ni sp orbitals present as well. The states between 0.5 and 4 eV have a roughly equal contribution from Ni d and Ni sp orbitals and a lesser contribution from Si p orbitals. The states at the Fermi level are mainly d-like. Bonding in the transition metal silicides has previously been interpreted (Rubloff and Ho, 1982; Weaver et al., 1984) in terms of the hybridization of Si p and Ni d orbitals, with the Si s orbitals not participating. In this interpretation the states below the nonbonding d peak at -1 eV (between -8 and -2 eV) are bonding Si p-Ni d hybrids while those above the Fermi level (between 0.5 and 4 eV) are antibonding Si p-Ni d hybrids.

The total and projected densities of states calculated by Bylander et al. (1982a) are shown in Figure 3.14. These show features the same as those seen in the present calculations: there is a prominent d feature which stretches down to -8 eV and which has a sharp peak just below the Fermi level, and there are a set of states below -8 eV which have split away from the rest.

Ni_2Si crystallizes into the orthorhombic $PbCl_2$ crystal structure. This structure (see Figure 3.15 and Tables 3.3 and 3.6) can be regarded as a considerably distorted close-packing of Ni atoms with the Si atoms accommodated in the same plane with them. Interatomic distances in Ni_2Si less than 3.3 Å are given in Table 3.7.

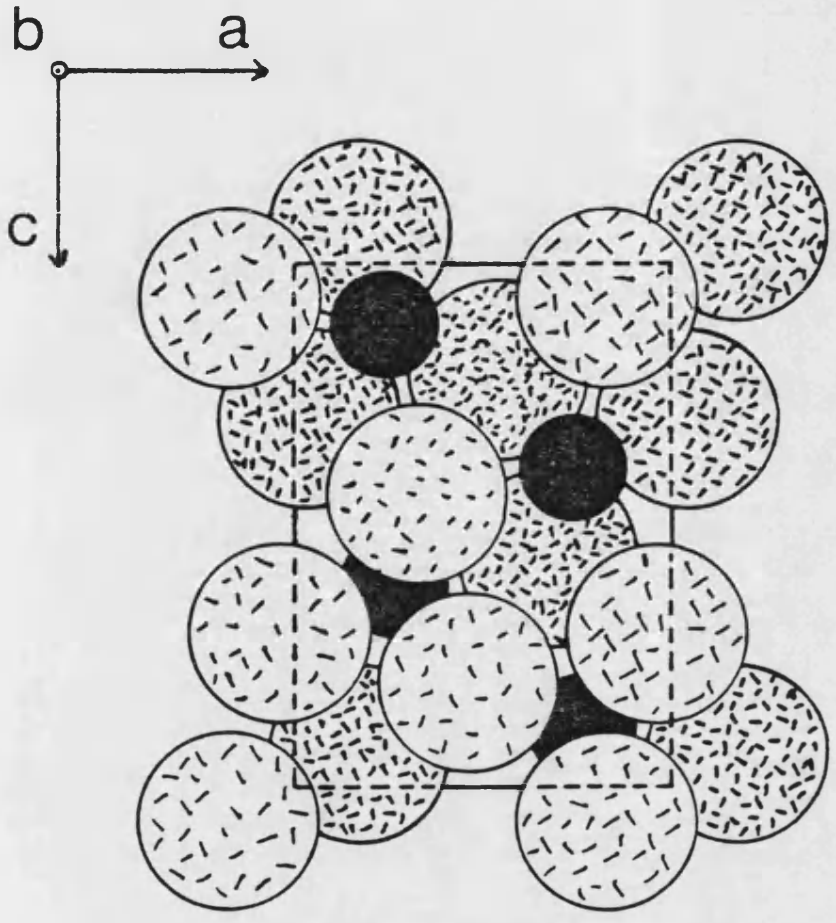

Figure 3.15 The Ni_2Si structure seen down the b axis. Two layers in the b direction are shown, one at $-\frac{1}{4}$ and the other at $+\frac{1}{4}$. The rectangle shows the boundary of a unit cell in the ac plane. The Si atoms are black.

Number of positions (Wyckoff notation)	Position coordinates
4(c)	$\pm(x,\frac{1}{4},z)$, $\pm(x+\frac{1}{2},\frac{1}{4},\overline{z+\frac{1}{2}})$

Table 3.6 The equivalent positions of the space group Pnma occupied in Ni_2Si.

Ni(I)-Ni	Ni(I)-Si	Ni(II)-Ni	Ni(II)-Si	Si-Ni	Si-Si
2.54 (2)	2.09	2.54 (2)	2.47 (2)	2.09	3.15
2.62 (2)	2.26 (2)	2.59 (2)	2.49 (3)	2.26 (2)	
2.71 (4)	2.32	2.62 (2)	3.21	2.32	
	2.97	2.71 (2)		2.47 (2)	
				2.49 (3)	
				2.97	
				3.21	

Table 3.7 Interatomic distances in Ni_2Si. The numbers in the columns headed X-Y give the distances in Å from an atom of type X to atoms of type Y. The numbers in parentheses indicate the number of Y atoms at the given distance when this number is greater than one.

The total and projected densities of states calculated for Ni_2Si are shown in Figure 3.16. Interactions between atoms separated by up to 3.3 Å were included in the calculation. The occupied band width is 13 eV. Again there is a band below -8 eV which has split away from the rest of the states. The band gap is over 1 eV so that the separation here is more definite than it is in Ni_3Si. This band is also again weighted on Si s and Ni sp and d orbitals. There is a partially filled band between -7 and 2 eV. This is almost entirely Ni d derived but it does have some contribution from the Si p orbitals and, to a lesser extent, from the Ni sp orbitals as well. Corresponding to the main Ni d peak, which lies from just below the Fermi level down to -4 eV and which is presumably mainly derived from Ni d-Ni d interactions, there is a dip in the Si p density of states. The states between -7 and -4 eV and the empty states above the Fermi level up to 2 eV correspond to two small peaks in the Si p density of states and would thus seem to arise from bonding and antibonding Si p-Ni d hybrids respectively. The states at the Fermi level are mainly Ni d derived.

The electronic structure of Ni_2Si has also been calculated by Bisi and Calandra (1981) who used an LCAO method known as the iterative extended Hückel method. Their results are shown in Figure 3.17. These are broadly similar to the present results if not indentical to them in detail. The electronic structure of Ni_2Si has been investigated experimentally using synchrontron-radiation photoemission

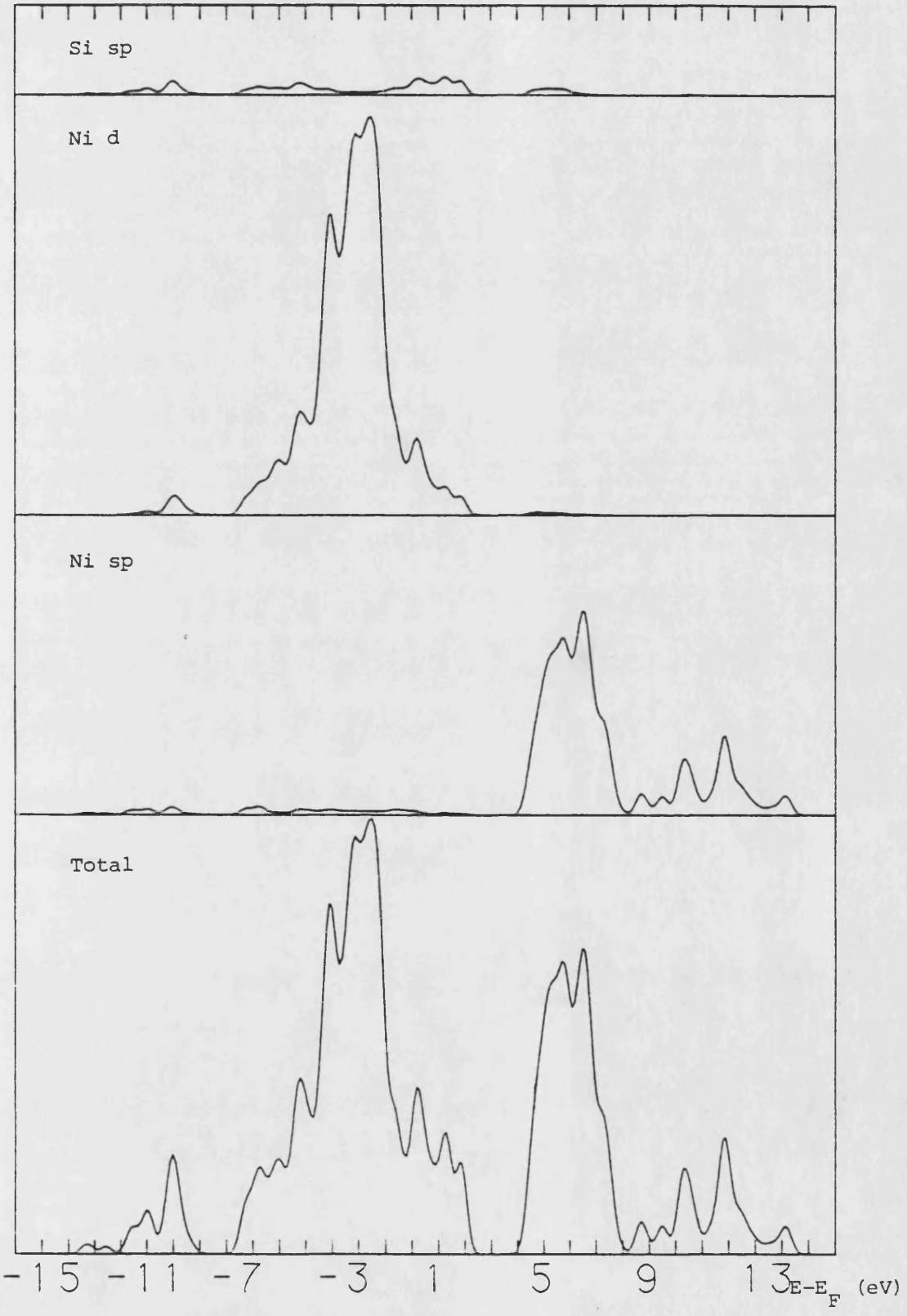

Figure 3.16 The calculated total and projected DOS for Ni_2Si.

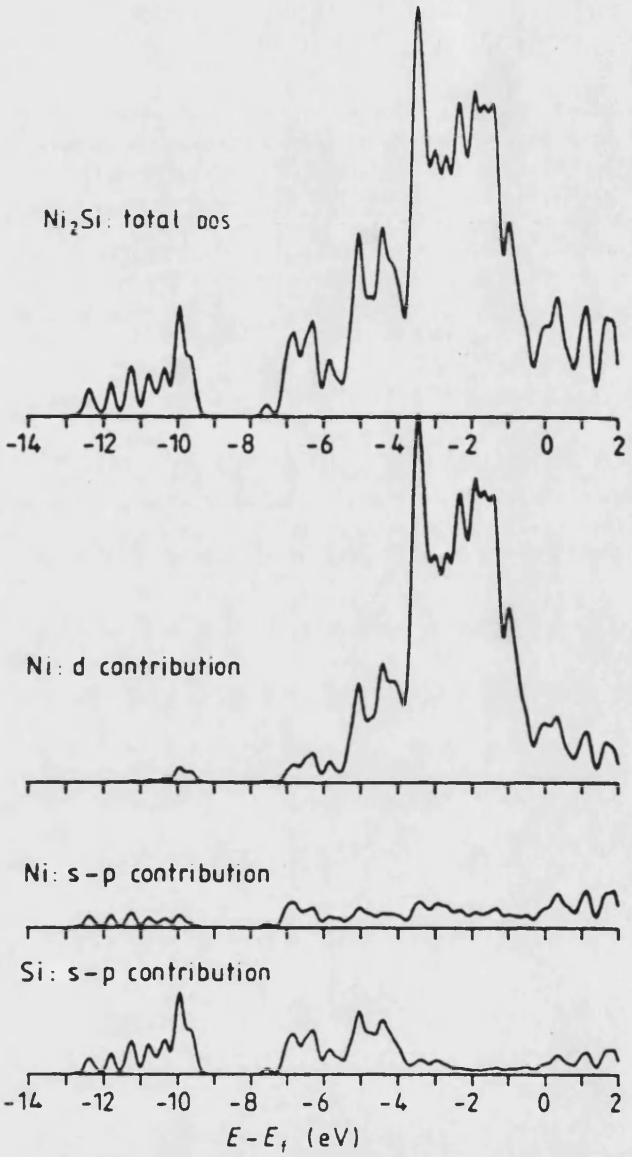

Figure 3.17 The total and projected DOS for Ni_2Si as calculated by Bisi and Calandra (1981).

spectroscopy by Franciosi et al. (1982). They found a main peak at -1.3 eV and a second at -2.7 eV. The first of these experimental features is just above the maximum of the Ni d peak in the present calculation, while the second is a little above a spike lower down in the Ni d states (see Figure 3.27a) so that there is a reasonable agreement between theory and experiment.

NiSi is isostructural with the other two near noble metal monosilicides PdSi and PtSi. They all crystallize into the orthorhombic MnP structure. The MnP structure is shown in Figure 3.18 and described in Table 3.8. The structural parameters for NiSi are given in Table 3.3. In the MnP structure (which is a distortion of the NiAs structure, Wyckoff, 1964) each metalloid atom is surrounded by six metal atoms at the corners of a distorted trigonal prism which has one base much larger than the other. The metal atoms are surrounded by six metalloid atoms at the corners of a distorted octahedron and four metal atoms at the corners of a distorted tetrahedron. Table 3.9 is a table of the interatomic distances in the three near noble metal monosilicides.

The calculated total and projected densities of states for NiSi are shown in Figure 3.19. (An interaction cut-off distance of 3.1 Å was used.) The occupied band width is 12 eV. The lowest states once again lie in a detached band, this time starting below -6 eV. This band has most weight on the Si s orbitals, somewhat less on the Ni d orbitals, and only a little on the Ni sp orbitals. There is a large

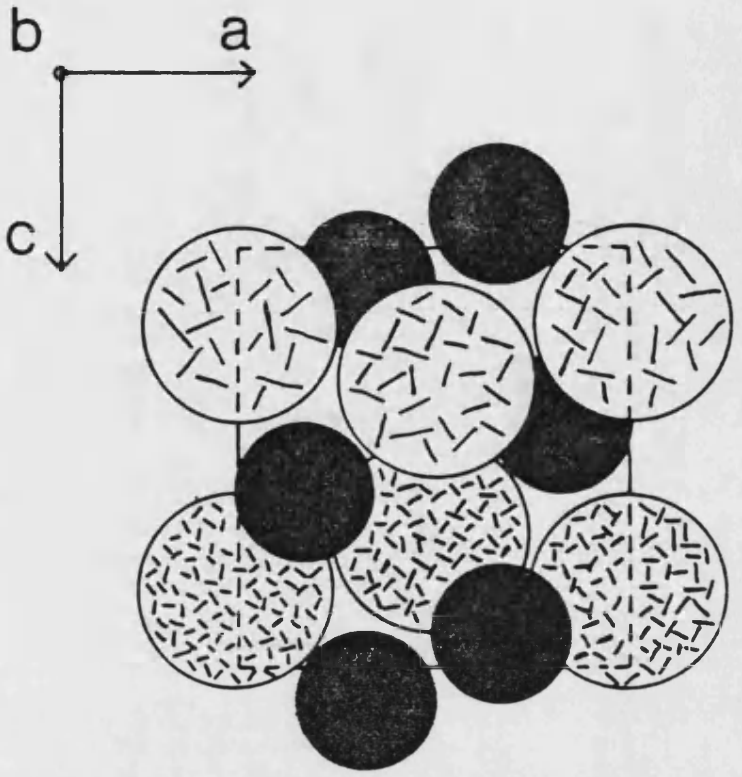

Figure 3.18 The MnP structure seen down the b axis. Two layers in the b direction are shown, one at $-\frac{1}{4}$ and the other at $+\frac{1}{4}$. The rectangle shows the boundary of a unit cell in the ac plane. The P atoms are black.

Number of positions (Wyckoff notation)	Position coordinates
4(c)	$\pm(x,\frac{1}{4},z)$, $\pm(x+\frac{1}{2},\frac{1}{4},\overline{z+\frac{1}{2}})$

Table 3. 8 The equivalent positions of the space group Pnma occupied in the MnP structure.

Phase	Distances in Å						
	M-M(2)	M-M(2)	M-Si(1)	M-Si(2)	M-Si(1)	M-Si(2)	Si-Si(2)
NiSi	2.66	2.69	2.29	2.32	2.38	2.44	2.59
PdSi	2.88	2.89	2.39	2.50	2.55	2.51	2.85
Ptsi	2.87	2.93	2.44	2.49	2.56	2.52	3.02

Table 3.9 Interatomic distances in the three near noble metal monosilicides. The headings X-Y(n) indicate that an atom of species X has n neighbours of species Y at the distances given. M stands for the metal atom species appropriate to the particular row.

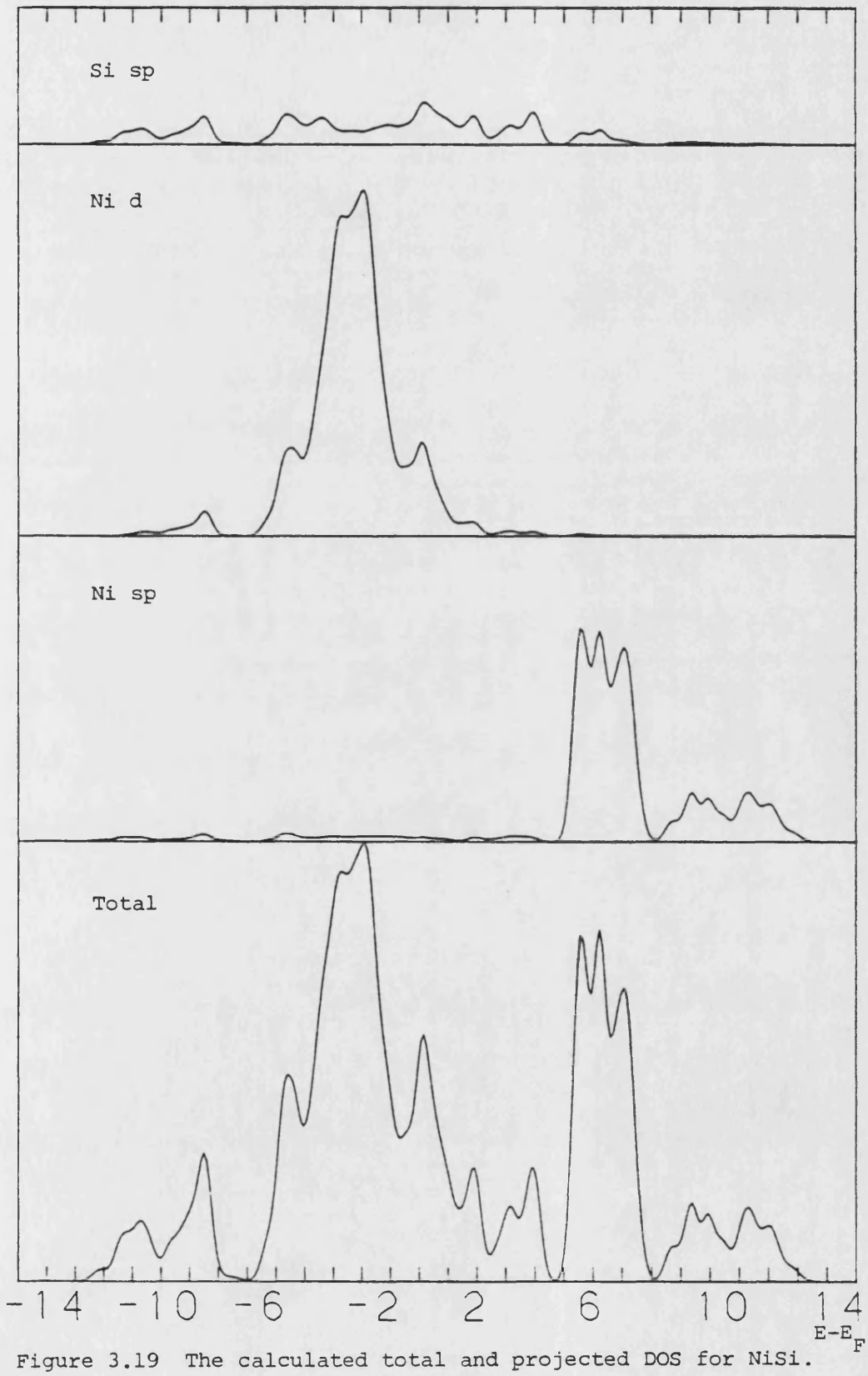

Figure 3.19 The calculated total and projected DOS for NiSi.

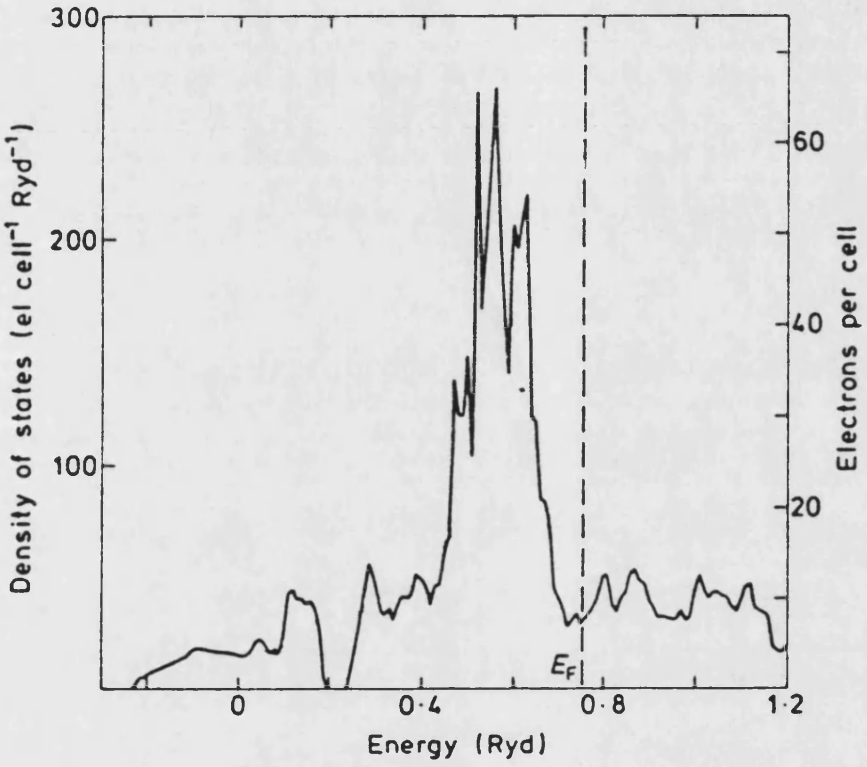

Figure 3.20 The total density of states for NiSi as calculated by Boulet et al. (1980).

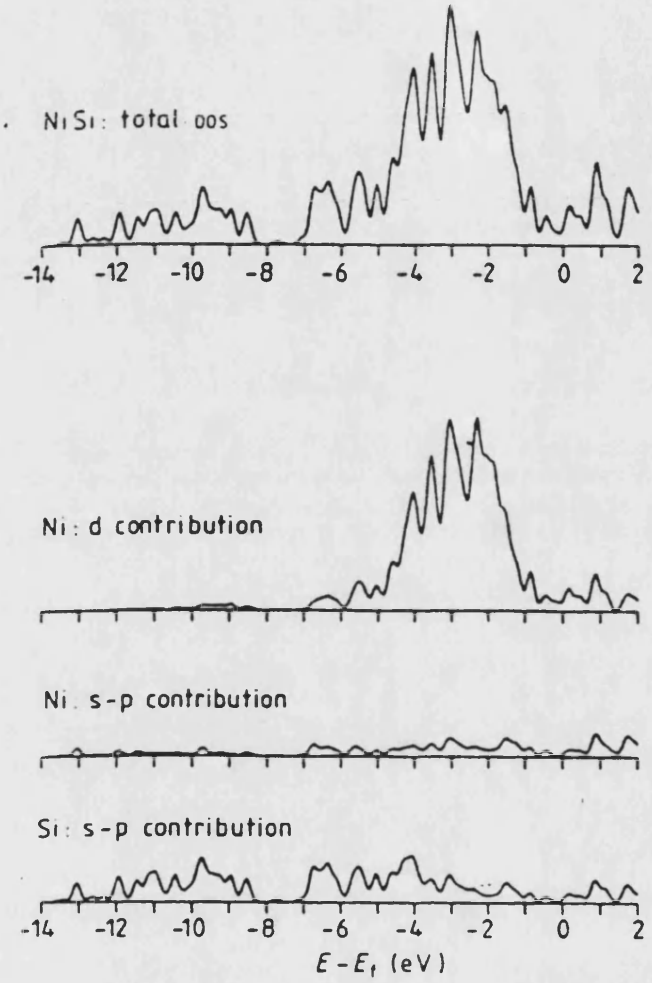

Figure 3.21 The total and projected DOS for NiSi as calculated by Bisi and Calandra (1981).

Ni d feature which starts at -6 eV and which continues up to 5 eV, but most of which lies between -4 and -1 eV. The states between -4 and -1 eV, although being mainly Ni d-like, also have a significant Si p character so that they must derive not only from Ni d-Ni d interactions but also from some Ni d-Si p interactions. There are two smaller peaks in the Ni density of states on either side of the main one at about -4.5 eV and just above the Fermi level. There are small peaks corresponding to these in the Si p density of states. The states between -6 and -4 eV and between -1 and 5 eV, being heavily weighted on the Ni d and Si p orbitals, are interpreted as arising from bonding and antibonding Si p-Ni d hybrids respectively. The Fermi level lies in the antibonding states. The Ni d contribution to the states here is about twice that from Si p with there being almost none from Ni sp.

Other theoretical investigations of the electronic structure of NiSi have been carried out by Bisi and Calandra (1981), Boulet et al. (1980) and Weaver et al. (1984). Weaver et al. (1984) performed a self-consistent augmented-spherical-wave calculation of the density of states of NiSi but with the monosilicide in the CuAu structure instead of the actual and more complicated MnP structure. This gave a Ni d peak (sharper than in the present calculation) a little below the Fermi level straddled by the bonding and antibonding Si p-Ni d hybrids but failed to reproduce the Si s-Ni d split-off band. The density of states for NiSi (as well as its band structure) was calculated by Boulet et al. (1980) using the

linear-combination-of-muffin-tin-orbitals (LMTO) method. Their calculated density of states is shown in Figure 3.20. The total and projected densities of states for NiSi calculated by Bisi and Calandra (1981) are shown in Figure 3.21. Both of these results are similar to the present one. However, they both have a smaller density of states at the Fermi level than the present calculation in which the Fermi level lies in an antibonding peak.

Synchrotron-radiation photoemission studies of NiSi (Franciosi et al., 1982) found structures at -1.8 and -3.0 eV. The first of these lie just above the Ni d peak maximum in the present calculation while the second lies just below a shoulder lower down in the Ni d states (see Figure 3.27b). These studies also found a very low density of states near the Fermi level, which fits rather better with the calculation of Bisi and Calandra (1981) and Boulet et al. (1980) than with the present one.

$NiSi_2$ has the face-centred cubic CaF_2 (Fluorite) structure (see Figure 3.22 and Tables 3.3 and 3.10). In this each Ni atom is surrounded by eight Si atoms at the corners of a cube and each Si atom is surrounded by four Ni atoms at the corners of a tetrahedron. The interatomic distances in $NiSi_2$ are given in Table 3.11.

In the calculations of the electronic structure of $NiSi_2$ an interaction cut-off distance of 3 Å was used. The band structure calculated for $NiSi_2$ along lines of high symmetry in the face-centred Brillouin zone (see Figure 3.8) is shown in figure 3.23. This is very similar below the Fermi level to the band structure obtained by Chabal et al.

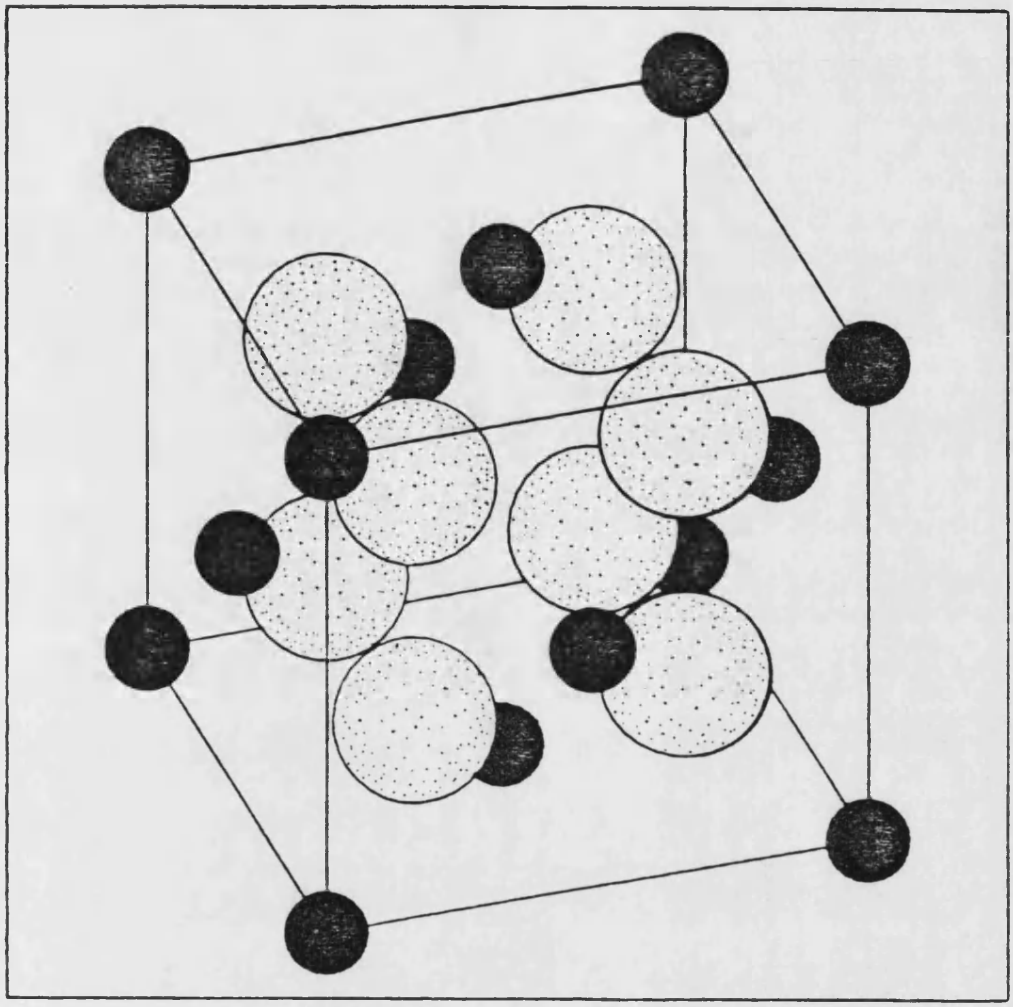

Figure 3.22 The unit cell of fuorite (CaF_2). The Ca atoms are black.

Number of positions (Wyckoff notation)	Position coordinates
	(0,0,0; 0,½,½; ½,0,½; ½,½,0)+
4(a)	(0,0,0)
8(c)	±(¼,¼,¼)

Table 3.10 The equivalent positions of the space group Fm3m occupied in the fluorite structure.

Ni:	has 8 Si neighbours at 2.34 Å	
	has 12 Ni neighbours at 3.82 Å	
Si:	has 4 Ni neighbours at 2.34 Å	
	has 6 Si neighbours at 2.70 Å	
	has 12 Si neighbours at 3.82 Å	

Table 3.11 Interatomic distances in $NiSi_2$.

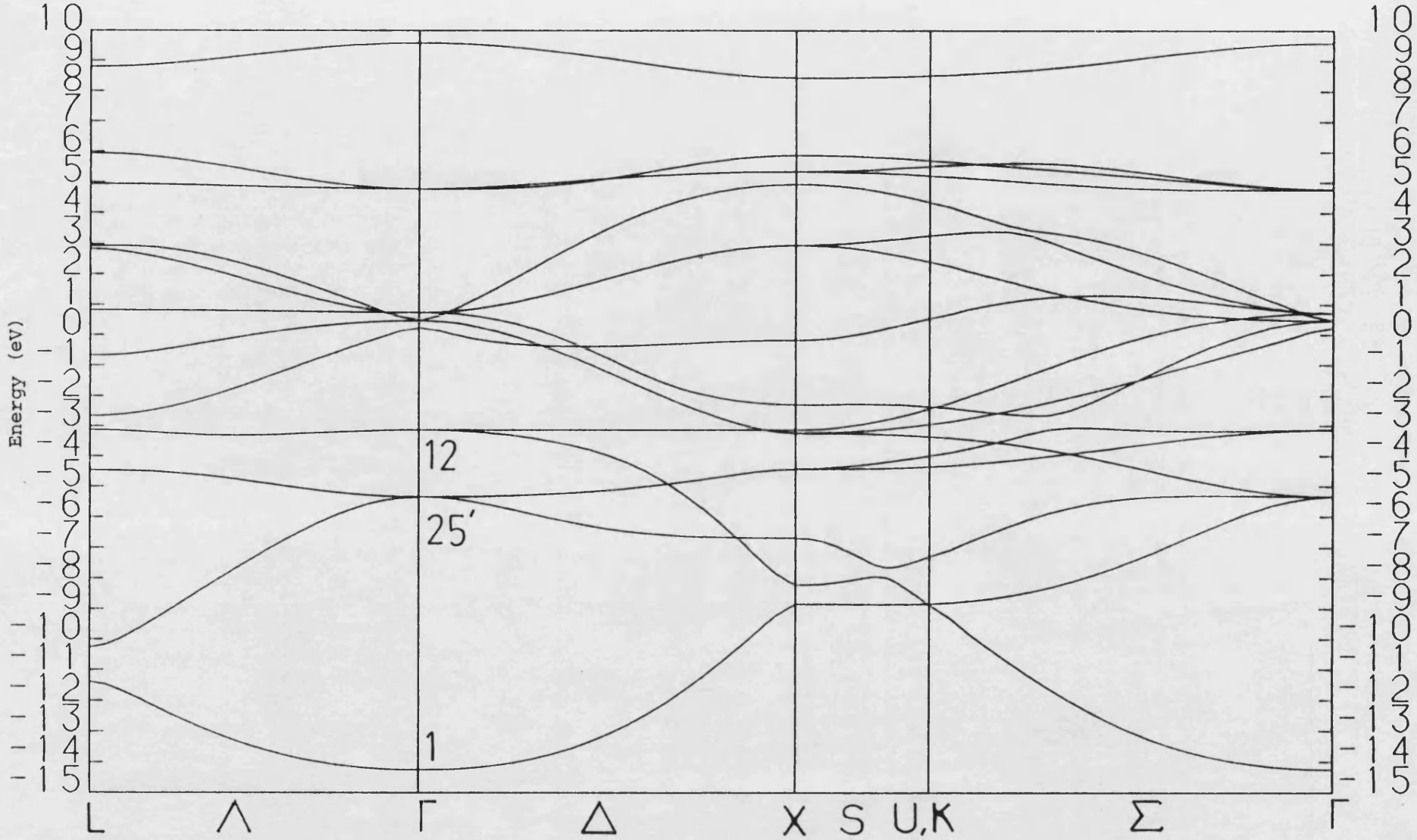

Figure 3.23 The energy bands of $NiSi_2$.

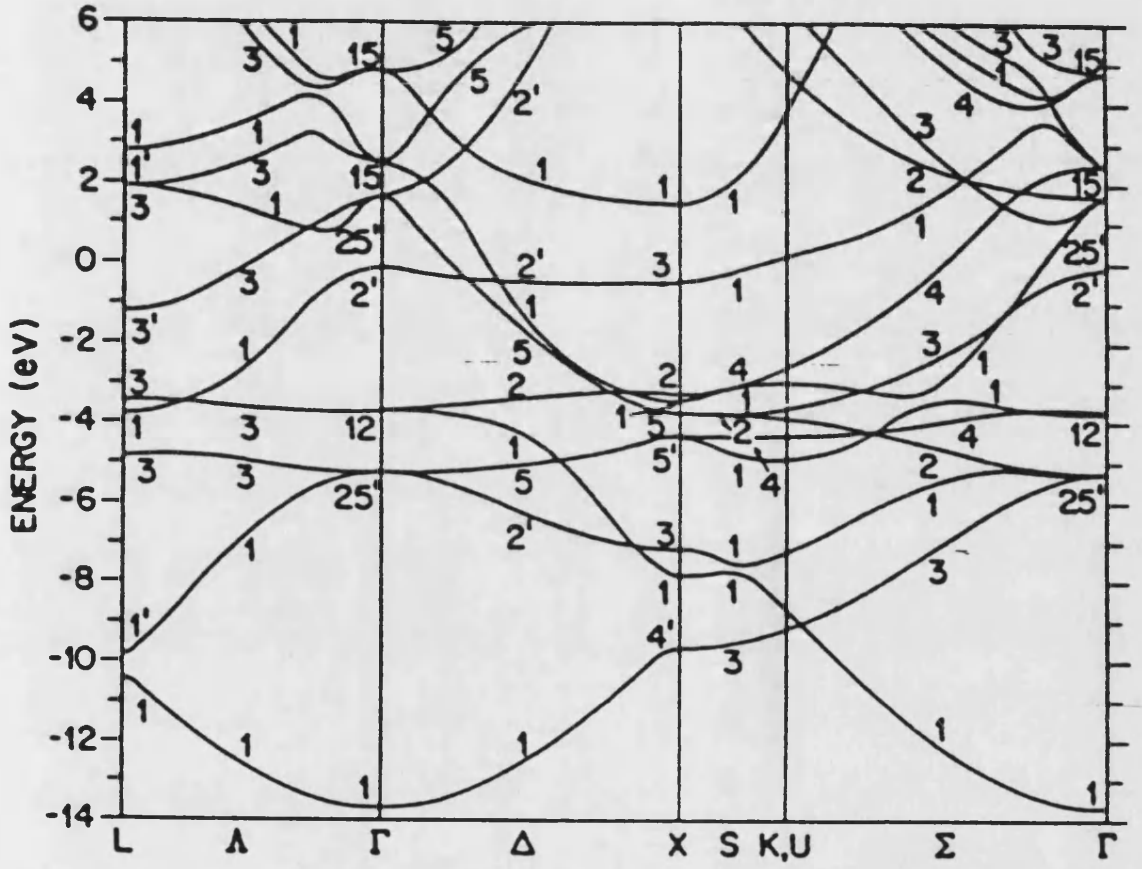

Figure 3.24 The energy bands of $NiSi_2$ as calculated by Chabal et al. (1982).

(1982) from an augmented-plane-wave calculation shown in Figure 3.24.

The total and projected densities of states obtained from the present calculations are shown in Figure 3.25. These are rather different in form from those of the other nickel silicides considered so far in that there is no split-off band: the Si sp states are nonvanishing everywhere below the Fermi level. The total density of states below -6 eV, infact, looks almost parabolic. These states, which are mainly Si s with a little Ni sp, correspond the almost-free-electron-like bands seen in Figure 3.23 below -6 eV. There is a narrow Ni d peak at -3 eV which, considering its narrowness, is probably derived from nonbonding orbitals. Looking at Figure 3.23 it can be seen that this feature arises from the very flat band which passes through Γ_{12} . Hence it can be deduced that the Ni $d_{x^2-y^2}$ and d_{z^2} orbitals (orbitals of Γ_{12} symmetry) are nonbonding in $NiSi_2$. There is a second, broader peak, a little below the nonbonding peak, at -5eV, where there are corresponding peaks in both the Ni d and the Si sp states. The states here must once again be due to the bonding Si p-Ni d hybrids also found in the other nickel silicides. The band which would seem to correspond to this feature passes through $\Gamma_{25'}$ just below -5 eV (see Figure 3.23). The orbitals which are of $\Gamma_{25'}$ symmetry are d_{xy}, d_{yz} and d_{zx}, and hence it must be these orbitals which are involved in the bonding in $NiSi_2$. Above the nonbonding peak, between -1 and 1 eV, there is a small plateau in the nickel d density of states, and at 1 eV there is a peak in the total density of

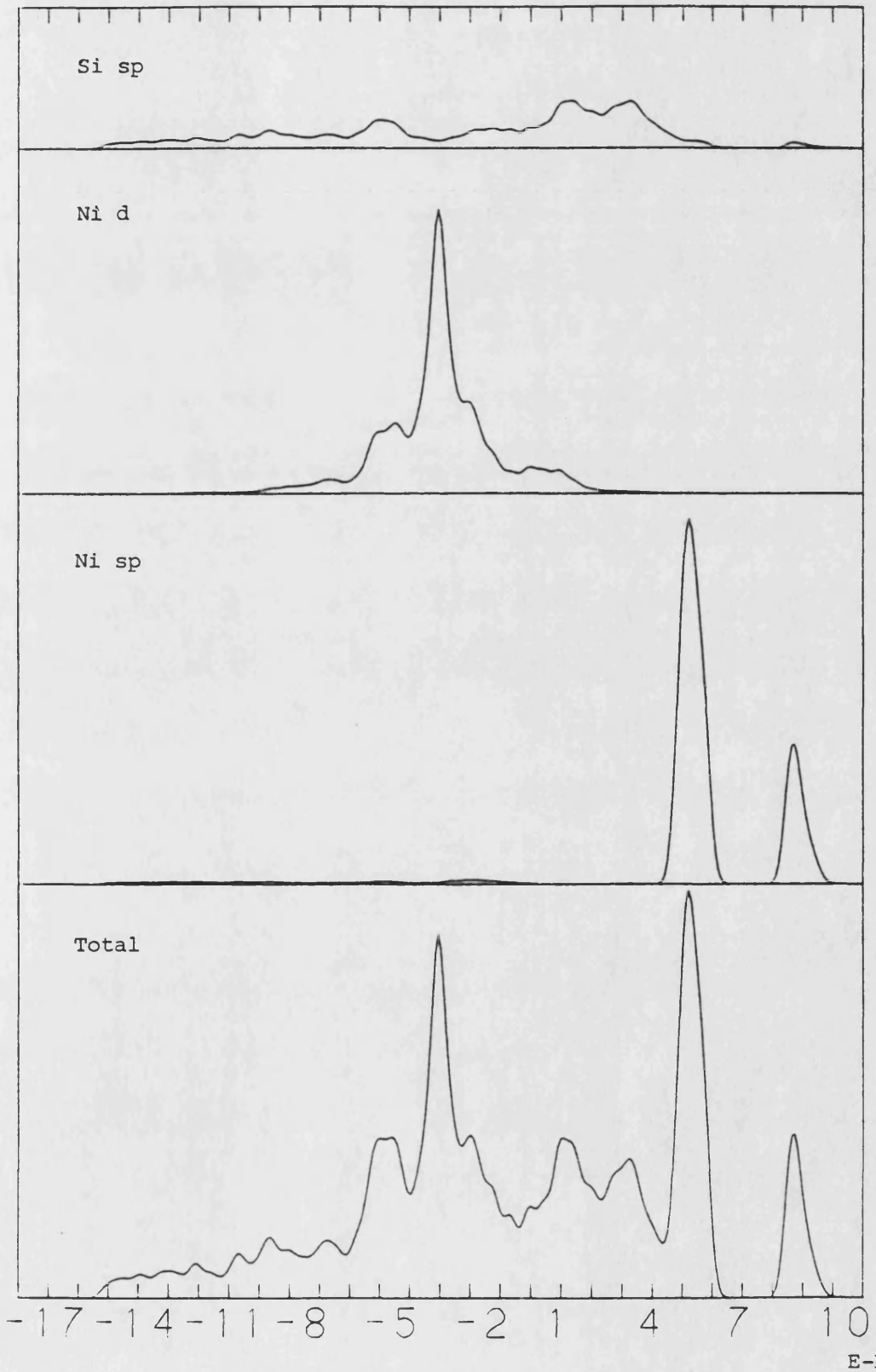

Figure 3.25 The calculated total and projected DOS for $NiSi_2$.

states which is mainly Si sp derived. These states will be the antibonding Si p-Ni d hybrids. Half an eV below the Fermi level there is a dip in the density of states. The states at the Fermi level are almost equally weighted on Ni d and Si sp orbitals. The bottom of the valence band is at -14.3 eV.

$NiSi_2$ has probably been studied more, both theoretically and experimentally, than any other silicide. Density of states calculations for $NiSi_2$ have been performed by BiSi and Calandra (1981), Chabal et al. (1982), Bylander et al. (1982b) and Tersoff and Hamann (1983). The results of these calculations are reproduced in Figure 3.26. The density of states calculated by Bisi and Calandra (1981) shows very little similarity to that of the present calculation: the nearly-free-electron-like states below -6 eV are completely absent. The results of the other three calculations, however, are all very similar to each other and to the present one: each one has an occupied band width of 14 eV, a 'quasiparabolic' band from -14 to -6 eV, a bonding peak at -5 eV, and a nonbonding peak at $\sim$-3.5 eV.

The arrows in Figure 3.27(c) indicate the features found by Franciosi et al. (1982) in a photoemission study of $NiSi_2$: a dominant feature at -3.15 eV and a weaker one at $\sim$-5 eV. These fit very well with the Si p-Ni d bonding and Ni d nonbonding features found theoretically. Similar results have been obtained from photoemission studies carried out by Chabal et al. (1982) and by Chang and Erskine (1982).

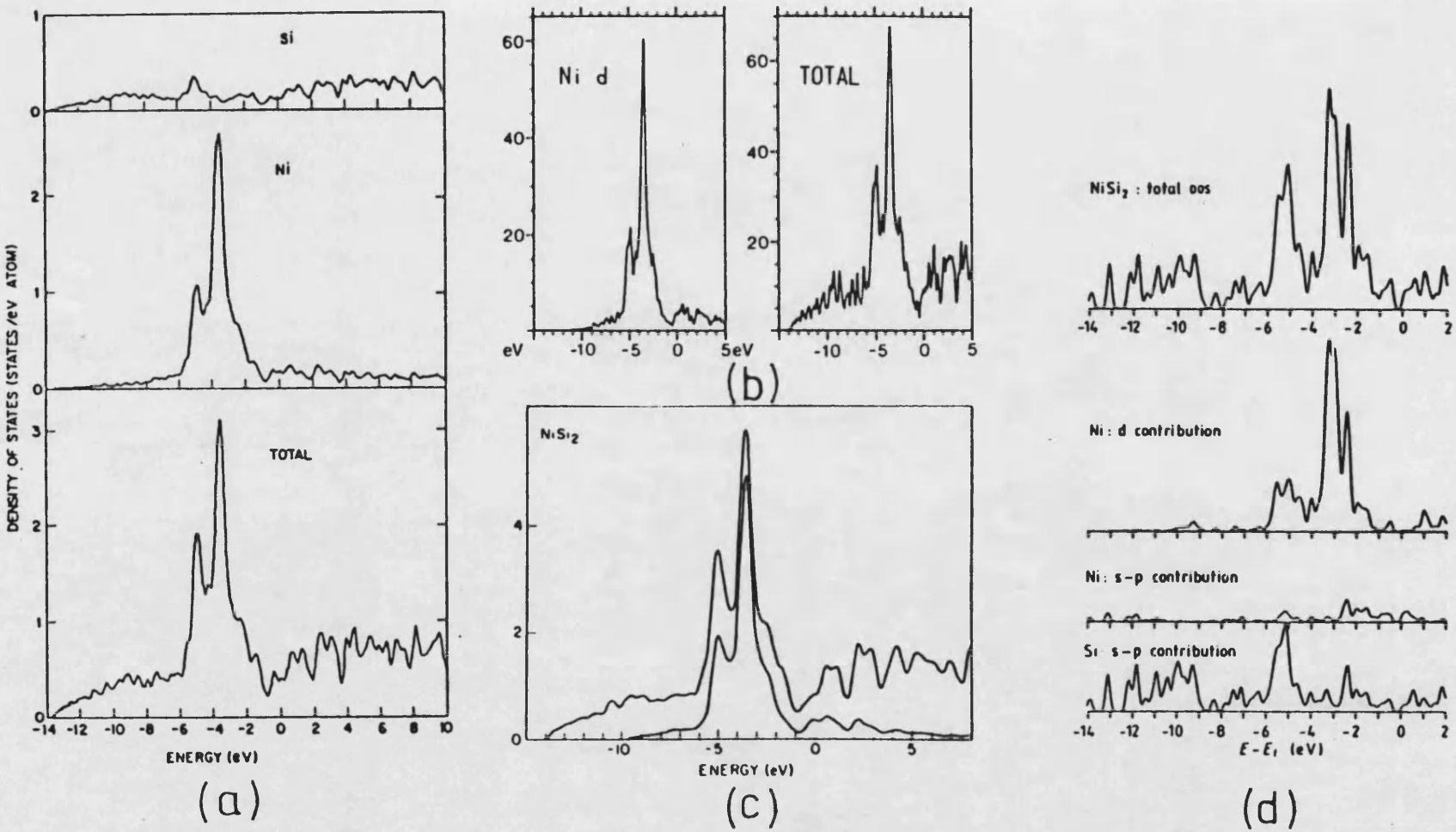

Figure 3.26 Total and projected densities of states for $NiSi_2$ as calculated by (a) Chabal et al. (1981), (b) Bylander et al. (1982b), (c) Tersoff and Hamann (1983) (the upper line shows the total and the lower the Ni d), and (d) Bisi and Calandra (1981).

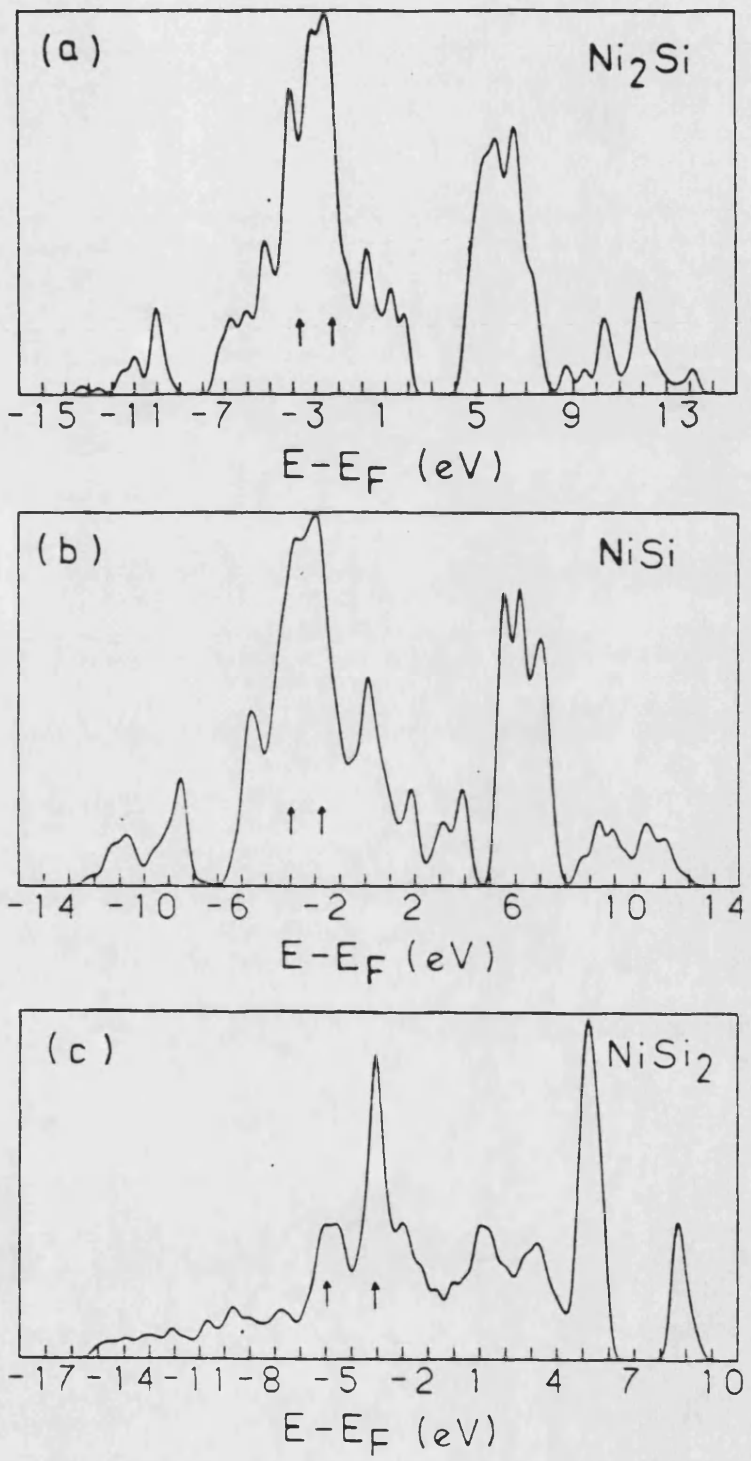

Figure 3.27 Comparison of the densities of states obtained in the present calculations for Ni_2Si, NiSi, and $NiSi_2$ with experimental features (marked by arrows) found by Franciosi et al. (1982).

For all the nickel silicides considered above only a small density of Ni sp states was found below the Fermi level. Above the Fermi level, however, prominent Ni sp peaks were found, but these are only a by-product of the method used: a minimal set of basis orbitals can not be expected to accurately reproduce a set of bands above the Fermi level. For each of the nickel silicides the maximum in the total density of states below the Fermi level is in the Ni d feature. These maxima occur at -1.1, -1.5, -2.0 and -3.0 eV for Ni_3Si, Ni_2Si, NiSi and $NiSi_2$ respectively. The Ni d band in Ni_3Si is similar to that in pure Ni (see Figures 3.7 and 3.13). The d bands in Ni_2Si and NiSi (phases in which there is less Ni-Ni interation) are narrower and are not. The d band in $NiSi_2$ is narrower yet. These trends, where the Ni d band shifts towards the Fermi level and broadens with increasing Ni concentration, have also been observed by others, both theoretically (Bisi and Calandra, 1981) and experimentally (Franciosi et al., 1982).

The calculated charges for the nickel silicides are given in Table 3.12. It can be seen that electrons are transferred from the Ni atoms to the Si atoms, but no trend is discernable. There is little agreement between other authors about charge transfer in silicides. For example, Bisi and Calandra (1981) find the negative charge transfer to Si to be less than 0.1 electrons per Si atom for Ni_2Si, NiSi and $NiSi_2$, while for $NiSi_2$ Bylander et al. (1982b) find 1.12 electrons transfer to each Ni atom. These differences are undoubtedly due at least in part to the different way in which the different authors assign charge to each atomic

Phase	Energy (eV) s	p	Ni d	(Ni d occupation)	Ni charge (electrons/atom)	Fermi energy (eV)
Si	-11.5	-5.2				-4.0
Ni	-6.0	-3.2	-5.6	(9.3)	10.0	-4.0
Ni_3Si			-5.2	(9.4)	9.9	-3.1
Ni_2Si			-5.7	(9.3)	9.8	-3.3
NiSi			-6.3	(9.1)	9.6	-3.9
$NiSi_2$			-5.6	(9.3)	9.8	-2.6

Table 3.12 The valence atomic energy levels used in and the nickel charges obtained from the electronic structure calculations for the nickel silicides together with the calculated Fermi energies.

species. When charge lies in a bond between two atoms there is no unique choice as how it should be divided between them. Bisi and Calandra (1981), for example, use, as here (see the end of section 2.3), the Mulliken projection (Mulliken, 1955), while Bylander et al. (1982b) use the Lowdin projection (Löwdin, 1950).

To summarize, the results of the present calculations of the electronic structure of the nickel silicides fit the consensus view of bonding in transition metal silicides: metal d and Si p orbitals hybridize and form bonding and antibonding states straddling the manifold of states derived from the remaining d orbitals while the Si s states participate relatively little and form a decoupled island of states at higher binding energy (see, for example, Rubloff and Ho, 1982). The slight exception to this, found here and by others, is $NiSi_2$, in which the Si s states are not decoupled. This has been interpreted (Tersoff and Hamann, 1983) as indicating the presence of Si sp^3 hybridization.

3.2.3 Palladium silicides

Two palladium silicide phases were considered: Pd_2Si and PdSi. The crystallographic parameters of these are given in Table 3.13.

Pd_2Si has the hexagonal Fe_2P structure (see Table 3.14). This can be thought of as being made up of two different types of hexagonal layer, A and α, (see Figure 3.28), stacked directly over each other separated by c/2 (i.e. the stacking in the silicide is ...AαAαAα...). Each Si atom is surrounded by nine Pd atoms, three at the corners

Phase	System	Structure Type	In Å a	b	c	Z	Space group	Atoms	Point Set	x	y	z
Pd_2Si	Hexagonal	Fe_2P	6.50		3.43	3	$P\bar{6}2m$	1Si	1b			
								2Si	2c			
								3Pd	3f	264		
								3Pd	3g	606		
PdSi	Orthorhombic	MnP	5.60	3.38	6.13	4	Pnma	4Pd	4c	007		190
								4Si	4c	190		570

Table 3.13 The crystallographic details of two palladium silicides.

Number of positions (Wyckoff notation)	Position coordinates
1(b)	$(0,0,\frac{1}{2})$
2(c)	$(1/3,2/3,0)$, $(2/3,1/3,0)$
3(f)	$(x,0,0)$, $(0,x,0)$, $(\bar{x},\bar{x},0)$
3(g)	$(x,0,\frac{1}{2})$, $(0,x,\frac{1}{2})$, $(\bar{x},\bar{x},\frac{1}{2})$

Table 3.14 The equivalent positions of the space group $P\bar{6}2m$ occupied in Pd_2Si.

Distances in Å			
Pd(f) - Pd	Pd(g) - Pd	Pd(f) - Si	Pd(g) - Si
2.81 (2)	2.81 (2)	2.42 (4)	2.51
2.84 (4)	2.84 (4)		2.63 (4)
2.97 (2)	3.43 (2)		3.94
3.43 (2)	3.46 (4)		
Si(b) - Pd	Si(c) - Pd	Si(b) - Si	Si(c) - Si
2.42 (6)	2.42 (3)	3.43 (2)	3.43 (2)
2.56 (3)	2.63 (6)		3.75 (3)
3.94 (3)			

Table 3.15 Interatomic distances in Pd_2Si.

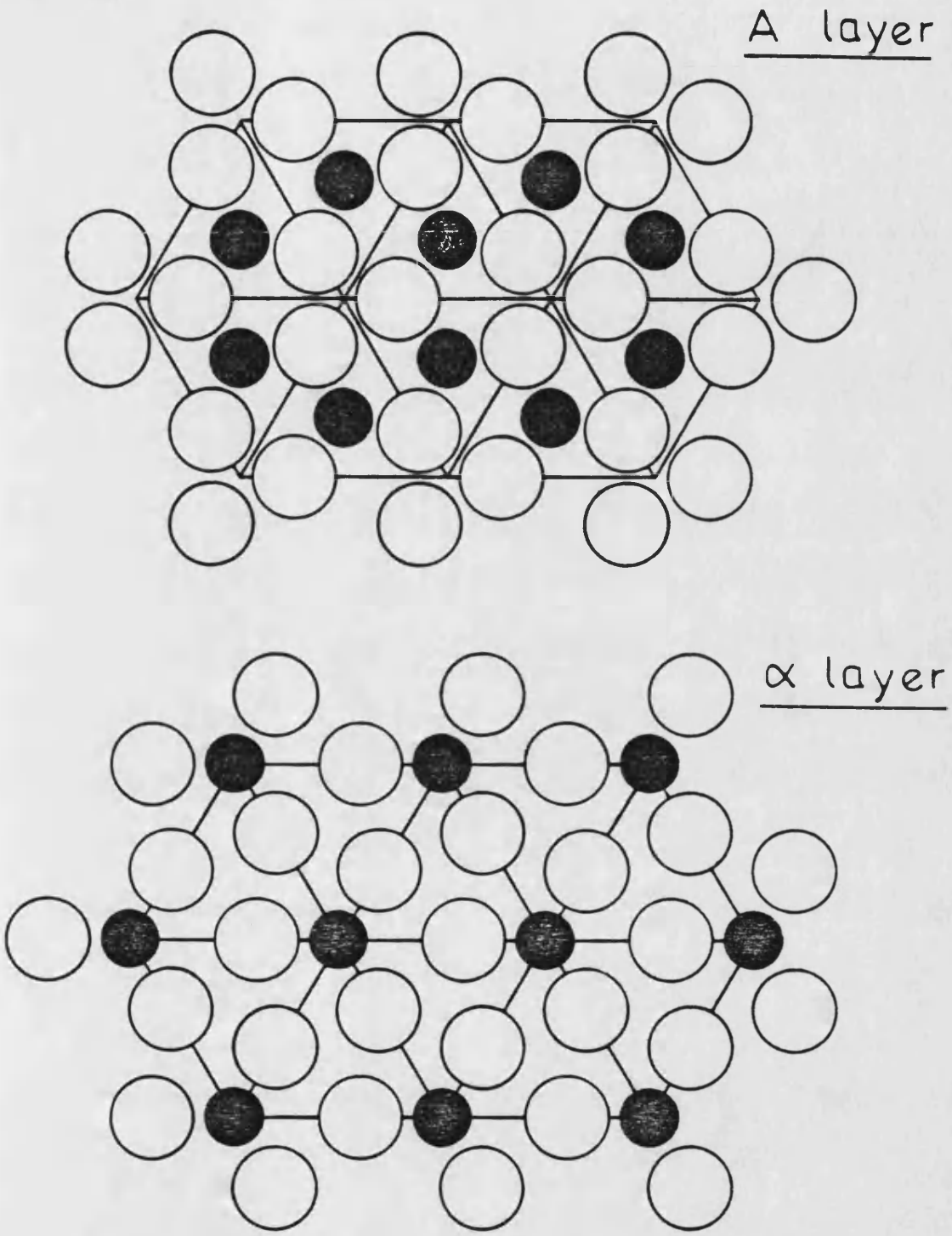

Figure 3.28 The two different (0001) layers in Pd_2Si. The A layer is at z = 0 and the α layer is at z = ½. The Si atoms are black.

of a triangle lying in the same plane as the Si atoms, and six at the corners of a triangular prism, the ends of which lie in the planes one above and one below the plane accommodating the Si atom. The interatomic distances in Pd_2Si are given in Table 3.15.

The total and projected densities of states for Pd_2Si were calculated using an interaction cut-off distance of 4.0 Å. They are shown in Figure 3.29. (See the Note at the end of this thesis.) The total density of states has the same form as those of the metal-rich nickel silicides. There is a weakly dispersive band between -10 and -8 eV which is weighted on the Si s and the Ni sp and d orbitals. This is separated by about 1.5 eV from the band lying between -6 and 3 eV which is overwhelmingly weighted on the Pd d orbitals. There are bonding Si p-Pd d hybrid derived states between -6 and -4 eV, antibonding Si p-Pd d hybrid states between -1 and 3 eV, and what appears to be a non-bonding Pd d peak at -2 eV. The Fermi level lies in the antibonding states and the states here are more heavily weighted on the Pd d than the Si p orbitals. The occupied band width is 10 eV.

Calculations of the electronic structure of palladium silicides were made by Ho et al. (1980) to help them with the interpretation of their ultraviolet photoemission sectroscopy and Auger electron spectroscopy results for Pd_2Si. They only considered PdSi and Pd_3Si however, and these not with their actual crystal structures but with simpler ones. The only other calculation of the electronic structure of Pd_2Si in its true Fe_2P-type crystal structure known to the author is that of Bisi and Calandra (1981).

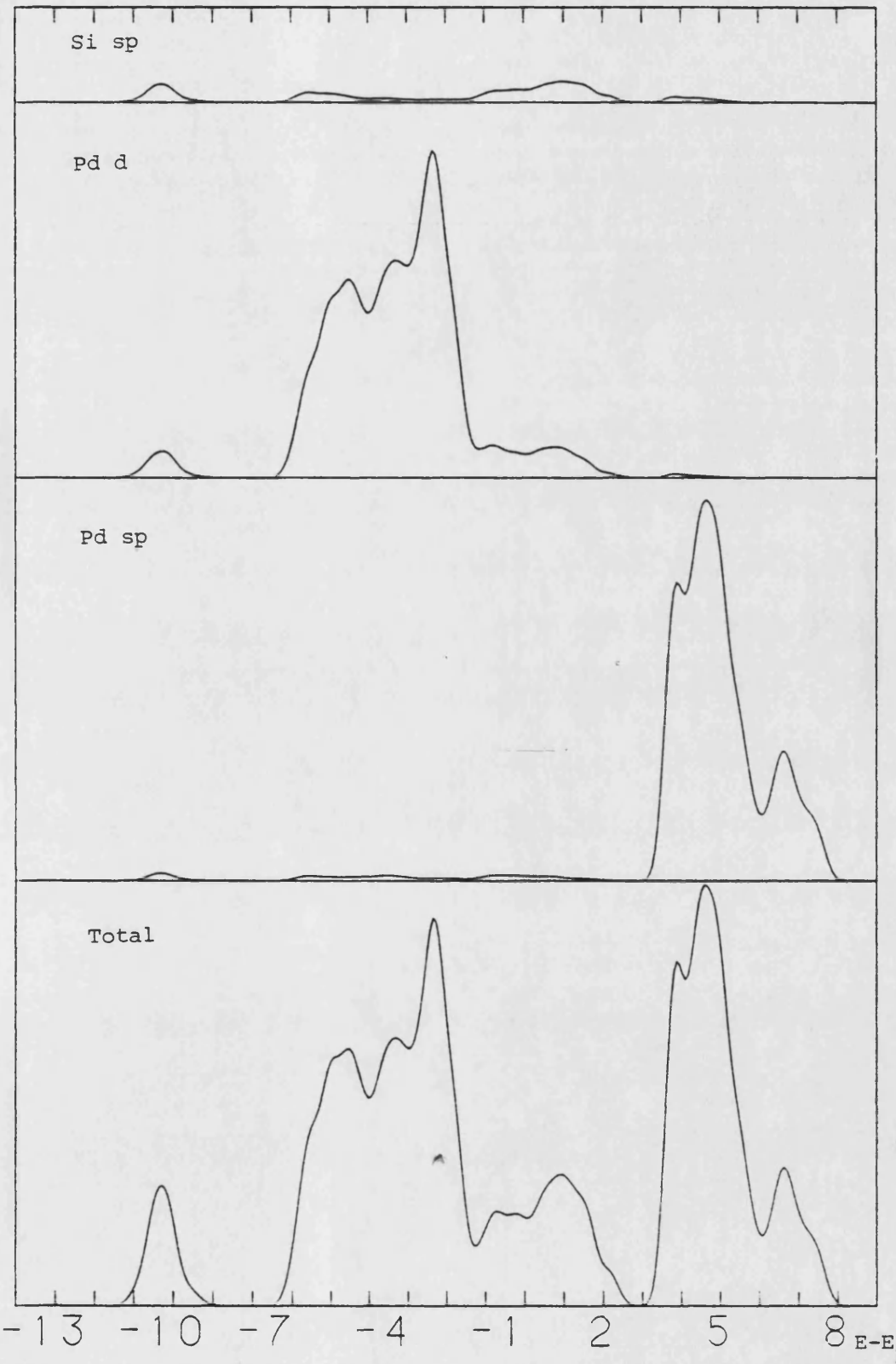

Figure 3.29 The calculated total and projected DOS for Pd_2Si.

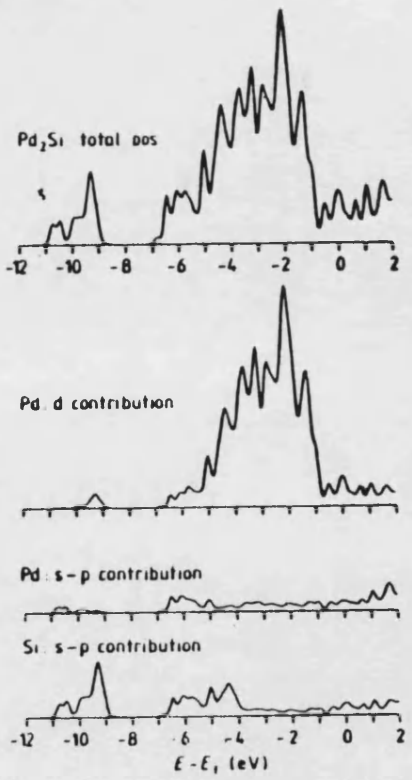

Figure 3.30 The total and projected DOS for Pd_2Si as calculated by Bisi and Calandra (1981).

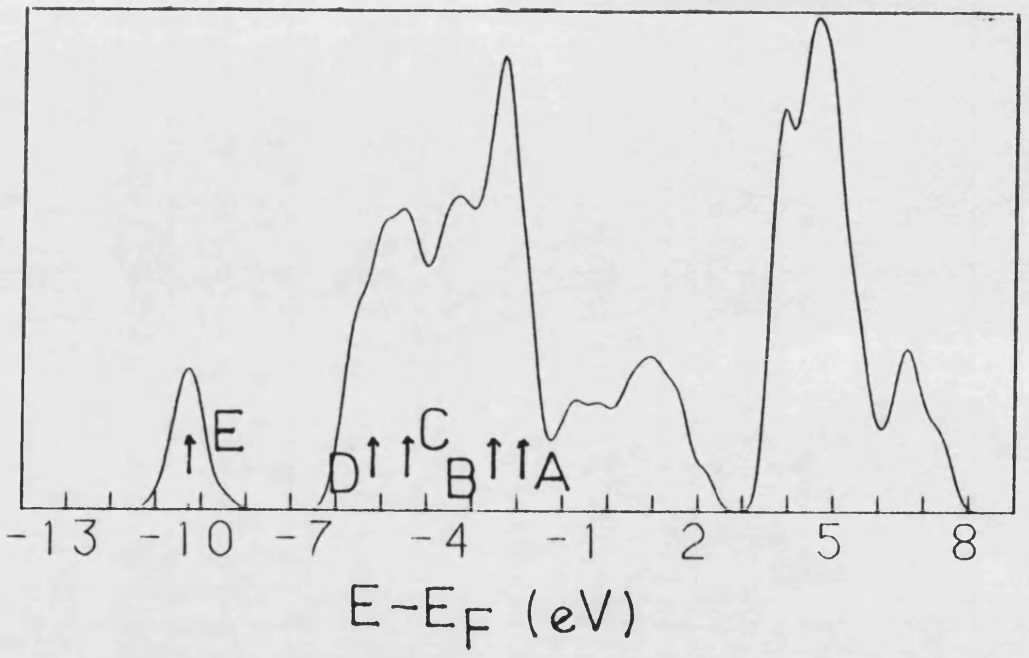

Figure 3.31 Comparison of the total DOS for Pd_2Si obtained in the present calculation with the experimental features (arrows A, B, C, D and E) found by Franciosi and Weaver (1983).

Their results are shown in Figure 3.30. These show much similarity to the results of the present calculation. The most prominent feature, the Pd d feature, starts at -6 eV, has a narrow peak at -2 eV, and falls away at about 1 eV below the Fermi level, though here it has more structure and a binding energy greater by about 1 eV.

The electronic structure of bulk Pd_2Si has been studied using synchrotron-radiation photoemission by Franciosi and Weaver (1983). The main feature they found (B) was at -2.5 eV. Above this they found a shoulder at -1.9 eV (A); below it they found a feature at -4.4 eV (C), a weak feature at $\sim$-5.2 eV (D), and, when using higher energy photons, a feature at -9.3 eV (E). The positions of these features are indicated in Figure 3.31 by labelled arrows. B, C and E correspond well to features in the calculated density of states: the nonbonding Pd d peak, the bonding Si p-Pd d peak and the split-off band respectively. A and D do not seem to match any calculated features. Using the Cooper minimum (Cooper, 1962) for the Pd 4d electrons Franciosi and Weaver (1983) indentified E as having Si s character. In the present calculation, however, although this band is weighted on the Si s orbitals it has a slightly greater weighting on the Pd d orbitals. They also identified the region from -6.5 eV to -3.5 eV as having Si p-Pd d character, which fits with the present calculation, and the states below the Fermi level down to -1.5 eV as having either Pd sp or Si p-Pd d character: the latter of these two possibilities also fits with the present calculation.

The monosilicide PdSi has the MnP structure type. This structure type has been discussed above for NiSi. The crystallographic parameters of PdSi are given in Table 3.13 and the interatomic distances in PdSi are given in Table 3.9.

The total and projected densities of states were calculated using an interaction cut-off distance of 3.1 Å. They are shown in Figure 3.32. As with all the other silicides considered so far, except $NiSi_2$, the lowest states (here between -10 and -7 eV) form a band weighted mainly on the Si s and the metal d orbitals. There is not here, however, a region which can be obviously ascribed only to bonding Si p-metal d hybrids. The region between -6 and -2 eV would seem to be a mixture of Pd d-Pd derived states as well as Si p-Pd d bonding states. The occupied band width is 10 eV.

The electronic density of states of PdSi has also been calculated by Bisi cand Calandra (1981). They obtained similar results to the present ones (see Figure 3.33), but they did find a region of bonding states below the metal d manifold, between -7 and -5 eV, and their occupied band width was slightly larger (at~12 eV).

The atomic valence orbital energies of Pd that were used in the present palladium silicide calculations and the Pd occupations and ionicities that were obtained are given in Table 3.16. It can be seen that, as with the nickel silicides, negative charge was found to transfer from the metal to the Si atoms. This was also found by Bisi and

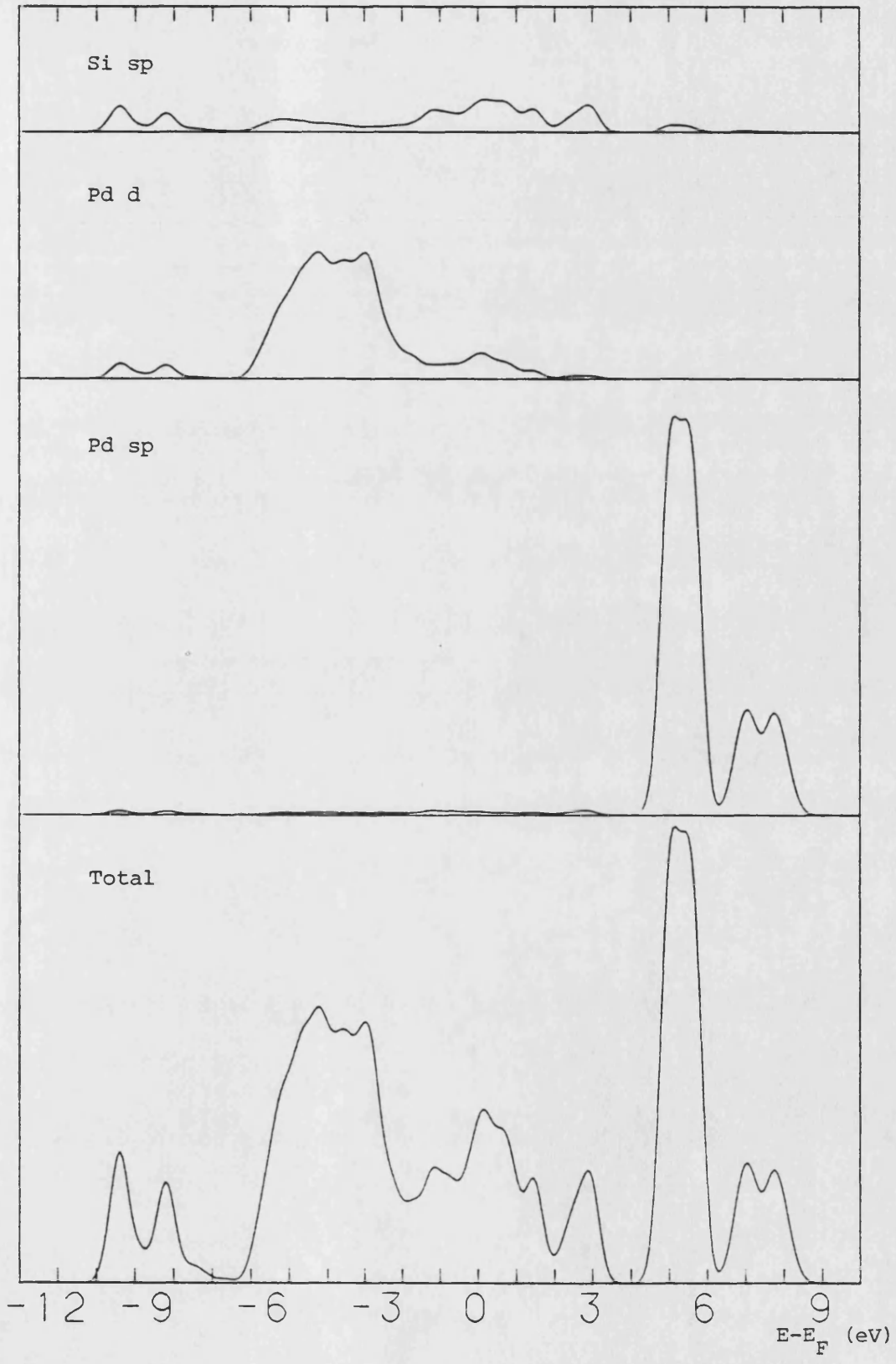

Figure 3.32 The calculated total and projected DOS for PdSi.

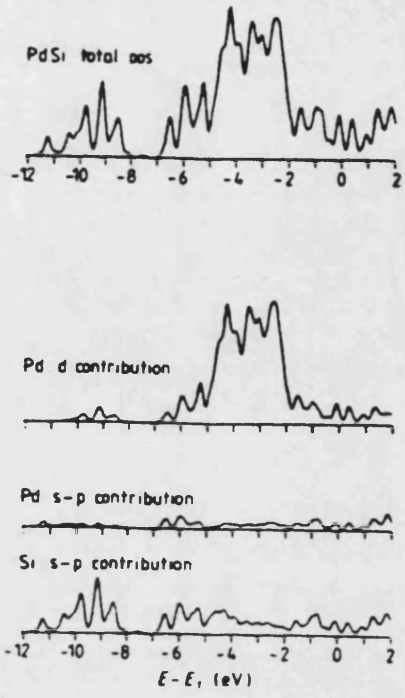

Figure 3.33 The total and projected DOS for PdSi as calculated by Bisi and Calandra (1981).

Phase	Pd orbital energies (eV) s	p	d	(d occupation)	Charge (electrons/atom) Pd	Si	Fermi energy (eV)
Pd_2Si	-5.4	-3.0	-7.0	(9.47)	9.77	4.46	-3.6
PdSi	-5.4	-3.0	-7.7	(9.30)	9.58	4.42	-4.1

Table 3.16 Energies and charges in the palladium silicides.

Calandra (1981), but they found negligible ionicity (less than 0.1 electrons per Si atom).

3.2.4 Platinum silicides

Electronic structure calculations for the two platinum silicide phases Pt_2Si and PtSi were performed and it it these which will now be considered here.

Pt_2Si crystallizes in the body-centred ZrH_2 type structure (see Table 3.18 and Figure 3.34). The crystallographic parameters of Pt_2Si are given in Table 3.17. In Pt_2Si each Si atom has eight Pt nearest neighbours at 2.46 Å and each Pt atom has four nearest neighbours, also at 2.46 Å. Further interatomic distances are given in Table 3.19.

The total and projected densities of states found for Pt_2Si, calculated using an interaction cut-off distance of 4.0 Å, are shown in Figure 3.35. (See the Note at the end of this thesis.) The density of states below the Fermi level is dominated by the broad feature between -9 and -1 eV. It has two peaks, one at -5 eV and a higher one at -3 eV. It is derived almost entirely from Pt d orbitals. There are two further peaks: one at about half an eV above the Fermi level, which also has a significant contribution from the Pt d orbitals, and one which is very sharp and at an energy of just less than -10 eV. The latter is weighted almost equally on the Pt d and the Si s orbitals, with a lesser contribution from the Pt sp orbitals. Once again here are the features observed in the other near noble metal silicides: a split-off band (-10 eV), nonbonding metal d

Phase	System	Structure Type	In Å a	b	c	Z	Space group	Atoms	Point Set	x	y	z
Pt_2Si	Tetragonal	ZrH_2	3.93		5.91	2	I4/mmm	2Si 4Pt	2a 4d			
PtSi	Orthorhombic	MnP	5.59	3.60	5.93	4	Pnma	4Pt 4Si	4c 4c	010 195	195 590	

Table 3.17 The crystallographic details of two platinum silicides.

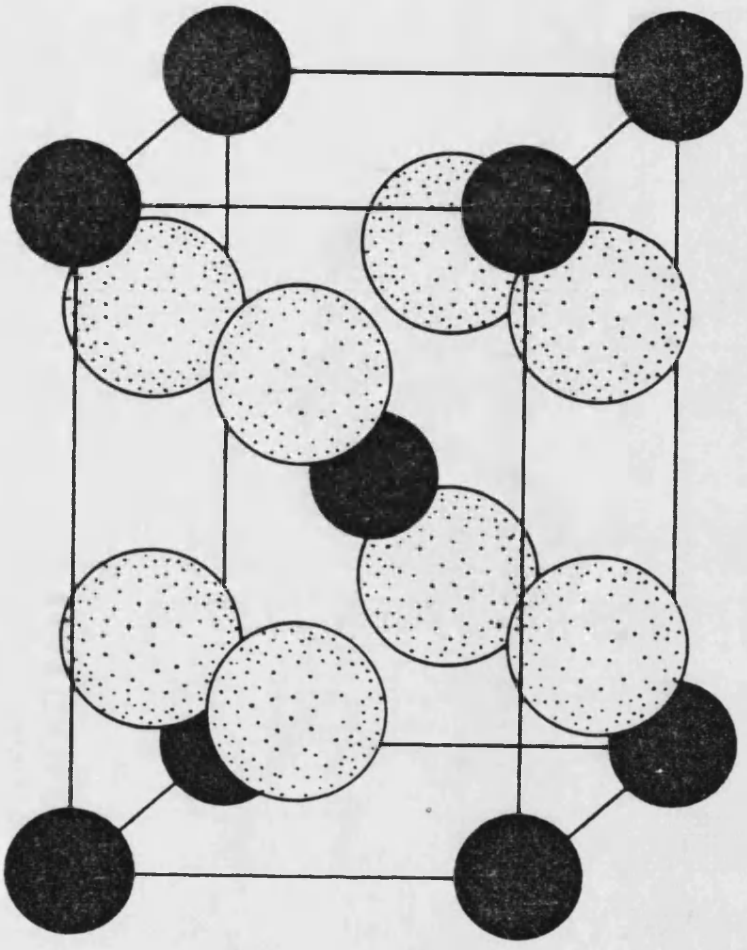

Figure 3.34 The Pt_2Si unit cell. The Si atoms are black.

Number of positions (Wyckoff notation)	Position coordinates
	(0,0,0; 1/2,1/2,1/2)+
2(a)	(0,0,0)
4(d)	(0,1/2,1/4), (1/2,0,1/4)

Table 3.18 The equivalent positions of the space group I4/mmm occupied in Pt_2Si.

Distances in Å			
Pt - Pt	Pt - Si	Si - Pt	Si - Si
2.78 (4)	2.46 (4)	2.46 (8)	3.93 (4)
2.96 (2)			
3.93 (4)			

Table 3.19 Interatomic distances in Pt_2Si.

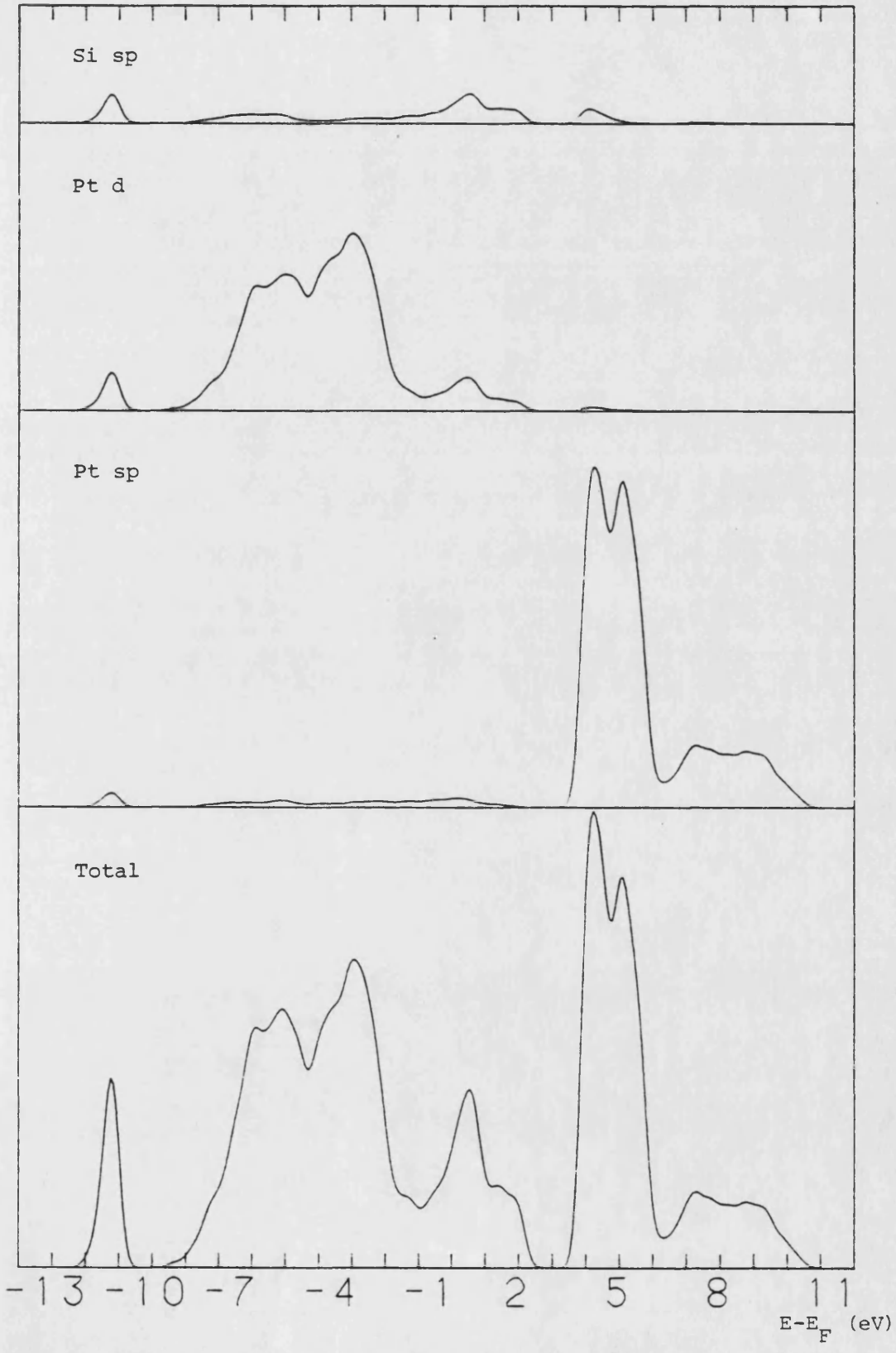

Figure 3.35 The calculated total and projected DOS for Pt_2Si.

states (-3 eV), and bonding and antibonding metal d-Si sp states (-5 and 0.5 eV respectively).

The theoretical total and projected densities of states for Pt_2Si found by Bisi and Calandra (1981) are shown in Figure 3.37a. They found a pronounced bonding-antibonding splitting, which left a gap (at -5 eV) between their bonding and nonbonding states, and which left their antibonding states above 1 eV. Indeed, compared to the present calculation they seemed to have found a greater degree of interaction overall, with their split-off band having a 2 eV greater binding energy. There is not a particularly good correspondence between the results of Bisi and Calandra (1981) and the present ones.

PtSi is the third near noble metal monosilicide and, like the other two, has the MnP structure. The crystallographic details of PtSi are given in Table 3.17 and interatomic distances in PtSi less than 3.1 Å (the interaction cut-off radius used in the electronic structure calculation) are given in Table 3.9.

The total and projected densities of states calculated for PtSi are shown in Figure 3.36. They are very similar in form to those of PdSi (see Figure 3.32). There is a band of states between -11 and -8 eV derived from, in order of magnitude of contribution, Si s, Pt d and Pt sp orbitals, a broad Pt derived feature between -7 and -3 eV, and antibonding Pt d-Si p states between -2 and 3 eV.

As with Pt_2Si, the calculations of Bisi and Calandra (1981) are rather different in form to the present ones (see Figure 3.37b). Here there are distinct bonding, nonbonding,

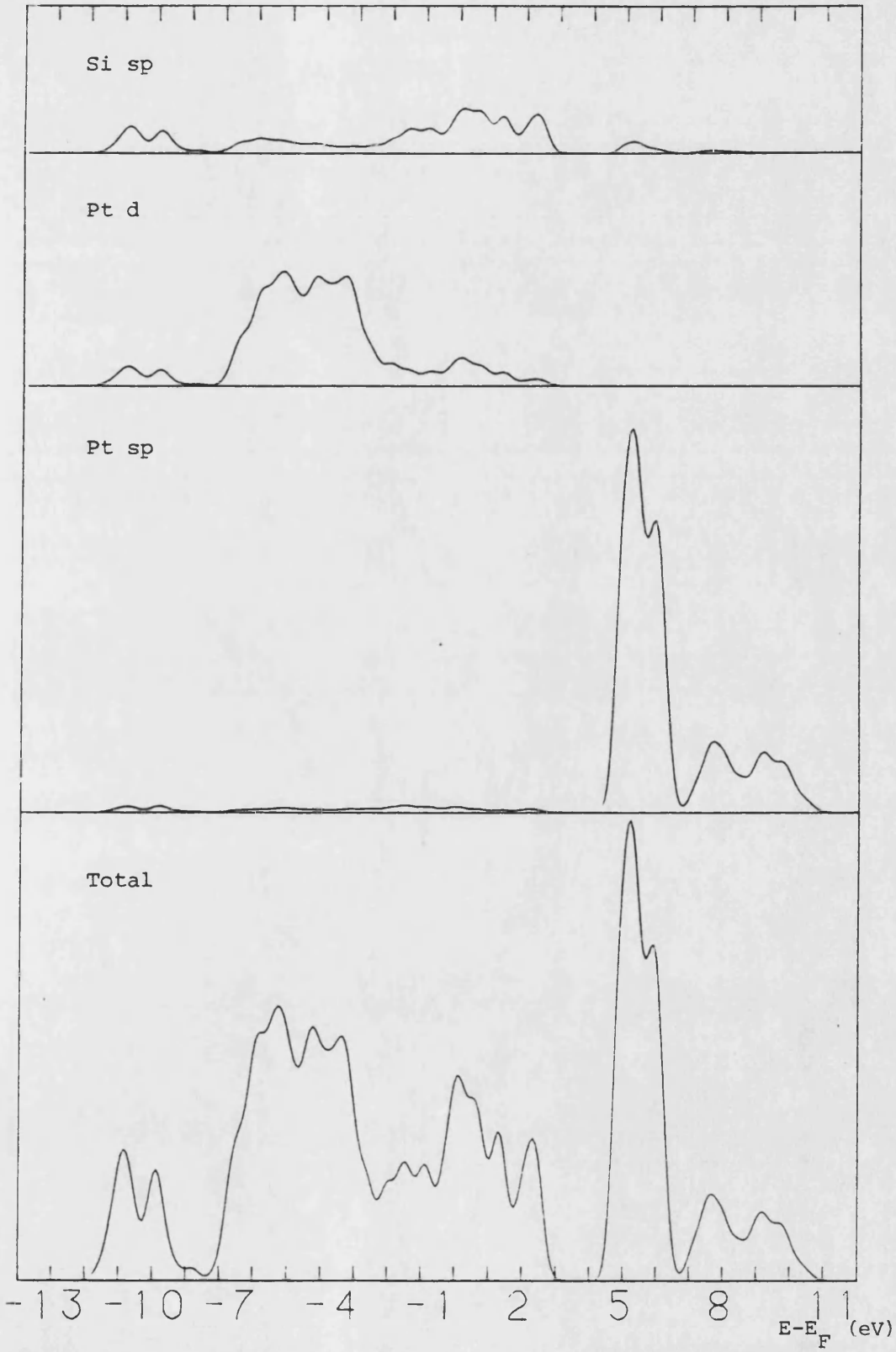

Figure 3.36 The calculated total and projected DOS for PtSi.

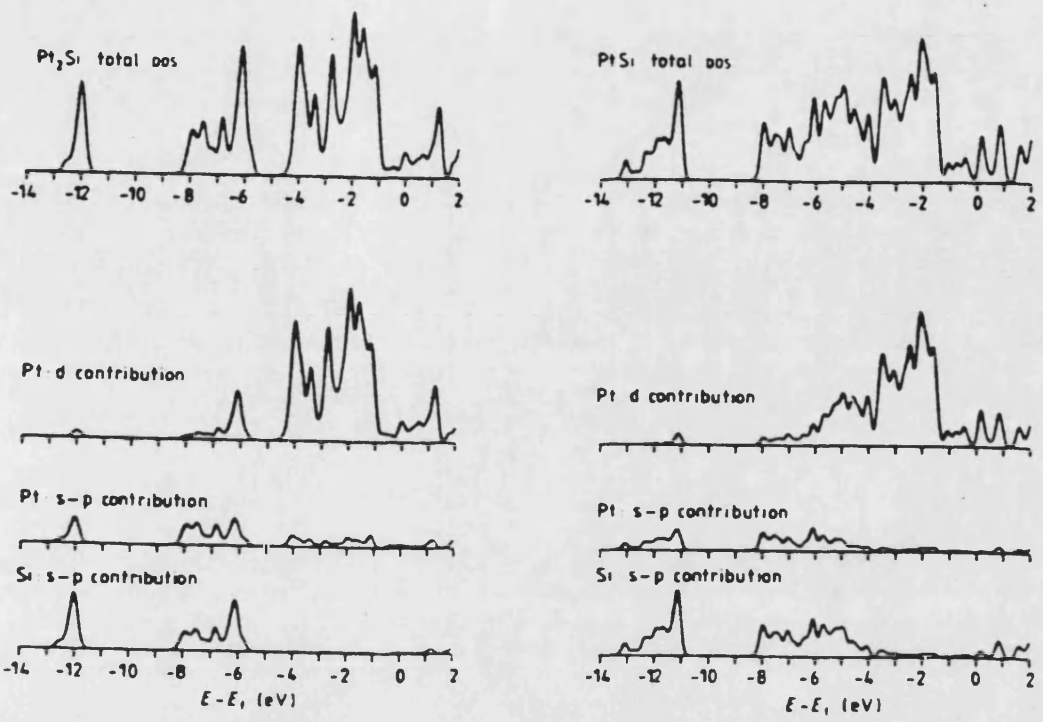

Figure 3.37 The total and projected DOS for (a) Pt_2Si and (b) PtSi as calculated by Bisi and Calandra (1981).

Phase	Pt orbital energies (eV) s	p	d	(d occupation)	Charge (electrons/atom) Pt	Si	Fermi energy (eV)
Pt_2Si	-5.4	-3.0	-7.5	(9.39)	9.85	4.30	-3.5
PtSi	-5.4	-3.0	-8.1	(9.23)	9.65	4.35	-3.8

Table 3.20 Energies and charges in the platinum silicides.

and antibonding regions, and the bonding and antibonding states are well separated.

Ultraviolet photoemission spectroscopy of both Pt_2Si and PtSi has been carried out by Abbati et al. (1981). For Pt_2Si they found a broad d peak at -3 eV, in good agreement with the present calculation. However, for PtSi they found the main d feature was narrower and nearer the Fermi level than in Pt_2Si, and this is not found here.

The charges found on the atoms in the platinum silicides are shown in Table 3.20 together with the platinum valence s, p and self-consistent d orbital energies that were used in the calculations. It can be seen that, as was the case for the nickel and palladium silicides, negative charge is transferred from the metal to the silicon atoms. This is contrary to the results of Bisi and Calandra (1981) who found that for the platinum silicides negative charge transfer occurs from silicon to metal atoms.

3.2.5 Conclusion

The densities of states of the near noble metal silicides have been interpreted above in terms of the concensus view of bonding in these materials (Rubloff and Ho, 1982). In this it is believed that Si p and metal d orbitals hybridize giving rise to bonding and antibonding states respectively below and above nonbonding metal d states and that the Si s orbitals do not participate in bonding and give rise to a band of states below the rest. The present calculations seem to fit this model well, with the slight exception, noted at the end of section 3.2, of

Energies (eV)					
(Ni	-0.3)				
Ni_3Si	-1.1				
Ni_2Si	-1.5	Pd_2Si	-2.2	Pt_2Si	-3.0
NiSi	-2.0	PdSi	-3.0	PtSi	-3.5
$NiSi_2$	-3.0				

Table 3.21 The calculated energies at which the metal d peaks in the near noble metal silicides were found.

$NiSi_2$. The "Si s bands" are found here, however, to have always also a weighting on the metal d and, to a lesser degree, on the metal sp orbitals, and from this it can be deduced that the Si s orbitals do enter into bonds in the near noble metal silicides.

Table 3.21 shows the energies at which the nonbonding metal d peaks were found in the calculations for the near noble metal silicides. It can be seen, especially clearly for the nickel silicides, but also for the others, that as the metal concentration decreases the d peak moves further below the Fermi level and its position in the corresponding pure metal. It can also be seen, not only for the monosilicides MSi, which all have the same structure, but also for the M_2Si silicides, each of which has a different structure, that the d peak also moves further below the Fermi level going down the group from Ni to Pt.

3.3 Refractory metal disilicides

3.3.1 The crystal structures of transition metal disilicides

The structure types of some of the transition metal disilicides are given in Table 3.22 and this information is summarized in Figure 3.38. The CaF_2 structure has been described in detail above, and the $CrSi_2$ and $MoSi_2$ structure types will be described in detail below. Here some general comments about these and other structure types referred to in Table 3.22 will be made.

The orthorhombic $TiSi_2$ structure, the hexagonal $CrSi_2$ structure, and the tetragonal $MoSi_2$ structure are all related in a surprisingly simple way (Nowotny, 1970). $TiSi_2$

Phases	Structure type	System	Space group	Z
$NiSi_2$, $CoSi_2$	CaF_2	Cubic	Fm3m	4
α-$FeSi_2$ (H.T.)		Tetragonal	P4/mmm	1
β-$FeSi_2$ (L.T.), $OsSi_2$	$OsSi_2$	Orthorhombic	Cmca	16
"$MnSi_2$" (Mn_nSi_{2n-m})	"Chimney ladder" structures			
$CrSi_2$, VSi_2, $NbSi_2$, $TaSi_2$	$CrSi_2$	Hexagonal	$P6_222$	3
$MoSi_2$, WSi_2, $ReSi_2$	$MoSi_2$	Tetragonal	I4/mmm	2
$TiSi_2$	$TiSi_2$	Orthorhombic	Fddd	8
$ZrSi_2$, $HfSi_2$	$ZrSi_2$	Orthorhombic	Cmcm	4

Table 3.22 The structure types of some transition metal disilicides.

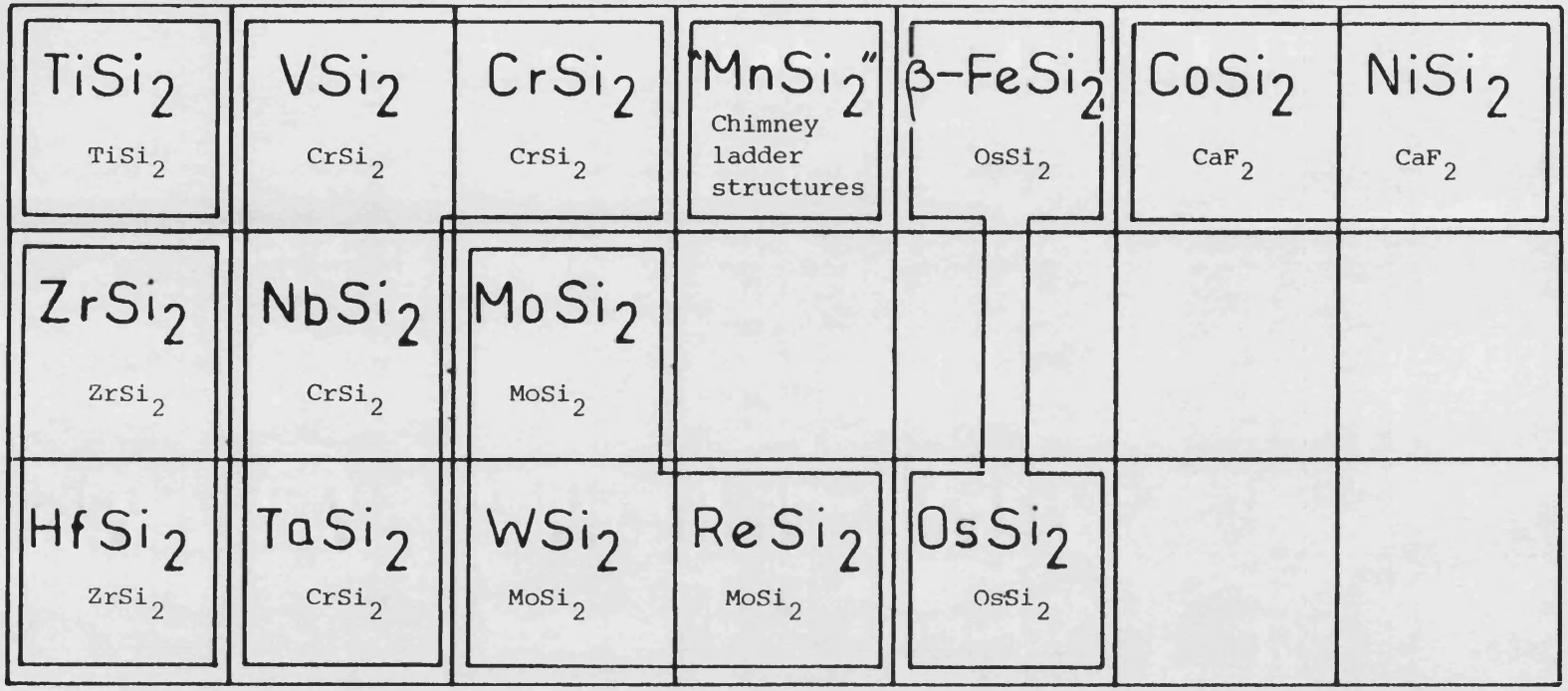

Figure 3.38 The structure types (small lettering) of some transition metal disilicides (large lettering).

is built out of close-packed metal disilicide layers of the type shown in Figure 3.39. In a structure which is close-packed overall (e.g. hcp and fcc) the next layer up would be positioned such that its atoms sit in the hollows between the atoms of this first layer (giving each atom twelve equidistant nearest neighbours). In $TiSi_2$, however, the next layer is positioned such that its atoms sit in bridge sites. The Ti atoms in the second, third and fourth layers fall respectively, infact, above the points labelled B, C, and D in Figure 3.39. The fifth layer lies directly over the first so that the stacking sequence in $TiSi_2$ is (...ABCDABCD...). $CrSi_2$ is also made up of close-packed layers of the type shown in Figure 3.39, with the atoms of one layer sitting in the bridge sites of the layer below it, but now with the stacking sequence (...ABDABD...). Finally $MoSi_2$ can also be regarded as being built up this way with a stacking sequence (...ABABAB...). In these three structures the atoms have tenfold coordination (compared to the already mentioned twelvefold coordination of the atoms in a close-packed structure) with each metal atom having 10 approximately equidistant Si neighbours, and each Si atom having 5 metal and 5 Si neighbours at approximately equal distances away.

There is no genuine disilicide of manganese. However, there exists a series of manganese silicides with formulae of the form Mn_nSi_{2n-m} (n,m integers, e.g. $Mn_{11}Si_{19}$) which can be regarded as defect disilicides $MnSi_{2-x}$ (Nowotny, 1970). These materials are known as Nowotny phases and Pearson (1972) has described them as having "chimney ladder"

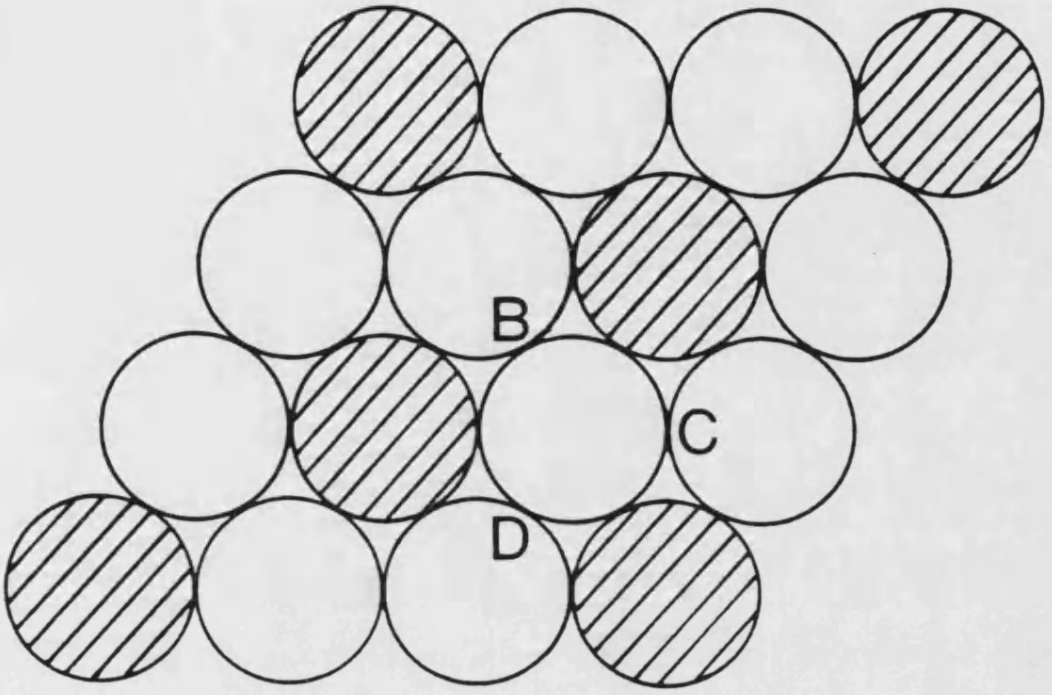

Figure 3.39 A hexagonal metal disilicide layer of the type found in some refractory metal disilicides. The metal atoms are shaded.

structures. These "chimney ladder" structures can be considered as derivatives of the $TiSi_2$ structure (Nowotny, 1970).

Iron disilicide occurs in two forms: α-$FeSi_2$, which is stable above 967°C and which is metallic, and β-$FeSi_2$, which is stable at low temperatures and which is a semiconductor (Birkholz and Schelm, 1968, 1969). The tetragonal α-phase has a simple structure with only one unit formula per unit cell, but the β-phase has a particularly complex structure with 16 unit formulae per unit cell (Dusausoy et al., 1971). The structure type of β-$FeSi_2$ is the same as that of $OsSi_2$, and can be regarded as a distorted fluorite structure.

Cobalt disilicide has the fluorite structure, which has been described above for the isostructural disilicide $NiSi_2$ (see Figure 3.22 and Table 3.10). In these disilicides the metal atoms have eightfold coordination compared with the tenfold coordination they have in the disilicides with the $TiSi_2$, $CrSi_2$, and $MoSi_2$ structures. The crystallographic parameters of $CoSi_2$ are given in Table 3.23 and the interatomic distances in $CoSi_2$ are shown in Table 3.24.

The crystal structures of the isostructural phases $CrSi_2$, VSi_2, $NbSi_2$, and $TaSi_2$ will now be considered in a little more detail, and below so will those of the isostructural phases $MoSi_2$, WSi_2, and $ReSi_2$. The $CrSi_2$ structure is described in Table 3.25 and Figure 3.40 shows three (0001) planes which all lie directly over one another in $CrSi_2$ at z=1/6, 1/2 and 5/6. The crystallographic parameters of the four disilicides with the $CrSi_2$ structure

Phase	System	Structure Type	In Å a	b	c	Z	Space group	Atoms	Point Set	x	y	z
$CoSi_2$	Cubic	CaF_2	5.37	5.37	5.37	4	Fm3m	4Co 8Si	4a 8c			
$CrSi_2$	Hexagonal	$CrSi_2$	4.43	4.43	6.36	3	$P6_222$	3Cr 6Si	3d 6j	 167		
VSi_2	Hexagonal	$CrSi_2$	4.57	4.57	6.37	3	$P6_222$	3V 6Si	3d 6j	 167		
$NbSi_2$	Hexagonal	$CrSi_2$	4.80	4.80	6.59	3	$P6_222$	3Nb 6Si	3d 6j	 167		
$TaSi_2$	Hexagonal	$CrSi_2$	4.78	4.78	6.57	3	$P6_222$	3Ta 6Si	3d 6j	 167		
$MoSi_2$	Tetragonal	$MoSi_2$	3.20	3.20	7.86	2	I4/mmm	2Mo 4Si	2a 4e			 333
$ReSi_2$	Tetragonal	$MoSi_2$	3.13	3.13	7.68	2	I4/mmm	2Re 4Si	2a 4e			 333
WSi_2	Tetragonal	$MoSi_2$	3.21	3.21	7.87	2	I4/mmm	2W 4Si	2a 4e			 333

Table 3.23 The crystallographic details of refractory metal disilicides.

Co:	has 8 Si neighbours at 2.32 Å	
	has 12 Co neighbours at 3.79 Å	
Si:	has 4 Co neighbours at 2.32 Å	
	has 6 Si neighbours at 2.68 Å	
	has 12 Si neighbours at 3.79 Å	

Table 3.24 Interatomic distances in $CoSi_2$.

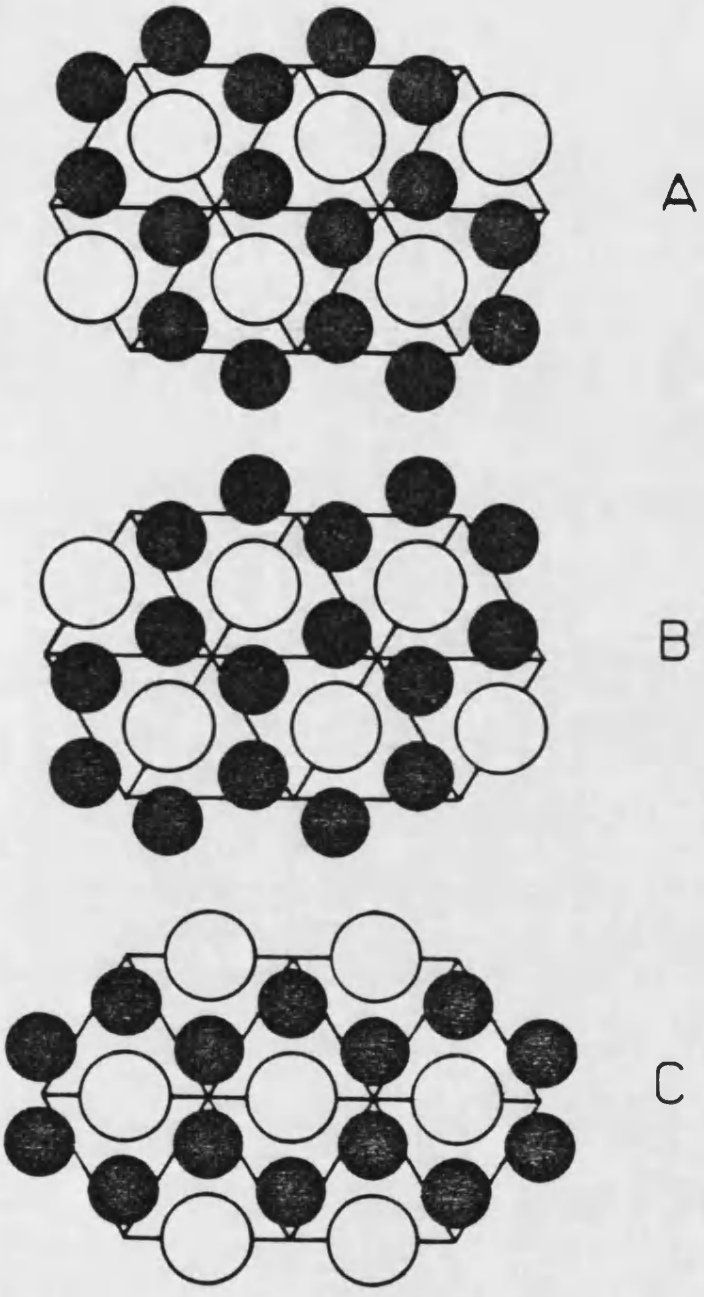

Figure 3.40 The three different (0001) layers in the $CrSi_2$ structure. A is at z = 1/6, B is at z = 1/2 and C is at z= 5/6. The Si atoms are black.

Number of positions (Wyckoff notation)	Position coordinates
3(d)	(1/2,0,1/2), (0,1/2,1/6), (1/2,1/2,5/6)
6(j)	(x,2x,1/2), (2x,x,1/6), (x,$\bar{x}$,5/6), ($\bar{x}$,2$\bar{x}$,1/2), (2$\bar{x}$,$\bar{x}$,1/6), ($\bar{x}$,x,5/6)

Table 3.25 The equivalent positions of the space group $P6_222$ occupied in the $CrSi_2$ structure.

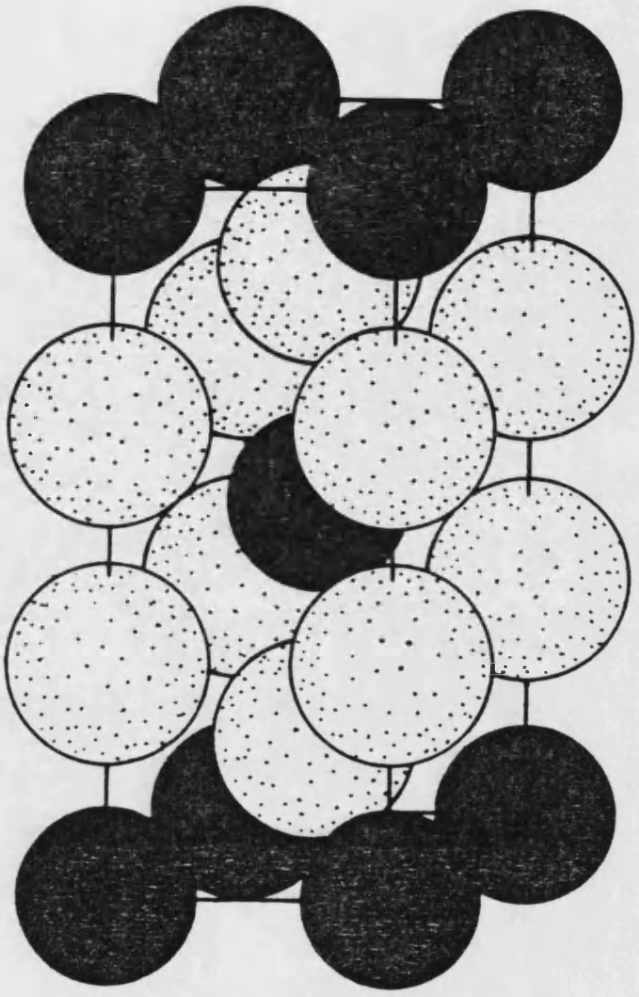

Figure 3.41 The $MoSi_2$ unit cell. The Mo atoms are black.

Number of positions (Wyckoff notation)	Position coordinates
	(0,0,0; ½,½,½)+
2(a)	(0,0,0)
4(e)	±(0,0,z)

Table 3.26 The equivalent positions of the space group I4/mmm occupied in the $MoSi_2$ structure.

Phase	Distances in Å (number of neighbours)					
	Metal-Si		Si-Metal		Si-Si	
	(4)	(6)	(2)	(3)	(2)	(3)
$CrSi_2$	2.48	2.55	2.48	2.55	2.48	2.55
VSi_2	2.50	2.64	2.50	2.64	2.50	2.64
$NbSi_2$	2.59	2.77	2.59	2.77	2.59	2.77
$TaSi_2$	2.59	2.76	2.59	2.76	2.59	2.76

Table 3.27 Interatomic distances in disilicides with the $CrSi_2$ structure.

Phase	Distances in Å (number of neighbours)		
	Metal-Si (10)	Si-Metal (5)	Si-Si (5)
$MoSi_2$	2.62	2.62	2.62
WSi_2	2.62	2.62	2.62
$ReSi_2$	2.56	2.56	2.56

Table 3.28 Interatomic distances in disilicides with the $MoSi_2$ structure.

are given in Table 3.23. The interatomic distances in these phases are given in Table 3.27.

The unit cell of $MoSi_2$ is shown in Figure 3.41 and it is described in Table 3.26. The hexagonal close-packed metal disilicide layers referred to above lie in (110) planes. The crystallographic details of and the interatomic distances in the three disilicides with the $MoSi_2$ structure are given in Tables 3.23 and 3.28 respectively.

3.3.2 The electronic structure of transition metal disilicides

3.3.2.1 $CoSi_2$

The calculated total and projected densities of states for $CoSi_2$ are shown in Figure 3.42 (see the Note at the end of this thesis.) They were calculated using a cut-off radius of 3.0 Å. They are, not surprisingly, very similar to those of $NiSi_2$: the occupied band is 14.5 eV, there is a quasiparabolic Si sp derived region below -5 eV, there is a narrow nonbonding Co d peak at -1.7 eV, there are bonding and antibonding Si p-Co d peaks below and above this at -4.4 and 1.8 eV respectively, and there is a dip in the density of states just above the Fermi level. In the density of states for $NiSi_2$ (see Figure 3.25) there is a dip just below the Fermi level and the d peak is further below the Fermi level than it is here. Here, as with $NiSi_2$, the bonding and nonbonding features are weighted on the (xy, yz, zx) d orbitals and the (x^2-y^2, z^2) d orbitals respectively.

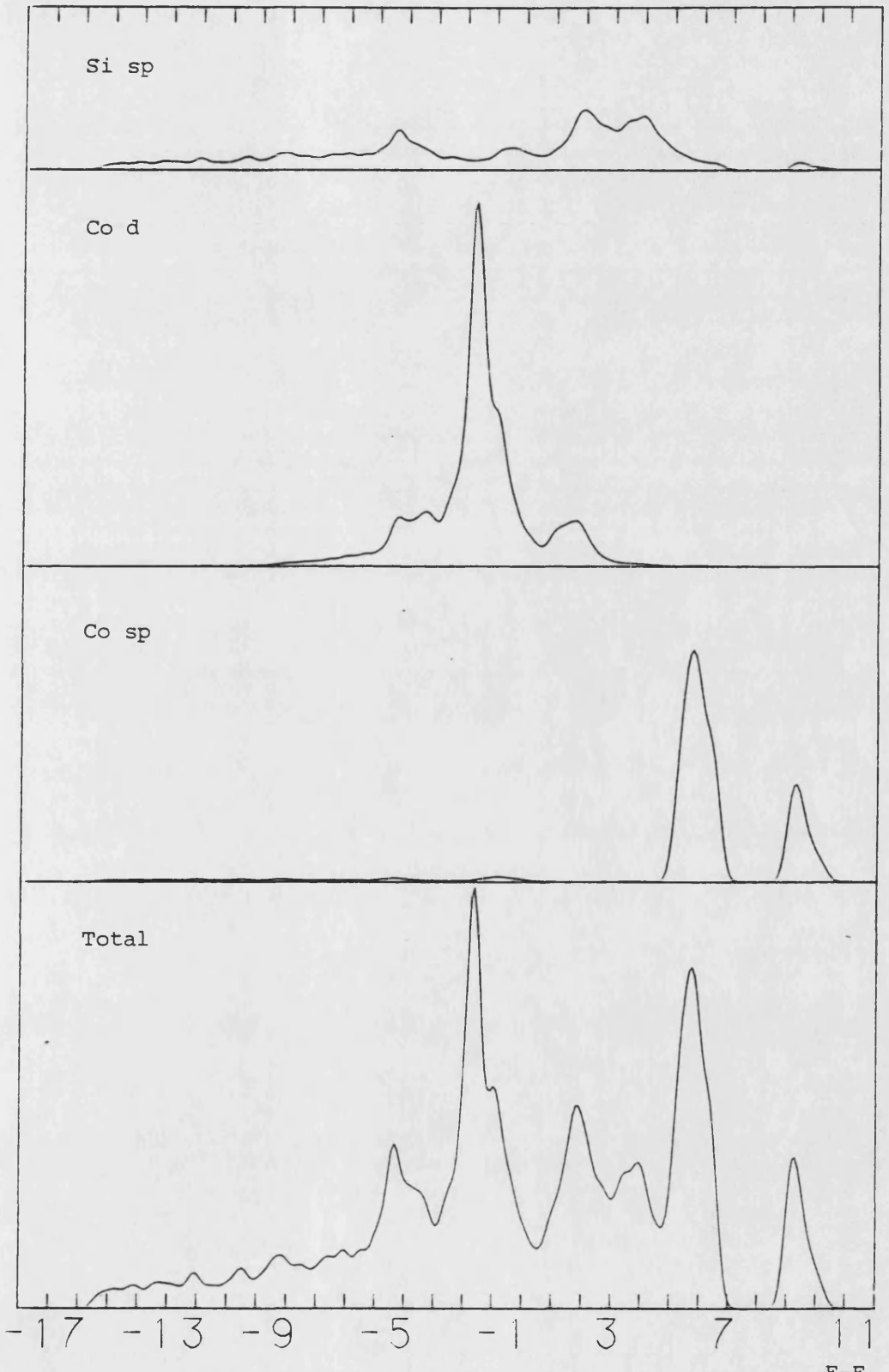

Figure 3.42 The calculated total and projected DOS for $CoSi_2$.

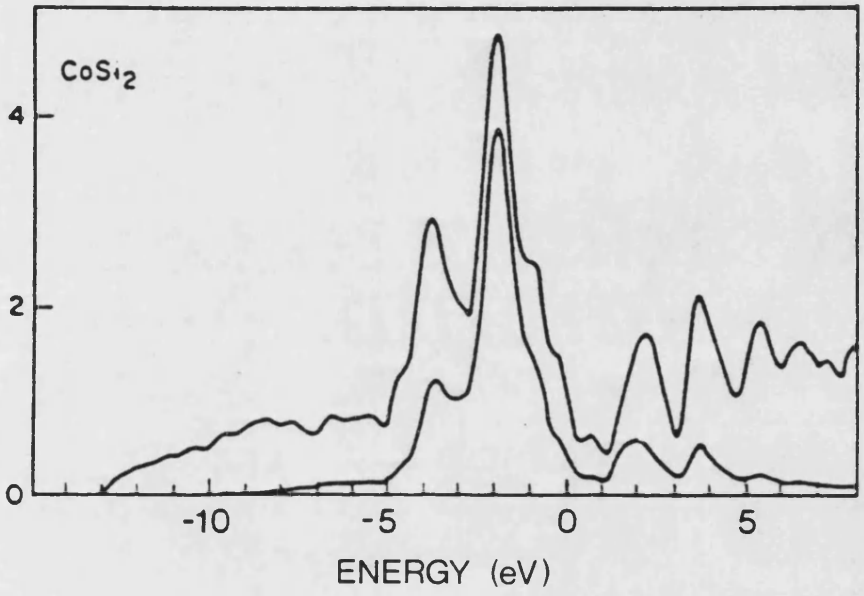

Figure 3.43 The density of states of $CoSi_2$ (the upper line shows the total and the lower the Co d) as calculated by Tersoff and Hamann (1983).

The density of states of $CoSi_2$ calculated by Tersoff and Hamann (1983) is shown in Figure 3.43. It is very similar to that found here with a narrow d peak at -2 eV, a smaller peak at -3.8 eV, and a dip just above the Fermi level.

A synchrotron radiation photoemission study of $CoSi_2$ by Weaver et al. (1984) found a sharp dominant emission feature at -1.45 eV, in reasonable agreement with the present calculation and a weaker structure at about -3.5 eV, which may indicate an overestimate here of the binding energy of the bonding peak by about 1 eV.

The energies and occupations used for the atomic valence levels are given in Table 3.29 and will be discussed below.

3.3.2.2 $CrSi_2$, VSi_2, $NbSi_2$ and $TaSi_2$

The electronic structure of the disilicides with the $CrSi_2$-type atomic structure will now be considered. The total and projected densities of states calculated for $CrSi_2$, VSi_2, $NbSi_2$, and $TaSi_2$ are shown in Figures 3.44, 3.45, 3.46, and 3.47 respectively. (See the Note at the end of this thesis.) All four densities of states have a similar structure: the occupied bands are between 12 and 14 eV wide, the states below -9 eV are weighted mainly on the Si s orbitals, the projection of the density of states onto the metal d orbitals has a double peak, one above and one below the Fermi level, the gap between which corresponds to the dip in the total density of states seen just above the Fermi level, and there is a secondary peak at about -5 eV which is weighted on both Si p and metal d orbitals. The

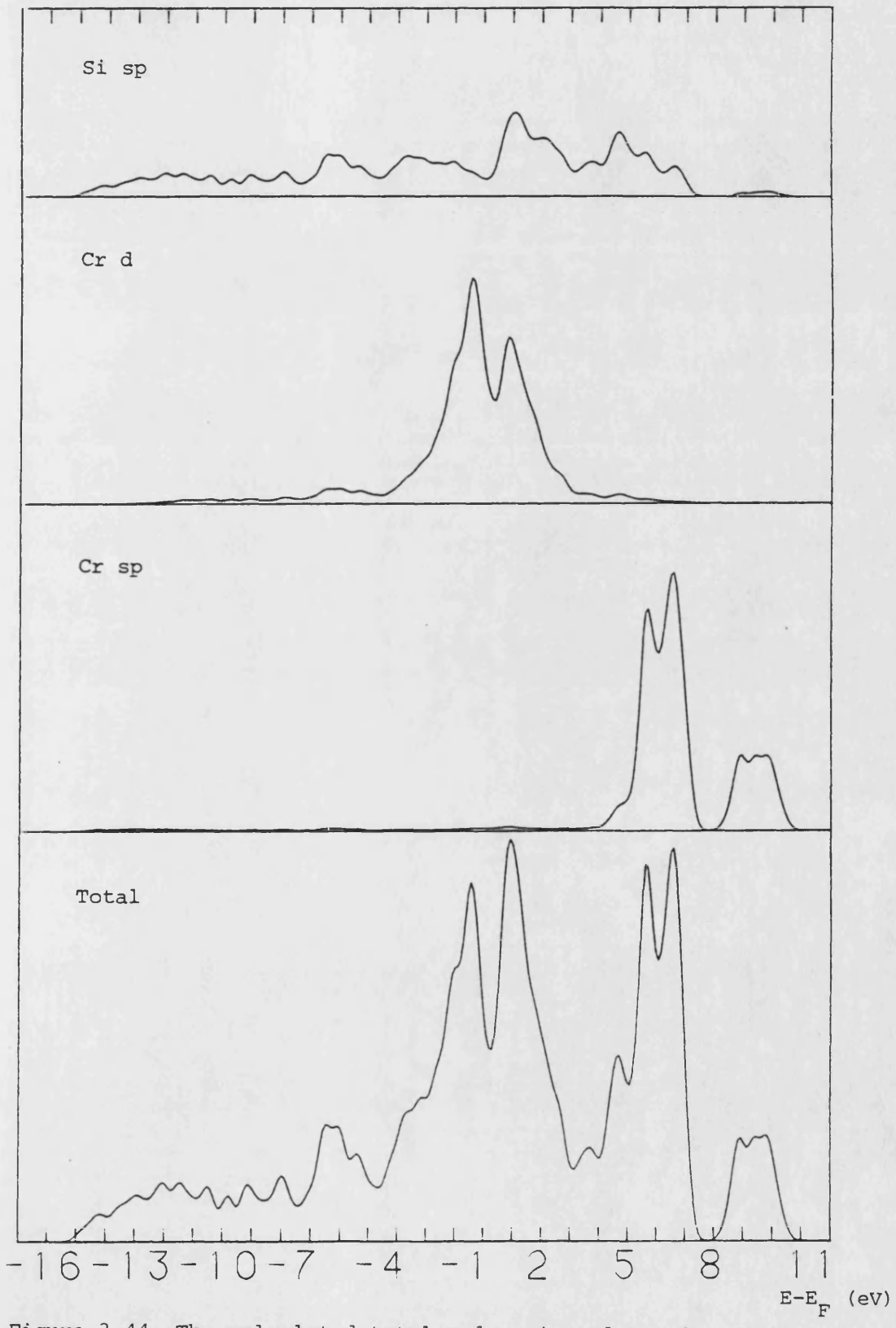

Figure 3.44 The calculated total and projected DOS for $CrSi_2$.

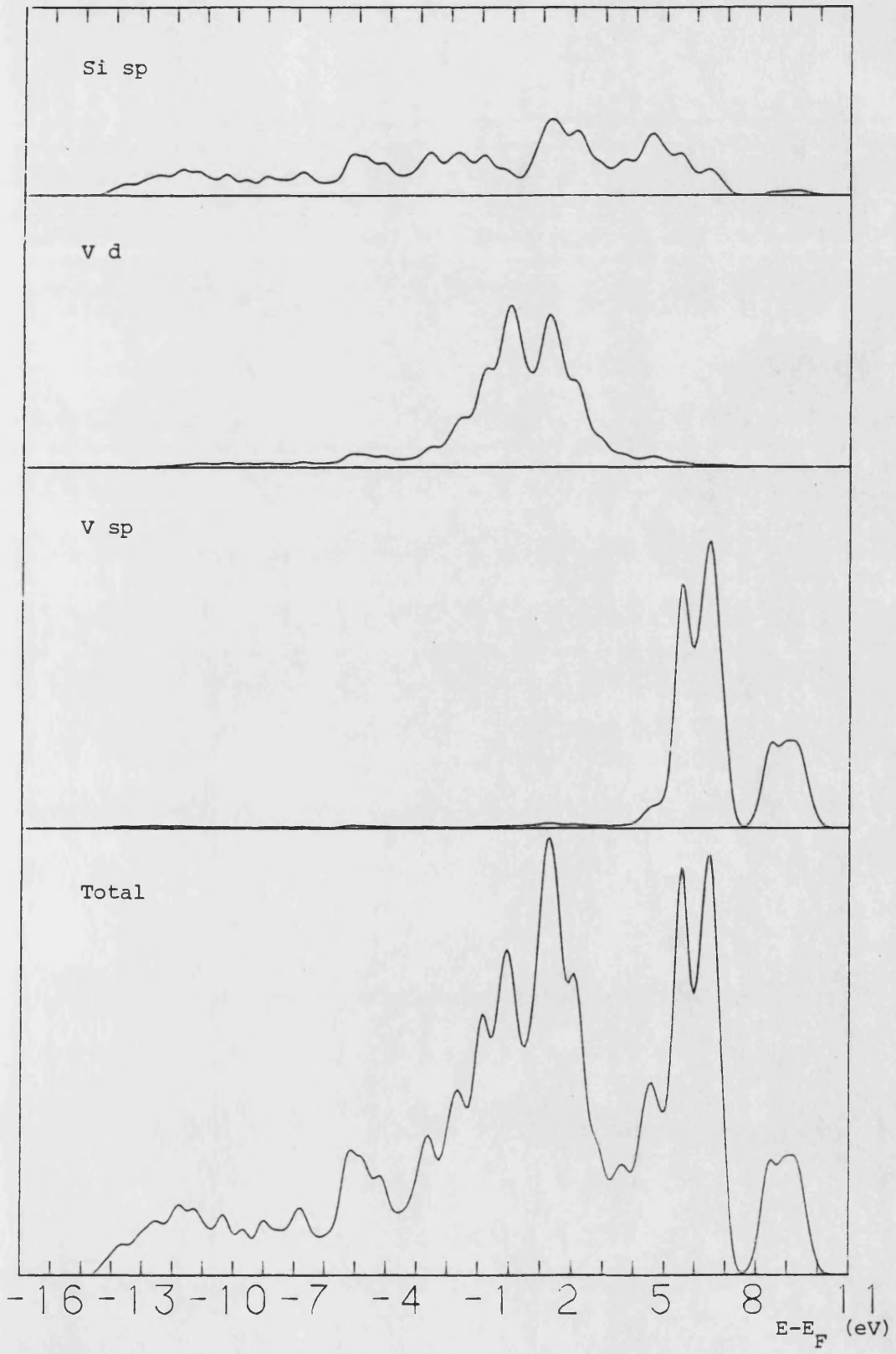

Figure 3.45 The calculated total and projected DOS for VSi_2.

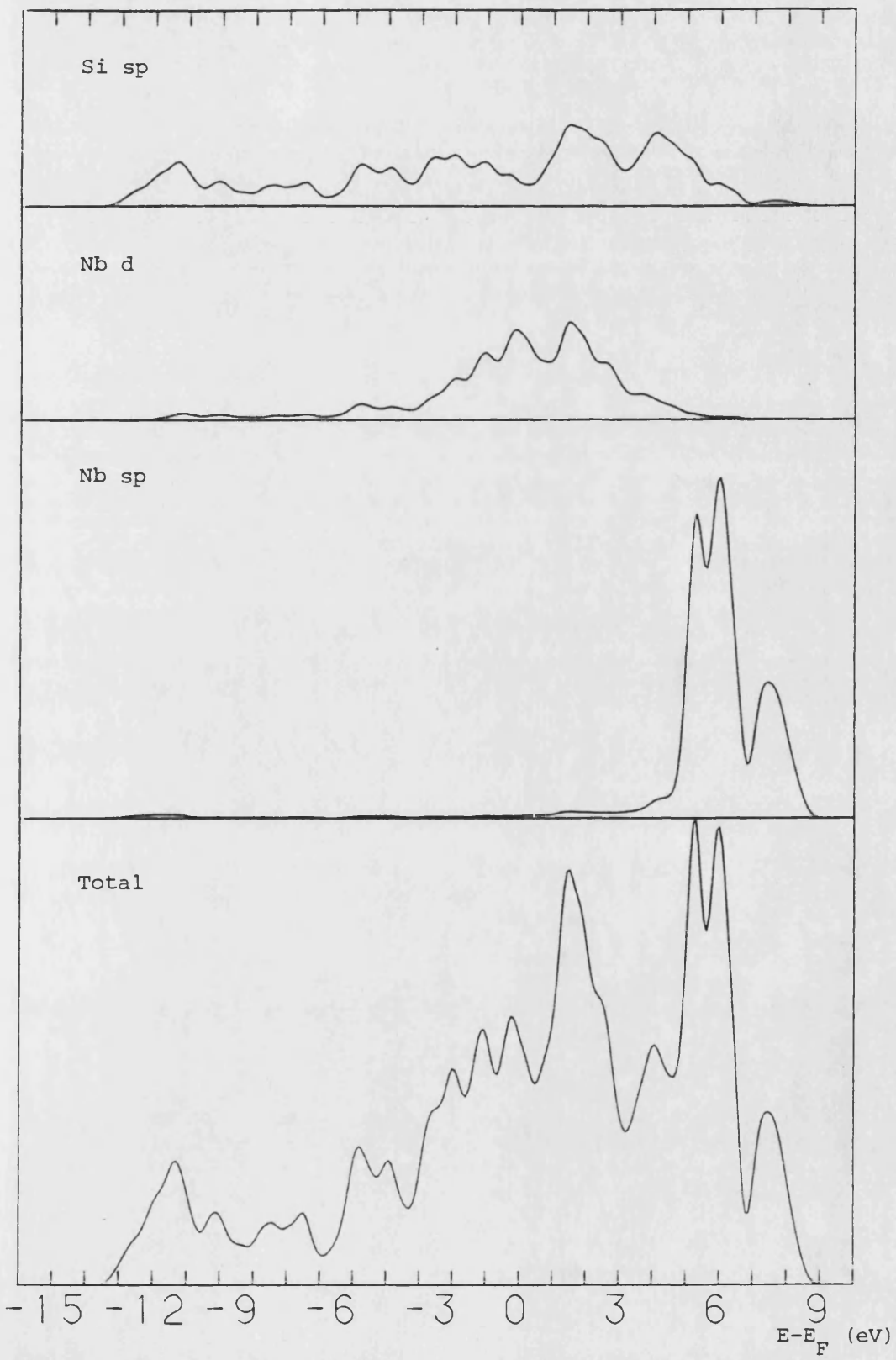

Figure 3.46 The calculated total and projected DOS for $NbSi_2$.

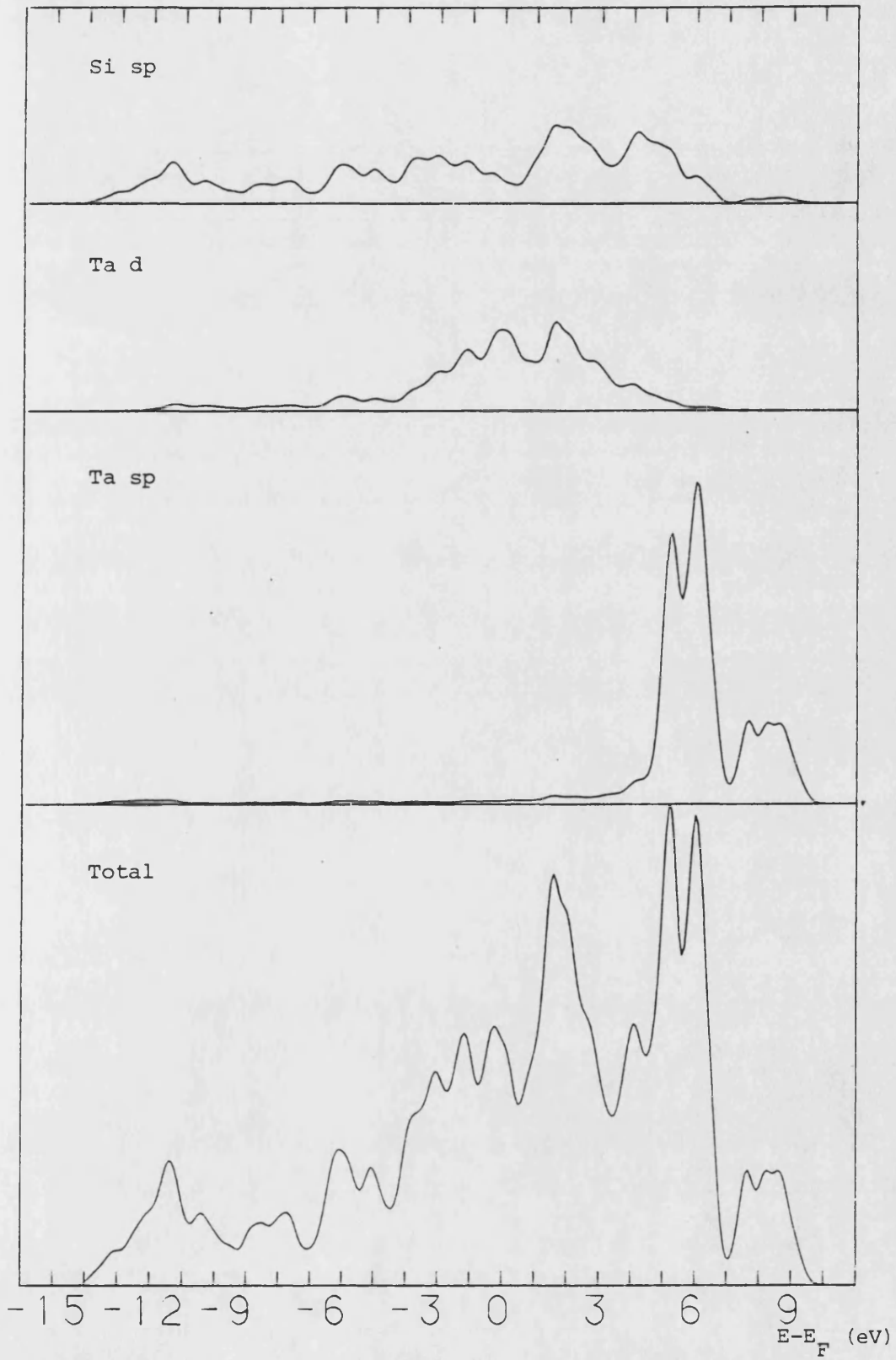

Figure 3.47 The calculated total and projected DOS for $TaSi_2$.

projection of the density of states onto the metal sp orbitals is almost vanishing below the Fermi level for the four silicides.

The peaks just below the Fermi level are due to nonbonding metal d orbitals, while those at -5 eV and just above the Fermi level can be interpreted as bonding and antibonding metal d-Si p features respectively. This kind of bonding has been found in the near noble metal silicides (see the previous section of this chapter) and by other authors for the refractory metal disilicides, as will be discussed below.

Electronic structure calculations using an LCAO approach in the extended Hückel approximation have been carried out for $CrSi_2$ (Franciosi et al., 1983) and for VSi_2 (Bisi and Chiao, 1982). The total densities of states obtained from these calculations are shown in Figures 3.48 ($CrSi_2$) and 3.49 (VSi_2).

The density of states from Franciosi et al. (1983) shown in Figure 3.48 differs markedly from that obtained in the present calculation shown in Figure 3.44. For example, in Figure 3.48 although there is a feature just below the Fermi level, unlike in the present results, this is not the most prominent feature of the valence band. This lies between -2 and -4 eV, where there is just a small shoulder in the present results. In both calculations the Fermi level lies very close to a deep dip in the density of states, but while in the present calculations the density of states at the Fermi level is found to be large, in Figure 3.48 the density of states at the Fermi level is seen to be

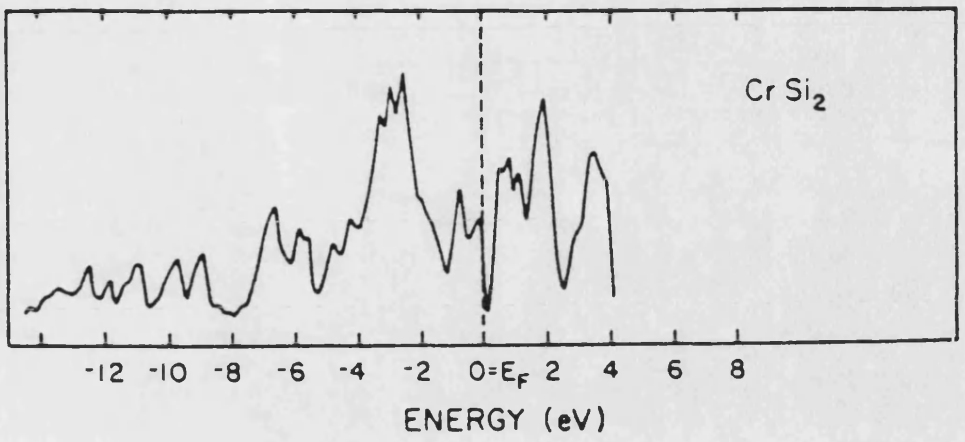

Figure 3.48 The total density of states for $CrSi_2$ from Franciosi et al. (1983).

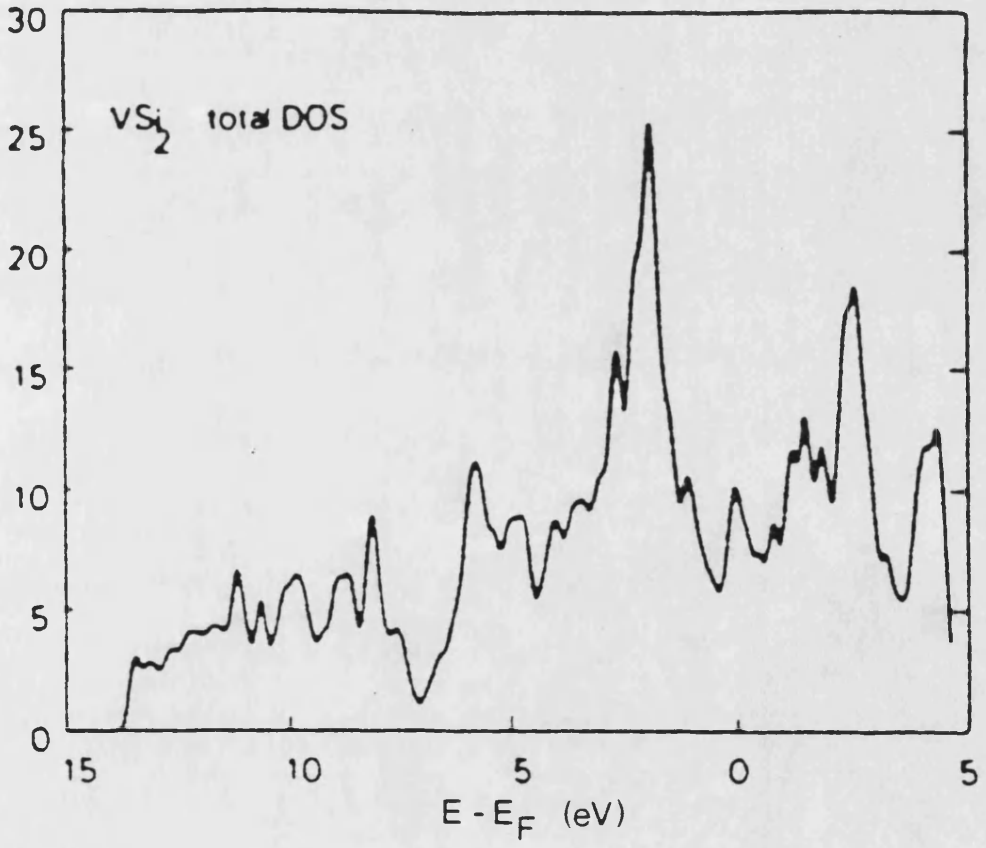

Figure 3.49 The total density of states for VSi_2 as calculated by Bisi and Chiao (1982).

small. Further, although it is not clear from Figure 3.48 how wide the occupied band is, it is certainly wider than 14 eV.

A synchrotron radiation photoemission study of bulk $CrSi_2$ (Franciosi et al., 1983) found a main peak in the density of states at -0.6 eV and a broad shoulder at $\sim$-1.7 eV. The first of these features corresponds well with the nonbonding metal d peak seen in the theoretical density of states shown in Figure 3.44. There is however no obvious feature in the theoretical density of states of the present calculation which corresponds to the broad shoulder found experimentally around -1.7 eV.

Comparing the theoretical density of states for VSi_2 found by Bisi and Chiao (1982) (Figure 3.49) with that of the present calculation (Figure 3.45) it can be seen that they have a similar occupied band width, both have a nonbonding d peak near the Fermi level, though in Figure 3.49 it is further below the Fermi level than in Figure 3.45, both have Si p-V d bonding features at about -5 eV and Si p-V d antibonding features above the Fermi level, and in both the states below -7 eV are mainly weighted on the Si s orbitals.

Experimentally, using synchrotron radiation photoemission spectroscopy, Weaver et al. (1981) have found in the valence band of VSi_2 a strong peak at -1.6 eV, a relatively weak peak at -0.8 eV, and further maxima at -5.5, -7.2, and -10.4 eV. Only the features at -10.4 and -5.5 eV are matched by features in the theoretical density of states

shown in Figure 3.45: a Si s peak at ∼-11 eV and a Si p-V d peak at ∼-5 eV.

Synchrotron radiation photoemission studies have also been made of $NbSi_2$ and $TaSi_2$. For $NbSi_2$ (Weaver et al., 1984) the dominant structure was found within ∼4 eV below the Fermi level and smaller peaks were found at -5.2, -8, and -11 eV. For $TaSi_2$ (Weaver et al., 1981) the main peak was found at -2.4 eV with smaller peaks at -5.8, -8, and -11 eV. As with these experimental results the theoretical results for $NbSi_2$ (Figure 3.46) and $TaSi_2$ (Figure 3.47) are very similar to each other. Both have their main valence feature between 0 and -3 eV, in reasonable agreement with what was found experimentally for $NbSi_2$, but both also have the highest point of this feature within half an eV below the Fermi level, which is at variance with that found experimentally for $TaSi_2$. The remaining three experimental features would seem in both cases to correspond to the theoretical features found at -5, -7, and -10.4 eV.

The charge transfer found theoretically in these silicides is shown in Table 3.29.

3.3.2.3 $MoSi_2$, WSi_2, and $ReSi_2$

The three disilicides $MoSi_2$, WSi_2 and $ReSi_2$, have, as discussed above, the same crystal structure. Their calculated total and projected densities of states are shown in Figures 3.50 ($MoSi_2$), 3.51 (WSi_2) and 3.52 ($ReSi_2$) (see the Note at the end of this thesis). The density of states of $MoSi_2$ is considered first. There is a sharp dip in the density of states at the Fermi level (0 eV), a prominent narrow metal d peak a little below the Fermi level at -0.8 eV, a Si p-metal d feature below this between -4 and -6 eV,

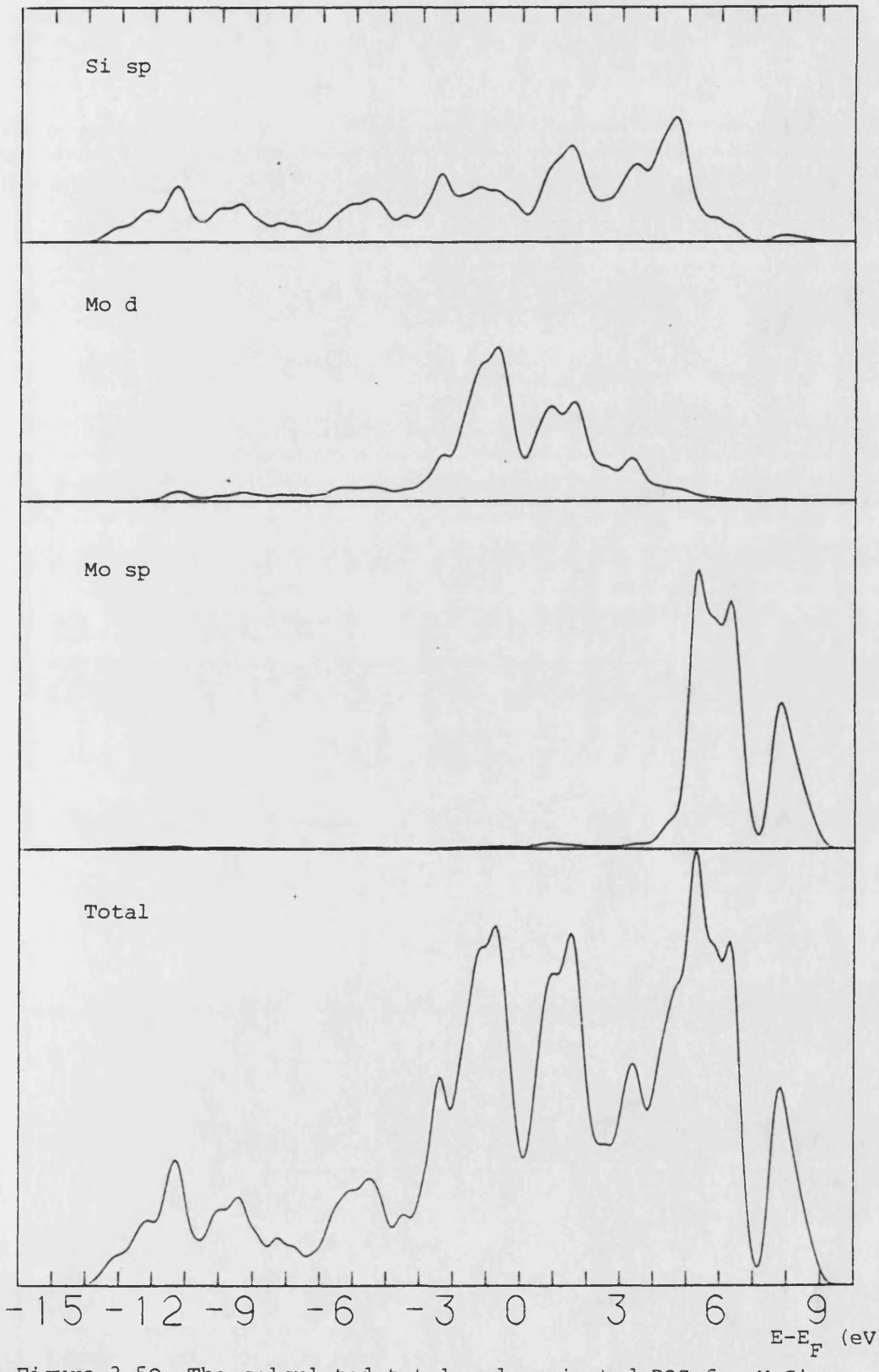

Figure 3.50 The calculated total and projected DOS for $MoSi_2$.

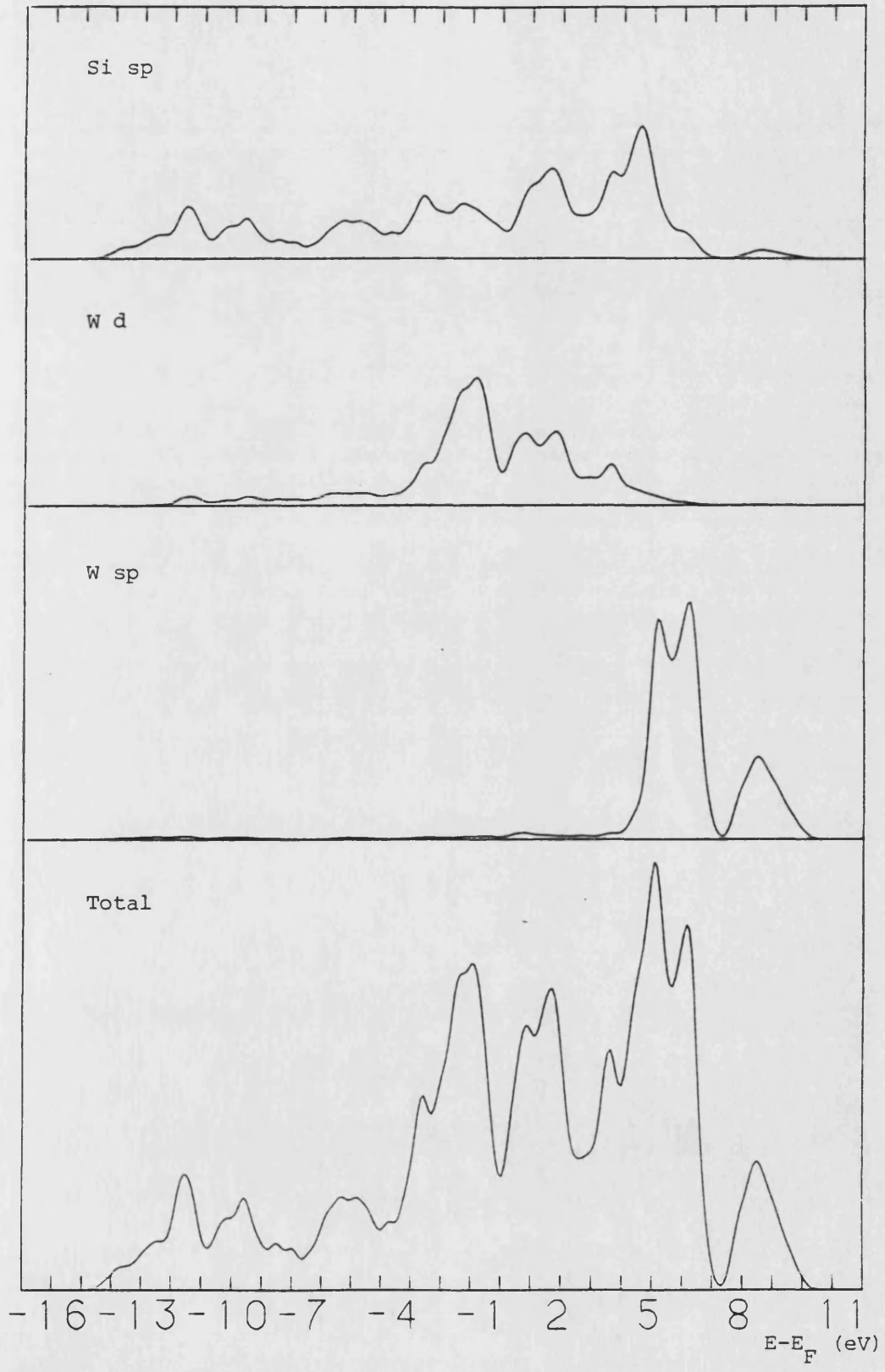

Figure 3.51 The calculated total and projected DOS for WSi_2.

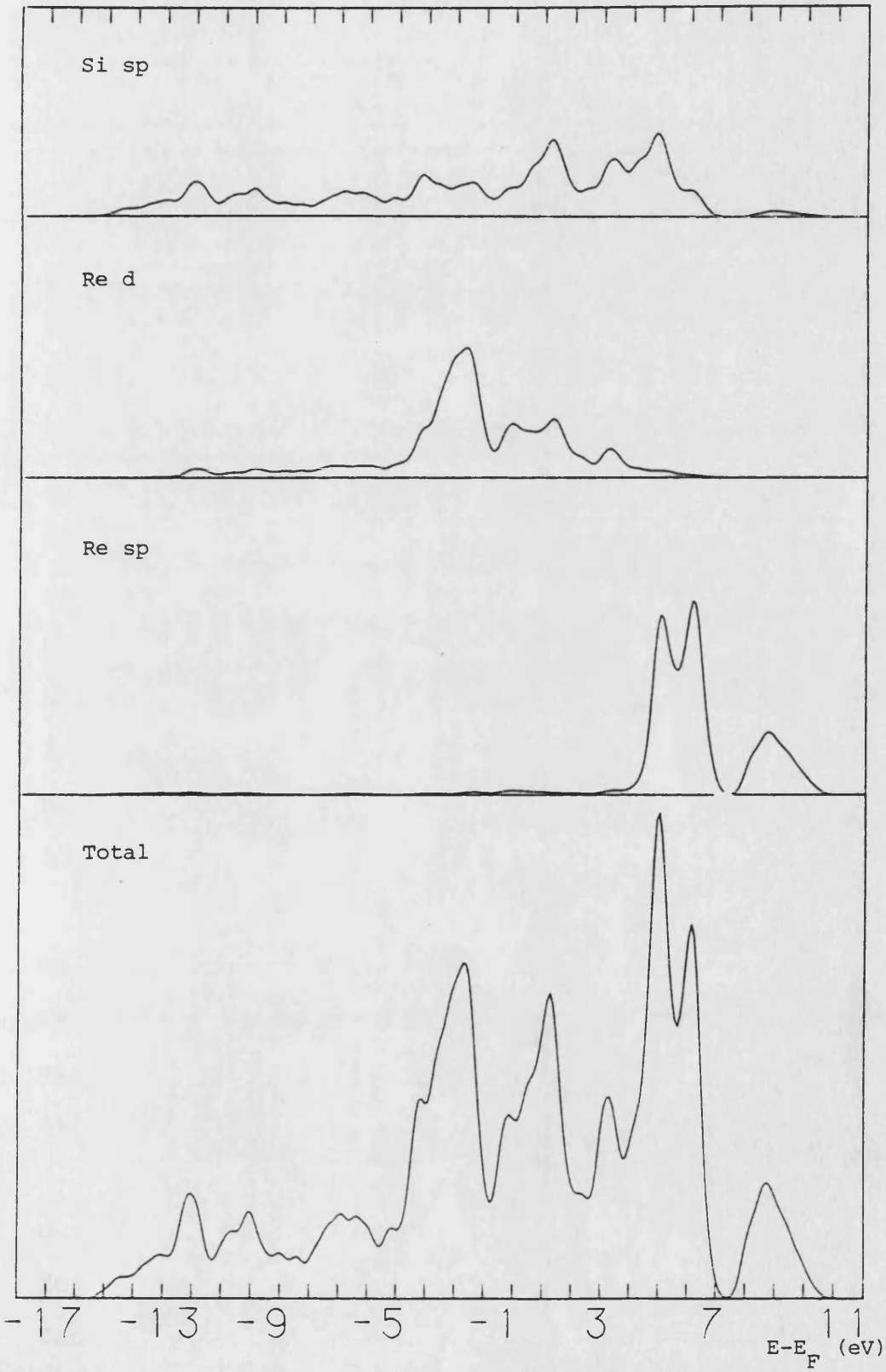

Figure 3.52 The calculated total and projected DOS for $ReSi_2$.

a peak at -8.3 eV, and a Si s peak at -10.2 eV. The densities of states of the other two disilicides are both very similar to this one and have corresponding features at 0, -1.0, -4 to -6, -8.5, and -10.5 eV (WSi_2), and -0.8, -1.8, -5 to -7, -9.0, and -11.0 eV ($ReSi_2$).

The density of states of WSi_2 has also been calculated by Bhattacharyya et al. (1985a) self-consistently with the use of a semirelativistic pseudopotential. They have also calculated the band structure of WSi_2 by the same method (Bhattacharyya et al., 1985a) and using a fully relativistic self-consistent pseudopotential method (Bhattacharyya et al., 1985b). Their calculated total and projected densities of states are shown in Figure 3.53. As in the present results they find a dip in the density of states at the Fermi level. Also in further general agreement they find the main feature to be a W d peak a little below the Fermi level and the valence band width to be 14 eV. (In the present calculation the WSi_2 valence band is found to be 13.5 eV wide.)

The electronic structure of bulk $MoSi_2$ has been examined using photoemission spectroscopy using synchrotron radiation by Weaver et al. (1981). They found it to be very similar to that of VSi_2 and $TaSi_2$ with the predominant peak at -2.2 eV and smaller features at -6, -8, and -11 eV.

The self-consistent atomic valence level energies and occupations found from the electronic structure calculations for the disilicides considered in this section are given in Table 3.29.

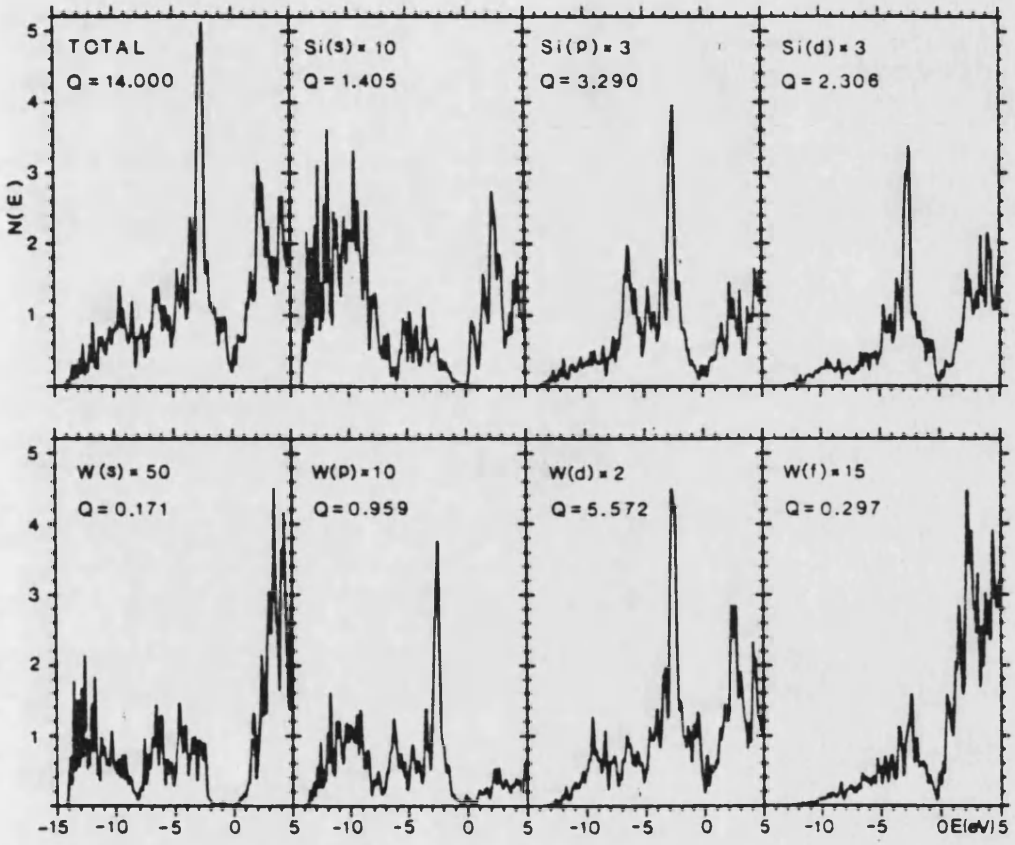

Figure 3.53 The total and projected DOS of WSi_2 as calculated by Bhattacharyya et al. (1985a). N(E) is in units of electrons per eV per unit cell. E=0 is E_F. Q is the total charge of each type integrated up to E_F.

3.3.3 Conclusion

The densities of states of the transition metal disilicides VSi_2, $NbSi_2$, $TaSi_2$, $CrSi_2$, $MoSi_2$, WSi_2 and $ReSi_2$ are all very similar to each other. Each has an occupied band width of 12-14 eV. They all have a metal d projected density of states with two peaks, one below the Fermi level and one above. Between these two peaks there is a corresponding dip in all the total densities of states near the Fermi level, this dip being particularly pronounced in $CrSi_2$, $MoSi_2$, WSi_2 and $ReSi_2$. The dominant feature of each valence band lies between the Fermi level and about -3 to -4 eV and is mainly weighted on the metal d orbitals. There is a small Si p-metal d feature in each at $\sim$-5 eV and a Si s one at around -11 eV.

Weaver et al. (1981, 1984) have studied the electronic structure of transition metal disilicides with experiment and model calculations. They concluded that Si p-metal d bonding takes place in the silicides. They further concluded that the states that dominate silicide photoemission spectra within 3-4 eV of the Fermi level are nonbonding d states, while the states at higher binding energies are Si p-metal d bonding states and those at the bottom of the valence band (at $\sim$-11 eV) are Si s states and are relatively unimportant in bonding.

These conclusions are drawn here also, supported as they are by the present theoretical results summarized above. In these results the states between 0 and -3 eV, at $\sim$-5 eV, and between 0 and 3 eV are thus now interpreted as nonbonding metal d, and bonding and antibonding Si p-metal d states respectively.

Although somewhat different in shape to the density of states of the other refractory metal disilicides, the density of states of $CoSi_2$ still shows the presence of Si p-metal d bonding with Si p-Co d bonding states between -5 and -3 eV, a nonbonding Co d peak (much narrower than that seen for the other disilicides) between -3 and 0 eV, and antibonding Si p- Co d states above the Fermi level. Unlike the other refractory metal disilicides, in which the Si s orbitals are not greatly involved in bonding and are found mainly near the bottom of the valence band, in $CoSi_2$ Si s states are found at up to -5 eV. The tetrahedral coordination of the Si atoms in $CoSi_2$ suggests that this is due to the presence of a degree of Si sp^3 hybridization.

The calculated charge transfer found in the refractory metal disilicides is shown in Table 3.29. In all but the disilicides of Co, W and Re electrons move from the metal to the Si atoms, as was found for the near noble metal silicides. The largest charge transfer found, in $ReSi_2$, is of 0.36 electrons to each Re atom.

Rather than calculating the charge transfer in $CoSi_2$ Tersoff and Hamann (1983) examined the number of electrons inside a sphere of radius 1 Å centred on a Si atom. They found it was only 0.05 less for $CoSi_2$ than it was for Si, suggesting minimal ionicity in $CoSi_2$. An extended Hückel LCAO calculation which used the Mulliken population analysis (Franciosi et al., 1983) found negligible ionicity in $CrSi_2$ with a charge transfer of 0.015 electrons to each Cr atom. The same calculational method has also been used for VSi_2 (Bisi and Chiao, 1982) where again very little charge

Phase	Metal atom valence orbital energies (eV)				Atomic charge (electrons/atom)		Fermi energy (eV)
	s	p	d	(d occupation)	metal	Si	
$CoSi_2$	-6.4	-3.3	-4.5	(8.58)	9.22	3.89	-2.9
VSi_2	-5.3	-3.0	-3.4	(4.39)	4.68	4.16	-2.9
$NbSi_2$	-4.9	-2.9	-3.8	(4.53)	4.78	4.11	-3.0
$TaSi_2$	-5.0	-2.9	-3.8	(4.55)	4.88	4.06	-2.9
$CrSi_2$	-5.4	-3.1	-3.5	(5.59)	5.92	4.04	-2.7
$MoSi_2$	-5.1	-2.9	-3.9	(5.77)	5.98	4.01	-2.9
WSi_2	-5.0	-2.9	-3.9	(5.83)	6.14	3.93	-2.8
$ReSi_2$	-5.1	-2.9	-4.3	(6.95)	7.36	3.82	-2.5

Table 3.29 Energies and charges in the refractory metal disilicides.

transfer was found: 0.017 electrons to each Si atom. For WSi_2 Bhattacharyya et al. (1985a) found 1.0 electrons transfer to each W atom, but used the Löwdin projection (Löwden, 1950) to get this result.

It is further concluded that there is little ionic contribution to the bonding in the refractory metal disilicides.

3.4 Conclusion

Calculations of the electronic structure of near noble metal silicides and refractory metal disilicides were carried out and presented in this chapter. They reveal that there are features which are common to all transition metal silicides, and it is these features that are now considered.

There is little ionic contribution to the bonding in the silicides. There is a negligible contribution to the valence electronic structure of the silicides from the metal s and p orbitals. The dominant feature of the valence band is a nonbonding metal d peak (which lies, with the exception of the monosilicides of Pd and Pt, within -4 eV of the Fermi level). Metal d-Si p hybridization takes place and gives rise to bonding states below and antibonding states above the nonbonding metal d peak. The Si s states are not greatly involved in bonding and are found mainly at the bottom of the valence band.

CHAPTER 4

THE ELECTRONIC STRUCTURE OF THE $NiSi_2$-Si(111) INTERFACE AND SUPERLATTICE

4.1 Introduction

Some silicides, as has already been discussed in the introduction to Chapter 3, grow epitaxially on silicon, and these epitaxial Si-silicide systems have excited considerable interest (Tung et al., 1982a, 1986a). Under ultrahigh vacuum conditions it has been found possible for two silicides, $CoSi_2$ and $NiSi_2$, to establish single crystal, homogeneous interfaces with silicon. It is the $NiSi_2$-Si(111) interface that is considered in this chapter.

Epitaxial silicon-silicide systems are generally formed by the reaction technique. In this a thin metal film is deposited by electron-gun evaporation onto a chemically cleaned substrate at room temperature and under vacuum. The sample is then annealed in vacuum or in a controlled atmosphere when reaction takes place between the deposited metal and the silicon to give an epitaxial layer of silicide on top of the substrate.

Samples of $NiSi_2$-Si(111) prepared in this way using vacuum conditions of about 10^{-6} Torr have been examined using Rutherford backscattering and channeling, transmission electron microscopy, and low energy electron diffraction (Chiu et al., 1980b, 1981; Föll et al., 1981; Cherns et al., 1982b). These studies revealed the silicon-silicide interfaces to be atomically abrupt and smooth and the metal overlayers to be of excellent crystalline quality. The metal $NiSi_2$ films were, however, found to be not monocrystalline but to contain grain boundaries.

Misfit dislocations were also found to be present (at the interface).

The grain boundaries occur between regions where the $NiSi_2$ has the same orientation as that of the substrate (type A orientation) and regions where the $NiSi_2$ is rotated about the interface normal [111] direction by 180° with respect to the substrate (type B orientation) and where there is thus twinning across the $NiSi_2$-Si interface (see the next section). Chiu et al. (1981) estimated that 60% of the grains were of type A while Föll et al. (1981) estimated that only 20% of the grains were of type A.

By using ultrahigh vacuum (UHV) conditions, that is using pressures of about 10^{-10} Torr, it has been found possible to grow epitaxial silicide-silicon systems of even higher quality using both reaction and molecular beam epitaxy (MBE) techniques. This was first done for $CoSi_2$ on Si(111) by Tung et al. (1982b). They reported that the MBE $CoSi_2$ films that they had grown had a crystalline quality not only better than any other silicide film on silicon but also among the best measured for any crystalline material. In particular they found the films to be free of grain boundaries, that is to say, monocrystalline.

It has also been found possible using UHV techniques to grow very thin (< 60 Å thick) epitaxial $NiSi_2$ films on Si(111) which are monocrystalline and free of misfit dislocations (Tung et al., 1983a). When formed by reaction, whether the single-crystal $NiSi_2$ overlayer is of type A or of type B depends on the thickness of deposited nickel: thin layers formed with 1-7 Å of Ni are type B while those formed

with 16-20 Å of Ni are type A. Thicker layers of either orientation can be grown by depositing further Ni at elevated temperature onto the appropriate thin layer (Tung et al., 1983b).

The existence of a metal-semiconductor interface as perfect as that of $NiSi_2$-Si(111) opens up many interesting possibilities. Most metal-semiconductor junctions are, as mentioned in the introduction to Chapter 3, very complicated and this makes understanding the mechanism by which the Schottky barrier is established at such junctions very difficult. The high degree of regularity and reproducibility of the single-crystal $NiSi_2$-Si(111) interface, however, makes it possible to sensibly consider its atomic structure, and indeed it has been studied by several methods, and models for it have been proposed. Knowledge of the interfacial atomic positions has then made it possible to carry out calculations of the interface electronic structure, and also to allow the measured Schottky barrier height (SBH) to be related to an interface geometry. The study of the electrical properties of single-crystal metal-semiconductor systems together with the study of their interface structure may lead to direct identification of the Schottky barrier mechanism. Single-crystal silicide-silicon systems are the systems nearest to being ideal for that purpose known (Gibson et al., 1983).

A very striking result concerning the SBH of single-crystal $NiSi_2$-Si(111) was obtained by Tung (1984b). It was found that the SBH for type A $NiSi_2$ on n-type Si(111)

was 0.65 eV, while for type B $NiSi_2$ on n-type Si(111) it was found to be 0.79 eV. That is the SBH for the B type system was found to be greater than that for the A type by 0.14 eV. This result, where the SBH of two chemically identical systems depends on the orientation of the overlayer, strongly suggests that the SBH is being determined by the regular interface structure. The existence of defects associated with only one interface cannot, however, be ruled out, and this too would cause a difference in the SBH between the two systems.

This result has been questioned by Liehr et al. (1985) who found the SBH for both A and B type systems to be 0.78 eV. They also found that incorporating only minute amounts of imperfection into the system lowered the SBH to 0.66 eV. They thus concluded that the SBH seems to be determined more by the degree of perfection of the interface than by the type of epitaxy. On the other hand, photoresponse measurements of the SBH of type A and type B $NiSi_2$-Si(111) made by Hauenstein et al. (1985) confirmed the behaviour found by Tung (1984b) and gave values in good agreement with his. Tung et al. (1986c) have also recently shown that, under carefully controlled experimental conditions, the dependence of the SBH on the silicide orientation is very reproducible.

Epitaxial silicon-silicide-silicon structures have also been grown. The best results have been obtained for $CoSi_2$ and $NiSi_2$ on Si(111) (Bean and Poate, 1980; Saitoh et al., 1980). In particular Tung et al. (1986b) have recently grown near-perfect epitaxial strained layer

Si(111)-$NiSi_2$-Si(111) structures with very thin (<100 Å thick) silicide layers. They were able to grow Si-$NiSi_2$-Si structures with both A-B-A and A-A-B orientations. It seems very likely that in the future it will be possible to repeat this process many times and to thus create silicon-silicide superlattices.

Such structures, where there is a single-crystal metallic layer buried in a semiconductor with which it has a perfect interface, doubtless make possible many novel high speed devices (Shiraki, 1985). Recently, for example, a Si-$CoSi_2$-Si heterostructure was grown by MBE and used as a permeable base transistor (Tung et al., 1986d). Also, buried metal layers would be the fundamental component of any three-dimensional integrated circuit.

For high speed device applications Si-silicide-Si structures using $CoSi_2$ are more attractive than those using $NiSi_2$ because cobalt disilicide has an excellent conductivity and a long electron mean free path: Hensel et al. (1984) found the room temperature resistivity of thin films of $CoSi_2$ and $NiSi_2$ to be 15 and 34 $\mu\Omega$cm respectively and estimated the elastic scattering lengths of electrons in $CoSi_2$ and $NiSi_2$ to be ~400 and ~50 Å respectively. However, because of the lattice mismatch of $CoSi_2$ with Si, which is larger than that of $NiSi_2$ with Si, it is difficult to fabricate perfect Si-$CoSi_2$-Si structures: there are always pinholes present in the silicide layer. (These pinholes, incidentally, are necessary to the working of the above mentioned permeable base transistor.) It is possible to grow Si-$NiSi_2$-Si structures essentially pinhole-free.

Studies and proposed models of the atomic structure of the $NiSi_2$-Si(111) interface are reviewed in Section 4.2. Section 4.3 presents the results of calculations for the electronic structure of the $NiSi_2$-Si(111) interface and superlattice.

4.2 The atomic structure of the $NiSi_2$-Si(111) interface

Nickel disilicide and silicon have similar structures. Nickel disilicide has the Fluorite (CaF_2) structure and silicon has the diamond structure. The space lattice of both of these is face-centered cubic (fcc), but the basis associated with each lattice point in silicon consists of one Si atom at (0,0,0) and another at (1/4, 1/4, 1/4) while in nickel disilicide it consists of a Ni atom at (0,0,0) and Si atoms at ±(1/4, 1/4, 1/4). For Si the lattice parameter a=5.4307 Å while for $NiSi_2$ a=5.406 Å. It is the similarity of these two lattice constants (the mismatch is 0.45%) that allows such good epitaxial growth of $NiSi_2$ on Si.

The structure of $NiSi_2$ has been considered previously (see Chapter 3 and Figure 3.22 and Tables 3.3, 3.10, and 3.11 in particular) but for completeness it is briefly described again here. Each Ni atom is surrounded by 8 equidistant Si atoms at the corners of a cube and each Si atom is surrounded by 4 equidistant Ni atoms at the corners of a tetrahedron. (The coordination of the Si atoms in $NiSi_2$ is thus the same as it is in silicon.) The nearest neighbour (Si-Ni) distances in $NiSi_2$ are all 2.34 Å. The $NiSi_2$ unit cell is shown in Figure 4.1. It can easily be

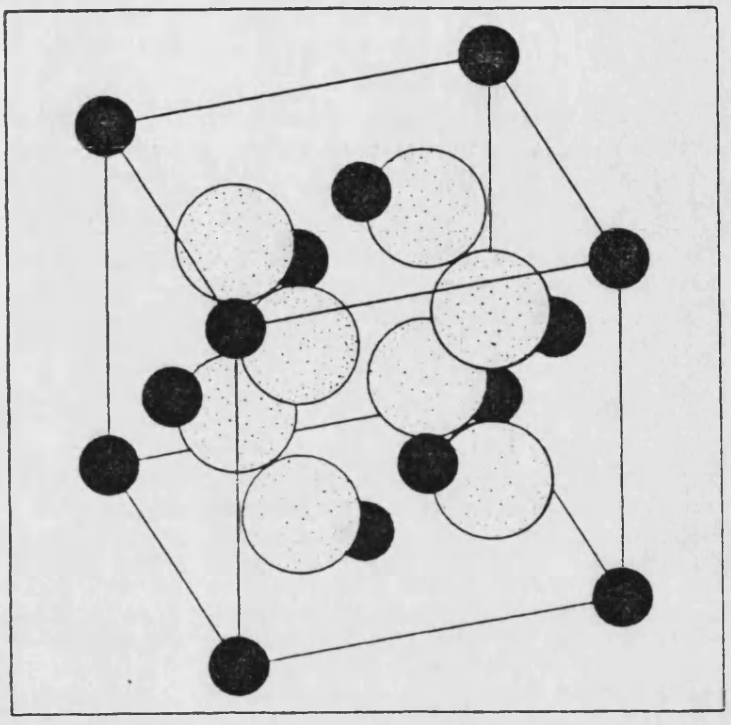

Figure 4.1 The $NiSi_2$ unit cell. The nickel atoms are black.

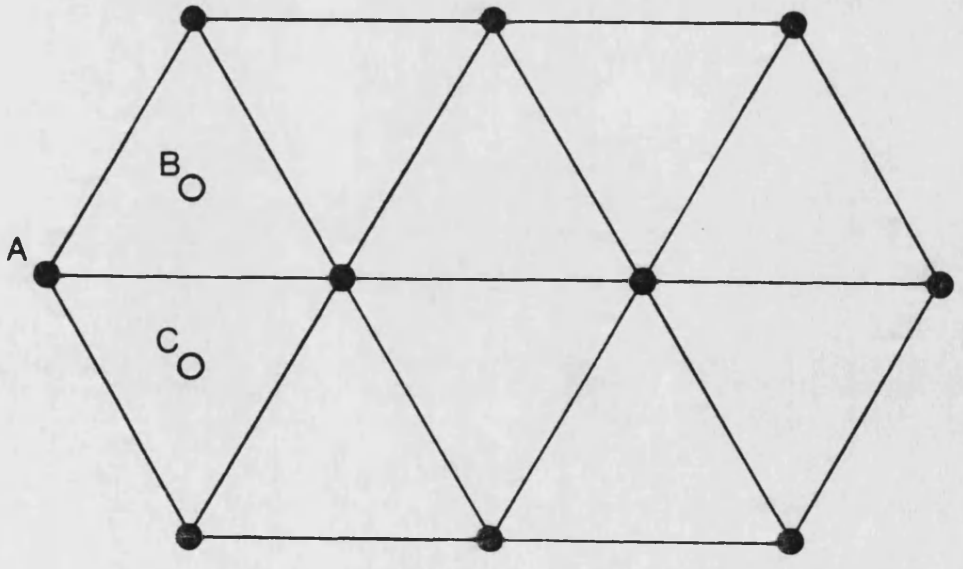

Figure 4.2 A hexagonal (111) layer from an fcc lattice. The fcc lattice is obtained by stacking such layers (along the [111] direction) in the sequence ...ABCABC...

seen from this that the $NiSi_2$ structure can be regarded as an fcc Ni lattice (lattice parameter a) together with an interpenetrating simple cubic silicon lattice (lattice parameter a/2).

When viewed along the [111] direction an fcc lattice can be regarded as consisting of close-packed hexagonal (111) layers with the stacking sequence ...ABCABC... Here the letters A, B and C refer to the displacement of the layer in its own plane (see Figure 4.2). Using the hexagonal unit cell (c-axis along the cubic [111] direction) instead of the fcc one the basis in silicon then consists of a Si atom at (0,0,0) and another at (0,0,1/4) while that in $NiSi_2$ then consists of a Ni atom at (0,0,0) and Si atoms at $\pm$(0,0,1/4).

The crystallinity of $NiSi_2$-Si(111) structures has been examined by Chiu et al. (1980b) using Rutherford backscattering (RBS) and channeling techniques. They found excellent epitaxy and little interfacial disorder. Later, using RBS and channeling, cross-section and plan view transmission electron microscopy (TEM), and low energy electron diffraction, Chiu et al. (1981) found the interface to be remarkably flat and showed that the $NiSi_2$ overlayer could grow with two orientations, type A and type B, related to each other by a rotation of 180° about the [111] direction. The $NiSi_2$-Si(111) interface has also been examined using TEM of cross-sectional specimens by Föll et al. (1981) and Cherns et al. (1982b). They found the interface to be atomically abrupt and smooth.

It has been noted already that Si atoms have the same (tetrahedral) coordination in both silicon and $NiSi_2$. Cherns et al. (1982b) proposed two models of the interface atomic structure built on the basis that the tetrahedral coordination of the Si atoms remains everywhere intact. These are shown in Figures 4.3 and 4.4. Both figures show (a) the type A and (b) the type B orientation for that model of the interface structure. In the (a) figures it can be seen that the (lattice point) stacking sequence across the interface is ...ABCAB... while in the (b) figures it is ...ABCBA... thus showing that for the B type orientations there is twinning across the interface.

In bulk $NiSi_2$ the Ni atoms are eightfold coordinated. The Ni atoms in the last Ni plane in the interface models shown in Figures 4.3 and 4.4 are sevenfold and fivefold coordinated respectively. Consequently these models are often referred to as the sevenfold and fivefold structures. Taking the position of the interface in the figures as given by the dashed line it can be seen that in the sevenfold structure (Figure 4.3) the silicide ends on a plane of Si atoms while in the fivefold structure (Figure 4.4) it ends on a plane of Ni atoms.

The TEM lattice imaging carried out by Cherns et al. (1982b) lead them to favour their sevenfold model for the $NiSi_2$-Si(111) interface. The results of ion focusing measurements carried out by van Loenen et al. (1985) and van Loenen (1986) were also in excellent agreement with the sevenfold model while they ruled out the fivefold model. They also indicated that the bonds across the interface were

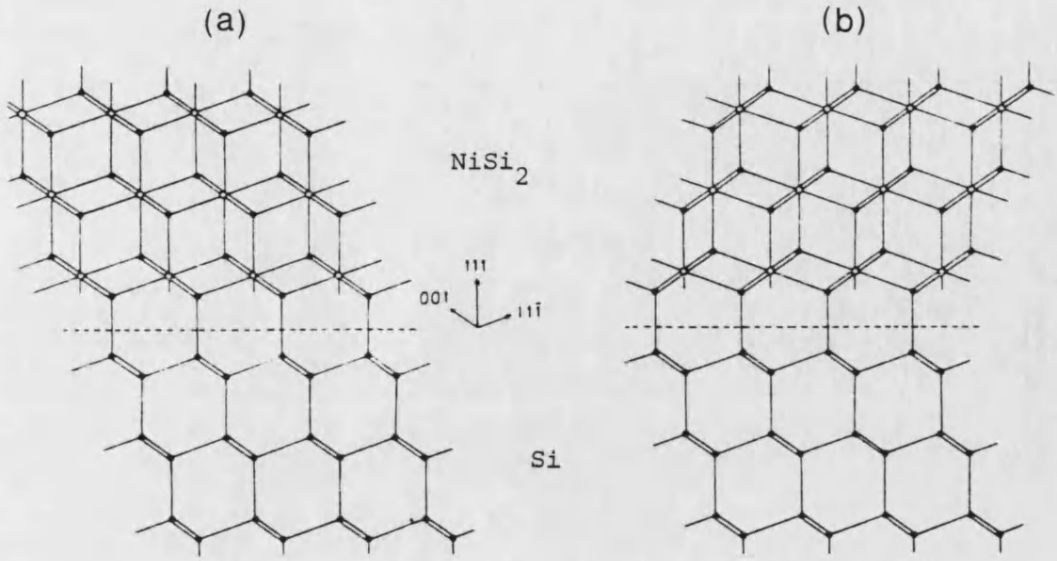

Figure 4.3 The "sevenfold model" of the atomic structure of the $NiSi_2$-Si(111) interface proposed by Cherns et al. (1982b) with (a) the type A and (b) the type B orientation. The view is down $[\bar{1}10]$.

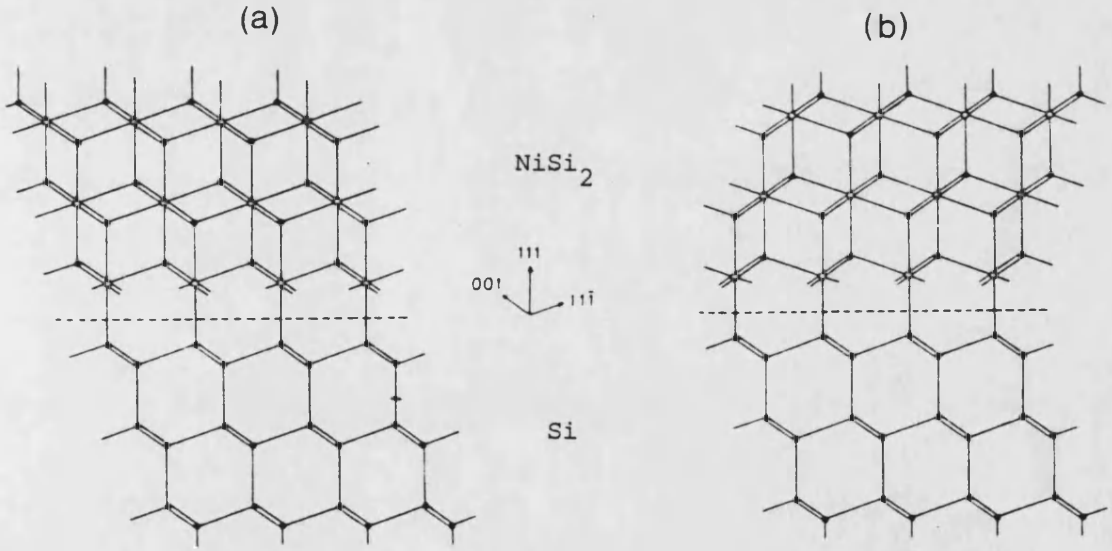

Figure 4.4 The "fivefold model" of the atomic structure of the $NiSi_2$-Si(111) interface proposed by Cherns et al. (1982b) with (a) the type A and (b) the type B orientation. The view is down $[\bar{1}10]$.

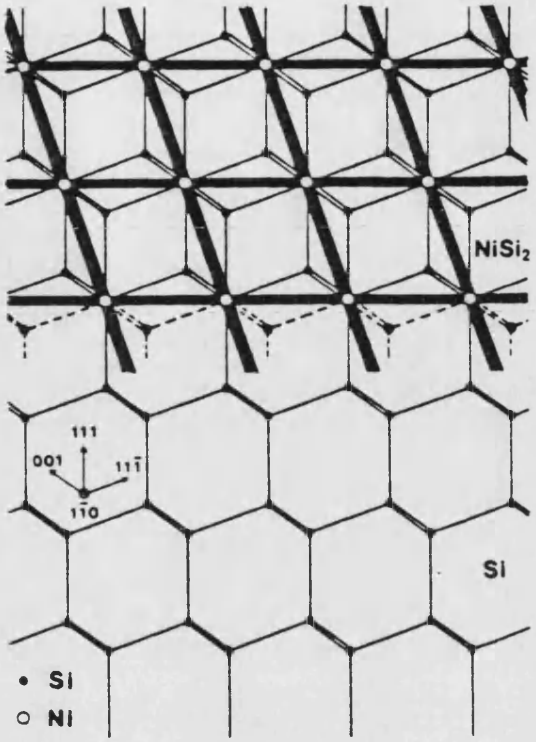

Figure 4.5 The atomic structure of the $NiSi_2$-Si(111) interface determined by Akimoto et al. (1985) using the X-ray standing-wave method. Ni atoms exist at the intersections of the black bands. The dashed circles and lines show an excess layer of silicon they proposed may exist at the interface.

not lengthened and were possibly contracted by 0.06 Å. Comin et al. (1983) studied the early formation of $NiSi_2$ on Si(111) (formed from depositing from 0.5 to 5 monolayers of Ni on silicon at room temperature). From their surface extended-X-ray-absorption fine structure (SEXAFS) measurements they concluded that the Ni atoms at the interface were sevenfold coordinated. However, Akimoto et al. (1983, 1985) studied the atomic structure of the $NiSi_2$-Si(111) interface by the X-ray standing-wave method and came to the conclusion that the interface had the fivefold structure. They also concluded that the $NiSi_2$ epitaxial film was dilated along the [111] direction and contracted along the [11$\bar{1}$] direction. To explain these lattice distortions they suggested the existence of a single excess silicon layer at the silicon-silicide interface (see Figure 4.5). There is thus not yet complete agreement as to the atomic structure of the $NiSi_2$-Si(111) interface.

4.3 The electronic structure of the $NiSi_2$-Si(111) interface and superlattice

Experimental investigations of the electronic structure of the $NiSi_2$-Si(111) interface have centred on measurements of the Schottky barrier height (SBH). One group (Wu et al., 1985; Ho et al., 1986), however, using a method they call accurate phase capacitance spectroscopy, have found a band of unoccupied interface states at around 0.65 eV above the silicon valence band edge for both type A and type B epitaxial interfaces. They found the density of these

states to be about 10^{12} per cm^2. (For the Si(111) surface, which has 7.83×10^{14} atoms per cm^2, this would correspond to about 1 state per 1000 atoms). Their technique does not, however, reveal occupied states. This result, where the interface electronic structure is independent of the interface type, seems to be at variance with the result referred to above found by other groups (Tung et al., 1986c; Hauenstein et al., 1985) that the SBH of the type A interface is different to that of the type B one.

Calculations of the electronic structure of a number of systems related to the $NiSi_2$-Si(111) interface have been carried out. Bisi et al. (1984) have calculated the electronic structure for a single layer of $NiSi_2$ on Si(111) in both the sevenfold and fivefold configuration. They used the iterative extended Hückel method. Also using a self-consistent tight binding method Robertson (1985) has calculated the electronic structure of Ni overlayers on Si(111) for a number of possible bonding geometries. Yongnian et al. (1986) have studied the trends in the electronic structure of the interface between Si(111) and a series of 3d transition metal disilicides (from $CaSi_2$ to $NiSi_2$). They used a tight binding method employing Harrison matrix elements (Harrison, 1980) and all the disilicides were taken to have the CaF_2 structure. For $NiSi_2$-Si(111) they considered both the type A and type B interfaces for both the sevenfold and the fivefold structures.

Lim and Allen (1985) have calculated the intrinsic interface states for the $NiSi_2$-Si(111) type A interface. They used a tight binding Hamiltonian which included only

nearest neighbour interactions and calculated the interface states using a Green's function technique. They found a prominent band of interface states near the Si valence band edge E_v. Later they calculated the dispersion of this band throughout the 2D Brillouin zone (Lim and Allen, 1986) and showed it extended from within the Si band gap to about 1 eV below E_v. They also calculated the interface states associated with a Si vacancy on the $NiSi_2$ side of the interface. They found one defect level in the Si band gap at what they point out is the right energy to explain the SBH's observed for $NiSi_2$ grown on n-type and p-type Si(111). While this result is suggestive of an extrinsic mechanism for the formation of the Schottky barrier, there exist experimental results (Chantre et al., 1986) consistent with an intrinsic mechanism.

In the present study a number of systems containing $NiSi_2$-Si(111) interfaces were considered. In order to avoid free surfaces these systems were, in fact, superlattices. Three superlattices were studied. These all had interfaces with the sevenfold structure and consisted of (a) 5 layers of Si and 1 layer of $NiSi_2$, (b) 7 layers of Si and 3 layers of $NiSi_2$, and (c) 6 layers of Si and 5 layers of $NiSi_2$. (Here a single (111) layer of Si is considered to consist of two (111) atomic planes of the type separated by 0.784 Å in the [111] direction.)

The unit cells of these three superlattices were hexagonal and are shown in Figure 4.6. In this figure the hexagonal c-axis of each of the unit cells (the hexagonal [0001] direction) is up the page and this corresponds to the

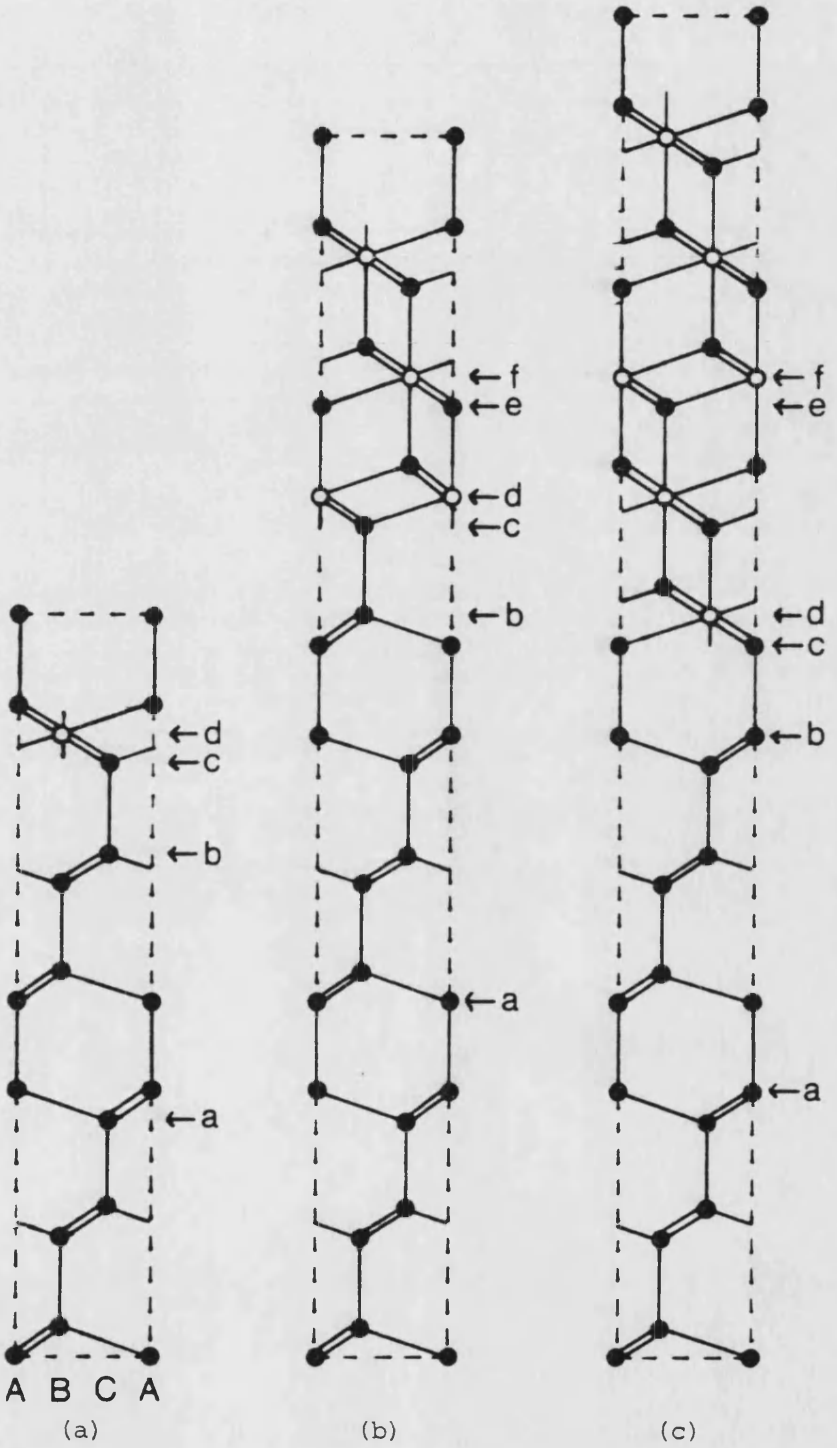

Figure 4.6 Figures (a) to (c) are representations of the hexagonal unit cells of the superlattice systems (a) to (c) respectively. The filled circles represent Si atoms and the open circles Ni atoms. [0001] is up the page and the view is along $[2\bar{1}\bar{1}0]$. The letters A, B and C indicate the position of atoms within a (0001) plane (see Figure 4.2). The significance of the atoms indicated by labelled arrows is explained in the text.

cubic [111] direction in bulk Si and $NiSi_2$. In all of these Si-$NiSi_2$-Si superlattices the orientation of the layers was A-B-A, that is to say all the interfaces were B type. Only up to second nearest neighbour interactions were included in the electronic structure calculations performed for these systems, and as the atomic structures of the type A and type B interfaces only differ from each other in the positions of the third and higher nearest neighbours it was not thought that there would be any gain from considering any type A interfaces as well.

The electronic structure of the systems (a) to (c) were calculated using the chemical pseudopotential method. The unit cells of these systems contained from 13 to 27 atoms and the chemical pseudopotential method is particularly well suited to dealing with systems with large unit cells. The matrix elements used were the same as those used for calculating the bulk density of states for Si and $NiSi_2$ (see Chapter 3) as was the interaction cut-off distance of 3 Å. This cut-off distance leaves nearest neighbour interactions in Si and up to second nearest neighbour interactions in $NiSi_2$. For these calculations, however, the lattice constant for $NiSi_2$ was taken to be the same as that of Si. The $NiSi_2$ in the model superlattices was thus dilated compared to bulk $NiSi_2$ and the interatomic distances were 0.45% larger. (In an actual superlattice perfect lattice matching between the $NiSi_2$ and the Si in the (111) plane at the interface would give rise to a bilateral strain in the $NiSi_2$ layer and thus doubtless to a contraction of its lattice parameter in the [111] direction.)

The unit cells for these systems were, as previously mentioned, hexagonal. For comparison the density of states of bulk Si and $NiSi_2$ (with its lattice parameter set equal to that of Si, i.e. 5.4307 Å) were also calculated using a non-primitive hexagonal unit cell and the same set of $\underline{k}$ points to sample the irreducible part of the Brillouin zone that were used in the superlattice calculations.

As in the other electronic structure calculations carried out for this thesis these calculations were carried through until self-consistency in the metal d orbital energies was achieved. Here, for the superlattices, the d orbital energies of Ni atoms in different (111) layers were allowed to vary independently.

Figure 4.7 shows the density of states for bulk $NiSi_2$ projected onto (a) a Ni atom and (b) a Si atom. (See the Note on the presentation of densities of states at the end of this thesis.) The position of the Fermi level is also shown. The density of states per atom for bulk Si is shown in Figure 4.8. The densities of states for the systems (a), (b) and (c) projected onto the atoms indicated by labelled arrows in Figure 4.6 are shown in Figures 4.9 to 4.13.

For each of the systems atom a is at the middle of the Si region of the superlattice. The density of states projected onto atom a for system (a) is shown in Figure 4.9, for system (b) in Figure 4.10, and for system (c) in Figure 4.12. By comparing these with the density of states for bulk Si (Figure 4.8) it can be seen that in each case the density of states projected onto atom a is essentially as it

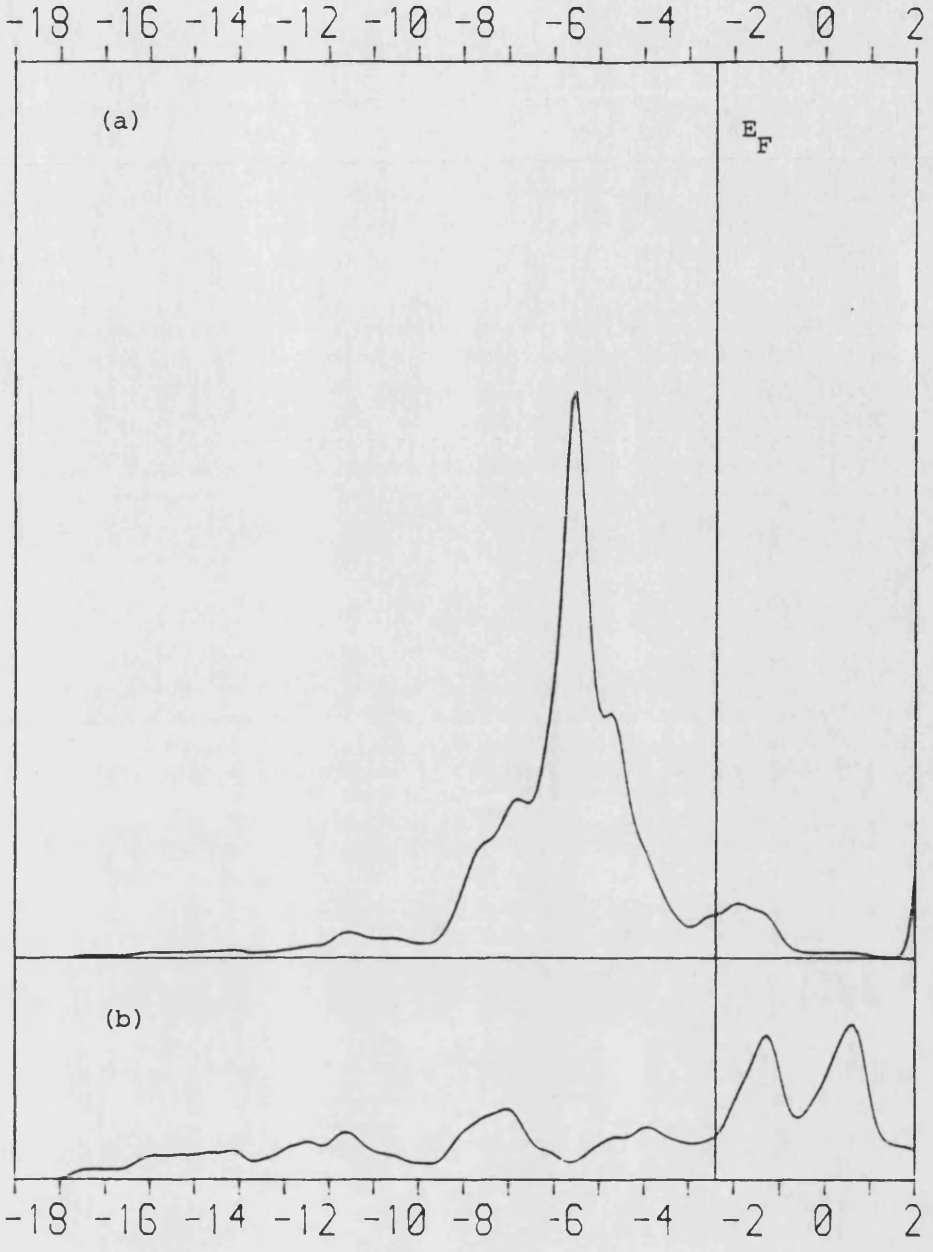

Figure 4.7 The density of states for bulk $NiSi_2$ projected onto (a) a Ni atom and (b) a Si atom.

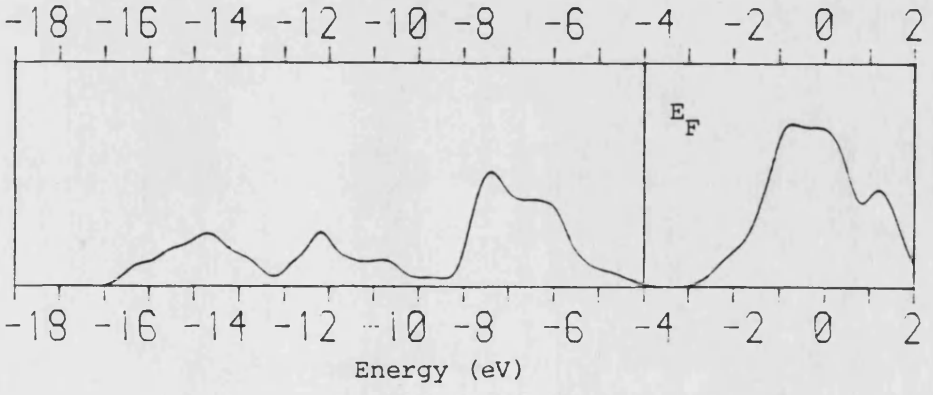

Figure 4.8 The density of states per atom for bulk Si.

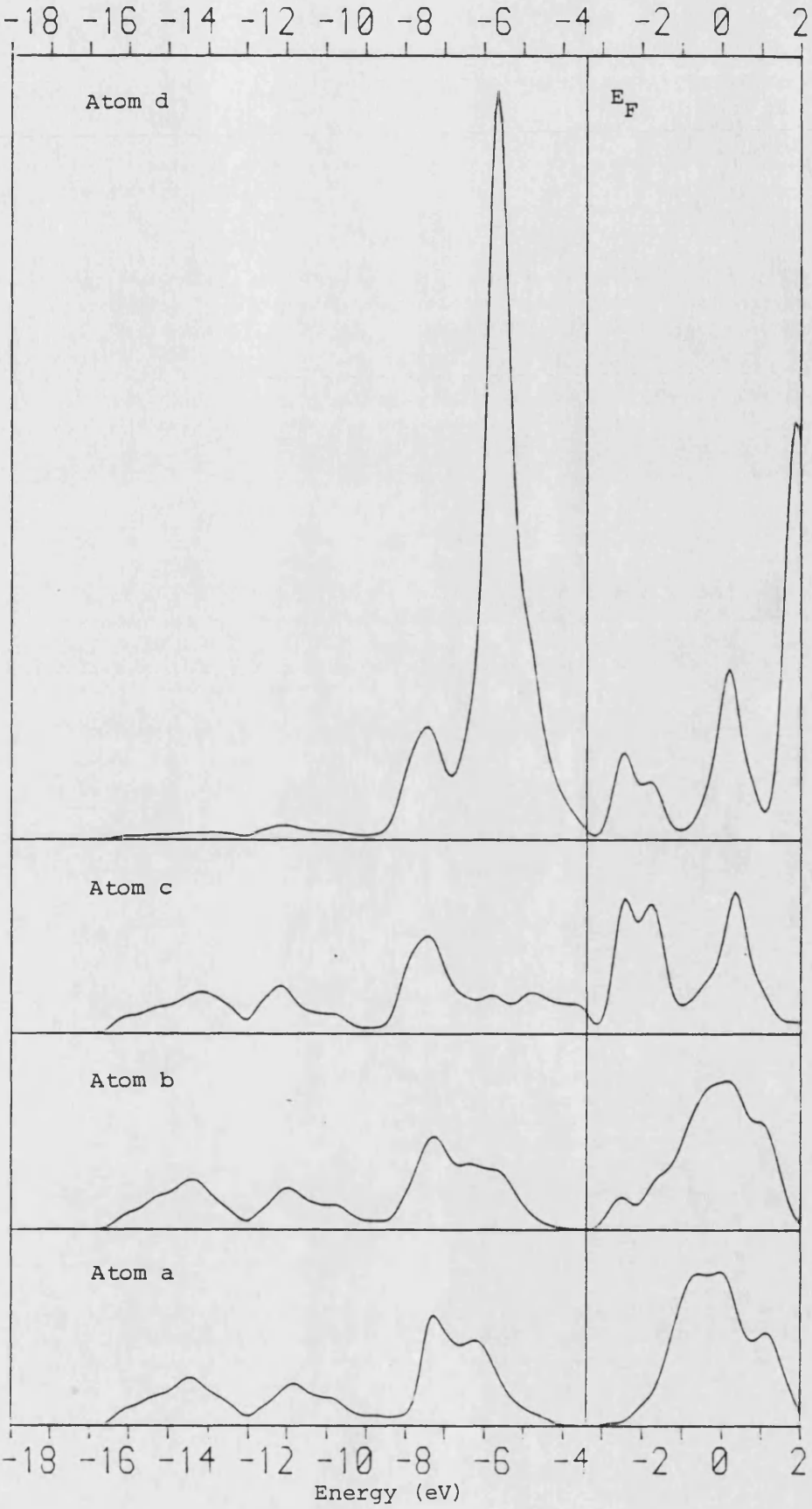

Figure 4.9 The density of states for superlattice (a) projected onto atoms a, b, c and d. (See Figure 4.6.)

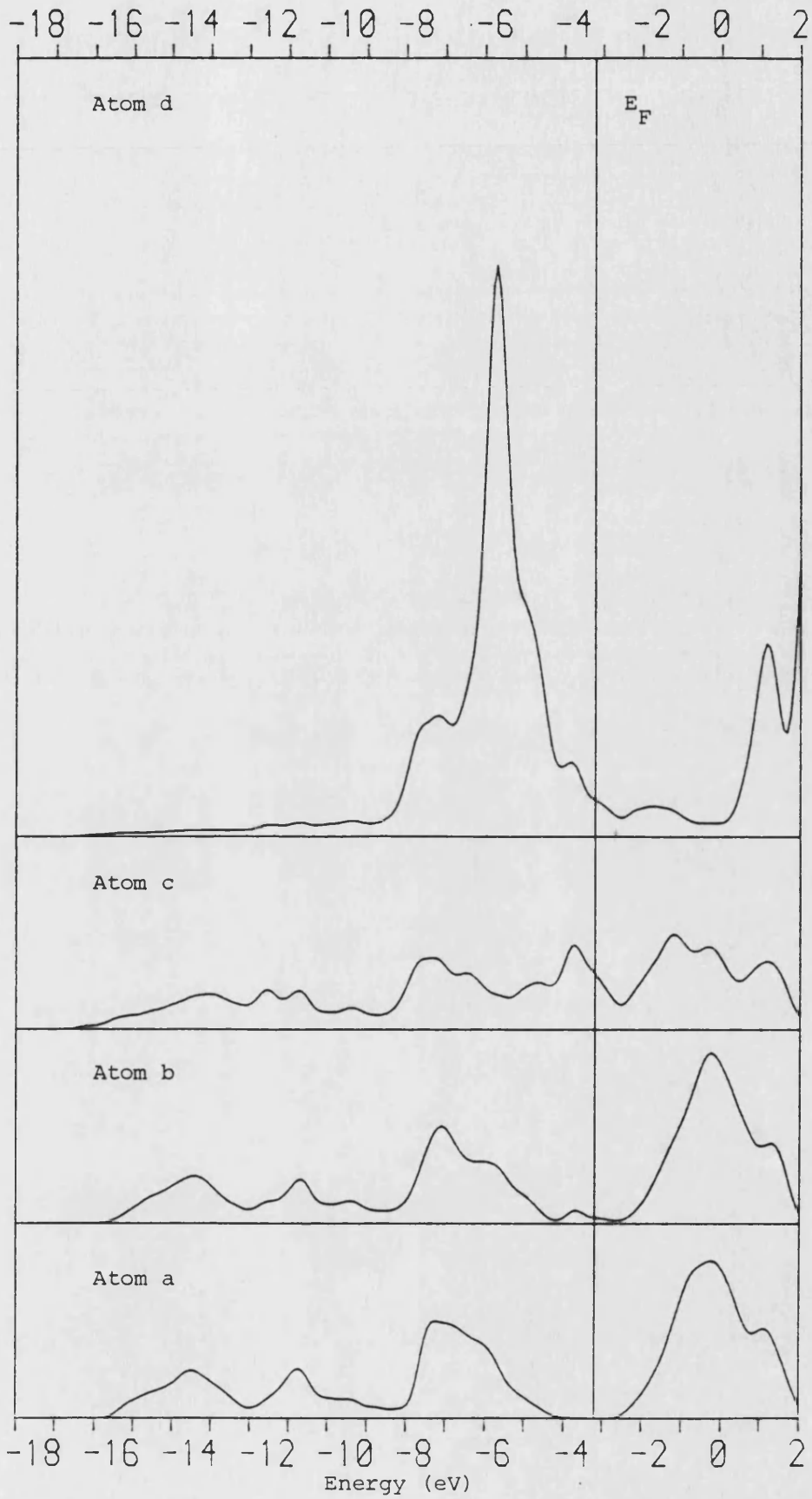

Figure 4.10 The density of states for superlattice (b) projected onto atoms a, b, c and d. (See Figure 4.6.)

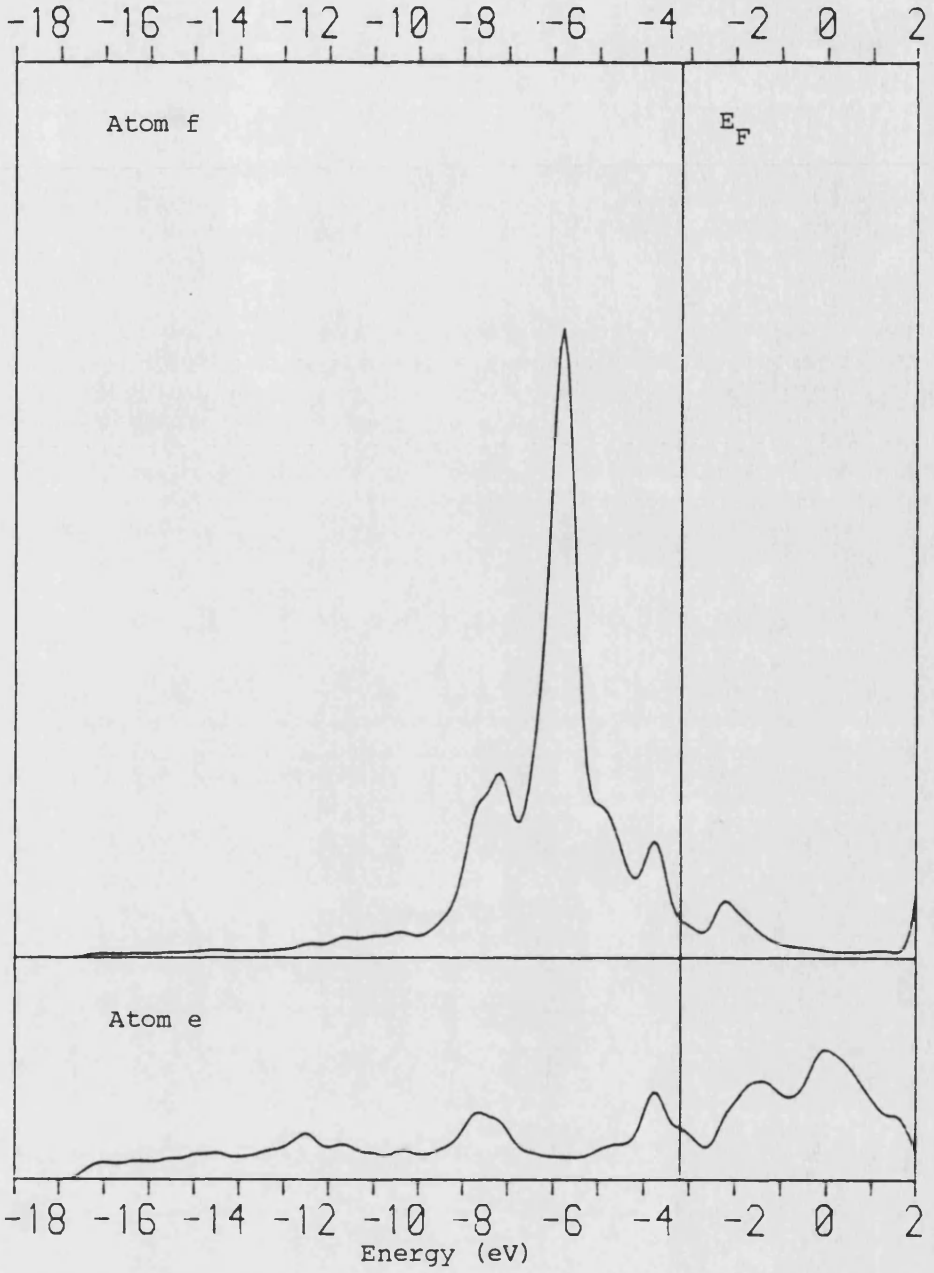

Figure 4.11 The density of states for superlattice (b) projected onto atoms e and f. (See Figure 4.6.)

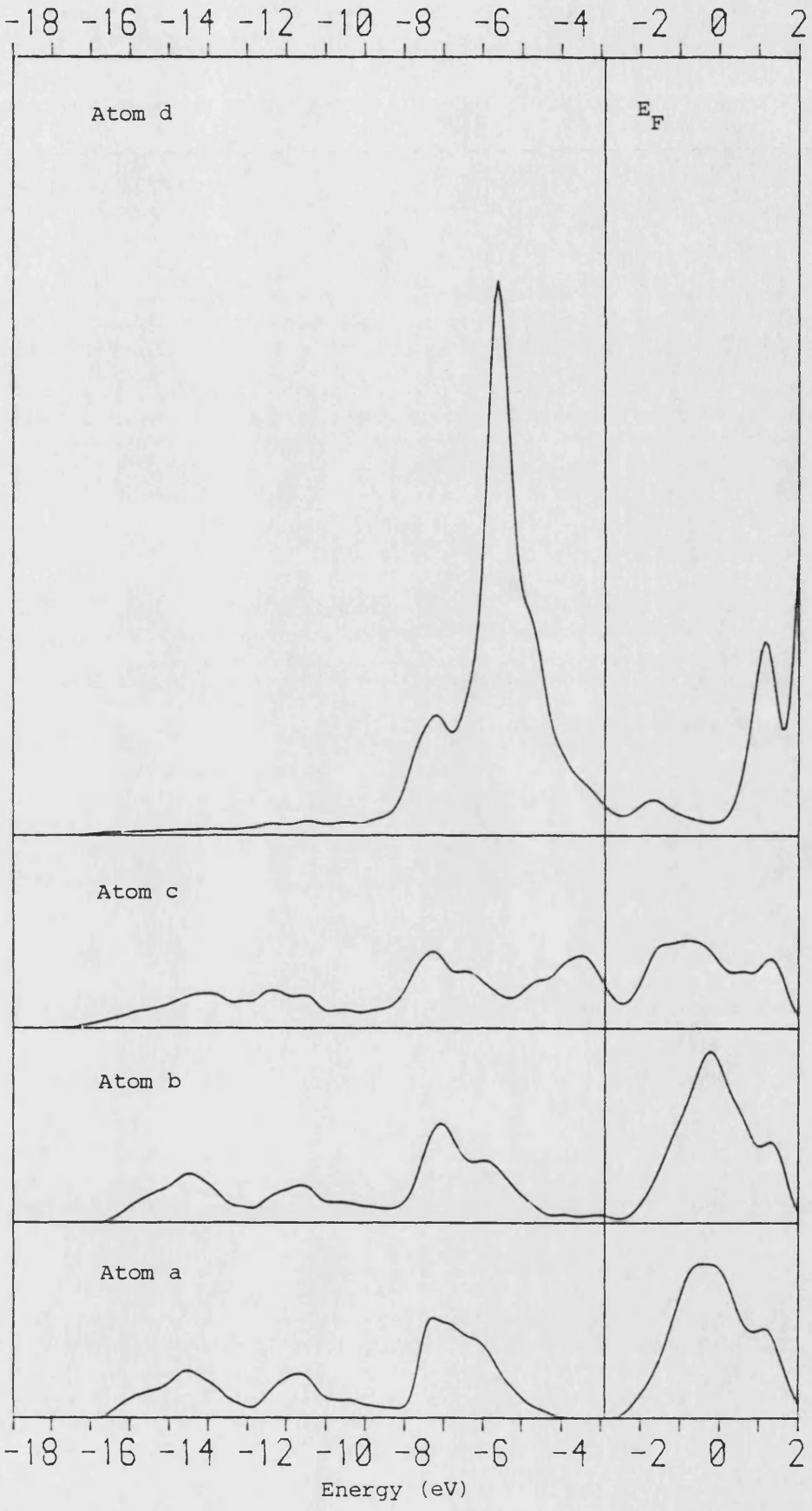

Figure 4.12 The density of states for superlattice (c) projected onto atoms a, b, c and d. (See Figure 4.6.)

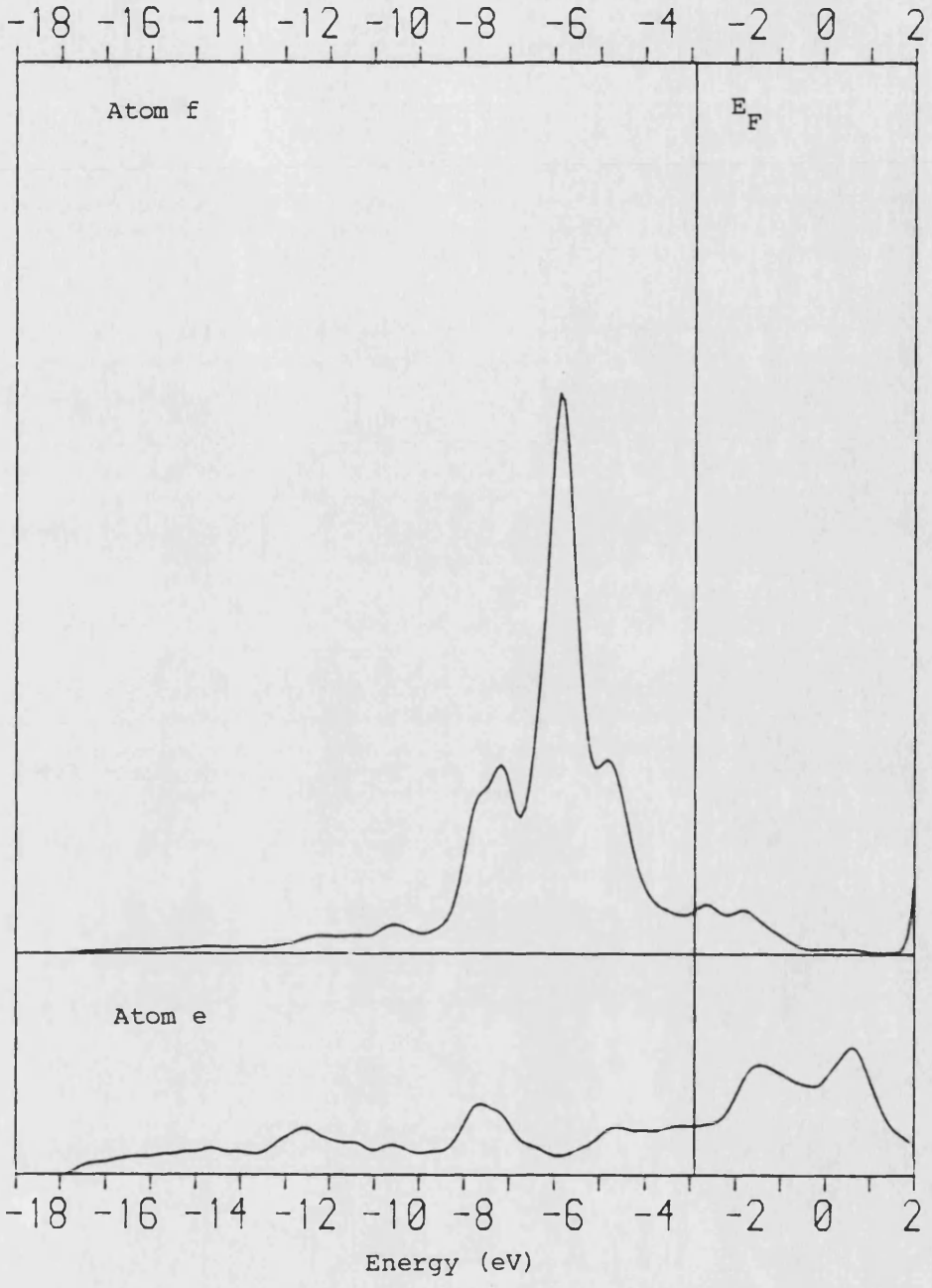

Figure 4.13 The density of states for superlattice (c) projected onto atoms e and f. (See Figure 4.6.)

is in bulk Si, although for superlattices (b) and (c) the energy gap is noticeably larger (0.3 to 0.4 eV larger) than it is in bulk Si.

Regarding the position of the $NiSi_2$-Si boundary in a $NiSi_2$-Si(111) sevenfold interface to be at the dashed line shown in Figure 4.3 atom b in the three superlattices (a Si atom) is then an interface atom on the Si side of the interface. Comparing the density of states projected onto this atom for the three superlattices with that for bulk Si it can be seen again that it is mainly as it is in bulk Si. The main difference is the presence in all three cases of states in the energy gap. For superlattice (a) (Figure 4.9) these interface states are at the top of the gap and at the bottom of the "conduction band". In superlattice (b) (Figure 4.10) they have moved further down into the middle of the gap and entirely span it so that there isn't actually any longer a gap. The interface states in superlattice (c) (Figure 4.12) also span the gap entirely. They have a greater dispersion than those in (a) or (b) and have no definite maximum. For all three superlattices the interface states are weighted only on the p_z orbitals of atom b.

Atom f, a nickel atom, is in the middle of the $NiSi_2$ region in superlattices (b) and (c). In superlattice (a) atom d is in the middle of the $NiSi_2$ region, but, as there is only one layer of $NiSi_2$ in this superlattice, it is also at two $NiSi_2$-Si interfaces and consequently has only sixfold coordination. The density of states for system (a) projected onto atom d is shown in Figure 4.9. Comparing it

to the density of states for bulk $NiSi_2$ projected onto a Ni atom (Figure 4.7) it can be seen that it has a narrower and taller nonbonding d peak. (The d peak is at about -5.7 eV in both.) This is because atom d in superlattice (a) has, as mentioned above, a coordination of only six while the coordination of a Ni atom in bulk $NiSi_2$ is eight. The densities of states projected onto atom f in superlattices (b) and (c) are shown in Figures 4.11 and 4.13 respectively. These have nonbonding d peaks (at about -5.9 eV) which are much more comparable in height to that seen in bulk $NiSi_2$ (Figure 4.7). (The coordination of atom f in both superlattices (b) and (c) is eight.) Infact for superlattice (c), which has six layers of $NiSi_2$ in each silicide region, the density of states projected onto atoms e and f (Figure 4.13) closely approaches the projected densities of states shown in Figure 4.7.

Atoms c and d are silicon and nickel atoms respectively and are interface atoms on the silicide side of the interface. Atom d in superlattice (a) is, however, as has been mentioned above, at two interfaces. The main feature of the density of states of each of the three superlattices projected onto atom d is the d peak between -5 and -6 eV. In superlattices (b) and (c) (Figures 4.10 and 4.12 respectively) this peak is less tall and narrow than it is in superlattice (a) (Figure 4.9) but it is still taller and narrower than the nonbonding Ni d peak seen in bulk $NiSi_2$ (Figure 4.7). This is because the coordination of atom d is six in superlattice (a) and seven in superlattices (b) and (c) while the coordination of a Ni atom in bulk $NiSi_2$ is eight.

The density of states projected onto atom c for superlattice (a) looks, below the Fermi level, much like that for bulk silicon while for superlattices (b) and (c) it looks much more like the density of states for bulk $NiSi_2$ projected onto a Si atom.

The charges calculated to be on the labelled atoms of the superlattices are given in Table 4.1 together with the charges calculated for bulk Si and $NiSi_2$. The calculated Fermi energies are also given. The Ni and Si s and p valence atomic orbital energies that were used are given in Table 4.2. The calculated self-consistent Ni d valence atomic orbital energies and occupations for $NiSi_2$ and the superlattices (a), (b) and (c) are gien in Table 4.3. There is not a great range in the values of the Ni d orbital occupations (from 9.20 to 9.31) and this variation does not appear to be particularly dependent upon the Ni atom coordination. For example the d orbital occupation for the (eightfold coordinated) Ni atoms in bulk $NiSi_2$ is 9.28 while for the (sixfold coordinated) Ni atoms in superlattice (a) it is 9.27.

In this section the electronic structures of three $NiSi_2$-Si(111) systems have been considered. In each case states were found which had finite weighting on the last Si atom (on the p_z orbital) in the Si region while having no weighting on Si atoms in the middle of the Si region. These states had energies lying in the bulk Si energy gap and were presumed to be interface states.

System	Atomic charges (electrons/atom) Atoms a	b	c	d	e	f	Fermi energy (eV)
Si	4.00						-4.0
$NiSi_2$					4.12	9.76	-2.4
Superlattice (a)	3.99	3.95	4.17	9.78			-3.4
Superlattice (b)	4.00	4.03	4.67	9.83	3.94	9.66	-3.2
Superlattice (c)	4.01	4.06	4.81	9.89	3.95	9.67	-2.9

Table 4.1 Calculated atomic charges and Fermi energies.

Atom	Orbital	Energy (eV)
Si	s	-11.5
	p	-5.2
Ni	s	-6.0
	p	-3.2

Table 4.2 Energies of s and p valence atomic orbitals.

System	Ni d orbital energy (eV)	Ni d orbital occupation
$NiSi_2$	-5.6	9.28
Superlattice (a)	-5.7	9.27
Superlattice (b)	-5.7	9.25
	-5.9	9.20
	-5.7	9.25
Superlattice (c)	-5.6	9.31
	-5.8	9.22
	-5.9	9.20
	-5.8	9.22
	-5.6	9.31

Table 4.3 Ni d atomic valence orbital energies and occupations.

CHAPTER 5

THE ELECTRONIC STRUCTURE OF NiP_2, AuGeAs, AND THREE SILVER CLUSTER COMPOUNDS

5.1 The electronic structure of NiP_2 and AuGeAs

The equiatomic ternary compound AuGeAs is formed in the interface region of Au-Ge-In Ohmic contacts to GaAs Gunn diodes. It is found as particles of about 5μm in diameter and its presence has been correlated with good device performance (Luveluck et al., 1978; Steeds et al., 1981; Rackham and Steeds, 1981). The structure of AuGeAs was recently determined by Vincent et al. (1984) using convergent-beam electron diffraction. They found it to be monoclinic with space group C2/c and to have the PdP_2 structure with the gold atoms occupying the 4(a) sites and the germanium and arsenic atoms in random occupation of the 8(f) sites (see Table 5.1). The lattice parameters and atomic parameters measured by Vincent et al. (1984) are given in Table 5.2. Also given are the lattice parameters and atomic parameters measured by Larsson (1964) for the isostructural NiP_2.

Figure 5.1 shows the PdP_2 structure projected down the b-axis onto the ac plane. The positive a-direction is from left to right, the positive c-direction is down the page, and the b-direction is up out of the page. Each metal atom has four equidistant metalloid nearest neighbours (at a distance of 2.51 Å in AuGeAS and 2.21 Å in NiP_2). These five atoms all lie in a single plane and the four metalloid atoms are to a good approximation at the corners of a square. (The X-Au-X angles in AuGeAs are 89° and 91°, where X is a metalloid atom.) The metalloid atoms are in approximate tetrahedral coordination with two metal atoms (at 2.51 Å in AuGeAs and 2.21 Å in NiP_2) and two other

Number of positions (Wyckoff notation)	Point Symmetry	Position coordinates
		$(0,0,0;\ \frac{1}{2},\frac{1}{2},0)+$
8(f)	1	$\pm(x,y,z),\ \pm(x,\bar{y},z+\frac{1}{2})$
4(a)	1	$(0,0,0),\ (0,0,\frac{1}{2})$

Table 5.1 Details of the equivalent positions of the space group C2/c occupied in a PdP_2 type structure.

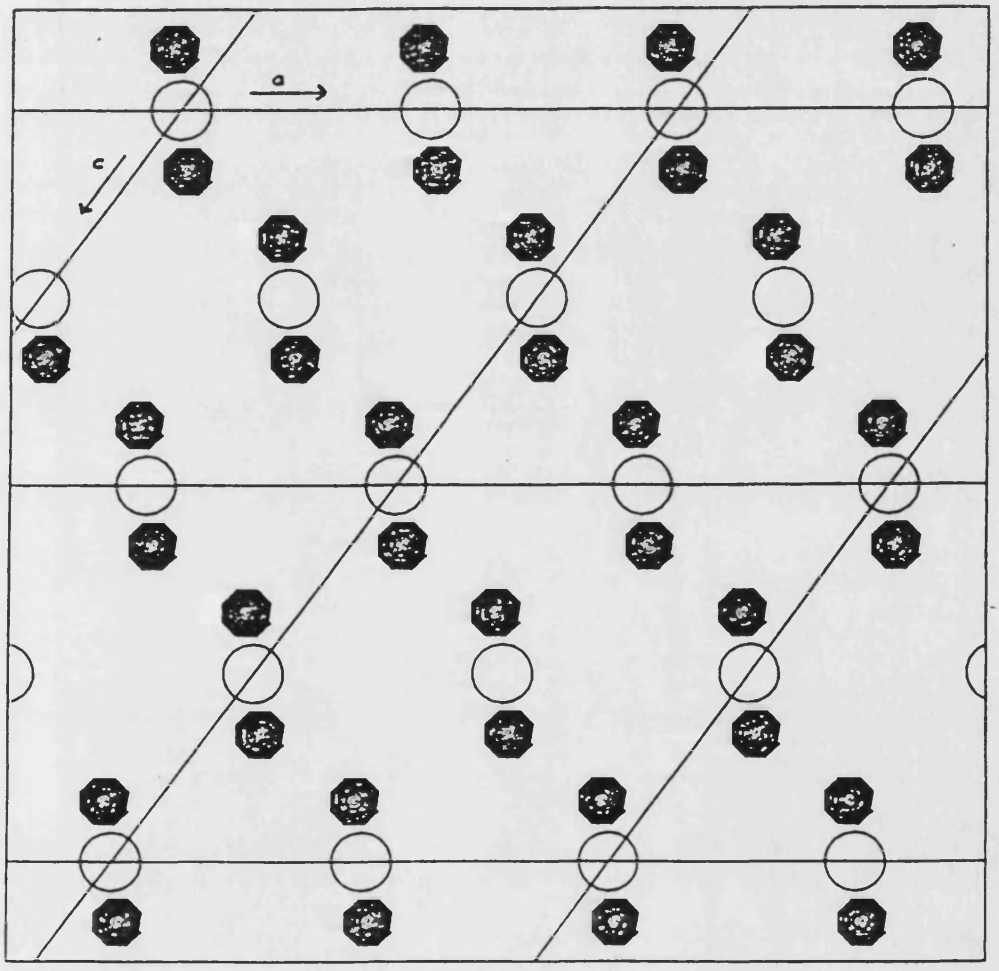

Figure 5.1 The PdP_2 structure viewed down the b axis. The open circles represent the metal atoms and the closed circles represent the metalloid atoms.

Phase	System	Structure Type	In Å a	b	c	β	Z	Space group	Atoms	Point Set	x	y	z
NiP_2	Monoclinic	PdP_2	6.37	5.62	6.07	126°	4	C2/c	4Ni	4(a)			
									8P	8(f)	113	365	164
AuGeAs	Monoclinic	PdP_2	7.11	6.34	6.84	126°	4	C2/c	4Au	4(a)			
									4Ge } 4As }	8(f)	105	370	161

Table 5.2 The crystallographic details of two materials with the PdP_2 structure.

Phase	Atom	Orbital energies (eV) s	p	d	Orbital occupations (electrons/atom) sp	d	Fermi energy (eV)
NiP_2	Ni	-6.0	-3.2	-6.0	0.3	9.2	-3.6
	P	-14.6	-6.5		5.2		
AuGeAs	Au	-6.5	-3.3	-11.0	0.7	9.8	-5.0
	Ge	-12.2	-5.1		} 9.5		
	As	-14.9	-6.2				

Table 5.3 Energies and occupations for NiP_2 and AuGeAs.

metalloid atoms (at 2.42 Å and 2.43 Å in AuGeAs and 2.22 Å in NiP_2). It has been noted by Zachariasen (1963) that the metalloid atoms form continuous zigzag chains parallel to the c-axis.

Zachariasen (1963) considered this bonding configuration (in the isostructural and isoelectronic PdP_2) to correspond to M^{2-} (dsp^2) and X^+ (sp^3), the hybridization of the four available orbitals giving square bonds for $M^{2-}$and tetrahedral bonds for X^+. The total number of electrons per formula unit is 20 and 12 of these would go into the bonding hybrids while the remaining 8 electrons would occupy the remaining four nonbonding d orbitals. If the nonbonding d levels were below the top of the bonding hybrid levels and there was a gap between bonding and antibonding hybrid levels this would give rise to the material being a semiconductor.

The calculated total and projected densities of states for NiP_2 are shown in Figure 5.2. (See the Note on the presentation of densities of states at the end of this chapter.) Only nearest neighbour interactions were included (that is an interaction cut-off distance of 3.0 Å was used) in the calculation. As can be seen in Figure 5.2 the occupied band width was calculated to be 17 eV. There are almost no Ni s and p contributions to states below the Fermi level, which rules out the bonding scheme discussed above. There is a prominent Ni d feature at about -2 eV, and infact there are found to be just over 8 Ni d states per formula unit in the range -4 to 0 eV. This suggests that this feature is mainly derived from four nonbonding Ni d

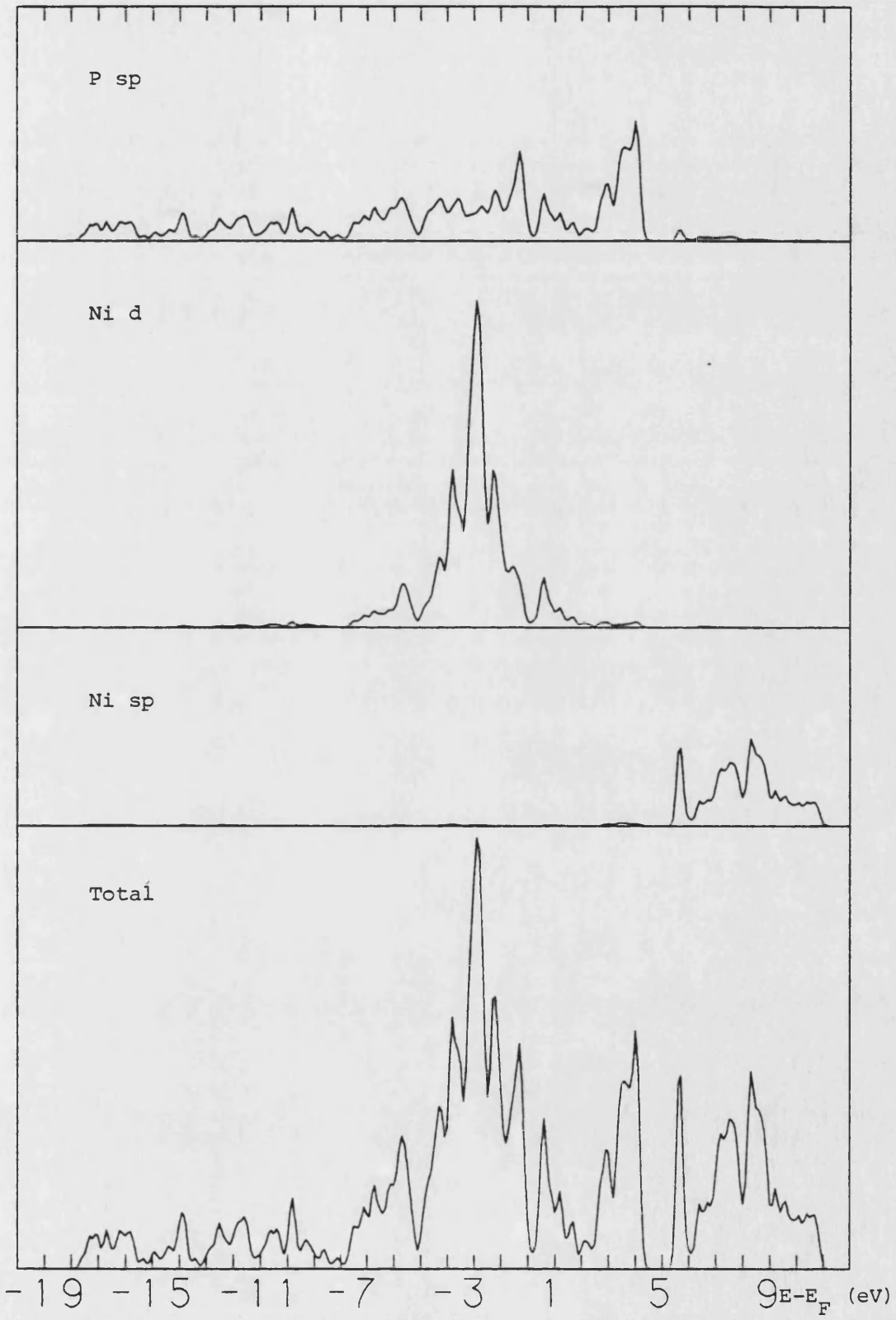

Figure 5.2 The calculated total and projected DOS for NiP_2.

orbitals. The remaining Ni d states lie in the region between -7 and -4 eV and the region between 0 and 5 eV where the states would appear to be derived from a single Ni d orbital per formula unit in a bonding and an antibonding configuration with P sp states respectively. This bonding scheme is consistent with the square planar arrangement of the P atoms with respect to the Ni atoms as in it each lobe of an interacting Ni d orbital can point towards a nearest neighbour P atom. The presence of tetrahedral coordination indicates that sp^3 hybridization of the P sp orbitals takes place. These hybrids would form
bonds between the P atoms and lone pairs pointing towards the Ni atoms and could give rise to the remaining density of states structure seen in Figure 5.2, particularly below -7 eV.

There is a sharp dip in the density of states at the Fermi level, between the nonbonding Ni d and the antibonding Ni d-P sp states, indicating the presence here of a small energy gap of 0.16 eV that has been lost in the smoothing of the data. NiP_2 has also been found to be a semiconductor experimentally, but with a band gap of 0.73 eV (Odile et al., 1978). As was mentioned in Chapter 1, however, the local density approximation, which was used in the construction of the crystal potentials for all the calculations performed in this work (see section 2.2) is known to lead to underestimates of semiconductor band gaps.

The energy and occupation of each valence orbital type is given in Table 5.3. It can be seen that negative charge transfers from the Ni to the P atoms, and this is what would

be expected from the energies of the Ni d and P s and p levels relative to each other.

The crystal AuGeAs, because the Ge and As atoms are in random occupation of the 8(f) sites, does not have a unit cell. However, in order to calculate the electronic structure of this material it was assumed that it did (of the PdP_2 type). In one calculation the same metalloid atom was placed in all of the 8(f) sites and the interactions of this atom with all the other atoms was taken to be the average of the interactions of a Ge and an As atom with those atoms. Such a procedure is generally referred to as a virtual crystal approximation (VCA). The total and projected densities of states calculated for this system, AuGeAs(a), are shown in Figure 5.3. Two further calculations were made in which a PdP_2 type unit cell was again used but in which a particular arrangement of four Ge and four As atoms in the 8(f) sites was used. In one arrangement, AuGeAs(b), two Au atoms had four Ge nearest neighbours, the remaining two Au atoms had four As nearest neighbours, and each metalloid atom had two Au, one Ge and one As nearest neighbour. In the second arrangement, AuGeAs(c), each Au atom had two Ge and two As nearest neighbours, each Ge had two Ge and two Au nearest neighbours, and each As had two As and two Au nearest neighbours. The total and projected densities of states for AuGeAs(b) and AuGeAs(c) are shown in Figures 5.4 and 5.5 respectively. The occupation of each valence orbital type was found to be the same in each of the three calculations, and these are given, together with the orbital energies, in

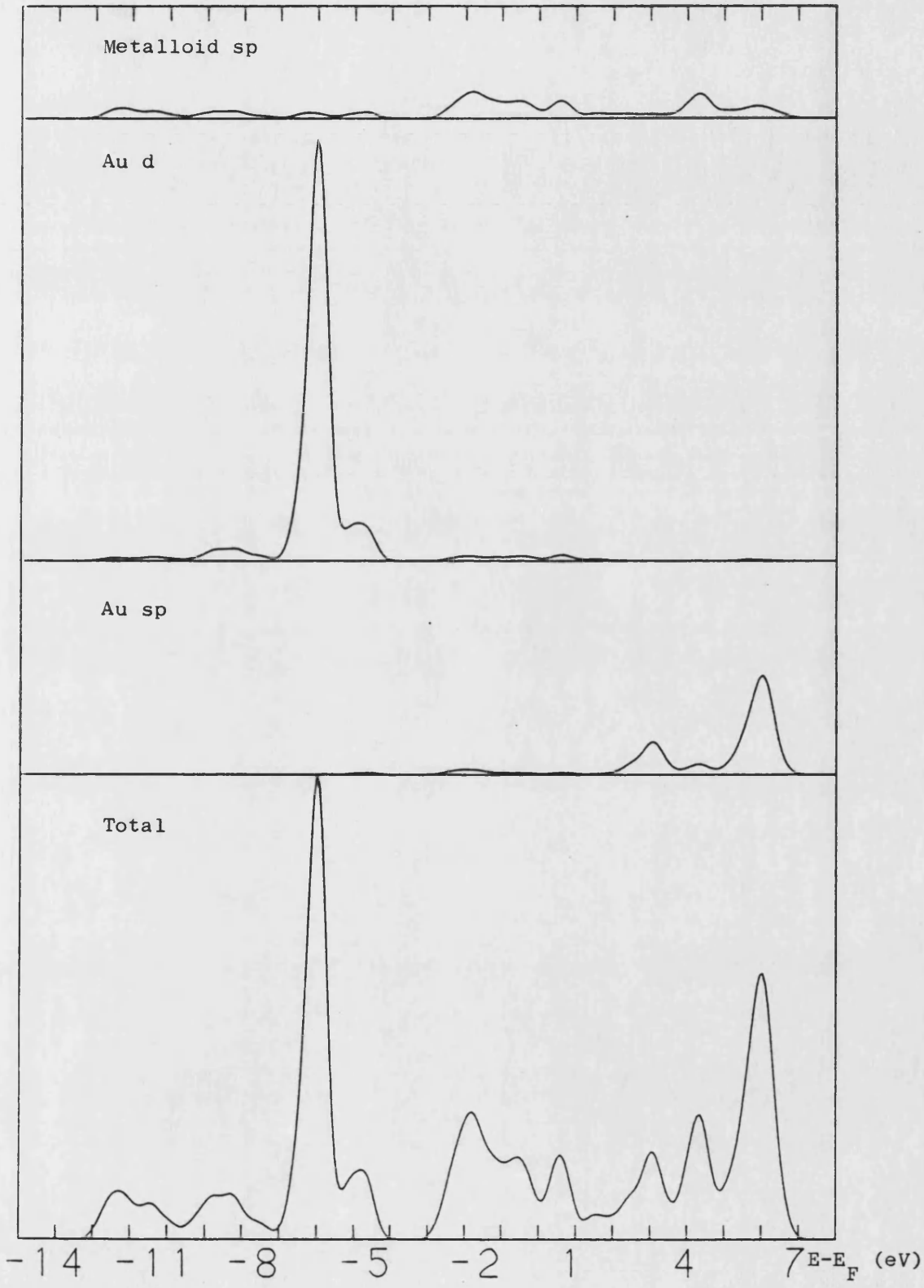

Figure 5.3 The calculated total and projected DOS for AuGeAs(a).

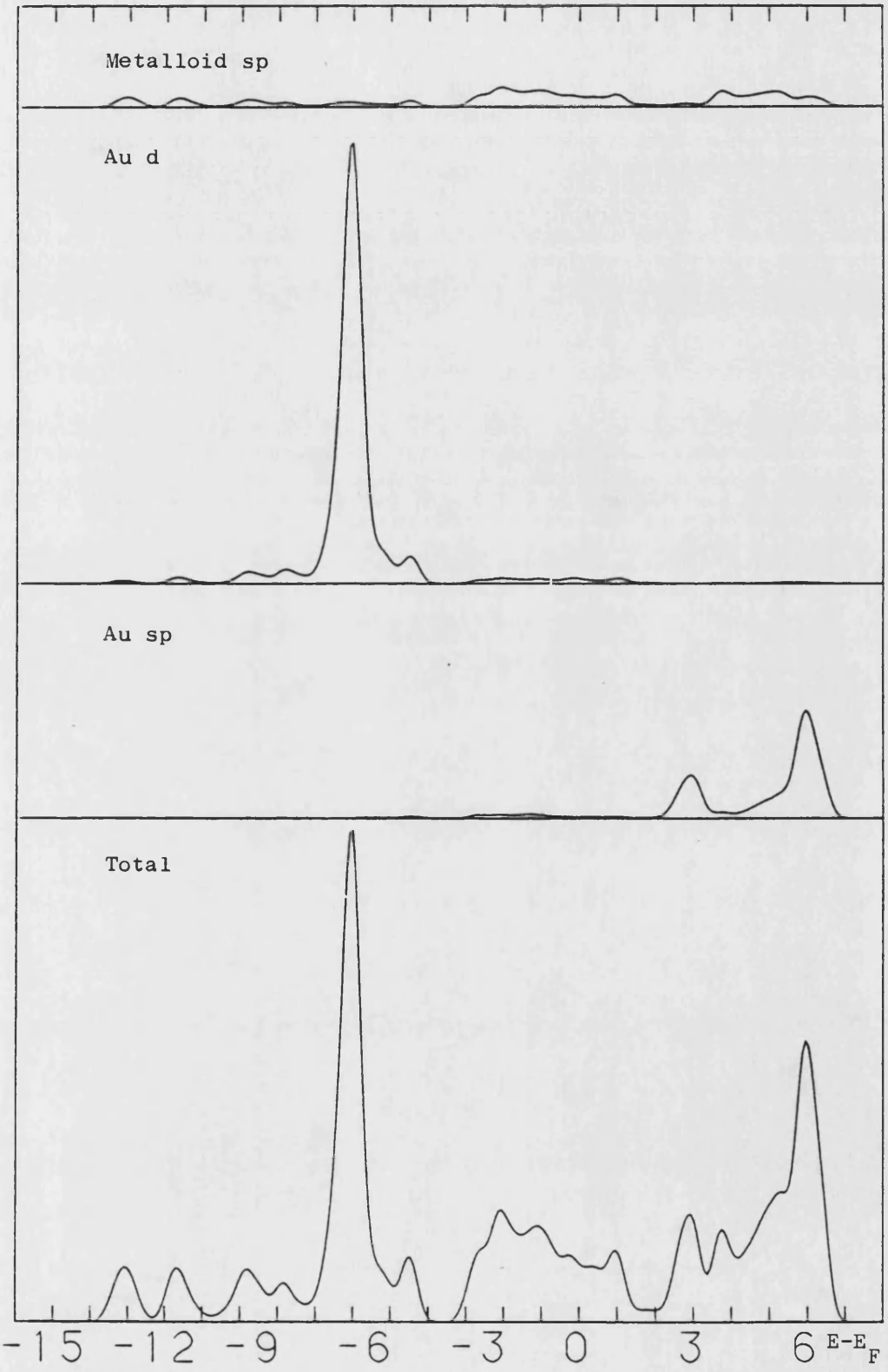

Figure 5.4 The calculated total and projected DOS for AuGeAs(b).

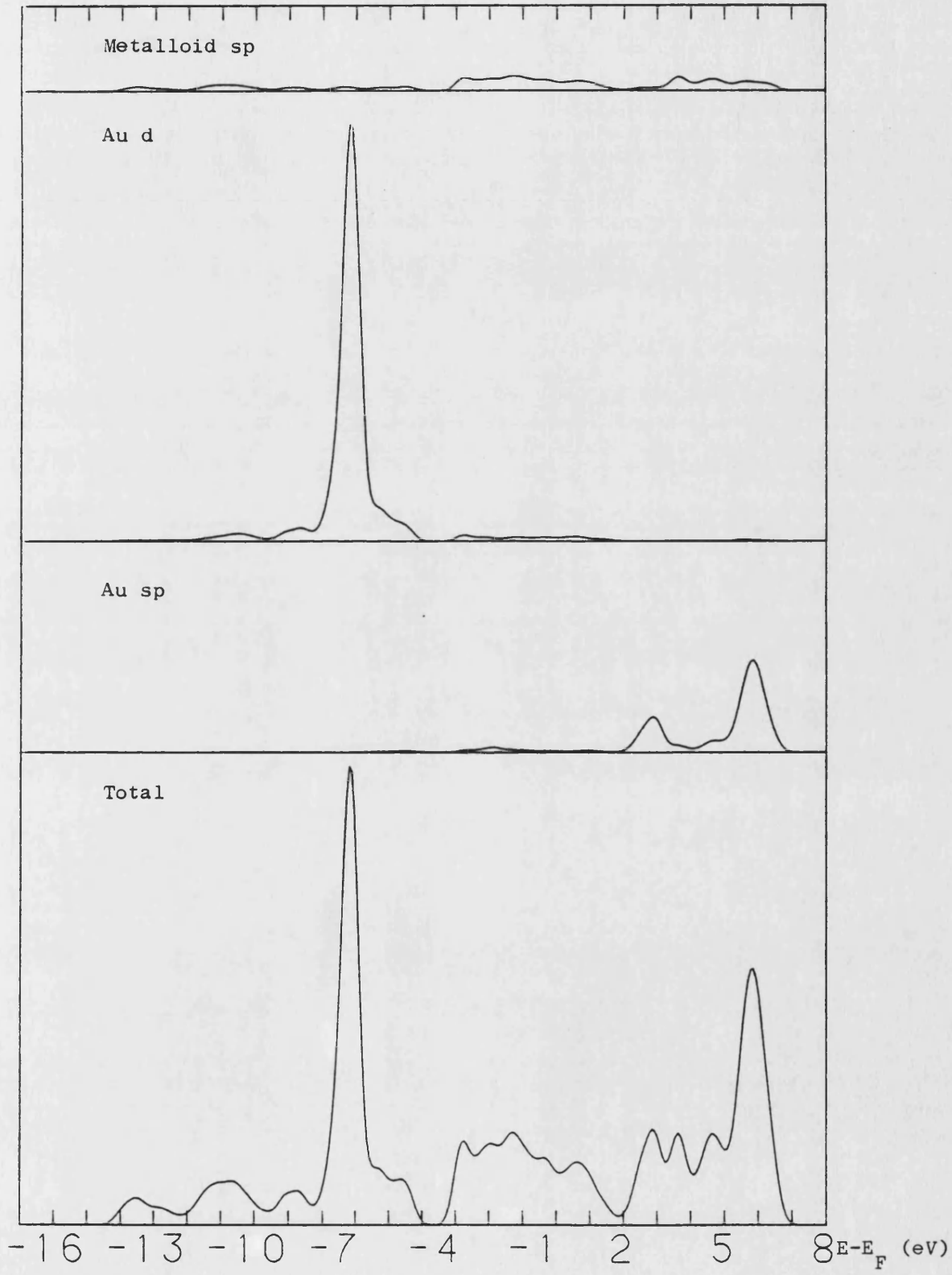

Figure 5.5 The calculated total and projected DOS for AuGeAs(c).

Table 5.3. As in NiP_2 there is negative charge transfer from the metal to the metalloid atoms.

All three calculations give AuGeAs to be a metal, although there is a dip in the density of states at the Fermi level in AuGeAs(a). The author knows of no experimental evidence for AuGeAs being a metal or otherwise. The occupied band width in the three calculations varies between about 12 to 14 eV. In all the calculations there is a narrow Au d feature at -6 eV and a gap above 4 eV (of between 0.5 and 1.0 eV). Below the gap there are 14 states (per formula unit) 8 of which are in the Au d peak. The metalloid states below the gap are mainly s-like. It would thus seem that the states below the gap are derived from four nonbonding Au d orbitals and a single Au d orbital interacting with the nearest neighbour metalloid atoms. This is like the situation in NiP_2, except that here, because the d level of Au has a lower energy than that of the Ni d level, both the bonding and the antibonding Ni d-metalloid s states are below the Fermi level. The states from above the gap up to the Fermi level are the metalloid sp hybrids which give rise to the tetrahedral bonding in the solid. The Au s and p states make almost no contribution to the density of states below the Fermi level.

5.2 The electronic structure of three silver cluster compounds

A family of three silver cluster compounds has recently been synthesised: $Ag_6Ge_{10}P_{12}$, $Ag_6Ge_6Sn_4P_{12}$, and $Ag_6Si_6Sn_4P_{12}$ (von Schnering and Häusler, 1976; Hönle and von Schnering,

1979, 1981). The members of this family all crystallize into the body-centred cubic space group $I\bar{4}3m$ with their atoms occupying the same set of four equivalent positions. The crystallographic details of these three materials are given in Table 5.4.

The structure of these materials will now be described by considering the structure of $Ag_6Si_6Sn_4P_{12}$ in particular. It can be regarded as consisting of $Ag_6Sn_4P_{12}$ clusters interconnected by Si atoms. An $Ag_6Sn_4P_{12}$ cluster is shown in Figure 5.6. It consists of an octahedron of six Ag atoms surrounded by four Sn atoms, one each above four of the eight triangular octahedron faces (forming four Ag_3Sn triangular based pyramids), and two P atoms bonded to each Ag. In the solid these clusters are interconnected (see Figure 5.7) in such a way that each Sn atom is bonded to three P atoms to form a SnP_3 triangular based pyramid, each Si atom is tetrahedrally bonded to four P atoms, and each P is tetrahedrally bonded to one Sn, one Ag, and two Si atoms. The interactomic distances in the three silver cluster compounds are given in Table 5.6.

The calculated total and projected densities of states for $Ag_6Ge_{10}P_{12}$, $AG_6Ge_6Sn_4P_{12}$, and $Ag_6Si_6Sn_4P_{12}$ are shown in Figures 5.8, 5.9 and 5.10 respectively. (See the Note at the end of this chapter). The self-consistent Ag d orbital occupation was found to be the same, 9.95, in all three materials. The valence atomic orbital energies used in the calculations are given in Table 5.7 and the charges found to be on each atomic species from the calculations are given in Table 5.8. The calculated Fermi energies are given in Table

Phase	System	a(A)	Z	Space Group	Atoms	Point Set	x	z
$Ag_6Ge_{10}P_{12}$	Cubic	10.322	2	$I\bar{4}3m$	8Ge	8(c)	2885	
					12Ge	12(d)		
					12Ag	12(e)	1954	
					24P	24(g)	1283	3605
$Ag_6Ge_6Sn_4P_{12}$	Cubic	10.430	2	$I\bar{4}3m$	8Sn	8(c)	2928	
					12Ge	12(d)		
					12Ag	12(e)	1950	
					24P	24(g)	1274	3624
$Ag_6Si_6Sn_4P_{12}$	Cubic	10.315	2	$I\bar{4}3m$	8Sn	8(c)	2960	
					12Si	12(d)		
					12Ag	12(e)	1981	
					24P	24(g)	1263	3716

Table 5.4 The crystallographic details of three silver cluster compounds (von Schnering and Häusler, 1976; Hönle and von Schnering,1979,1981).

Number of positions (Wyckoff notation) and point symmetry		Position coordinates			
		$(0,0,0;\ \frac{1}{2},\frac{1}{2},\frac{1}{2})+$			
8(c)	3m	$x,x,x;$	$x,\bar{x},\bar{x};$	$\bar{x},x,\bar{x};$	$\bar{x},\bar{x},x.$
12(d)	$\bar{4}$	$0,\frac{1}{4},\frac{1}{2};$	$\frac{1}{4},0,\frac{1}{2};$	$\frac{1}{4},\frac{1}{2},0;$	
		$0,\frac{1}{2},\frac{1}{4};$	$\frac{1}{2},0,\frac{1}{4};$	$\frac{1}{2},\frac{1}{4},0.$	
12(e)	mm	$x,0,0;$	$0,x,0;$	$0,0,x;$	
		$\bar{x},0,0;$	$0,\bar{x},0;$	$0,0,\bar{x}.$	
24(g)	m	$z,x,x;$	$x,z,x;$	$x,x,z;$	
		$\bar{z},\bar{x},x;$	$\bar{x},\bar{z},x;$	$\bar{x},\bar{x},z;$	
		$\bar{z},x,\bar{x};$	$\bar{x},z,\bar{x};$	$\bar{x},x,\bar{z};$	
		$z,\bar{x},\bar{x};$	$x,\bar{z},\bar{x};$	$x,\bar{x},\bar{z}.$	

Table 5.5 The equivalent positions of the space group $I\bar{4}3m$ occupied in the silver cluster compounds.

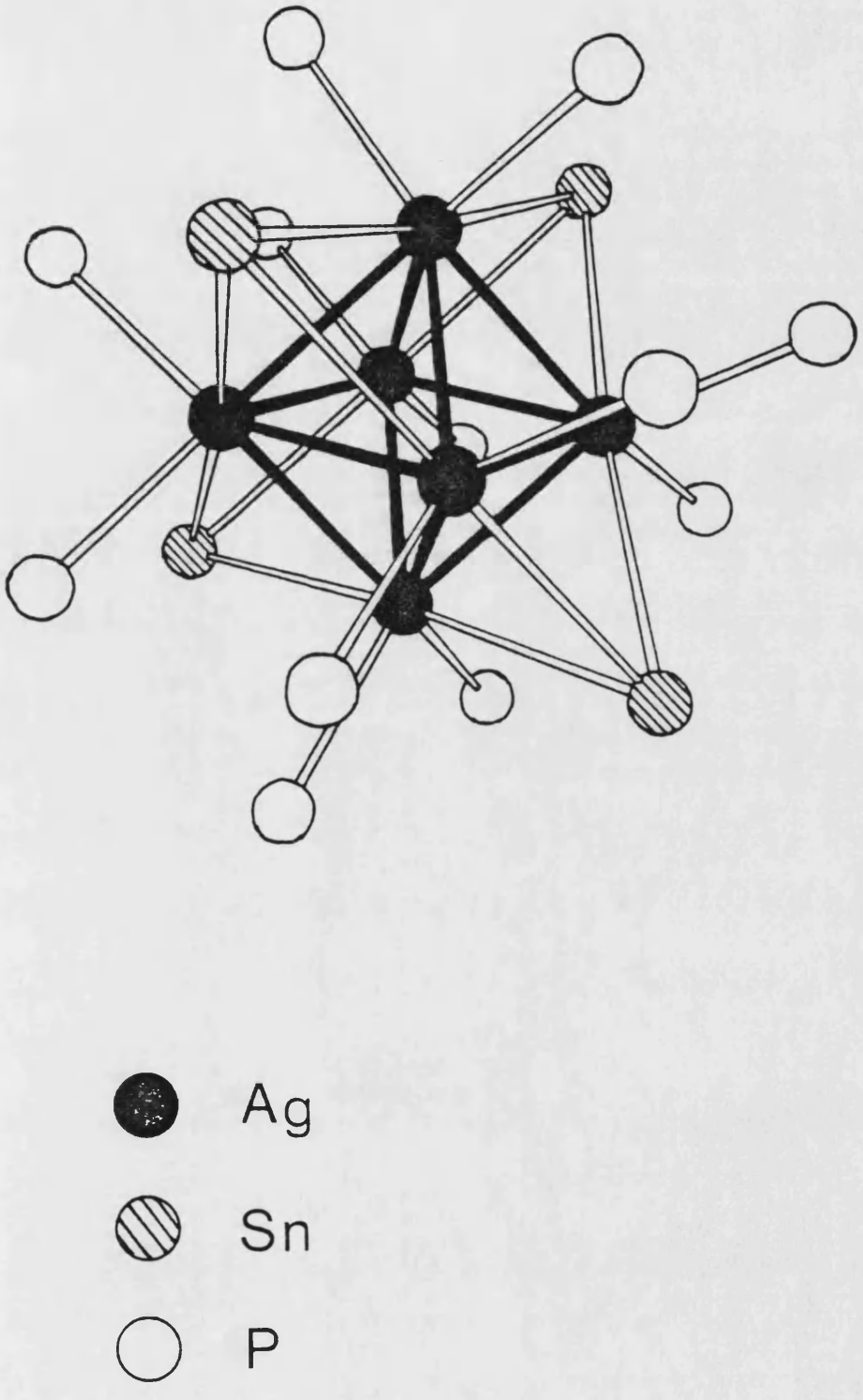

Figure 5.6 An $Ag_6Sn_4P_{12}$ cluster.

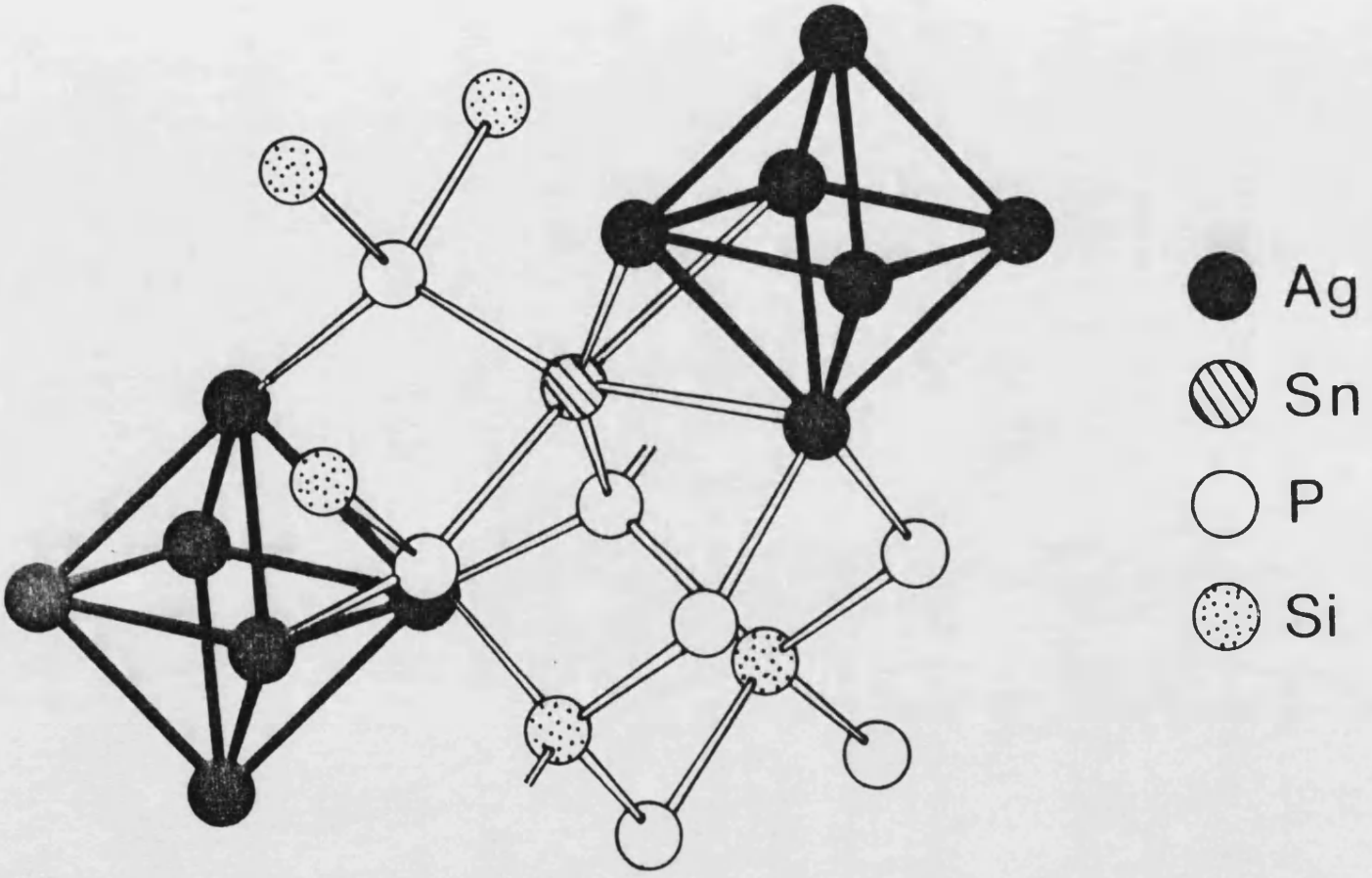

Figure 5.7 A section of the $Ag_6Si_6Sn_4P_{12}$ structure.

Phase	Distances in Å								
$Ag_6Ge_{10}P_{12}$	Ag-Ag(4) 2.85	Ag-Ge(2) 3.09	Ag-P(2) 2.53	Ge-Ag(3) 3.09	Ge-P(3) 2.45	Ge-P(4) 2.33	P-Ag 2.53	P-Ge 2.45	P-Ge(2) 2.33
$Ag_6Ge_6Sn_4P_{12}$	Ag-Ag(4) 2.88	Ag-Sn(2) 3.06	Ag-P(2) 2.57	Sn-Ag(3) 3.06	Sn-P(3) 2.55	Ge-P(4) 2.34	P-Ag 2.57	P-Sn 2.55	P-Ge(2) 2.34
$Ag_6Si_6Sn_4P_{12}$	Ag-Ag(4) 2.89	Ag-Sn(2) 2.98	Ag-P(2) 2.57	Sn-Ag(3) 2.98	Sn-P(3) 2.59	Si-P(4) 2.25	P-Ag 2.57	P-Sn 2.59	P-Si(2) 2.25

Table 5.6 The interatomic distances in three silver cluster compounds. The heading X-Y(n) indicates that an atom of species X has n neighbours of species Y at the distance given.

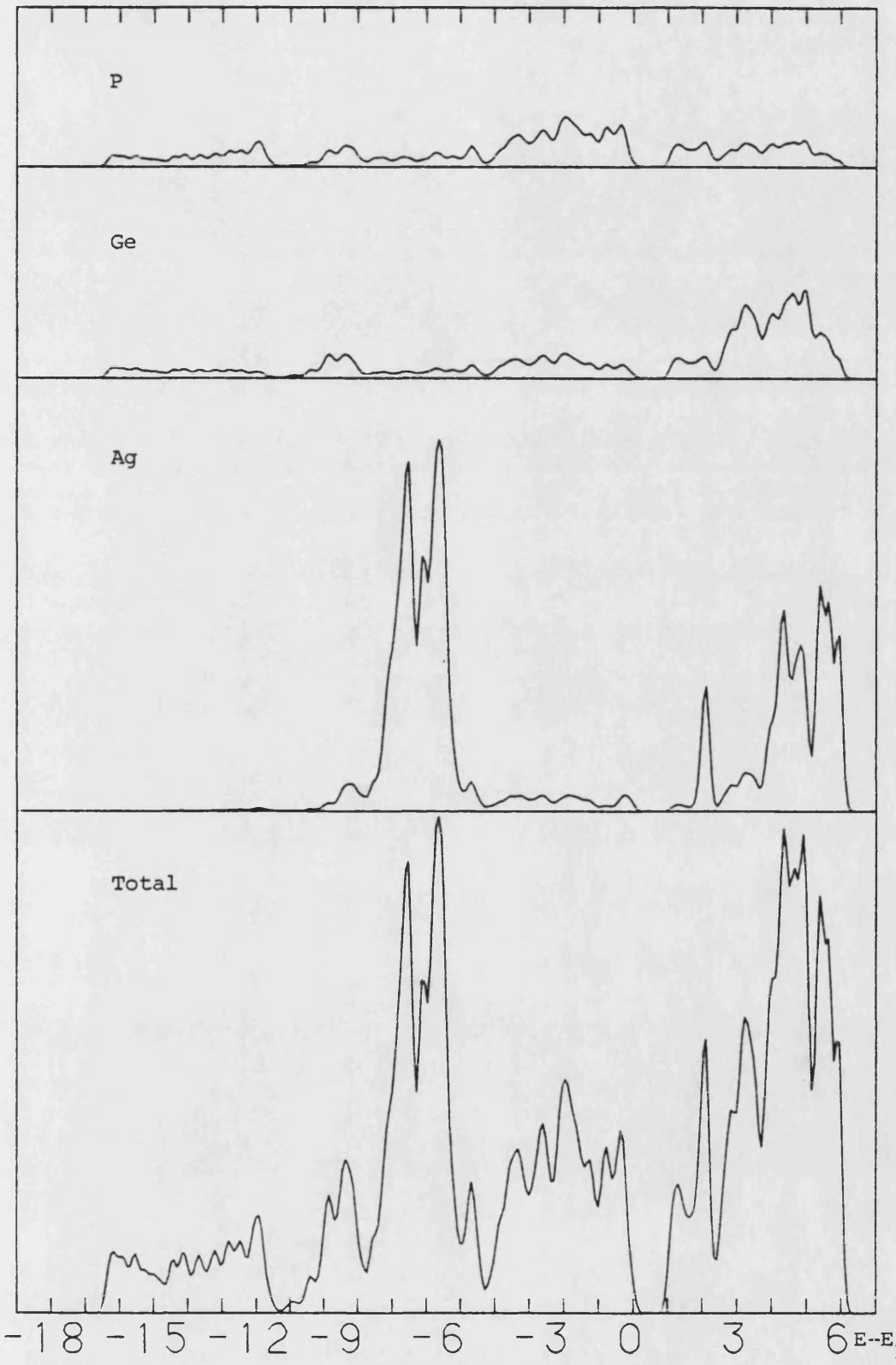

Figure 5.8 The calculated total and projected DOS for $Ag_6Ge_{10}P_{12}$.

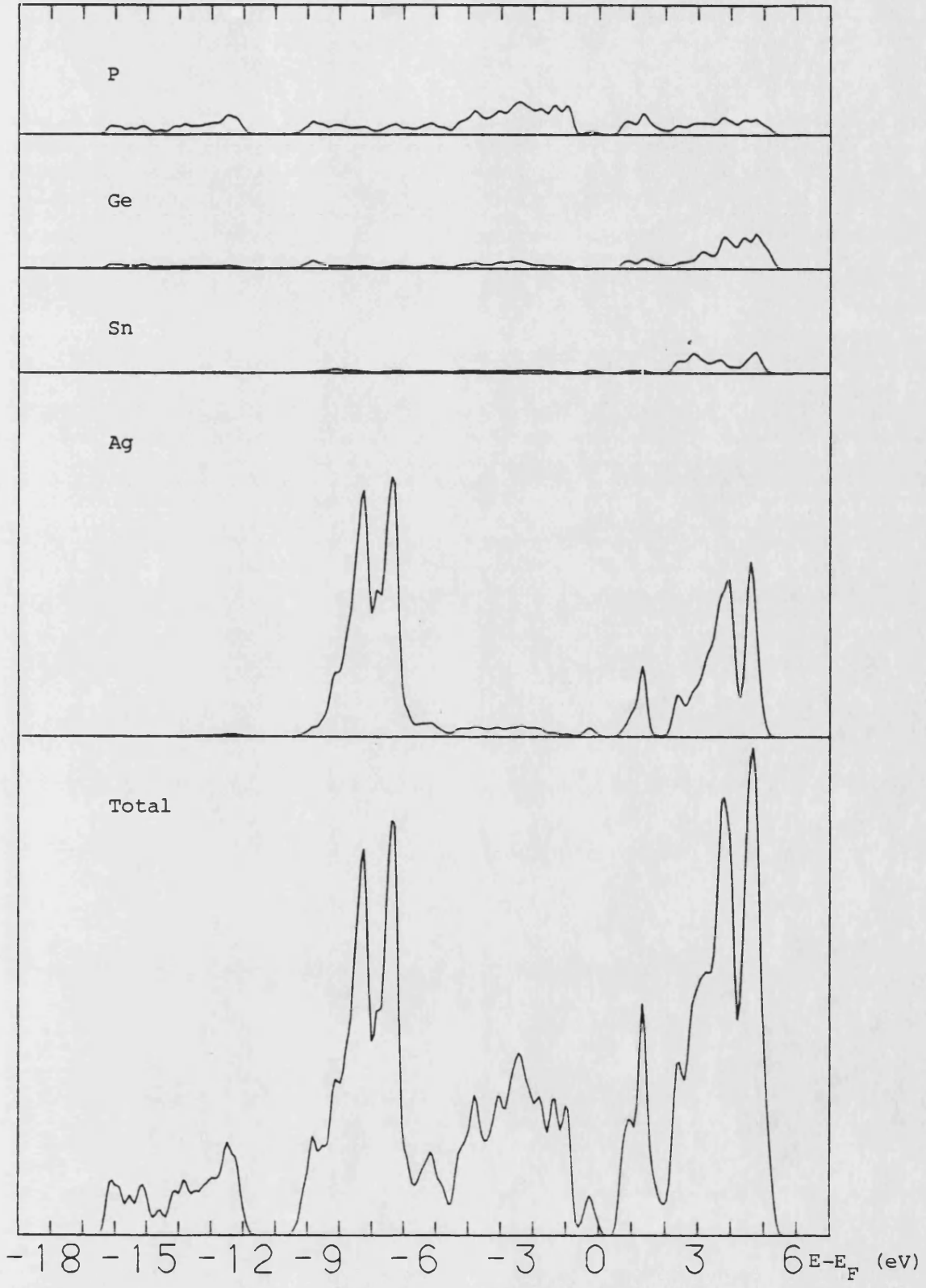

Figure 5.9 The calculated total and projected DOS for $Ag_6Ge_6Sn_4P_{12}$.

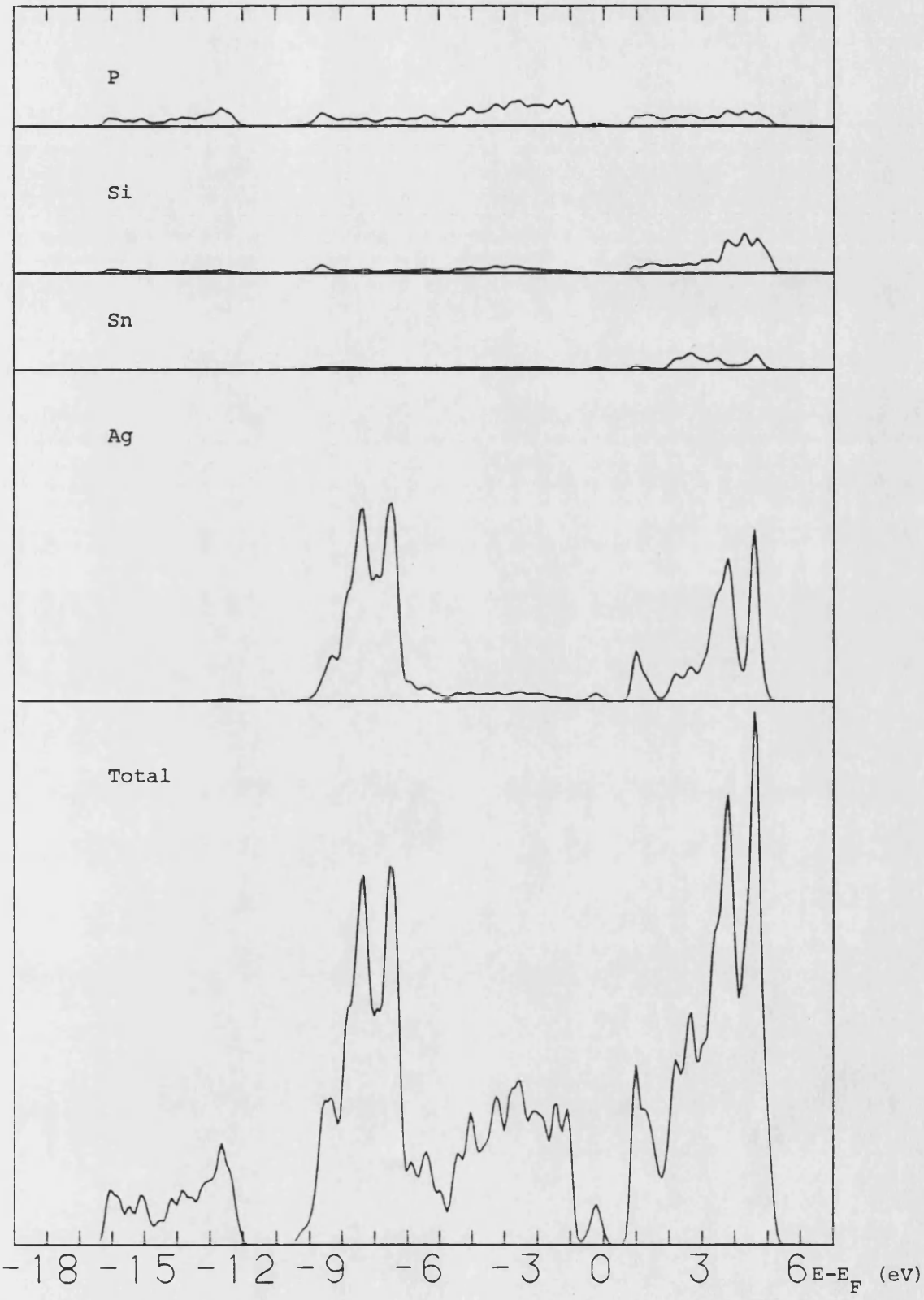

Figure 5.10 The calculated total and projected DOS for $Ag_6Si_6Sn_4P_{12}$.

Atom	Energy (eV)		
	s	p	d
Ag	-6.3	-3.2	-10.2
Si	-11.5	-5.2	
Ge	-12.2	-5.1	
Sn	-10.5	-4.7	
P	-14.6	-6.5	

Table 5.7 Atomic valence orbital energies.

Phase	Charge in electrons/atom				
	Ag	Si	Ge	Sn	P
$Ag_6Ge_{10}P_{12}$	10.7		3.2		5.8
$Ag_6Ge_6Sn_4P_{12}$	10.8		3.0	2.8	6.0
$Ag_6Si_6Sn_4P_{12}$	10.8	2.8		2.8	6.1

Table 5.8 The calculated charges on each atomic species.

Phase	Fermi energy (eV)
$Ag_6Ge_{10}P_{12}$	-4.1
$Ag_6Ge_6Sn_4P_{12}$	-3.4
$Ag_6Si_6Sn_4P_{12}$	-3.3

Table 5.9 The calculated Fermi energies.

Phase	Band gap (eV)
$Ag_6Ge_{10}P_{12}$	1.0
$Ag_6Ge_6Sn_4P_{12}$	0.7
$Ag_6Si_6Sn_4P_{12}$	0.8

Table 5.10 The calculated band gaps.

5.9. In all three materials the lowest energy states, between -10 and -16 eV, have split away from the rest. These are derived mainly from bonding s orbitals on the Group IV and P atoms, particularly the P atoms in $Ag_6Ge_6Sn_4P_{12}$ and $Ag_6Si_6Sn_4P_{12}$. The heavier weighting of these states on the P atoms is due to the lower energy of the P s orbitals relative to those of the Group IV atoms. This also explains the electron transfer from the Group IV atoms to P seen in Table 5.8. The states from just below the Fermi level down to -10 eV are due mainly to bonding group IV and P sp hybrids. At the bottom of this band (between -5 and -8 eV in $Ag_6Ge_{10}P_{12}$ and slightly lower, between -6 and -9 eV, in the other two materials) is a prominent feature derived from nonbonding Ag d orbitals. All three materials have semiconducting gaps the values of which are given in Table 5.10. (Optical and electrical measurements of $Ag_6Ge_{10}P_{12}$ (Köhler et al., 1985) have shown it to be a semiconductor with an absorption edge of 0.76 eV at 300 K which increases to about 0.85 eV at 77 and 10 K.) In $Ag_6Ge_{10}P_{12}$ there is an Ag derived feature which is just below the absolute gap and which is just above the gap in the metalloid density of states. In the other two materials this feature is seen more clearly as it has moved further up into the metalloid gap.

The origin of the semiconducting gap has been explained by the following formal electron counting (Bullett and Witchlow, 1986). A single unit cell will be considered and this has 166 valence electrons. The d orbitals of the six Ag atoms are formally full so that these account for 60

electrons. Each of the twelve P atoms is bonded to three other atoms and supplies one electron to each of the two P-Ge bonds, and one electron to the P-Sn bond. Two more electrons form a lone pair pointing at an Ag atom. This leaves the P atoms formally neutral and accounts for a further 60 electrons. Each of the six Ge atoms is bonded to four P atoms and donates one electron to each of these bonds leaving it also formally neutral and accounting for another 24 electrons. Each of the four Sn atoms is regarded as an Sn^- : each has three Sn-P bonds, each of which takes a single electron from the Sn, and a lone pair pointing towards one of the triangular faces of the Ag octahedron, which take two electrons. (These dangling bonds interact with the triangle of Ag atoms towards which they are directed so that the lone pairs of electrons could alternatively be regarded as taking part in four-centre two-electron bonds, Köhler et al., 1985). This takes care of another 20 electrons and leaves only 2 valence electrons unaccounted for. These go into a bonding sp hybrid formed from a totally symmetric combination of all the Ag s states and p states on a single Ag cluster where the p states are all directed towards the centre of the octahedron. This is the highest filled state and is the Ag derived feature at the Fermi level remarked upon above. Thus, formally, the semiconducting gap occurs above the neutral configuration $(Ag_6)^{4+}Ge_6(Sn^-)_4P_{12}$.

An investigation of the electronic structure of $Ag_6Ge_{10}P_{12}$ has previously been made by Köhler et al.

(1985). In this an extended Hückel calculation using only s and p orbitals was performed for a single $Ag_6Ge_4P_{12}$ cluster. This calculation gave the result that the states near the Fermi level are mainly Ge derived. This is in disagreement with the present calculation in which the states at the Fermi level are heavily weighted on the Ag atoms and the states at the bottom of the conduction band have a large P component.

NOTE ON THE PRESENTATION OF DENSITIES OF STATES IN THIS THESIS

In the figures of this thesis which present densities of states calculated by the author values and tick marks on the abscissa (energy axis) are associated in the following way: positive values are associated with the tick mark directly above the first digit of the number; negative values are associated with the tick mark directly above the minus sign.

APPENDIX A

THE DECOMPOSITION OF A GENERAL TWO-CENTRE INTEGRAL INTO A LINEAR COMBINATION OF SLATER-KOSTER INTEGRALS

When performing an LCAO calculation two-centre integrals such as

$$\langle j_1 m_1 | V | j_2 m_2 \rangle \qquad (A.1)$$

often have to be evaluated. The states $|j_1 m_1\rangle$ and $|j_2 m_2\rangle$ are atomic orbitals. (Dirac notation will be used throughout this appendix.) They have been labelled with their angular momentum quantum numbers and are quantized with respect to the z-axis of the coordinate system xyz of the crystal. The other quantum numbers of the orbitals have been suppressed for convenience. Some integrals of the type (A.1) have both orbitals on the same site (with the potential V centred on a second site), but here only integrals with orbitals on two different sites will be considered. The analysis pertaining to the former kind of integral is practically identical.

First consider a new system of axes x'y'z' which has z' directed along the axis joining the two orbitals (AB in Figure 2.3) and let $\theta\phi\psi$ be the Euler angles for the transformation from xyz to x'y'z' . The state $|j_2 m_2\rangle$, which is quantized with respect to the z-axis, can be expanded in states $|j_2 m_2\rangle'$, which are quantized with respect to the z'-axis, thus:

$$|j_2 m_2\rangle = \sum_{m_2'} |j_2 m_2'\rangle' \; D^{j_2}_{m_2' m_2}(\theta\phi\psi) \qquad (A.2)$$

(Merzbacher, 1970). The state $\langle j_2 m_2|$ can be expanded similarly and hence a term such as (A.1) can be expanded thus:

$$\langle j_1 m_1 | V | j_2 m_2 \rangle = \sum_{m_1' m_2'} {}'\langle j_1 m_1' | V | j_2 m_2' \rangle' \; D^{j_1 *}_{m_1 m_1'} D^{j_2}_{m_2' m_2}. \qquad (A.3)$$

If $V(\underline{r})$ is spherically symmetric so that it is invariant to rotations about the z'-axis however it is chosen then the fundamental matrix element theorem (Heine, 1960) requires that

$$\langle j_1 m_1' | V | j_2 m_2' \rangle' = \langle j_1 m_1' | V | j_2 m_1' \rangle' \, \delta_{m_1' m_2'} \qquad (A.4)$$

and (A.3) becomes

$$\langle j_1 m_1 | V | j_2 m_2 \rangle = \sum_{\mu} \langle j_1 \mu | V | j_2 \mu \rangle' \, D^{j_1 *}_{m_1 \mu} \, D^{j_2}_{\mu m_2} . \qquad (A.5)$$

The terms '$\langle j_1 \mu | V | j_2 \mu \rangle$' are almost universally denoted in the literature by $V_{j_1 j_2 \mu}$. For example '$\langle 00 | V | 10 \rangle$' would be called $V_{sp\sigma}$. Here the letters $\sigma, \pi, \delta, \ldots$ are used for μ running over 0,1,2,... instead of the usual s, p, d, ... so as to indicate that here quantization is with respect to the two-centre axis. Notice that the integrals '$\langle j_1 \mu | V | j_2 \mu \rangle$', the Slater-Koster integrals, do not depend on θ, ϕ, or ψ, but only on the two-centre separation and that the angular dependence of $\langle j_1 m_1 | V | j_2 m_2 \rangle$ is now contained in the terms. $D^{j_1 *}_{m_1 \mu}(\theta\phi\psi)$ $D^{j_2}_{\mu m_2}(\theta\phi\psi)$, the Slater-Koster coefficients. A table of Slate-Koster coefficients is given in Slater and Koster (1954) (and reproduced in Table 2.3) and general expressions for them are given in Sharma (1979). It should be noted that the coefficients given in Slater and Koster (1954) are not exactly given by the expression above as they are for the expansion of integrals between orbitals such as p_x and $d_{x^2-y^2}$ which are not space quantized but which are linear combinations of orbitals that are (see Table 2.1).

APPENDIX B

SOME PROPERTIES OF COMPLETE BUT NON-ORTHOGONAL SETS OF BASIS FUNCTIONS

In this appendix some properties of complete but non-orthogonal sets of basis functions will be considered. Dirac notation will be used together with some notation borrowed from tensor calculus.

Let $\{|\phi_i\rangle\}$ be a complete set of non-orthogonal basis functions (the atomic orbitals used in an LCAO calculation, for example). This set will be referred to here as the covariant basis vectors. Usually the overlap of the basis vectors is written as

$$\langle \phi_i | \phi_j \rangle = S_{ij} \tag{B.1}$$

but here, following tensor notation, this will also be written as

$$\langle \phi_i | \phi_j \rangle = g_{ij} \tag{B.2}$$

where

$$g_{ij} = S_{ij} \, . \tag{B.3}$$

Now another complete set of non-orthogonal basis functions $\{|\phi^i\rangle\}$, the contravariant basis vectors, will be introduced. They are chosen such that

$$\langle \phi^i | \phi_j \rangle = \delta_{ij} \, . \tag{B.4}$$

The relationship of these vectors to the covariant basis set is analogous to that of the primitive reciprocal vectors of a crystal to the direct space primitive vectors of that

crystal. In line with (B.2) equation (B.4) will be also written as

$$\langle \phi^i | \phi_j \rangle = g^i_j \qquad (B.5)$$

where

$$g^i_j = \delta_{ij} \qquad (B.6)$$

and the overlap of the contravariant basis vectors will be written as

$$\langle \phi^i | \phi^j \rangle = g^{ij} . \qquad (B.7)$$

Any general state $|\psi\rangle$ can now be expanded in two different ways. It can either be expanded in the covariant basis vectors

$$|\psi\rangle = \sum_i a^i |\phi_i\rangle \qquad (B.8)$$

or in the contravariant set

$$|\psi\rangle = \sum_i a_i |\phi^i\rangle . \qquad (B.9)$$

The sets of coefficients $\{a^i\}$ and $\{a_i\}$ are the contravariant and covariant components of the vector $|\psi\rangle$ respectively. Multiplying equation (B.8) (equation (B.9)) on the left with the contravariant basis vector $\langle \phi^j |$ (the covariant basis vector $\langle \phi_j |$) and using (B.5) gives

$$a^j = \langle \phi^j | \psi \rangle \qquad (B.10a)$$

$$\left(a_j = \langle \phi_j | \psi \rangle \right) \qquad (B.10b)$$

Substituting this back into equation (B.8) (equation (B.9)) gives

$$|\psi\rangle = \sum_j |\phi_j\rangle\langle\phi^j|\psi\rangle \qquad \text{(B.11a)}$$

$$|\psi\rangle = \sum_j |\phi^j\rangle\langle\phi_j|\psi\rangle \qquad \text{(B.11b)}$$

and hence that

$$\sum_j |\phi^j\rangle\langle\phi_j| = \sum_j |\phi_j\rangle\langle\phi^j| = 1. \qquad \text{(B.12)}$$

This is evidently the closure statement for a complete set of non-orthogonal orbitals. Inserting a unit operator (B.12) into equation (B.10b) gives

$$a_j = \sum_k \langle\phi_j|\phi_k\rangle\langle\phi^k|\psi\rangle \qquad \text{(B.13)}$$

or, using (B.2),

$$a_j = \sum_k g_{jk}\, a^k \qquad \text{(B.14)}$$

which, using (B.3), can also be written as

$$a_j = \sum_k S_{jk}\, a^k . \qquad \text{(B.15)}$$

This relationship is used in section 2.3. Similarly it can be shown that

$$a^j = \sum_k g^{jk} a_k . \qquad \text{(B.16)}$$

Further, expanding out the sum $\sum_j g^{ij} g_{jk}$ using the definitions (B.2) and (B.7) and then using (B.12), (B.5) and (B.6) gives that

$$\sum_j g^{ij} g_{jk} = g^i_k = \delta_{ik} . \qquad \text{(B.17)}$$

The index raising and lowering properties of g^{ij} and g_{ij} shown in (B.14), (B.16) and (B.17) are those that they have in tensor calculus.

Inserting the unit operator (B.12) into the identity

$$|\phi^j\rangle = |\phi^j\rangle \tag{B.18}$$

gives

$$|\phi^j\rangle = \sum_i |\phi_i\rangle\langle\phi^i|\phi^j\rangle \tag{B.19}$$

or, using (B.7),

$$|\phi^j\rangle = \sum_i |\phi_i\rangle g^{ij} \,. \tag{B.20}$$

Inserting (B.20) into the expression for the unit operator (B.12) gives

$$\sum_{ij} |\phi_i\rangle g^{ij}\langle\phi_j| = 1 \,. \tag{B.21}$$

From (B.17) it can be seen that

$$g^{ij} = (g^{-1})_{ij} \tag{B.22}$$

and using this and (B.3) equation (B.21) can be rewritten as

$$\sum_{ij} |\phi_i\rangle (S^{-1})_{ij}\langle\phi_j| = 1 \tag{B.23}$$

which is the more usual expression for a projection operator in terms of non-orthogonal basis functions.

Written in operator form the Schrödinger equation is

$$H|\psi\rangle = E|\psi\rangle. \tag{B.24}$$

The corresponding equation for the eigenbra of the same eigenenergy E is

$$\langle\psi|H = E\langle\psi| \,. \tag{B.25}$$

(The operator H does not have to be altered when acting to the left because it is, of course, a self-adjoint operator.)

Using the expansion (B.8) in (B.24) gives

$$\sum_i H|\phi_i\rangle a^i = \sum_i E|\phi_i\rangle a^i . \qquad (B.26)$$

Multiplying this on the left with the bra $\langle\phi^j|$ gives

$$\sum_i H^j{}_i a^i = E a^j \qquad (B.27)$$

where

$$H^j{}_i = \langle\phi^j|H|\phi_i\rangle . \qquad (B.28)$$

Using the expansion (B.9) in (B.25) gives

$$\sum_j a_j \langle\phi^j| H = \sum_j E a_j \langle\phi^j| \qquad (B.29)$$

and multiplying this on the right with the ket $|\phi_i\rangle$ gives

$$\sum_j a_j H^j{}_i = E a_i \qquad (B.30)$$

where $H^j{}_i$ is again given by (B.28). Hence the right and left eigenvectors of $H^j{}_i$ are the contravariant and covariant components of the eigenvector $|\psi\rangle$ respectively. Using the index raising property of g^{ik} it is possible to write

$$H^j{}_i = \sum_k g^{jk} H_{ki} \qquad (B.31)$$

where

$$H_{ki} = \langle\phi_k|H|\phi_i\rangle . \qquad (B.32)$$

Using (B.22) and (B.3) equation (B.31) can be rewritten as

$$H^j{}_i = \sum_k (S^{-1})_{jk} H_{ki} . \qquad (B.33)$$

Hence it can be seen that the matrix D introduced in section 2.3 is H^j_i, that is to say the mixed (contravariant and covariant) components of H, and that its right and left eigenvectors, a_i and b_i, are the contravariant and covariant components, a^i and a_i, of the eigenfunction respectively.

REFERENCES

I. Abbati, L. Braicovich, B. De Michelis, O. Bisi, and R. Rovetta (1981), Solid St. Comm. 37, 119

W.H. Adams (1961), J. Chem. Phys. 34, 89

W.H. Adams (1962), J. Chem. Phys. 37, 2009

W.H. Adams (1971a), Chem. Phys. Lett. 11, 71

W.H. Adams (1971b), Chem. Phys. Lett. 11, 441

W.H. Adams (1971c), Chem. Phys. Lett. 12, 295

W.H. Adams (1974), Phys. Rev. Lett. 32, 1093

K. Akimoto, T. Ishikawa, T. Takahashi, and S. Kikuta (1983), Jpn. J. Appl. Phys. 22, L798

K. Akimoto, T. Ishikawa, T. Takahashi, and S. Kikuta (1985), Jpn. J. Appl. Phys. 24, 1425

P.W. Anderson (1968a), Phys. Rev. Lett. 20, 413

P.W. Anderson (1968b), Phys. Rev. Lett. 21, 13

P.W. Anderson (1969), Phys. Rev. 181, 25

P.W. Anderson (1984), Physics Reports 110, 311

N.W. Ashcroft and N.D. Mermin (1976), Solid State Physics, Holt, Rhinehart and Winston, New York.

B.J. Austin, V. Heine, and L.J. Sham (1962), Phys. Rev. 127, 276

J. Bardeen (1947), Phys. Rev. 71, 717

J.C. Bean and J.M. Poate (1980), Appl. Phys. Lett. 37, 643

B.K. Bhattacharyya, D.M. Bylander, and L. Kleinman (1985a), Phys. Rev. B 31, 2049

B.K. Bhattacharyya, D.M. Bylander, and L. Kleinman (1985b), Phys. Rev. B 31, 5462

U. Birkholz and J. Schelm (1968), Phys. Stat. Sol. 27, 413

U. Birkholz and J. Schelm (1969), Phys. Stat. Sol. 34, K117

O. Bisi and C. Calandra (1981), J. Phys. C 14, 5479

O. Bisi and L.W. Chiao (1982), Phys. Rev. B 25, 4943

O. Bisi, L.W. Chiao, and K.N. Tu (1984), Phys. Rev. B 30, 4664

F. Bloch (1928), Z. Phys. 52, 555

M. Born and R. Oppenheimer (1927), Ann. d. Phys. 84, 457

R.M. Boulet, A.E. Dunsworth, J.-P. Jan, and H.L. Skriver (1980), J. Phys. F 10, 2197

R.W. Bower, D. Sigurd, and R.E. Scott (1973), Solid-State Electron. 16, 1416

L.J. Brillson (1982), Surface Science Reports 2, 123

L.J. Brillson (1983), J. Phys. Chem. Solids 44, 703

W.D. Buckley and S.C. Moss (1972), Solid-State Electron. 15, 1331

D.W. Bullett (1975), J. Phys. C 8, 2695

D.W. Bullett (1978), J. Phys. C 11, 4501

D.W. Bullett (1979), J. Phys. C 12, 277

D.W. Bullett (1980a), in Solid State Physics: Advances in Research and Applications 35, H. Ehrenreich, F. Seitz, and D. Turnbull, eds., Academic Press, New York.

D.W. Bullett (1980b), J. Phys. C 13, 1267

D.W. Bullett (1982a), J. Phys. C 15, 3069

D.W. Bullett (1982b), J. Phys. C 15, 6163

D.W. Bullett (1982c), J. Phys. C 15, 415

D.W. Bullett and G.P. Witchlow (1986), Phys. Rev. B 33, 2429

D.M. Bylander, L. Kleinman, and K. Mednick (1982a), Phys. Rev. B 25, 1090

D.M. Bylander, L. Kleinman, K. Mednick and W.R. Grise (182b), Phys. Rev. B 26, 6379

C. Calandra, O. Bisi, and G. Ottaviani (1985), Surface Science Reports 4, 271

J. Callaway and N.H. March (1984), in Solid State Physics: Advances in Research and Applications 38, H. Ehrenreich and D. Turnbull, eds., Academic Press, New York.

C. Canali, G. Majni, and G. Celotti (1979), J. Appl. Phys. 50, 255

Y.J. Chabal, D.R. Hamann, J.E. Rowe, and M. Schluter (1982), Phys. Rev. B 25, 7598

Y.-J. Chang and J.L. Erskine (1982), Phys. Rev. B 26, 4766

A. Chantre, A.F.J. Levi, R.T. Tung, W.C. Dautremont-Smith, and M. Anzlowar (1986), Phys. Rev. B 34, 4415

L.J. Chen, J.W. Mayer, K.N. Tu, and T.T. Sheng (1982), Thin Solid Films 93, 91

D. Cherns, D.A. Smith, W. Krakow, and P.E. Batson (1982a), Phil. Mag. A 45, 107

D. Cherns, G.R. Anstis, J.L. Hutchinson, and J.C.H. Spence (1982b), Phil. Mag. A 46, 849

D. Cherns, C.J.D. Hetherington, and C.J. Humphreys (1984), Phil. Mag. A 49, 165

K.C.R. Chiu, J.M. Poate, L.C. Feldman, and C.J. Doherty (1980a) in Thin Film Interfaces and Interactions, J.E.E. Baglin and J.M. Poate, eds., Electrochemical Society, Princeton, NJ.

K.C.R. Chiu, J.M. Poate, L.C. Feldman, and C.J. Doherty (1980b), Appl. Phys. Lett. 36, 544

K.C.R. Chiu, J.M. Poate, J.E. Rowe, T.T. Sheng, and A.G. Cullis (1981), Appl. Phys. Lett. 38, 988

M.L. Cohen (1980), Ad. Electron. Electron Phys. 51, 1

F. Comin, J.E. Rowe, and P.H. Citrin (1983), Phys. Rev. Lett. 51, 2402

J.W. Cooper (1962), Phys. Rev. 128, 681

B.L. Crowder and S. Zirinsky (1979), IEEE J. Solid State Circuits 14, 291

A.S. Davydov (1965), Quantum Mechanics, Pergamon Press, Oxford.

P.A.M. Dirac (1930), Proc. Cambridge Philos. Soc. 26, 376

P.Y. Dusausoy, J. Protas, R. Wandji, and B. Roques (1971), Acta Cryst. B 27, 1209

F. Föll, P.S. Ho, and K.N. Tu (1981), J. Appl. Phys. 52, 250

A. Franciosi and J.H. Weaver (1983), Phys. Rev. B 27, 3554

A. Franciosi, J.H. Weaver, and F.A. Schmidt (1982), Phys. Rev. B 26 546

A. Franciosi, J.H. Weaver, D.G. O'Neill, F.A. Schmidt, O. Bisi, and C. Calandra (1983), Phys. Rev. B 28, 7000

J.L. Freeouf, G.W. Rubloff, P.S. Ho, and T.S. Kuan (1979), Phys. Rev. Lett. 43, 1836

J.M. Gibson, R.T. Tung, and J.M. Poate (1983), in Defects in Semiconductors II, Symposium Proceedings, Boston, MA, USA, Nov. 1982, North-Holland, New York.

T.L. Gilbert (1964), in Molecular Orbitals in Chemistry, Physics and Biology, P.-O. Lowdin and B. Pullman, eds., Academic Press, New York.

W.A. Harrison (1980), Phys. Rev. B 21, 3214

R.J. Hauenstein, T.E. Schlesinger, T.C. McGill, B.D. Hunt, and L.J. Schowalter (1985), Appl. Phys. Lett. 47, 853

L. Hedin and S. Lundqvist (1969), in Solid State Physics: Advances in Research and Applications 23, F. Seitz, D. Turnbull, and H. Ehrenreich, eds., Academic Press, New York.

V. Heine (1960), Group Theory in Quantum Mechanics, Pergamon Press, Oxford.

V. Heine (1980), in Solid State Physcis: Advances in Research and Applications, H. Ehrenreich, F. Seitz, and D. Turnbull, eds., Academic Press, New York.

J.C. Hensel, R.T. Tung, J.M. Poate, and F.C. Unterwald (1984), Appl. Phys. Lett. 44 913

F. Herman and S. Skillman (1963), Atomic Structure Calculations, Prentice-Hall, Englewood Cliffs, New Jersey.

P.S. Ho (1983), J. Vac. Sci. Technol. A 1, 745

P.S. Ho and G.W. Rubloff (1982), Thin Solid Films 89, 433

P.S. Ho, T.Y. Tan, J.E. Lewis, and G.W. Rubloff (1979), J. Vac. Sci. Technol. 16, 1120

P.S. Ho, G.W. Rubloff, J.E. Lewis, V.L. Moruzzi, and A.R. Williams (1980), Phys. Rev. B 22, 4784

P.S. Ho, E.S. Yang, H.L. Evans, and X. Wu (1986), Phys. Rev. Lett. 56, 177

P. Hohenberg and W. Kohn (1964), Phys. Rev. 136 B864

W. Hönle and H.G. von Schnering (1979), Z. Krystallogr. 149, 125

W. Hönle and H.G. von Schnering (1981), Z. Krystallogr. 153, 339

G.A. Hutchins and A. Shepela (1973), Thin Solid Films 18, 313

H. Ishiwara, K. Hikosaka, and S. Furukawa (1979a), J. Appl. Phys. 50, 5302

H. Ishiwara, K. Hikosaka, M. Nagatomo, and S. Furukawa (1979b), Surf. Sci. 86, 711

D.J. Joyner, O. Johnson, D.M. Hercules, D.W. Bullett, and J.H. Weaver (1981), Phys. Rev. B 24, 3122

T. Kawamura, D. Shinoda, and H. Muta (1967), Appl. Phys. Lett. 11, 101

C. Kittel (1976), Introduction to Solid State Physics, Wiley, New York.

K. Köhler, H.J. Queisser, W. Hönle, H.G. von Schnering, and M.C. Böhm (1985), Phys. Rev. B 31, 6514

W. Kohn and L.J. Sham (1965), Phys. Rev. 140, A1133

W. Krakow (1982), Thin Solid Films 93, 109

E. Larsson (1964), Ark. Kemi. 23, 335

M. Lax (1974), Symmetry Principles in Solid State and Molecular Physics, Wiley, New York.

M. Liehr, P.E. Schmid, F.K. LeGouse, and P.S. Ho (1985), Phys. Rev. Lett. 54, 2139

H. Lim and R.E. Allen (1985), J. Vac. Sci. Technol. B 3, 1221

H. Lim and R.E. Allen (1986), J. Vac. Sci. Technol. A 4, 2328

P.O. Löwdin (1950), J. Chem. Phys. 18, 365

J.E. Luveluck, G.M. Rackham, and J.W. Steeds (1978), in

Developments in Electron Microscopy and Analysis 1977, D.L. Misell, ed., The Institute of Physics, London.

O. Madelung (1978), Introduction to Solid-State Theory, Springer-Verlag, Berlin.

J.W. Mayer and K.N. Tu (1971), J. Vac. Sci. Technol. 11, 86

E. Merzbacher (1970), Quantum Mechanics, Wiley, New York.

A. Messiah (1961), Quantum Mechanics, North-Holland, Amsterdam.

R.S. Mulliken (1955), J. Chem. Phys. 23, 1833

S.P. Murarka (1980), J. Vac. Sci. Technol. 17 775

H. Neumann, D.W. Bullett, H. Sommer, R.D. Tomlinson, and W. John (1984), Phys. Stat. Sol. (b) 121, 641

H. Nowotny (1970), in The Chemistry of Extended Defects in Non-Metallic Solids, L. Eyring and M. O'Keeffe, eds., North-Holland, Amsterdam.

J.P. Odile, S. Soled, C.A. Castro, and A. Wold (1978), Inorganic Chemistry 17, 283

G. Ottaviani (1979), J. Vac. Sci. Technol. 16, 1112

G. Ottaviani (1981), J. Vac. Sci. Technol. 18, 924

G. Ottaviani and M. Costato (1978), J. Crystal Growth 45, 365

W.B. Pearson (1972), The Crystal Chemistry and Physics of Metals and Alloys, Wiley-Inerscience, New York.

W.E. Pickett and C.S. Wang (1984), Phys. Rev. B 30, 4719

G.M. Rackham and J.W. Steeds (1981), in Microscopy of Semiconducting Materials 1981, A.G. Cullis and D.C. Joy, eds., The Institute of Physics, London.

J. Robertson (1985), J. Phys. C. 18, 947

G.W. Rubloff (1983a), Advances in Solid State Physics 23, 179

G.W. Rubloff (1983b), Surf. Sci. 132, 268

G.W. Rubloff and P.S. Ho (1982), Thin Solid Films 93, 21

S. Saitoh, H. Ishiwara, and S. Furukawa (1980), Appl. Phys. Lett. 37, 203

S. Saitoh, H. Ishiwara, T. Asano, and S. Furukawa (1981), Jpn. J. Appl. Phys. 22, 1118

M. Schluter (1982), Thin Solid Films 93, 3

W. Schottky (1939), Z. Phys. 113, 367

F. Seitz (1940), Modern Theory of Solids, McGraw-Hill, New York.

R.R. Sharma (1979), Phys. Rev. B 19, 2813

Y. Shiraki (1985), J. Vac. Sci. Technol. B 3, 725

A.K. Sinha, R.B. Marcus, T.T. Sheng, and S.E. Haszko (1972), J. Appl. Phys. 43, 3637

J.C. Slater (1951), Phys. Rev. 81, 385

J.C. Slater (1965), Quantum Theory of Molecules and Solids Vol. 4, McGraw-Hill, New York.

J.C. Slater and G.F. Koster (1954), Phys. Rev. 94, 1498

J.W. Steeds, G.M. Rackham, and D. Merton-Lyn (1981), in Microscopy of Semiconducting Materials 1981, A.G. Cullis and D.C. Joy, eds., The Institute of Physics, London.

K.E. Sundström, S. Petersson, and P.A. Tove (1973), Phys. Stat. Sol. (a) 20, 653

J. Tersoff and D.R. Hamann (1983), Phys. Rev. B 28, 1168

R.D. Thompson and K.N. Tu (1982), Thin Solid Films 93, 265

K.N. Tu and J.W. Mayer (1978), in Thin Films - Interdiffusion and Reactions, J.M. Poate, K.N. Tu, and J.W. Mayer, eds., Wiley-Interscience, New York.

K.N. Tu, E.I. Alessandrini, W.K. Chu, H. Krautle, and J.W. Mayer (1974), Jpn. J. Appl. Phys., Suppl. 2, Part 1, 669

R.T. Tung (1984a), J. Vac. Sci. Technol. B 2, 465

R.T. Tung (1984b), Phys. Rev. Lett. 52, 461

R.T. Tung, J.M. Poate, J.C. Bean, J.M. Gibson, and D.C. Jacobson (1982a), Thin Solid Films 93, 77

R.T. Tung, J.C. Bean, J.M. Gibson, J.M. Poate, and D.C. Jacobson (1982b), Appl. Phys. Lett. 40, 684

R.T. Tung, J.M. Gibson, and J.M. Poate (1983a), Phys. Rev. Lett. 50, 429

R.T. Tung, J.M. Gibson, and J.M. Poate (1983b), Appl. Phys. Lett. 42, 888

R.T. Tung, A.F.J. Levi, and J.M. Gibson (1986a), J. Vac. Sci. Technol. B 4, 1435

R.T. Tung, J.M. Gibson, and A.F.J. Levi (1986b), Appl. Phys. Lett. 48, 1264

R.T. Tung, K.K. Ng, J.M. Gibson, and A.F.J. Levi (1986c), Phys. Rev. B 33, 7077

R.T. Tung, A.F.J. Levi, and J.M. Gibson (1986d), Appl. Phys. Lett. 48, 635

E.J. van Loenen (1986), J. Vac. Sci. Technol. A 4, 939

E.J. van Loenen, J.W.M. Frenken, J.F. van der Veen, and S. Valeri (1985), Phys. Rev. Lett. 54, 827

H.G. von Schnering and K.-G. Häusler (1976), Rev. Chim. Mineral 13, 71

R. Vincent, D.M. Bird, and J.W. Steeds (1984), Phil. Mag. A 50, 745, 765

G.H. Wannier (1937), Phys. Rev. 52, 191

J.H. Weaver, V.L. Moruzzi, and F.A. Schmidt (1981), Phys. Rev. B 23, 2916

J.H. Weaver, A. Franciosi, and V.L. Moruzzi (1984), Phys. Rev. B 29, 3293

J.D. Weeks, P.W. Anderson, and A.G.H. Davidson (1973), J. Chem. Phys. 58, 1388

E.P. Wigner and F. Seitz (1933), Phys. Rev. 43, 804

R.H. Williams (1981), J. Vac. Sci. Technol. 18, 929

R.H. Williams (1982a), Contemp. Phys. 23, 329

R.H. Williams (1982b), Surf. Sci. 132, 122

R.H. Williams (1983), Vacuum 33, 587

X. Wu, H.L. Evans, E.S. Yang, M. Liehr, and P.S. Ho (1985), J. Vac. Sci. Technol. B 3, 1151

R.W.G. Wyckoff (1964), Crystal Structures 1, Wiley -Interscience, New York.

X. Yongnian, Z. Kaiming, and X. Xide (1986), Phys. Rev. B 33, 8602

W.H. Zachariasen (1963), Acta Cryst. 16, 1253

J.M. Ziman (1971), in Solid State Physics: Advances in Research and Applications 26, H. Ehrenreich, F. Seitz, and D. Turnbull, eds., Academic Press, New York.

J.M. Ziman (1972), Principles of the Theory of Solids, CUP, London.